ULTRAFAST MOLECULAR DYNAMICS IN COMPLEXED *TRANS*-STILBENE

Thesis by

Ahmed Abdou Heikal

In Partial Fulfillment of the Requirements
for the Degree of
Doctor of Philosophy

California Institute of Technology
Pasadena, California

1996

(Submitted August 28, 1995)

Acknowledgments

There are a great many people who should be acknowledged for their help and support both before and during my graduate education. To all of those, not mentioned here specifically, you have my deepest gratitude for your efforts. There are, however, a number of individuals who deserve special attention, and I would like to take this opportunity to thank them.

First and foremost, I would like thank the committee members of my candidacy exam (Professors Ahmed H. Zewail, Fred E. Culick, Noel R. Corngold, Rudolph Marcus, Vincent B. McKoy, and William A. Goddard III) for their kindness and generosity. Without your support I would not be here as of today.

I owe my gratitude to my thesis advisor, Professor Zewail, for affording me the rare opportunity of collaborating on many interesting and exciting scientific projects as a member of his group here at Caltech. His patience and willingness to give me the time to try things, learn, and grow as a person is deeply appreciated.

Among the members of Zewail's group whom I have worked beside through the years, I wish to thank in particular: Luis Bañares, Maurice Janssen, Jack Breen, and Christoph Lienau. They introduced me to the field of laser spectroscopy and taught me most of what I know about it.

Besides working with Spencer Baskin in the last few months, I had the pleasure to spend many hours with him, not only in the subbasement of Noyes, but also in a variety of ethnic restaurants here in Pasadena. Spencer is a unique individual with a very rich personality which I have come to appreciate deeply. I learned a great deal from Spencer during long hours of discussion.

Though I have never worked with Chuck Williamson, I owe him a fundamental debt of gratitude for his friendship and support. I shall remember with pleasure all the

time that we have spent playing pool and chatting. His proofreading of this thesis and his suggestions were of great help. I also wish Chuck and Jeanine a very happy life together.

I had the chance to know, on a personal level, other members from Zewail's group, in particular Jennifer Herek, Sang Kyu Kim, Abderrazzak Douhal, Hans Frey, Dean Willberg, and SØren Pedersen. I am thankful for their help during the years and for proofreading some parts of this thesis. I also have had the pleasure to share both the laboratory and the soccer field with Sing Chong and Hakno Lee. I wish them the best in their future endeavors.

Without intending to minimize the contributions of other staff members from the Caltech community too numerous to list by name, I would like to mention a few who helped me during my Ph. D. program. I would like to thank Tom Dunn for his countless visit to our laboratory to repair equipment essential to our research. His problem-solving expertise was always available for us whenever needed. The help of Tony Stark, Guy Duremburg, and Ray Garcia, from the machine shop in the Chemistry Department, is deeply appreciated. I must acknowledge the help of Ruth Brambila who made sure that our purchase orders were delivered on time and as fast as we usually wanted them.

Without the friendship and support of Victoria and Gary Valentine, Yanqin Wu, and Ivett Leyva, my life here in Pasadena would not have been as enjoyable as it has. I am also thankful for the understanding and support of Nahed Ibrahim with whom I have shared a part of my life.

Finally, if my work here at Caltech has been of value, I hope I have succeeded in making my family and friends in Kafr El-Mansoura, a small village somewhere in Egypt, proud. I myself am very proud to relate to all of them and would never have been able to go this far without their love and support through the years.

To my mother

Abstract

Ultrafast molecular dynamics in large molecular systems have been studied using either pump/probe time-of-flight mass spectrometry, or laser-induced fluorescence with time-correlated single photon counting technique. Intramolecular vibrational energy redistribution (IVR) and photoisomerization reaction in alkane-solvated and substituted *trans*-stilbenes are presented. Absent, restricted, and dissipative IVR were identified in stilbene-hexane$_1$ van der Waals complex. The dramatic increase of the density of states upon hexane solvation shifts the threshold for an efficient IVR to much lower excess-energy (~300 cm^{-1} for the dissipative regime) in comparison with the bare molecule (~1170 cm^{-1}). The effects of symmetry, density of states, and number of atoms on IVR were studied by using 4-methoxystilbene, 4,4'-dimethoxystilbene, and 2-phenylindene as model systems. The solvation and structural effects on the isomerization reaction in trans-stilbene is even more dramatic. For the first time, the lowering of the isomerization barrier (~700±100 cm^{-1}) in *trans*-stilbene upon one-hexane complexation is observed experimentally upon and compared with that in the bare molecule (~1250±100 cm^{-1}). Furthermore, the isomerization rate above the barrier in stilbene-(hexane)$_1$ complex is slightly slower than that in bare *trans*-stilbene. As the excess-vibrational energy exceeds the calculated binding energy of the (1:1) complex, the vibrational predissociation channel become open and was accounted for by using a simple kinetic model. Further decrease in the isomerization rate in stilbene-hexane$_n$ clusters was observed as the number of solvent molecules ($n \leq 5$) increases. As the cluster size increases, the rate becomes less dependent on the excess energy in the S_1-state and the separation of the barrier must await theoretical calculations. The solvent polarity (in stilbene-hexanenitrile$_n$ complexes) and isotope effects (in stilbene-hexane-d_{14} complex) on the overall isomerization reaction were also examined. Similar studies were carried out on stilbene-(ethane)$_n$ clusters which has a lower binding energy than stilbene-(hexane)$_n$

clusters which, in turn, make the fragmentation of the cluster more severe. On the other hand, interesting observations were made on the reaction dynamics in a designed set of substituted stilbenes. 4-Methoxystilbene, 4,4'-dimethoxystilbene, 4,4'-dihydroxystilbene, *trans*-β-1-cyclohexene-styrene and 2-phenylindene were used as model systems to study the role of electron conjugation and the torsional motion around C_e-C_{ph} single bond in the isomerization reaction in *trans*-stilbene.

Thesis Advisor: Professor Ahmed H. Zewail

Table of Contents

Part One

PART TWO

PART ONE

Chapter 1

INTRODUCTION

The time evolution of molecular dynamics is mainly on the order of the atomic-scale motion. A microscopic description of the change in chemical reaction rates with temperature is usually described by Arrhenius-type formula in which the rate constant *(k)* is given by:

$$k = A\exp\left(-E_a / KT\right) \tag{1}$$

where A, T, K, and E_a are pre-exponential factor, temperature, Boltzmann constant, and the activation energy, respectively. The revolution in the experimental studies of molecular reaction dynamics started with two technological advances: molecular beams and lasers [1]. With ultrashort laser pulses (10^{-12}-10^{-15} s), molecular dynamics and elementary chemical reaction can be studied in real-time. On the other hand, large molecular systems seeded in a molecular beam can be isolated from any external perturbations with well defined energy in their ground state. In our group here at Caltech, three fundamental type of molecular dynamics are of a great interest to us: intramolecular vibrational energy redistribution (IVR), reactant-to-product state rates, and the transition state dynamics. In general, the time scale for these dynamics extends from a few hundred of picoseconds (IVR and reactant-product rates) to femtoseconds (transition-state lifetime).

How does the energy, initially localized (a time zero) in a specific vibrational mode in a large molecule, evolve in time to other isoenergetic modes ? This is an essential question behind IVR studies in a large spectrum of molecules [1]. The relevance of IVR to chemical reaction dynamics lies in a possible reduction of the dimentionality (mode or bond specificity) of a given reaction. If IVR rate is faster than the rate of a reaction, then the reaction is a statistical and can be characterized only by conserved energy and total angular momentum. In this case, statistical theories can be applied for describing the reaction and the rate will be given by (RRKM theory [2]),

$$k(E_x) = \frac{N^*(E^+)}{h\rho(E_x)} \tag{2}$$

where $N^*(E^+)$ is the total number of quantum states in the transition state in the energy region $E^+ = E_x - E_0$ (where E_0 is the reaction barrier), h is Planck constant, and $\rho(E_x)$ is the density of states in the reactant at excess-vibrational energy E_x. On the other hand, if IVR rate is slower than the reaction rate, then a single rate constant of the reaction can not be defined and all possible combinations of initial and final quantum states have to be considered for a complete description of the reaction [1].

IVR and unimolecular reactions (such as isomerizatoion, dissociation, proton transfer, etc.) have been studied in a large number of molecular systems (see ref. [1]). Among all these molecules, *trans*-stilbene (1,2-diphenyl-ethylene), as a model system for studying IVR and photoinduced *trans-cis* isomerization reaction, has been the center of attention in the last decade [1-7]. There are unique features of the stilbene isomerization which are fundamental to the reaction in a range of different environments: jet-expansion, high pressure gas-phase, and solution [1-7].In the isolated *trans*-stilbene (t-S), the barrier crossing rate (k_{iso}) during the isomerization reaction in the S_1-state is determined by the excess energy above the electronic origin of the first excited state. If this excess energy is lower than the isomerization barrier (E_0), no barrier crossing takes place and the fluorescence lifetime is essentially the radiative lifetime of the *trans* configuration. However, once the excess energy surpass the barrier, the fluorescence lifetime decreases with increasing energy [11-18].

In solution and high pressure gas, the fluorescence lifetime and quantum yield of trans-stilbene no longer depend on the excess energy in the S_1-state [19]. It is likely that the energy transfer from the solute to the solvent molecules is taking place on a very short time scale compared with the fluorescence lifetime. The isomerization-barrier crossing in solution is determined by *the strength of the coupling between the solute and the solvent.* Firstly, for a very weak solute-solvent coupling, the rate limiting-step in isomerization reaction is the rate of collision between these molecules. This collision excites the solute molecules above the barrier and the isomerization rate is expected to increases as the coupling strength increases. The isomerization rate is then expected to increase with the strength of the coupling. Secondly, if the coupling is very strong, a local equilibrium in energy is established for the intermediate species located on the top of the barrier. In this case, a reversible reaction becomes possible and the molecule will recross the barrier in the direction of the *trans*-configuration. Consequently, the rate decreases as the solute-solvent coupling increases. Between these two extremes there is an intermediate case, in which the isomerization rate reaches a maximum.

A controversial feature of the isomerization reaction rate of *trans*-stilbene in solution is that the isomerization rate is an order of magnitude faster than that in the jet-cooled molecule energized above the barrier [3-10]. This behavior contradicts the conventional notion that reactions which undergo large-amplitude motions (*e.g.* the phenyl-ring twisting around the ethylenic double-bond in trans-stilbene) are impeded in the condensed phase. The discrepancy has been explained as a collision-induced reduction in the high degree of nonadiabaticity of the reaction in the isolated molecule [20-22]. The influence of the solute-solvent cluster formation on both the shape and barrier height of the reaction potential energy surface has been proposed as another explanation for these observations

[24-26]. However, different aspects of the reaction dynamics in solution, such as energy transfer, solute-solvent friction, and the modification of the potential energy surface of the reaction, are difficult to be separated experimentally in solution.

To provide some additional insight into the microscopic solute-solvent interaction, studies on the isomerization reaction of isolated stilbene-alkane clusters were conducted using the pump-probe technique with time-of-flight (TOF) mass-spectrometry. With this experimental approach, the effect of solvent-solute interactions can be investigated in the absence of the statistical interaction that characterizes collisional friction in solution and compressed-gas phase. The stilbene-hexane cluster is an excellent candidate for studying solvation effects on photoisomerization reactions for the following reasons: (1) the relatively high binding energy [26] of this cluster provides an opportunity to observe the isomerization reaction at excess energies larger than E_0 without the complication of dissociation dynamics, (2) the spectroscopy and structure [25,26], of the parent molecule and 1:1 complex is known, and (3) intramolecular vibrational energy redistribution (IVR) dynamics is also characterized [26]. Similar studies were also conducted on stilbene-ethane clusters to examine solvent specificity and solute-solvent size ratio effects on the isomerization reaction. Ethane studies play an important role in testing the kinetic model used for the interpretation of hexane-cluster results.

The nature of the potential energy surface and the reaction coordinates involved in the isomerization dynamics can be investigated by using substituted stilbenes. For example, studies on the isomerization dynamics in 1,1'-biindanylidene and 5,6,11,12-tetrahydrochrysene show that the primary motion for isomerization is ethylene torsion and that the phenyl torsion is less important in the reaction [29-33]. The influence of the substituent on the state-dependence of the isomerization has been studied by directly monitoring the triplet state with transient-absorption spectroscopy and by triplet-quenching studies of the isomerization yields [3,4]. Furthermore, the nature of the substituent can have a profound effect on the excited-state mechanism depending on the coupling between the singlet and triplet manifolds. When the substituent enhances the singlet-triplet coupling (*e.g.* nitro-group), the triplet mechanism becomes more competitive. On the other hand, alkyl substitution favors the singlet mechanism. In some cases, such as bromostilbene, a combination of singlet and triplet mechanisms can be involved in the isomerization process [3,4]. Jortner and co-workers [33,34] have tested the RRKM theory by alkyl substitutions in the para position of the phenyl moiety (using 4-methyl-, 4-ethyl-, and 4-propyl-stilbene as model systems). Their results oppose the predictions of RRKM calculations [33,34]. Asymmetrically substituted stilbenes (with electron-donating and electron-accepting groups in the two para positions) can display even more varied behavior [35,4]. In these systems, intramolecular charge transfer becomes possible and the charge-transfer state can provide another relaxation pathway for the S_1-state which competes with the isomerization channel(s) [35,4].

To understand specific structural effects on the overall intramolecular dynamics (IVR as well as photoisomerization reaction dynamics) in jet-cooled *trans*-stilbene, picosecond time-resolved laser induced fluorescence measurements were conducted on a designed set of stilbene derivatives. The role of density of states, symmetry, number of vibrational modes, electronic conjugation, and the intramolecular chemical-bridging of the C_e-C_e double-bond in the molecular dynamics in stilbenes was investigated. 4-Methoxystilbene, 4,4'-dimethoxystilbene, 4,4'-dihydroxystilbene, *trans*-β-1-cyclo-hexane-styrene, and 2-phenylindene were used as model systems for the studies presented in this thesis.

The thesis consists of two parts. Studies of solvation effects on IVR and photoisomerization dynamics in *trans*-stilbene-(alkane)$_n$ clusters are described in part one (from Chapter 1 to Chapter 6) of the thesis. The second part (Chapter 7 and Chapter 8) contains a full account of experimental investigations of structural effects on the same type of molecular dynamics (*i.e.* IVR and isomerization) in a desigened set of *trans*-stilbene derivatives. The thesis is organized as follows: Chapter 2 contains a detailed description of the two experimental techniques which were utilized in the picosecond molecular dynamics research. A background on the S_1-state dynamics in isolated *trans*-stilbene, including IVR and photoisomerization reactions, is given in Chapter 3. Chapter 4 describes studies on picosecond vibrational dynamics in *trans*-stilbene-(hexane)$_1$ cluster using Time-Correlated Single Photon Counting technique (TCSPC). In Chapter 5, a full account of solvation effects on the photoisomerization reaction in *trans*-stilbene-(hexane)$_n$ clusters is presented. Similar studies on the isomerization reaction in *trans*-stilbene-(ethane)$_n$ clusters are described in Chapter 6. Different types of studies on the same type of dynamics but with focusing on structural effects on both IVR and photoisomerization reaction in substituted *trans*-stilbenes constitute Chapter 7 and 8, respectively.

1.1 REFERENCES

1. A. H. Zewail, in: *Femtochemistry: Ultrafast Dynamics of the Chemical Bond* (World Scientific Series in 20th Century Chemistry, Singapore, 1994); and articles therein.
2. L. R. Khundkar, R. A. Marcus, and A. H. Zewail, *J. Phys. Chem.* **87**, 2473 (1983).
3. J. Saltiel and Y. P. Sun, in: Photochromism: Molecules and Systems, eds. H. Dürr, and H. Bouas-Laurent (Elsevier, Amsterdam, 1990) p. 64.
4. D. H. Waldeck, *Chem. Rev.* **91** (1991) 415.
5. M. Lee, J. N. Haseltine, A. B. Smith III, and R. M. Hochstrasser, *J. Am. Chem. Soc.* **111**, 5044 (1989); and references therein.
6. G. R. Fleming, S. H. Courtney, and M. W. Balk, *J. Stat. Phys.* **42**, 83 (1986).
7. R. Mohrschladt, J. Schroeder, D. Schwarzer, J. Troe, and P. Vöhringer *J. Chem. Phys.* **101**, 7566 (1994); and references therein.
8. F. H. Long and K. B. Eisenthal in: *Ultrafast Processes in Chemistry and Photobiology*, eds. M. A. El Sayed, I. Tanaka, and Y. Molin, (Blackwell Science, Oxford, 1995) p. 129.
9. U. Åberg, E. Åkesson, J.-L. Alverez, I. Fedchenia, and V. Sundström, *Chem. Phys.* **183**, 269 (1994).
10. J. A. Syage, *Laser Focus World* vol. **30**, no. 10, 73 (1994).
11. L. Bañares, A. A. Heikal, and A. H. Zewail, *J. Phys. Chem.* **96**, 4127 (1992).
12. J. A. Syage, P. M. Felker, and A. H. Zewail, *J. Chem. Phys.* **81**, 4706 (1984).
13. P. M. Felker and A.H. Zewail, *J. Phys. Chem.* **89,** 5402 (1985).

14. J. A. Syage, W. R. Lambert, P. M. Felker, A. H. Zewail, and R. M. Hochstrasser, *Chem. Phys. Lett.* **88**, 266 (1982).

15. J. Troe and J. Schroeder, *J. Phys. Chem.* **90**, 4215 (1986).

16. J. Troe, *Chem. Phys. Lett.* **114**, 241 (1985).

17. T. J. Majors, U. Even, and J. Jortner, *J. Chem. Phys.*, **81**, 2330 (1984).

18. A. Amirav and J. Jortner *Chem. Phys. Lett.* **95**, 295 (1983).

19. R. M. Hochstrasser, *Can. J. Chem.* **37**, 1367 (1959).

20. J. A. Syage, P. M. Felker, and A. H. Zewail, *J. Chem. Phys.* **81**, 4706 (1984).

21. P. M. Felker and A. H. Zewail, *J. Phys. Chem.* **89,** 5402 (1985).

22. P. M. Felker, W. R. Lambert, and A. H. Zewail, *J. Chem. Phys.* **82**, 3003 (1985).

23. G. Maneke, J. Schroeder, J. Troe, and F. Voss, *Ber. Bunsen-Ges. Phys. Chem.* **89**, 896 (1985).

24. J. Schroeder, D. Schwarzer, J. Troe, and F. Voss, *J. Chem. Phys.* **93**, 2393 (1990).

25. J. Schroeder and J. Troe, *Chem. Phys. Lett.* **116**, 453 (1985).

26. C. Lienau, A. A. Heikal, and A. H. Zewail, *Chem. Phys.* **175**, 171 (1993).

27. C. Lienau, Ph.D. Dissertation work at Göttingen (1992).

28. J. Saltiel and J. T. D'Agostino, *J. Am. Chem. Soc.* **94**, 6445 (1972).

29. M. Lee, A. J. Bain, P. J. McCarthy, C. H. Han, J. N. Haseltine, A. B. Smith, and R. M. Hochstrasser, *J. Chem. Phys.* **85**, 4341 (1986).

30. S. C. Shim and J. S. Chae, *Bull. Chem. Soc. Jpn.* **55**, 1310 (1982),

31. J. Saltiel, O. C. Zifiriou, E. D. Megarity, and A. A. Lamola, *J. Am. Chem. Soc.* **90**, 4759 (1968).

32. C. Pyun, T. A. Lyle, G. H. Daub, and S. M. Park, *Chem. Phys. Lett.* **124**, 48 (1986).

33. T. J. Majors, U. Even, and J. Jortner, *J. Chem. Phys.* **81**, 2330 (1984).

34. K. Rademann, U. Even, S. Rosez, and J. Jortner, *Chem. Phys. Lett* **125**, 5 (1986).

35. W. Rettig and W. Majenz, *Chem. Phys. Lett.* **154**, 335 (1989).

Chapter 2

EXPERIMENTAL TECHNIQUES

2.1 INTRODUCTION

The experiments which are described in this thesis were performed using either pump-probe with time-of-flight mass selectivity (TOFMS), or laser-induced fluorescence with time-correlated single-photon counting (TCSPC) techniques. Molecules (or clusters) of interest were seeded into a molecular beam to be isolated from any external perturbations. This chapter will describe the two experimental setups. The rest of this chapter is organized as follows. In Section 2.2, a brief description of the pump/probe time-of-flight mass-selection technique will be presented. This will include the picosecond laser system (Sec. 2.2.1), the molecular beam apparatus (Sec. 2.2.2), and data acquisition (Sec. 2.2.3). In Section 2.3, the laser induced fluorescence with time-correlated single photon counting technique is described. This will include the picosecond laser system (Sec. 2.3.1), the supersonic jet expansion (Sec. 2.3.2), the fluorescence detection system (Sec. 2.3.3), and data analysis (Sec. 2.3.4).

2.2 PUMP-PROBE TIME-OF-FLIGHT MASS-SELECTION TECHNIQUE

In pump/probe TOFMS experiments (shown schematically in Fig. 2.1), the reaction of interest, *e.g.*, the isomerization in *trans*-stilbene, is initiated by a picosecond laser-pulse (pump laser). A second picosecond laser-pulse (probe laser), at a latter time, samples the remaining population of the reactants by exciting them to the ionization continuum. The total ion signal is mass-selected and detected as a function of the delay time between pump and probe pulses. The time resolution of a pump-probe experiment depends solely on the cross-correlation of the pump and probe laser pulses. General applications of this methodology have been reviewed in detail elsewhere [1].

2.2.1 The Picosecond Laser System

The picosecond laser system [2, 3] is consisted of a mode-locked (ML), *Q*-switched (QS) and frequency doubled Nd:YAG laser which synchronously pumped two tunable cavity-dumped picosecond dye lasers. Along with the three lasers, there is the delay-line required for the pump-probe experiments, the optics required for second harmonic generation (SHG), and the necessary optics to steer the lasers into the molecular beam, see Fig. 2.2.

2.2.1.1 The Nd:YAG Laser

The mode-locked (Quantronix, model number 351) and Q-switched (Quantronix, model number 352) Nd:YAG laser (henceforth referred to as the YAG laser) was homebuilt with components intended for building the Quantronix 416 laser system [3]. The laser was mode-locked at 76 MHz, and could be operated at various Q-switching repetition rates, typically at 90 Hz for the use with the pulsed nozzle. The Q-switch repetition rate was 500 Hz, and was fired by an external trigger (the dual pulse generator which also controlled the pulsed nozzle). Vertical polarization (with respect to the optical table) *inside* the laser cavity was selected via a fused quartz plate mounted at the Brewster angle. A KTP crystal (cut for type II phase matching) was used to frequency double the 1.06 μm output of the YAG laser, which produced an energy of 800 μJ per *Q*-switched pulse envelope at 532 nm. The polarization of the 532 nm light was selected using a λ/2-waveplate, and the 532 nm was separated from the 1064 nm fundamental with a dichroic beam splitter. The temporal width of a mode-locked pulse within the Q-switched pulse envelope was measured to be ~100 ps (full width at half maximum (FWHM)).

The mode-locked pulses and *Q*-switch envelopes were monitored on daily basis by directing the leakage out of the high reflector onto a photodiode (E. G. & G. FND-100) [4]. The signal from this photodiode was used to monitor the YAG laser's performance, and to trigger the cavity dumpers in the dye lasers. These photodiodes have a rise- and fall-time on the order of a few nanoseconds, which is sufficient to resolve the mode-locked pulses (12.8 ns peak-to-peak spacing).

2.2.1.2 The Synchronously Pumped Cavity Dumped Dye Lasers

The 532 nm light from the YAG laser was split with a 30/70 beam splitter in order to synchronously pump the two (pump and probe) cavity dumped, etalon-tuned dye lasers (see Fig. 2.2). two independent dye lasers (pump and probe). The cavity of each one [5] is bound by two flat, broadband, high reflecting mirrors (the mirrors were coated for 600 nm). A plano-convex lens is the focusing element in the cavity, and is placed at its focal length (25 cm) relative to the end of the cavity (M_1). The front mirror (M_2) of the cavity is mounted on a Klinger TR80 transitional stage so that the optical path in the dye laser can be matched to the optical path in the YAG laser. Synchronously pumping of the dye laser requires matching the cavity lengths.

The flowing dye cell (with 1.6 mm quartz windows spaced 1 mm apart) is mounted at the Brewster angle and is placed close to M_1. The 532 nm pulse train from the YAG is brought in as collinear as possible to the optical path inside the dye laser. In order to enhance the pumping efficiency, the 532 nm laser beam is focused (with the 40 cm plano-convex lens) to match the dye laser spot size at the dye cell. Both the 532 nm light from the YAG laser and the lasing *inside* the dye-laser cavity are horizontally polarized with respect to the optical table.

The cavity dumper consists of an electro-optic Pockels' cell (Quantum Technology, model QK-10-1) operated at its quarter-wave-plate voltage coupled with Glan laser prism (Karl Lambrecht, model MGLA-SW-8). The Pockels' cell contains a deuterated KDP crystal, acting as a $\lambda/4$-waveplate when a 2.4 kV (determined empirically for 600 nm) voltage is placed transversely across the crystal. The trigger source for the Pockels' cell was a SRS model DG535 digital delay generator. The Glan prism allows horizontally-polarized light to pass through, while vertically-polarized light is ejected out of the cavity.

The wavelength of the dye lasers was selected by angle-tuning the intracavity Fabry-Perot etalon (Virgo Corp) and using a laser dye with the appropriate gain profile. Lasing would occur at a frequency where the transmission bandwidths of the etalon would overlap with the gain profile of the dye. The etalon is a 5 μm fixed air gap etalon [6]; the inner surfaces of this etalon were coated for 70% reflectivity (at 600 nm). Figure 2.3 shows the bandwidth of the pump laser set at 630 nm with the 5 mm etalon and the cross-correlation of both pump and probe laser (visible) pulses. The energy of the visible dye-laser pulse was ~5 μJ and that of the frequency-doubled laser pulse was ~0.2 μJ. The bandwidth of both lasers (close to Gaussian in profile) had FWHM of ~18 cm^{-1}.

The pump laser was collimated, frequency-doubled, and delayed (in time) with respect to the probe laser. The variable temporal delay was achieved by using a Michelson interferometer type delay line which was operated by a linear positioning stage (Aerotech ATS224) derived by a stepper motor. This stage had a spatial resolution of 1 μm/step and total range of 60 cm (*i.e.* full delay time of 4 ns can be achieved). Typically, 2250 steps per data point (which correspond to a temporal delay of ~14.1 ps) was used. A corner cube (Precision Lapping, 1 s accuracy) was mounted on the stage to reflect the pump laser. The probe laser was simply collimated and directed along a static delay line. Both pump and probe lasers were directed, parallel to each other, to the molecular beam through a quartz window.

2.2.2 The Molecular Beam Apparatus

The molecular beam apparatus is shown schematically in Fig. 2.4. The beam apparatus consists of three chambers: the source, buffer, and time-of-flight (TOF) compartment. A thorough description of the dimensions of the vacuum chambers is given in reference [1]. The source chamber is pumped by a Varian VHS-10 diffusion pump, while each of the buffer and TOF chambers are pumped by Varian VHS-6 diffusion pumps. In order to minimize liquid nitrogen expenditures, a VHS-10 cryobaffle was converted to operate with institutional chilled water as a coolant. The VHS-10 diffusion pump is backed by a Leybold-Heraeus D90A mechanical pump, while a single Leybold-Heraeus D60A mechanical pump backs the other two VHS-6 diffusion pumps.

The pulsed nozzle (General Valve Series 9) has a pinhole diameter *(d)* of 150 μm with a conical cross-section (35°) for maximum cluster formation [7]. A diagram of the nozzle and sample holder configuration is shown in ref. [4]. The nozzle is mounted on a carriage which can be translated along the molecular beam axis. This design allows adjustment of the x/d ratio; x is the nozzle-to-laser distance. The pulsed nozzle driver was limited to a repetition rate of 90 Hz to achieve very high stagnation pressures. The triggering of the pulsed nozzle was controlled by a homebuilt dual pulse generator, which also controlled the firing of the Q-switch in the YAG laser. Furthermore, the pulse generator controlled the following three parameters that were crucial for proper operation of the nozzle:

(1) pulse width one (PW1) (250 - 380 μs), which determined how long the nozzle was open; (2) delay time two (DL2), typically 550-740 μs, which synchronized the gas pulse with the laser *Q*-switch; and (3) the repetition rate of the nozzle, typically 90 Hz. The pulsed nozzle was located at ~2 cm from the first of the two skimmers. Both pump and probe lasers were focused and spatially overlapped on the skimmed molecular beam at a distance of ~5 cm from the second skimmer, in the buffer chamber. The ions were then extracted, accelerated and focused on the ion detector after traveling through a field-free region in the TOF compartment.

2.2.3 Data Acquisition System

The data acquisition system was described in detail elsewhere [1] and only a brief description will be presented here. As shown in Fig. 2.1, two types of data acquisition schemes could be employed depending on whether one wanted to obtain the TOF mass spectrum of the ionization products, or the integrated signal of a mass-selected ion.

To measure the intensity of one particular ion species, the amplified MCP signal was sent to a Stanford Research Systems Gated Integrator (henceforth referred to as the boxcar). The gate of the boxcar could be adjusted so that only the signal of a mass-selected ion would be integrated over. The averaged signal from the boxcar was sent to a National Instruments A/D board (model NB-MIO-16H-9), which was interfaced with a Macintosh II computer. Both the boxcar and the A/D board required triggering from the SRS-535 digital delay generator. Rates were determined by fitting the transients to a single (or double) exponential decay function including convolution with the system response function. A Marquardt nonlinear least squares fitting routine was used [6,8]. The rising edge of each of the transients was well fit by the system response of 60-70 ps (see Fig.

2.3), corresponding to the measured cross correlation between our pump and probe laser pulses.

For recording a TOF mass spectrum of the ionization products, the amplified signal from the MCP was sent to a fast waveform analyzer consisting of a 100 MHz transient digitizer (LeCroy 8818A), a memory module (LeCroy MM8103A), and controller unit (LeCroy 6010 Interface Controller Unit). The analyzer was based in a CAMAC crate (LeCroy 8013A) and triggered by the delay generator (Stanford Research Systems, model DG535). The digitized TOF mass spectrum was transferred to the Macintosh II computer via a National Instruments interface board (NB-DMA-8-G GPIB).

2.3 LASER INDUCED FLUORESCENCE WITH TIME CORRELATED SINGLE-PHOTON COUNTING TECHNIQUE

In this technique, the time-evolution of the S_1-state population is monitored by time- and frequency-resolving the laser-induced fluorescence of the jet-cooled molecules using time-correlated single-photon counting (TCSPC) In the following Sections, a detailed description of the experimental setup for this technique is given, see Fig. 2.5.

2.3.1 Picosecond-Laser System

The 514 nm line of Ar^+ laser (Spectra-Physics 2030-20) was mode-locked (81.6 MHz) to produce ~170 ps pulses. These pulses synchronously pumped a cavity-dumped (Spectra-Physics 344) dye laser (Spectra-Physics 371). The output was picosecond pulses of ~4 MHz repetition rate in the visible, which were then frequency doubled to generate a UV wavelength, Fig. 2.6. The resulting temporal and frequency pulse widths (FWHM) of the UV laser were ~15 ps and ~5 cm^{-1}, respectively [1]. The tuning element of the dye laser wavelength is a three-plate birefringent filter.

2.3.2 Supersonic-Jet Expansion

A carrier gas (helium) with a backing pressure of 20-70 psi was passed over the molecule (*e.g. trans*-stilbene) of interest which was heated in a pyrex nozzle to a temperature lower than the melting point of that molecule (*e.g.* 120 °C for *trans*-stilbene). The resulting gas mixture was expanded through a ~60 μm pinhole as a continuous supersonic jet into a 36"x12" cylindrical stainless-steel chamber. The chamber was evacuated with a 12" booster diffusion pump (Edwards 18B4A) with a pumping speed of 4000 $l.s^{-1}$ ($<10^{-2}$ Torr) which was backed with a 250 $m^3.hr^{-1}$ roughing pump (Kinney KT-150). The pressure inside the chamber was less than 5 mTorr during the expansion. To create stilbene-(hexane) clusters in the expansion, the carrier gas was seeded with hexane molecules by passing the gas over hot hexane before reaching the stilbene compartment inside the chamber.

The jet-cooled molecules (or clusters) were excited with tunable UV picosecond-laser pulses at a nozzle-to-laser distance *(x)* of about thirty times the pinhole diameter *(d)*, *x/d* ~30.

2.3.3 Fluorescence Detection System

The laser-induced fluorescence (LIF) from the jet-cooled molecules (clusters) was focused on the slit of a 0.5 m monochromator (Spex, model 1870) and detected by a microchannel plate photomultiplier tube (PMT) (Hamamatsu, model R2287U) in an orthogonal configuration relative to both the jet expansion and laser beam. The temporal data were measured using the time-correlated single photon counting method [11]. The PMT signal was amplified by a video amplifier (Comlin CDC100, 500 MHz), shaped and discriminated against by a discriminator (Tennelec 455), and then used to start charging a capacitor in a time-to-amplitude converter (TAC) (Ortec 457). Stop pulses for the TAC were provided by intercepting the visible laser with a modified Hewlett-Packard 5082 fast photodiode [12]. The photodiode signal was delayed, amplified (by a 1.3 GHz Hewlett-Packard 8447 amplifier), shaped, and discriminated against as with the PMT pulses. The TAC output was collected by a Tracor Northern TN-1706 multichannel analyzer (MCA) operated in the pulse-height analysis mode. The frequency-resolved fluorescence was measured by counting the total number of detected fluorescence photons using the MCA (operated in multichannel scaling mode), while the grating of the 0.5 m monochromator was scanned by a microprocessor control (Spex CD2). The data was read, stored, and analyzed using a DEC-PDP 11/23 computer (see Fig. 2.5).

2.3.4 Data Analysis

For the time-resolved fluorescence measurements, the fluorescence decays were fit to the most simple exponential form possible. To correctly account for the limited temporal resolution of the excitation source and the detection system, the convolution of such decays with the system response function has to be considered. The temporal system response function was measured by moving the nozzle assembly into the path of the laser beam and detecting the slightly-scattered laser. The response function had a FWHM of 60 - 90 ps. The shape and stability of the response function were monitored before and after each decay.

The measured decays were convoluted with the system response function and fit using the nonlinear least-squares method with Marquardt's algorithm [10, 11]. The least-squares method minimizes the deviation of the measured data from a fit of an assumed functional form, *i.e.* the chi-squared statistic (χ^2). The distribution of the residual (*i.e.* the number of standard deviations each point is away from the fit) and the values of χ^2 were used to judge the goodness of the fit.

The wavelength of the 0^0_0-transition band in *trans*-stilbene (3101.4 Å) and the 6328 Å line of the He-Ne laser were used for the monochromator calibration and alignment.

2.4 REFERENCES

1. L. R. Khundkar and A. H. Zewail, *Ann. Rev. Phys. Chem.* **41**, 15 (1990).
2. L. W. Peng, Ph.D. Thesis, California Institute of Technology, (1991).
3. D. M. Willberg, Ph.D. Thesis, California Institute of Technology, (1993).
4. G. H. McCall, *Rev. Sci. Instr.* **43**, 865 (1972).
5. F. G. Patterson, Ph. D. Thesis, Stanford University (1985).
6. W. Demtroder, *Laser Spectroscopy, Basic Concepts and Instumentation*, (Springer-Verlag, Berlin, 1982) p.157.
7. M. Kappes, and S. Leutwyler, in *Atomic and Molecular Beam Methods* Vol.**1**, ed. By G. Scoles, (Oxford University Press, 1988) p.38.
8. J. C. Postelwaite, J. B. Meirs, C. C. Reiner, and D. D. Dlott, *IEEE J. Quantum Electronics*, **24**, 411 (1988).
9. J. N. Demas, *Excited State Lifetimes Measurements* (Academic Press, New York, 1983).
10. P. R. Bevington, *Data Reduction and Error Analysis for the Sciences* (McGraw-Hill, New York, 1969).
11. D. V. O'Connor and D. Phillips, *Time-Correlated Single Photon Counting*, Academic Press, New York, 1984.
12. G. H. McCall, *Rev. Sci. Inst.* **43**, 865 (1972).

2.5 FIGURE CAPTIONS

2.1. Schematic diagram for pump/probe and time-of-flight mass spectrometry. The applied voltage on the repeller, extractor, lens, and microchannel plate (MCP) are V_R, V_E, V_L, and V_{MCP}, respectively. PA: pre-amplifier, BC: boxcar, A/D: National Instruments A/D interface board, TD: transient digitizer, and IB: NB-DMA-8-G GPIB board.

2.2. Schematic diagram for the picosecond laser system for the pump/probe technique. Mi: mirror, LH: laser head, A: aperture, P: polarizer, ML: modelocker, L: plano-convex lens, KTP: KTP doubling-crystal, BS: 30/70 beam splitter, SHG: crystal for single harmonic generation, DC: dye cell, E: 5-μm etalone, GW: Glan prism, PC: Pockel cell, CC: corner cube, and VDL: variable delay line.

2.3. The molecular beam apparatus with the expansion, buffer, and time-of-flight chambers. There is a diffusion pump for each chamber.

2.4. Top: a Gaussian cross-correlation between the pump (620 nm) and probe (650 nm) laser pulses with FWHM of ~70 ps. Bottom: the dye laser (620 nm) bandwindth.

2.5. An experimental scheme for the laser induced fluorescnce and time-correlated single photon counting system. In this diagram, BS: beam splitter, L: lens, PMT: multichannel plate, AMPi: amplifier, D: discrimenator, TAC: time-to-amplitude converter, PD: photodiode, and MCA: multichannel analyzer.

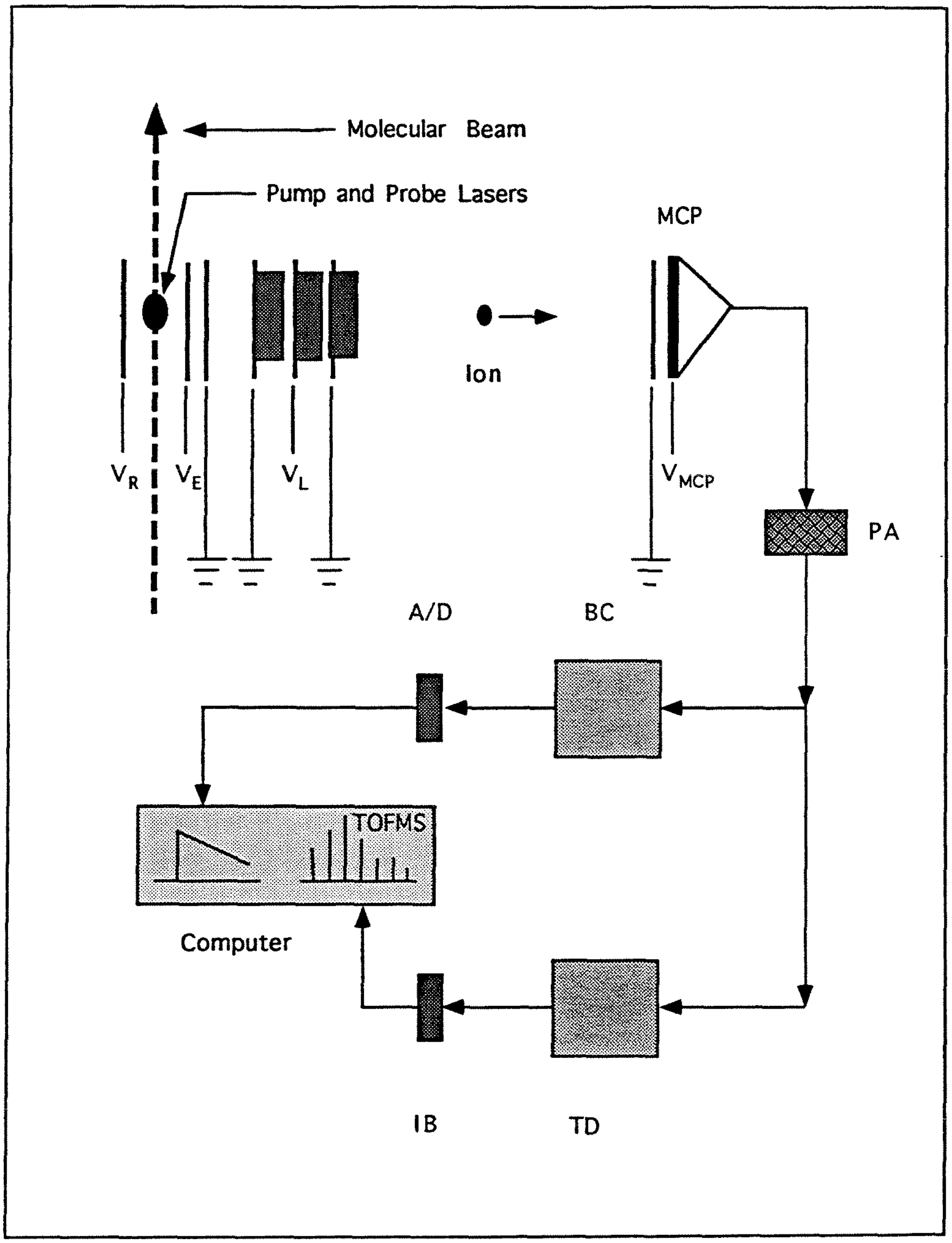
Molecular Beam
Pump and Probe Lasers
MCP
Ion
V_R
V_E
V_L
V_{MCP}
PA
A/D
BC
TOFMS
Computer
IB
TD

Fig. 2.1

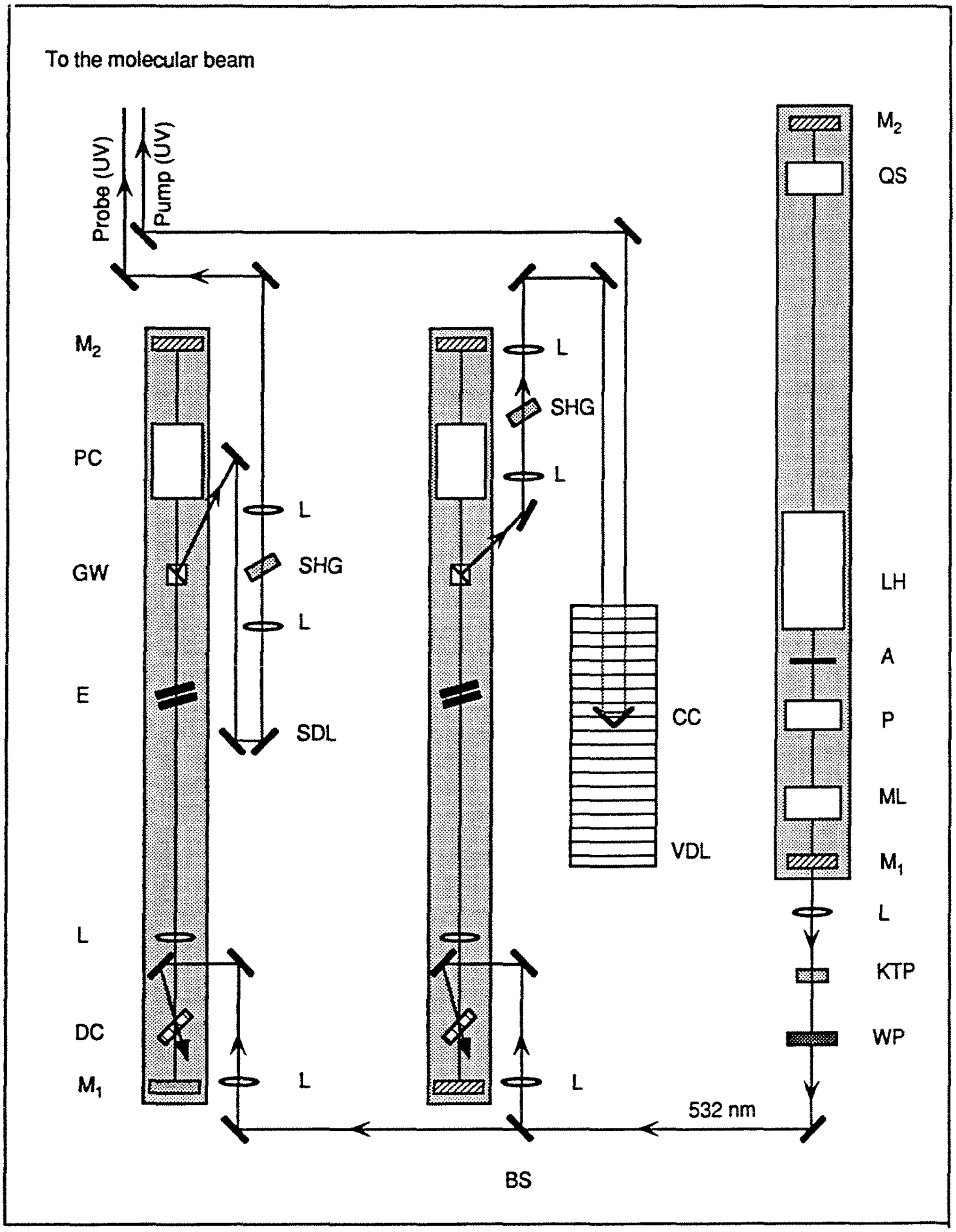
To the molecular beam
Probe (UV)
Pump (UV)
M2
PC
GW
E
L
DC
M1
L
SHG
L
SDL
L
L
SHG
L
L
CC
VDL
M2
QS
LH
A
P
ML
M1
L
KTP
WP
532 nm
BS

Fig. 2.2

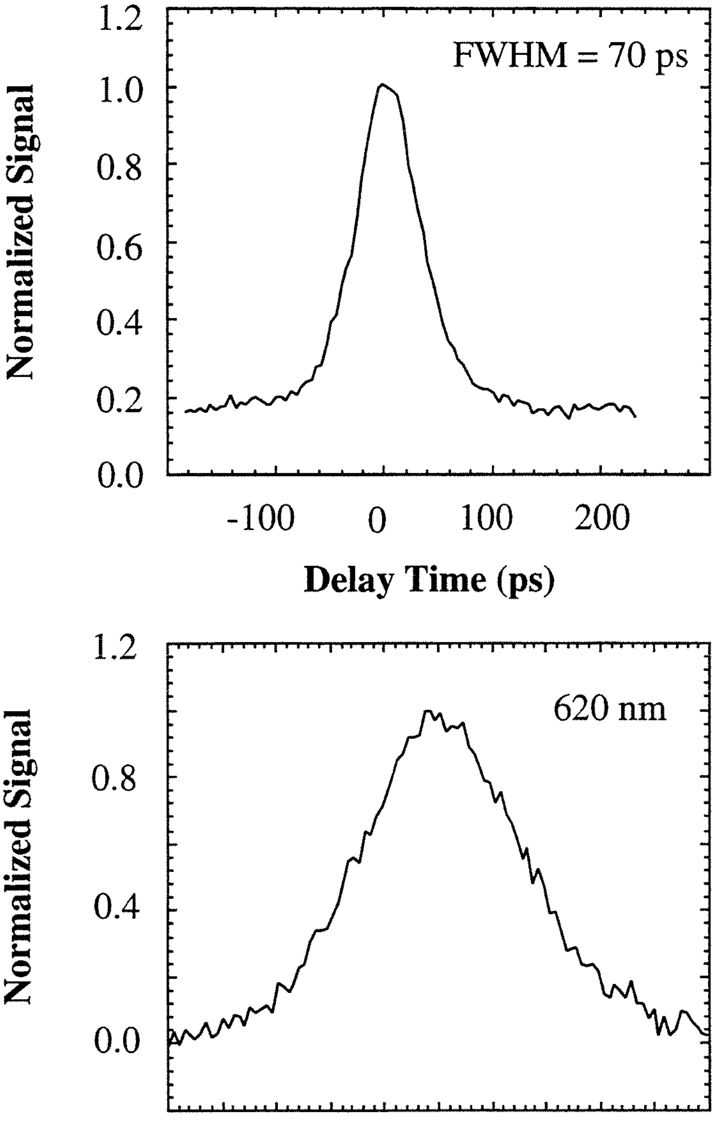
1.2
1.0
0.8
0.6
0.4
0.2
0.0
Normalized Signal
FWHM = 70 ps
-100
0
100
200
Delay Time (ps)
1.2
0.8
0.4
0.0
Normalized Signal
620 nm
-20
-10
0
10
20
Laser Bandwidth (cm-1)

Fig. 2.3

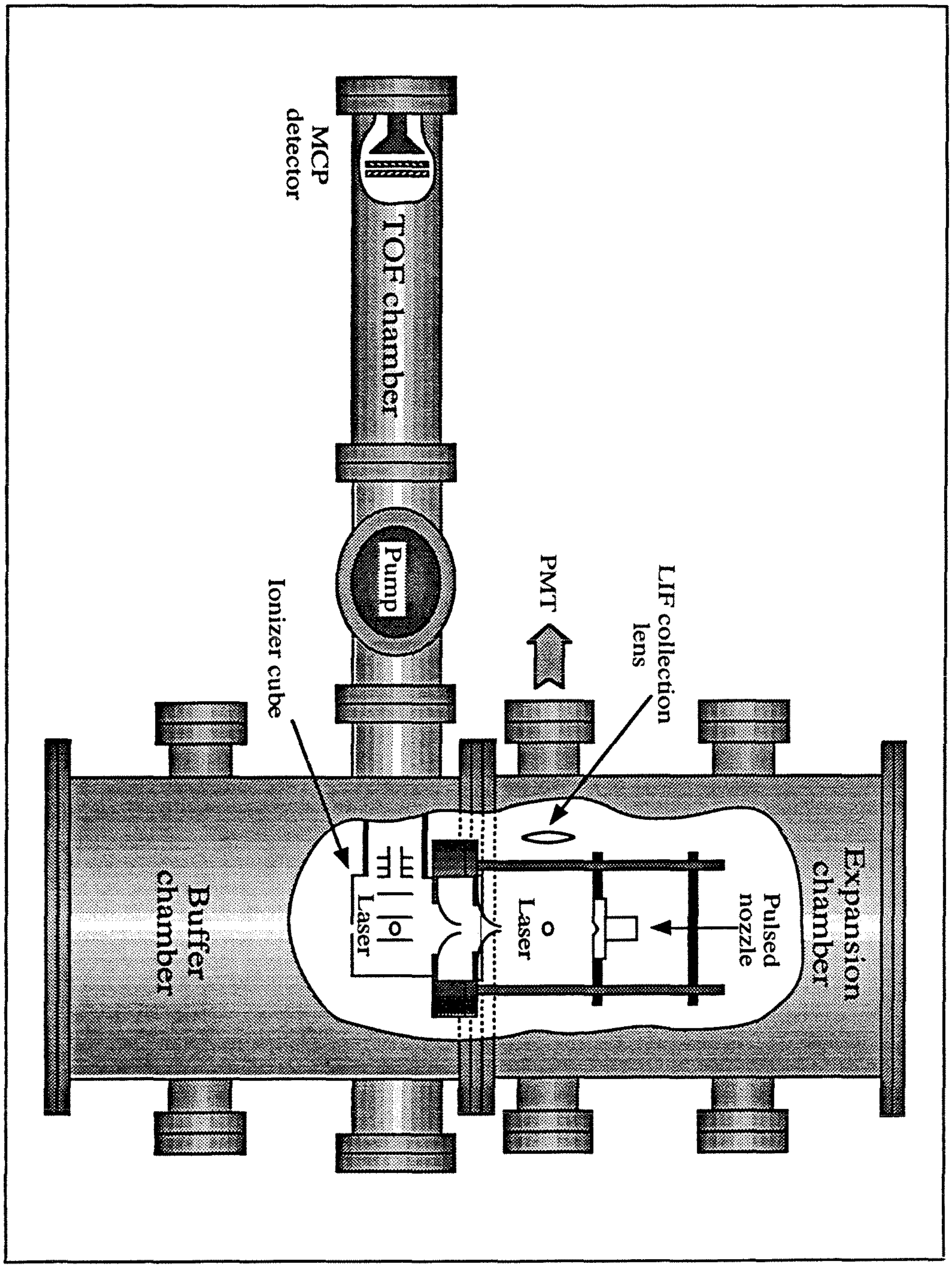
MCP detector
TOF chamber
Pump
PMT
LIF collection lens
Ionizer cube
Expansion chamber
Pulsed nozzle
Laser
Laser
Buffer chamber

Fig. 2.4

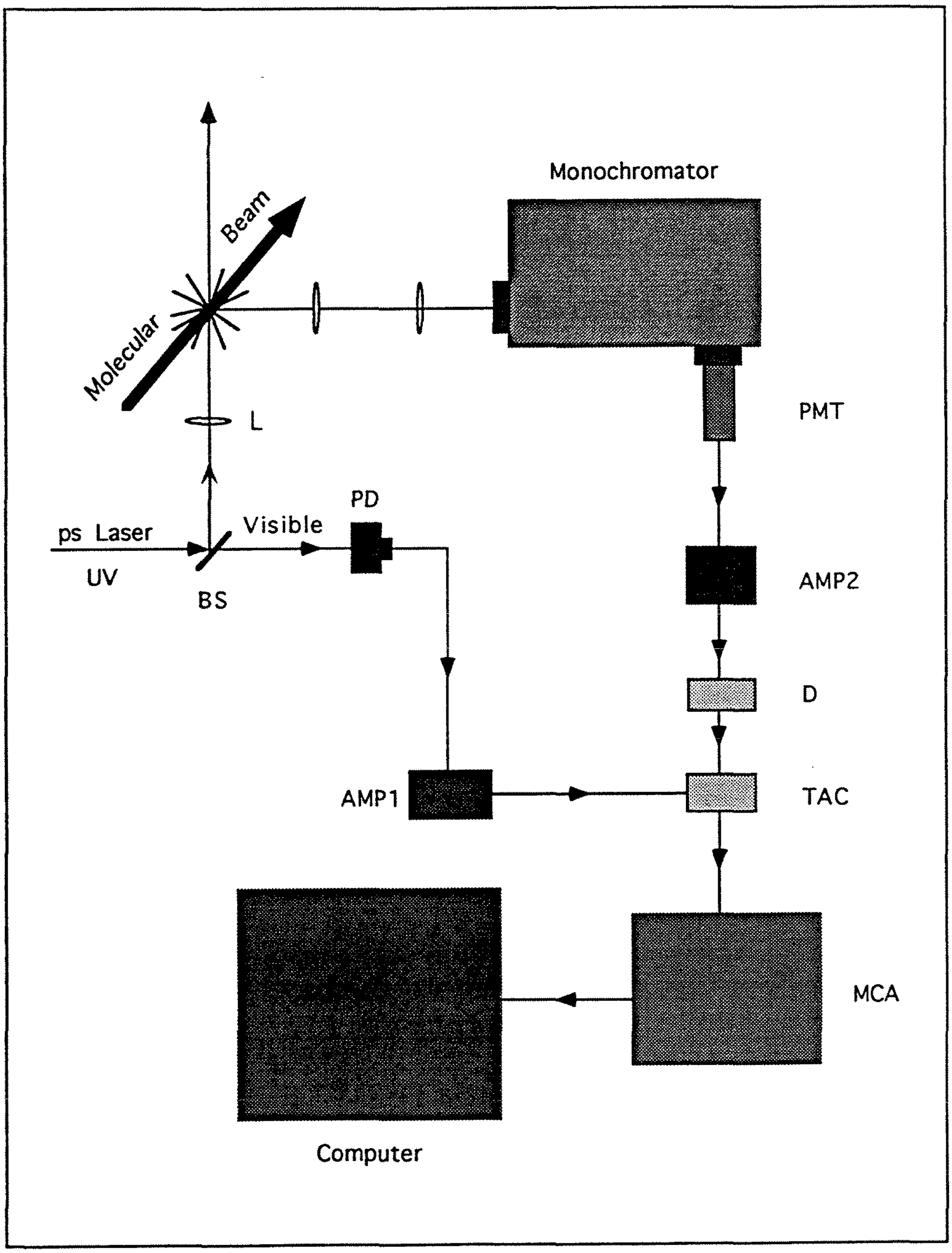
Monochromator
Molecular
Beam
L
PMT
PD
Visible
ps Laser
UV
BS
AMP2
D
AMP1
TAC
MCA
Computer

Fig. 2.5

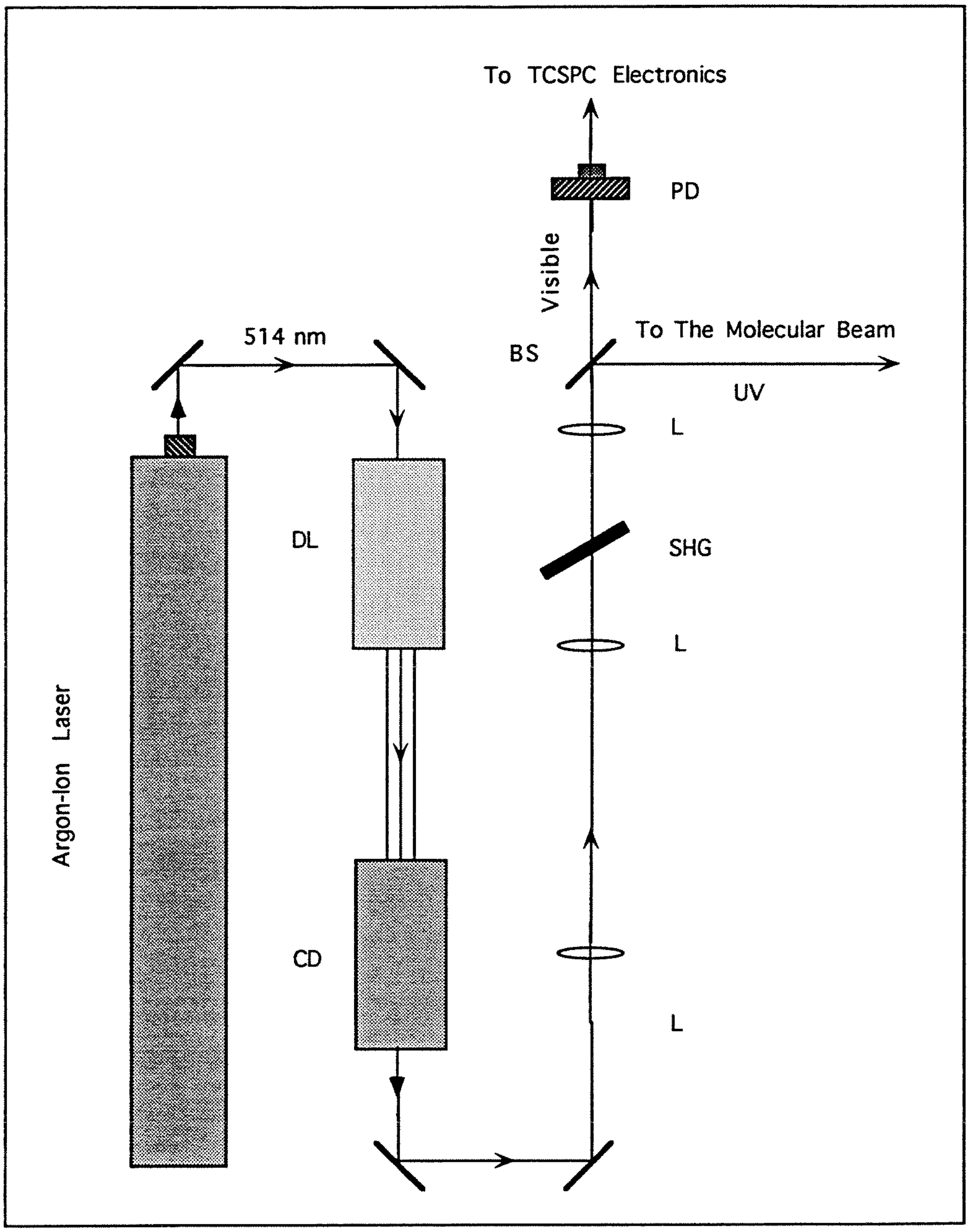
To TCSPC Electronics
PD
Visible
514 nm
To The Molecular Beam
BS
UV
L
DL
SHG
L
Argon-Ion Laser
CD
L

Fig. 2.6

Chapter 3

S_1-STATE DYNAMICS OF JET-COOLED BARE *TRANS*-STILBENE: A BACKGROUND

3.1 PRELIMINARIES

The structure of jet-cooled *trans*-stilbene, in both the ground and excited states, with no excess vibrational energy, is planar. Three primary sources provided evidence for that conclusion. First, the rotational constants of the molecule were estimated using the rotational band contour measurements of *trans*-stilbene at the zero-point vibrational level (with <1 MHz resolution) [1]. A rigid-rotor model fits the spectrum well and the calculated moments of inertia place strict constraints on the geometry. Furthermore, it was concluded that the transition moment lies within 12° of the long axis of the molecule (a-axis). Second, the assignment of the vibronic spectral bands of *trans*-stilbene [2-11], particularly for the low-frequency modes, indicates a C_{2h} symmetry which is consistent with the planar configuration. Third, rotational coherence fluorescence spectroscopy [12] was also used to measure the rotational constant of *trans*-stilbene and a similar conclusion was reached for the S_1-state geometry of molecule.

The topic of this thesis is the picosecond molecular dynamics on alkane - solvated and substituted *trans*-stilbene. In particular, intramolecular vibrational energy redistribution (IVR) and photoisomerization reaction dynamics are investigated. To understand the solvation and structural effects on both IVR and the isomerization reaction in *rans*-stilbene, a comparison with the S_1-state dynamics in the jet-cooled molecule must be made. For this purpose, IVR and isomerization dynamics in the isolated *trans*-stilbene are outlined in the following Sections.

3.2 PHOTOISOMERIZATION REACTION DYNAMICS

3.2.1 Reaction Coordinate(s)

The torsional motion around the ethylenic $C_e{=}C_e$ double-bond (where C_e stands for ethylenic carbon) is established as the reaction coordinate for the isomerization dynamics in *trans*-stilbene [13] (Fig. 3.1). However, studies on the temperature dependence of the isomerization dynamics of *m*-methyl-stilbenes in decane solution suggest that the phenyl torsion around the C_e-C_{ph} single-bond (where C_{ph} stands for the phenyl carbon) could be a competitive reaction coordinate with the ethylenic torsion and must be considered as the second dimension of the potential energy surface [14]. Furthermore, the spectral features of 1,1'-biindanylindene, in which the phenyl torsion is restricted by intramolecular chemical bridging, are similar to that of *trans*-stilbene at a very low temperature in a viscous environment [15] and the isomerization rate increases [16]. On the other hand, when the torsion around both the $C_e{=}C_e$ double bond and the C_e-C_{ph} single bonds are restricted (as in 5,6,11,12-tetrahydrochrysene), the isomerization yield is zero and the fluorescence quantum yield approaches unity [17-19] (see Fig. 3.1). Recently, quantum calculations on multidimensional isomerization-dynamics in *trans*-stilbene where carried out [20]. In these calculations, both $C_e{=}C_e$ double-bond torsion and C_e-C_{ph} single-bond rotation (with higher energy) represent the reaction coordinates for the isomerization dynamics.

3.2.2 Reaction Mechanisms and Potential Energy Surface

There are three possible mechanisms for the *trans*-to-*cis* isomerization [21,22]. First, the internal conversion from the first excited singlet state to highly-excited vibrational levels of the ground state on which the isomerization then proceeds. Second, the isomerization pathway through a triplet state, *i.e.* an intersystem crossing, followed by isomerization on the triplet surface that either crosses or nearly crosses with the ground singlet surface near the torsional angle of 90° [23-25] is important in some substituted stilbenes, see ref. [26]. The third mechanism involves a one-dimensional potential energy surface (PES), shown in Fig. 3.2, was proposed by Saltiel [15] and it is widely used to describe the isomerization reaction in *trans*-stilbene. In this PES, the reaction coordinate corresponds to a large-amplitude motion of the phenyl rings and presumably involves the ethylenic torsion. In the ground electronic state, the activation energy for the thermal *trans-cis* isomerization in solution was estimated as 46±2 kcal/mol [28]. In the vapor phase, values of 42.8±2 [29] and 42.6±1 kcal/mol [30] were obtained. Theoretical calculations have been made and a broad range (70-130 kcal/mole [31-33]) of the activation energy values for the thermal isomerization were given. In the first excited state of *trans*-stilbene, there is a potential energy minimum and a barrier for the twisting motion about the ethylene bond exists. On the *cis* side, there appears to be little or no barrier to the torsional motion, see ref. [26]. The adiabatic PES of the S_1-state isomerization in *trans*-stilbene arises from a mixing (avoided crossing) of the first excited state (^1B_u), following a $\pi \rightarrow \pi^*$ transition of stilbene, with one or more higher lying, doubly excited states ^1A_g state configurations that have a minimum at the 90° twisted form. This PES corresponds to the adiabatic limit. After the *cis*- or *trans*-stilbene arrives at the twisted configuration (90°), the molecule is internally converted to the ground state PES very rapidly (<1 ps in alkane solutions, see ref. [26]). Once on the ground state PES, the product molecule branches to either the *trans* or *cis* form. A third but minor reaction channel is open from the *cis* side and produces dihydrophenanthrene (DPH) [26] on the S_1-state surface.

Using semiemperical quantum chemistry calculations, Kawaguchi [27] proposed a new model that the photoisomerization of *trans*-stilbene arises from the cutting off process of the intramolecular hydrogen interaction (IMHI). In that model, both hydrogens of the ethylenic and phenylic groups of trans-stilbene interact to stabilize the planar structure of the molecule. Consequently, the barrier of the isomerization reaction in *trans*-stilbene arises from the cutting off process of the IMHI bond after which the phenyl groups might rotate (twist) around the central double-bond.

3.2.3 Isomerization Rate in Jet-Cooled Trans-Stilbene

The photoisomerization rate in jet-cooled *trans*-stilbene has been studied as a function of the excess-energy above the electronic origin in the S_1-state by Zewail and coworkers [34-36], Jortner and coworkers [37,38], Troe and coworkers [39,40], and others (for a review see [26]), Fig. 3.2.

In supersonic-jet cooled *trans*-stilbene, microcanonical rates are measured with low accuracy due to the narrow energy-level distribution. The time-resolved fluorescence signal (using total or wide-band fluorescence detection) exhibits single exponential decay with energy-dependent rate constant $k(E)$, where E is the rovibrational energy in the electronic origin of the S_1-state. The $k(E)$ curve shows a threshold energy (E_0) ($\sim 1250 \pm 100$ cm^{-1}) which separate two energy domains, see Fig. 3.2. When *trans*-stilbene is excited below the threshold energy, $k(E)$ is essentially independent of energy. In the vicinity of E_0, the rate begins to increase and above the threshold the $k(E)$ increases significantly and approaches a linear function of energy over a range of several thousand wavenumbers.

The intersystem crossing rate is too slow to compete with fluorescence and isomerization in the deactivation process of the S_1-state in *trans*-stilbene [37]. This implies that the observed threshold energy in $k(E)$ represents the barrier to the isomerization reaction. Below the isomerization barrier, $k(E)$ is just the radiative decay rate k_{rad}, which is $\sim 0.385\ 10^9$ s^{-1} and energy independent. Once the excess energy (E_x) exceeds the isomerization barrier, the isomerization rate increases rapidly to reach ~14×10^9 s^{-1} at E_x~3500 cm^{-1} [36], Fig. 3.2.

3.2.4 RRKM Calculations

In the case of complete IVR in isolated *trans*-stilbene, the excess-energy dependence of the isomerization rate, k_{iso}, could in principle, be reproduced using RRKM theory. Troe [39-45] and Zewail *et al.* [34,35,46,47] have carried out RRKM calculations for *trans*-stilbene. Optimized RRKM calculations, in which the transition-state frequencies and E_0 were treated as fitting parameters, show an excellent agreement with the experimental rates [39-45]. When identical reactant and activated complex frequencies (with a 400 cm^{-1} rather than a 88 cm^{-1} frequency for the reaction coordinate) were used, the RRKM rates were almost an order of magnitude larger than the experimental rates [34,35,46,47]. To explain this discrepancy, restricted IVR, reversible reaction, multidimensional effects, and nonadiabatic effects on the isomerization reaction were proposed [34,35,46,47]. Using a nonadiabaticity factor for crossing at the transition state with a higher lying state brought RRKM predictions into agreement with the observed rates. As a self-consistency check, these authors found that the energy dependence for the decay rate of perdeuteriostilbene was in good agreement with this modified RRKM model when one used the same nonadiabaticity parameter for stilbene (h_{12}) and perdeuteriostilbene (d_{12}). Troe and coworkers [39-45] pointed out that good agreement between the modified RRKM model and the observed rate constant, $k_{iso}(E)$ is not unique because of the number of adjustable parameters one can vary for a good fit.

3.4 INTRAMOLECULAR VIBRATIONAL ENERGY REDISTRIBUTION (IVR)

The magnitude of the isomerization rate k_{iso} is determined in part by the fraction of the total vibrational energy that resides in the reactive modes, those modes which contribute to the motion along the isomerization reaction coordinate. If the energy is distributed randomly among all the vibrational modes on a time scale much faster than the isomerization rate, then it should be possible to calculate $k_{iso}(E)$ using statistical methods such as RRKM theory.

Zewail and coworkers [5,34,35,47,50] utilized time- and frequency-resolved fluorescence techniques to study intramolecular vibrational energy redistribution (IVR) in the S_1-state of jet-cooled *trans*-stilbene (IVR rates from ref. [47] is also plotted versus excess-energy with k_{iso} in Fig.3.2). These authors classified IVR into three categories (namely, absent, restricted, and dissipative IVR) depending on the amount of excess-energy (low, intermediate, and high energy) available.

3.4.1 No IVR:

At low energies (*i.e.* $E_X<752$ cm^{-1}), with a density of states <10 per cm^{-1}, no apparent vibrational evolution of the initially excited states was observed on a time scale comparable to the fluorescence lifetime of the molecule (~2.67 ns); *i.e.* IVR is absent. In contrast with the other excitation bands in this region, the fluorescence from the S_1+663 cm^{-1} excitation band decays with a quantum beat modulation. This restricted IVR occurs on a time scale of ~1.28 ns. Furthermore, the dispersed fluorescence spectra of single vibronic levels (SVL) in this energy domain show sharp features with no spectral congestion and the fluorescence decays as a single exponential.

3.4.2 Restricted IVR:

In an intermediate energy range (789 $\mathrm{cm}^{-1} < E_X < 1170\ \mathrm{cm}^{-1}$), *restricted* IVR was observed. The SVL fluorescence decays display phase-shifted quantum beat modulation. The time scale of IVR in this energy domain, is 1.8 ns to 135 ps. In the same energy range, minor congestion in the SVL dispersed fluorescence spectra was observed. This regime corresponds to a case where the vibrational energy oscillates between the initially excited *"optically-active"* level and a small number of isoenergetic *"dark"* states.

3.4.3 Dissipative IVR:

At higher energies ($E_X > 1200\ \mathrm{cm}^{-1}$) where the a density of states is more than 150 per cm^{-1}, energy redistribution occurs irreversibly into a large number (typically $N > 10$) of vibrational levels, though some residual quantum beat modulation could still be identified. This *dissipative* regime is characterized by quasi-biexponential decays with a fast component on the order of tens of picoseconds typically the estimated IVR time scale is 24-47 ps. On the other hand, the dispersed fluorescence spectra are congested and show no spectral structure. The onset of dissipative IVR corresponds well to the threshold for isomerization, and may reflect a connection between these two processes.

From the above mentioned results and assuming that the IVR rate (k_{IVR}) is proportional to the density of vibrational states, the IVR time scale will be expected to be as short as ~1 ps at an excess energy of ~2000 cm^{-1} [48]. This IVR time scale is substantially shorter than the isomerization time scale (~640 ps) at the same excess-energy. Consequently, IVR could be considered as being complete before the molecules could isomerize (see Fig. 3.2).

The above sequence of three distinct IVR regimes, from *absent* to *restricted* to *dissipative* IVR, has been observed in other molecules, such as Anthracene [49-50], and *trans*-stilbene [51] by resolving the picosecond dynamics (in time and frequency domains) of beam-cooled molecules. A number of other aromatic molecules have been shown to exhibit the same kind of behavior, and these include perylene [52], fluorene [53] and azulene [54], *n*-alkyl anilines [55], 1-methylindole [56], naphthol [57], *p*-cyclohexylaniline [58,59], 2,5-diphenylfuran [60], deuterated analogs of anthracene [61], and derivatives of *trans*-stilbene [36] and seems to be established as a general characteristic of large polyatomic molecules. Density of states, symmetry, vibrational coupling, the number of low-frequency modes and the anharmonicity of the potential energy surface are key parameters in the IVR dynamics in large molecules. Unfortunately, there is no model systems in which these parameters and their effect on IVR can be tested separately. Instead the general features of IVR are determined by the interplay between all of these parameters.

3.5 REFERENCES

1. B. B. Champagne, J. F. Pfanstiel, D. F. Plusquellic, D. W. Pratt, W. M. van Herpen, and W. L. Meerts, *J. Phys. Chem.* **94,** 6 (1990).
2. T. Urano, H. Hamaguchi, M. Tasumi, K. Yamanouchi, and S. Tsuchiya, *Chem. Phys. Lett.* **137**, 559 (1987).
3 T. Urano, M. Maegawa, K. Yamanouchi, and S. Tsuchiya, *J. Phys. Chem.*, **93** , 3459(1989).
4. T. Urano, H. Hamaguchi, M. Tasumi, K. Yamanouchi, S. Tsuchiya, and T. L. Gustafson, *J. Phys. Chem.*, **91**, 3884 (1989).
5. J. A. Syage, P. M. Felker, and A. H. Zewail, *J. Chem. Phys.* **81**, 4685 (1984).
6. T. S. Zwier, E. M. Carrasquillo, and D. H. Levy, *J. Chem. Phys.* **78** , 5493 (1983).
7. L. H. Spangler, R. van Zee, and T. S. Zwier, *J. Phys. Chem.* **91**, 2782 (1987).
8. R. H. Dyck, and D. S. McClure, J. *Chem. Phys.* **36**, 2326 (1962) .
9. T. Suzuki, N. Mikami, and M. Ito, *J. Phys. Chem.*, **90**, 6431 (1986).
10. M. Ito, *J. Chem. Phys.* **91**, 517 (1987).
11. G. Baranovic, Z. Meic, H. Gusten, H. Mink, and G. Keresztury, *J. Phys. Chem.* **94**, 2833 (1990).
12. J. S. Baskin and A. H. Zewail, *J. Phys. Chem.* **93**, 5701 (1989).
13. J. Saltiel, *J. Am. Chem. Soc.* **89**, 1036 (1967).
14. N. S. Park and D. H. Waldeck, *Ultrafast Phenomena VII*, edited by C. B. Harris, E. P. Ippen, G. A. Mourou, and A. H. Zewail (Springer, New York, 1990).
15. J. Saltiel and J. T. D'Agostino, *J. Am. Chem. Soc.* **94**, 6445 (1972) .

16. M. Lee, A. J. Bain, P. J. McCarthy, C. H. Han, J. N. Haseltine, A. B. Smith, III, and R. M. Hochstrasser, *J. Chem. Phys.* **85**, 4341 (1986).

17 S. C. Shim and J. S. Chae, *Bull. Chem. Soc. Jpn.* **55**, 1310 (1982).

18. J. Saltiel, O. C. Zifiriou, E. D. Megarity, and A. A. Lamola, *J. Am. Chem. Soc.* **90**, 4759 (1968).

19. C. Pyun, T. A. Lyle, G. H. Daub, and S. M. Park, *Chem. Phys. Lett.* **124**, 48 (1986).

20. V. D. Vachev, J. H. Frederick, B. A. Grishanin, V. N. Zadkov, and N. I. Koroteev, *J. Phys. Chem.* **99**, 5247 (1995).

21. J. Saltiel, J. T. D'Agostino, E. D. Megarity, L. Metts, K. R. Neuberger, M. Wrighton, and O. C. Zafiriou, *Organic Photochemistry*; O. L. Chapman, Ed. Marcel Dekker: New York, 1973; Vol. 3.

22. J. Saltiel and J. L. Charlton, *Rearrangments in Ground and Excited States*; Mayo, Ed. Academic Press: New York, 1980; Vol 3.

23. J. Saltiel, G. R. Marchand, E. Kirkor-Kaminska, W. K. Smothers, W. B. Mueller, and J. L. Charlton, *J. Am. Chem. Soc.* **106**, 3144 (1984).

24. J. Saltiel, S. Ganapathy, and C. Werking, *J. Phys. Chem.* **91**, 2755 (1987).

25. J. Saltiel, A. D. Rousseau, and B. Thomas, *J. Am. Chem. Soc.* **105**, 7631 (1983).

26. D. H. Waldeck, *Chem. Rev.* **91**, 415 (1991).

27. Y. Kawaguchi, *J. Chem. Phys.* **100**, 8856 (1994).

28. A. V. Santoro, E. J. Barrett, and H. H. Hoyer, *J. Am. Chem. Soc.* **89**, 4545 (1967).

29. G. B. Kistiakowsky and W. R. Smith, *J. Am. Chem. Soc.* **56**, 638 (1934).

30. W. W. Schmiegel, F. A. Litt, and D. O. Cowan, *J. Org. Chem.* **33**, 3334 (1968).

31. G. Orlandi, P. Palmieri, and G. Poggi, *J. Am. Chem. Soc.* **101**, 3492 (1979).

32. P. Tavan and K. Schulten, *Chem. Phys. Lett.* **56**, 200 (1978).

33. G. Olbrich, *Ber. Bunsen-Ges. Phys. Chem.* **86**, 209 (1982).

34. J. A. Syage, P. M. Felker, and A. H. Zewail, *J. Chem. Phys.* **81**, 4706 (1984).

35. J. A. Syage, W. R. Lambert, P. M. Felker, A. H. Zewail, and R. M. Hochstrasser, *Chem. Phys. Lett.* **88** , 266 (1982).

36. L. Bañares, A. A. Heikal, and A. H. Zewail, *J. Phys. Chem.* **96** , 2782 (1992).

37. T. J. Majors, U. Even, and J. Jortner, *J. Chem. Phys.* **81**, 2330 (1984) .

38. A. Amirave and J. Jortner, *Chem. Phys. Lett.* **95** , 295 (1983).

39. J. Troe, *J. Chem. Phys. Lett.* **114**, 241 (1985).

40. J. Troe, and J. Schroeder, J. *Phys. Chem.* **90**, 4215 (1986).

41. J. Schroeder, and J. Troe, *Annu. Rev. Phys. Chem.* **38**, 163 (1987).

42. J. Troe, *J. Phys. Chem.* **90**, 357 (1986).

43. C. Gehrke, J. Schroeder, J. Troe, and F. Voss, *J. Chem. Phys.* **92**, 4805 (1990).

44. G. Maneke, J. Schroeder, J. Troe, and F. Voss, *Ber. Bunsen-Ges. Phys. Chem.* **89**, 896 (1985).

45. J. Schroeder, D. Schwarzer, J. Troe, and F. Voss, *J. Chem. Phys.* **93**, 2393 (1990).

46. P. M. Felker and A. H. Zewail, *J. Phys. Chem.* **89,** 5402 (1985).

47. P. M. Felker, W. R. Lambert, and A. H. Zewail *J. Chem. Phys.* **82**, 3003 (1985).

48. G. R. Fleming, S. H. Courtney, and M. W. Balk, *J. Stat. Phys.* **42**, 83 (1986).

49. W. R. Lambert, P. M. Felker, and A. H. Zewail, *J. Chem. Phys.* **81,** 2217 (1984).

50. P. M. Felker and A. H. Zewail, *J. Chem. Phys.* **82** , 2961, 2975, 2994 (1985) .

51. P. M. Felker and A. H. Zewail, *Adv. Chem. Phys.* **70**, 265 (1988).

52. A. J. Kaziska, S. A. Wittmeyer, A. L. Motyka, and M. R. Topp, *Chem. Phys. Lett.* **136**, 199 (1987).

53. J. F. Kaufmann, M. J. Côté, P. G. Smith, and J. D. McDonald, *J. Chem. Phys.* **90**, 2874 (1989).

54. D. R. Demmer, J. W. Hager, G. W. Leach, and S. C. Wallace, *Chem. Phys. Lett.* **136**, 329 (1987).

55. J. S. Baskin, M. Dantus, and A. H. Zewail, *Chem. Phys. Lett.* **130**, 473 (1986).

56. G. A. Bickel, D. R. Demmer, G. W. Leach, and S. C. Wallace, *Chem. Phys. Lett.* **145**, 423 (1988).

57. C. Lakshminarayan and J. L. Knee, *J. Phys. Chem.* **94**, 2637 (1990).

58. P. G. Smith and J. D. McDonald, *J. Chem. Phys*. **92**, 1004 (1990).

59. P. G. Smith and J. D. McDonald, *J. Chem. Phys*. **96**, 7344 (1992).

60. A. J. Kaziska and M. R. Topp, *Chem. Phys. Letters* **180**, 423 (1991).

61. L. W. Peng, B. W. Keelan, D. H. Semmes, and A. H. Zewail, *J. Phys. Chem*. **92**, 5540 (1988).

3.6 FIGURE CAPTIONS

3.1 *Trans-cis* isomerization reaction in *trans*-stilbene (top). The intermediate state (Phantom state) represents a perpendicular configuration of the two phenyl rings in the molecule. A schematic diagram of the potential energy surface of the isomerization reaction in *trans*-stilbene (bottom). In this figure, k_{rad}, k_{iso}, and k_{IC} represent the radiative, isomerization and internal conversion rates, respectively.

3.2 The excess-energy dependence of both IVR and isomerization rate in *trans*-stilbene. These rates are adapted from refs. [47] (IVR) and [36] (isomerization).

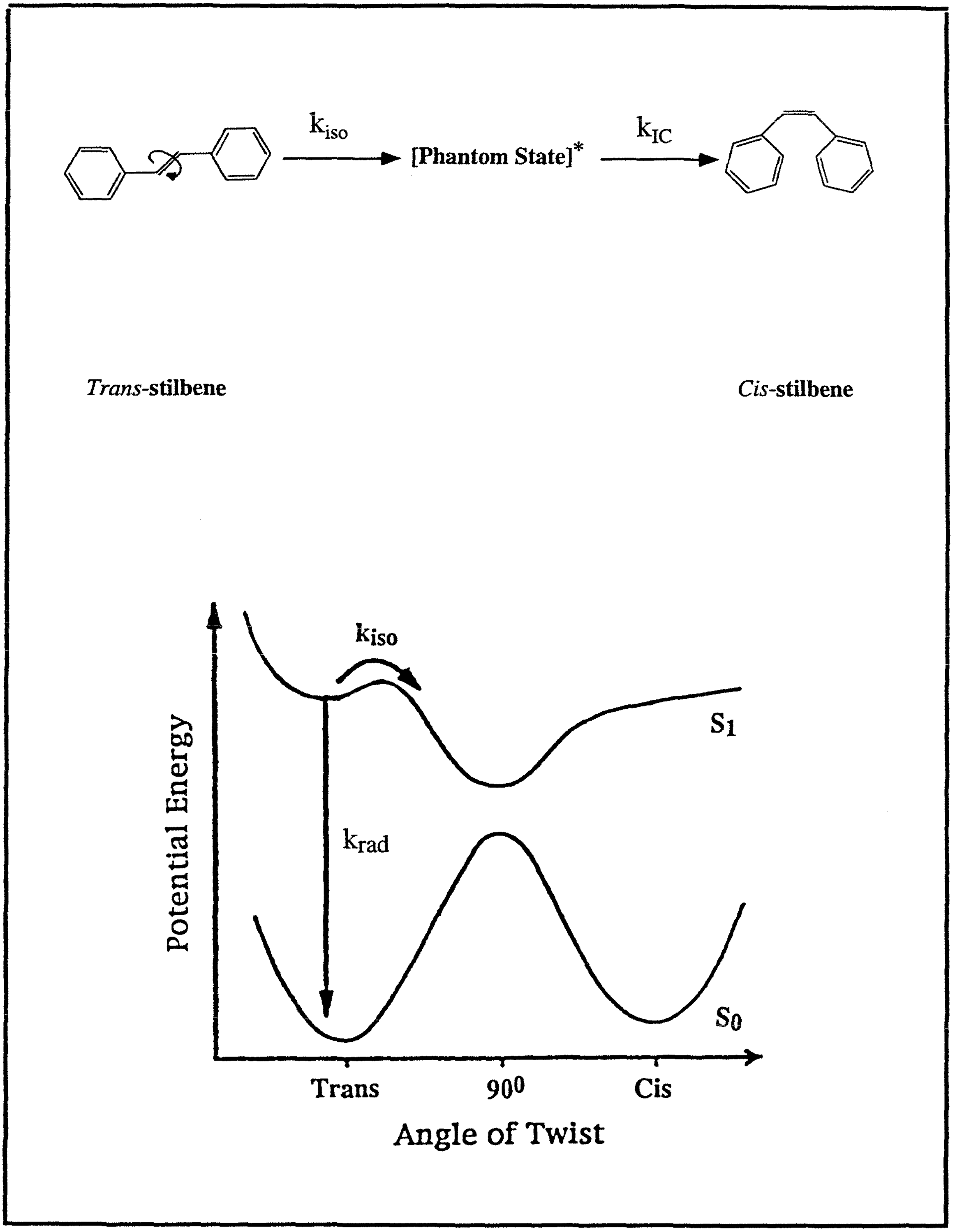
k_iso
[Phantom State]*
k_IC
Trans-stilbene
Cis-stilbene
k_iso
Potential Energy
S1
k_rad
S0
Trans
90⁰
Cis
Angle of Twist

Fig. 3.1

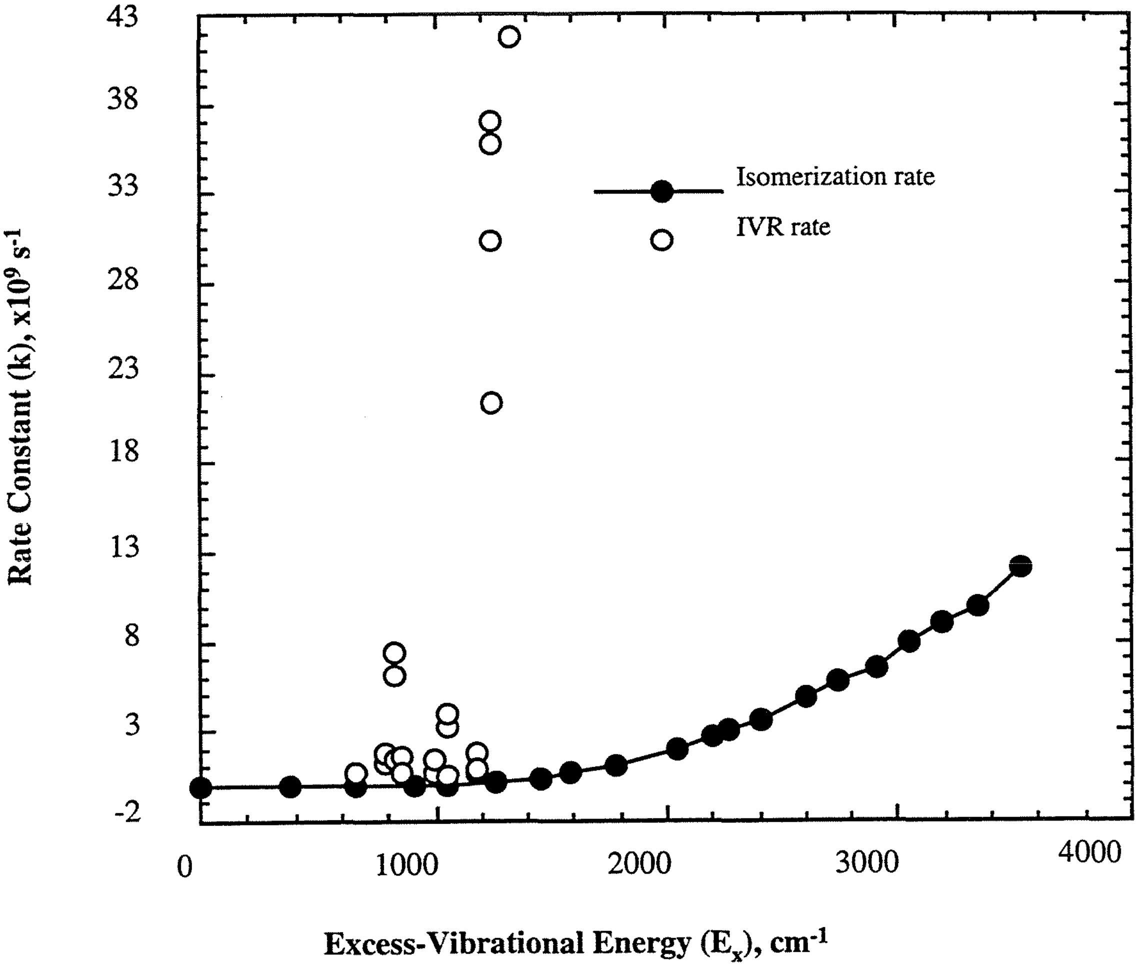
43
38
33
28
23
18
13
8
3
-2
0
1000
2000
3000
4000
Rate Constant (k), x10⁹ s⁻¹
Excess-Vibrational Energy (Eₓ), cm⁻¹
Isomerization rate
IVR rate

Fig. 3.2

Chapter 4

SOLVATION EFFECTS ON PICOSECOND MOLECULAR DYNAMICS (I): IVR IN *TRANS*-STILBENE-(HEXANE)$_1$ COMPLEX

Most of this chapter is taken from the following published article:

"Picosecond Dynamics of *n*-Hexane Solvated *Trans*-Stilbene,"

by C. Lienau, A. A. Heikal, and A. H. Zewail, *Chem. Phys.* **175,** 171 (1993).

4.1 INTRODUCTION

The intramolecular vibrational energy redistribution (IVR) dynamics can be generally divided into three different regimes [1-6]: *no* IVR at very low vibrational energies; *restricted* IVR in an intermediate energy range, characterized by quantum-beat modulated fluorescence decay profiles; and *dissipative* IVR at higher energies, occurring within tens of picoseconds. These regimes of IVR have been identified and studied in prototype molecular systems such as anthracene [1,2] and *trans*-stilbene [3-6] by resolving the picosecond dynamics (in time and frequency domains) of beam-cooled molecules. A number of other aromatic molecules have been shown to exhibit the same kind of behavior, and these include perylene [7], fluorene [8] and azulene [9], *n*-alkyl anilines [10], 1-methylindole [11], naphthol [12], *p*-cyclohexylaniline [13,14], 2,5-diphenylfuran [16], deuterated analogs of anthracene [15], and derivatives of *trans*-stilbene [17]. As of yet, there is no quantitative theory to predict the onset of IVR in these large systems, but one can relate the role of two key factors, the density of states and the coupling matrix elements, to the dynamics.

Isolated van der Waals (vdW) complexes are of especial interest as model systems for studying IVR dynamics. The impact of the large number of low-frequency intermolecular modes and the high density of states on IVR can be tested in these complexes. Furthermore, unlike small molecular systems [18-21], the possibility of both inter- and intra-molecular energy flow can be monitored. One class of vdW systems involves complexes of aromatic molecules with one or more rare gas atoms. Such complexes are characterized by a low binding energy on the order of some hundreds of wavenumbers, so that IVR is generally followed by fast vibrational predissociation of the complex [22-24]. The time scale of IVR depends on the coupling of the initially excited mode to other modes in the molecule. In

Rettschnick's original work on tetrazine-(argon) complexes [25,26], IVR was found to occur on a time scale of several nanoseconds at excess vibrational energies of 500 cm^{-1} to 800 cm^{-1}. This is in marked contrast to the extremely slow energy redistribution in the electronic ground state of clusters [27]. Experiments on anthracene [23] and *trans*-stilbene [22] solvated in rare gas complexes show that in the energy range from 300 cm^{-1} to 800 cm^{-1} IVR is extensive within hundreds of picoseconds, considerably faster than in the bare molecule. This was attributed to the increase in the density of ro-vibrational states caused by the low-frequency intermolecular vibrations. Topp and coworkers [15] observed a quantum-beat modulated fluorescence decay in 2,5-diphenylfuran-(argon) complexes, indicating that restricted IVR occurs on a scale of some hundreds of picoseconds.

For some solute-solvent clusters, the binding energy is generally much larger than that of the rare gas complexes. IVR should be observable without dissociating the complex, and these systems should provide an opportunity to test the influence of intermolecular modes and solute-solvent interactions on IVR. Topp and coworkers [28,29] reported that the vibrational energy redistribution from molecular into cluster modes is more than one order of magnitude slower in the case of perylene-(naphthalene) than for perylene-(benzene) or perylene-(alkane) complexes. These results are not expected if intermolecular modes are the dominating states for redistribution in both complexes.

As a model system for solute-solvent complexes, *trans*-stilbene solvated by hexane clusters has many attractive features. First, the spectroscopy of stilbene-(hexane) complex is available [30]. Second, the fluorescence excitation spectrum [30] of these complexes shows intramolecular stilbene-type modes, several overtones of a low-frequency intermolecular vibration, and combination bands of both. In principle, the energy transfer from the stilbene molecule into the cluster as well as between different intermolecular modes can be examined. Third, a large binding energy for stilbene-(hexane)$_n$ clusters is predicted (see below) and consequently the complications of vibrational predissociation can be eliminated. The fact that bare *trans*-stilbene dynamics are known [3-6] makes the comparison in this study particularly important. In this chapter, the picosecond dynamics of IVR in the stilbene-(hexane) complex are presented. In these studies, time- and frequency-resolved fluorescence spectroscopy are utilized.

4.2 EXPERIMENTAL

The molecular beam system, the laser system and the time-correlated single photon counting electronics have been described in Chapter II. A heatable stainless steel reservoir filled with *n*-hexane (Aldrich, UV spectroscopy grade, 99% purity) was connected to the gas supply via a T-shaped short capillary ($\varnothing$ =3 mm, L = 50 mm), so that the amount of *n*-hexane vapor above the liquid could diffuse into the rare gas stream through the capillary. In this way, the partial pressure of n-hexane (~50 mbar) in the expansion was considerably lower than the hexane vapor pressure above the liquid. *Trans*-stilbene (Aldrich, 96% purity, used without further purification), heated to ~100 °C, was seeded in the carrier gas-mixture (~70 psi of helium with ~1% of hexane). Heating the hexane sample provided, to some extent, a control over the beam composition.

4.3 RESULTS AND DISCUSSIONS

4.3.1 Structure

Potential energy calculations based on an atom-atom pair-potential [31] together with measurements of the rotational constants of 2,5-diphenylfurane-(alkane) complexes, using rotational coherence spectroscopy [32,29], provide evidence that in this case the long axis of the diphenylfuran and alkane molecules are oriented parallel to each other. A similar structure will be proposed for the stilbene-(hexane)$_1$ cluster.

Atom-atom pair-potential energy calculations have been carried out to deduce the most energetically favorable configuration for the stilbene-hexane$_1$ cluster. In these calculations, we used intermolecular potentials of the Buckingham 6-exp-1 type:

$$V=\sum_i\sum_j\left(-\frac{A}{r_{ij}^6}+B\exp\left(-Cr_{ij}\right)+\frac{q_iq_j}{r_{ij}}\right), \tag{1}$$

and Lennard-Jones 6-12-1 type

$$V=\sum_i\sum_j\left(-\frac{A}{r_{ij}^6}+\frac{B}{r_{ij}^{12}}+\frac{q_iq_j}{r_{ij}}\right). \tag{2}$$

In these equations the Coulombic third term [33-37] provides a correction for the electrostatic interaction for non-uniform charge distributions. The potential parameters were taken from the work of Williams [33,34] and Scheraga [35,36]. The distribution of partial charges was also based on the work of Williams [33,34]. The partial charge of all H-atoms was assumed to be q_H=-0.153, whereas for the carbon atoms q_C=-n_H q_H, with n_H denoting the number of hydrogen atoms connected to the respective carbon atom.

The structural parameters of *trans*-stilbene in the electronic ground state were taken from the theoretical study of Negri *et al.* [38], and those of n-hexane from ref. [39]. We note that the excited state geometry is also planar [40], so that, as far as the calculations are concerned, the structures of *trans*-stilbene in the ground and excited electronic states are similar.

The most energetically favorable geometry of the cluster (isomer A) is characterized by the carbon atoms of the hexane molecule being located in a plane parallel to that spanned by the two phenyl rings, with the long axis of hexane parallel to the *trans*-stilbene long axis (see Fig. 4.1). Using eq. (1) and the parameter set given in ref. [33,35], we find a binding energy for this configuration of 2040 cm^{-1}, whereas the use of eq. (2) with the parameters taken from ref. [35,36] results in a binding energy of 2260 cm^{-1}.

For this specific cluster, the introduction of the Coulombic term in eqs. (1) and (2) has no effect on the most energetically favorable configuration. Here, the Coulombic energy (~100 cm^{-1}) is much smaller than the attractive and repulsive energies calculated from the first and second term of eqs.(1) and (2).

The potential energy calculations predict a second stable configuration (labeled isomer C), with a binding energy of 2170 cm^{-1}. This configuration differs in that the hexane molecule is rotated by 180° around its long axis, and that the long axes of both *trans*-stilbene and hexane are no longer parallel to each other (see Fig. 4.1). The distance between the center of mass of both molecules (3.72 Å) is slightly larger than that in the isomer A configuration (3.67 Å).

The above binding energies should be regarded as approximate estimates. Our purpose here is to illustrate the consistency of the large spectral red shift for hexane complexes as compared to, *e.g.*, rare gas complexes under normal conditions. The structures are consistent with recent rotational coherence experiments [30] and more refinement can be done in further experimental studies.

4.3.2 Spectroscopy

4.3.2.1 Fluorescence Excitation Spectrum

The fluorescence excitation spectrum of the first excited electronic state (S_1) of stilbene-(hexane) (1:1) complexes (shown in Fig. 4.2) reveals the presence of three structural isomers, labeled A, B, and C. The S_1-electronic origins of these isomers are red-shifted by 380 cm^{-1} (A-isomer), 348 cm^{-1} (B-isomer), and 265 cm^{-1} (C-isomer) relative to the electronic origin of *trans*-stilbene at 32234.744 ± 0.002 cm^{-1} [3,4,31]. The assignments of these isomers were based on a series of measurements of the fluorescence excitation spectrum as a function of hexane concentration and on an analysis of vibrational spacing in the spectrum [30]. The fluorescence intensity of the origin transition of the B- and C-isomer relative to the intensity of the A-isomer is 0.04 and 0.5, respectively. The prominent feature of the excitation spectrum is a long progression of one optically active low-frequency cluster mode (labeled X) with a frequency spacing (υ) of 20.0 ± 0.5 cm^{-1} for the A-isomer (B: 18 ± 1 cm^{-1}, C: 17.2 ± 0.5 cm^{-1}) [30]. Following the interpretation given by Mangle *et al.* [31] for the low-frequency mode observed in the excitation spectrum of 2,5-diphenylfuran-(hexane) (1:1) complexes, this mode is presumably related to a torsion motion of the alkane molecule around an axis perpendicular to the plane of the stilbene molecule. For each isomer this progression is found again shifted by 200 cm^{-1} to the blue due to the excitation of a combination of the symmetric in-plane, in-phase vibration υ_{25} [41,3,4,31] of the stilbene molecule and the low-frequency cluster mode X.

Using the above mentioned potential energy calculations, and following the external force field method outlined by Li and Bernstein [42], the eigenfrequencies of the six cluster normal modes were calculated. Using eq. (2) together with Scheraga's parameter set, these frequencies are 17, 19, 23, 50, 77, and 154 cm^{-1} [35,36]. In a Cartesian coordinate system where the x-axis points along the stilbene long axis, the y-axis lies in the plane spanned by the stilbene molecule, and the z-axis connects the center of mass of stilbene and hexane in the equilibrium A-configuration, the two lowest eigenfrequencies correspond to vibrational motions along the *y*- and *x*-axis, respectively. The third eigenvalue (22 cm^{-1}) represents a torsion motion around the *z*-axis, and the fifth (77 cm^{-1}) is a vibrational motion along the *z*-axis. The remaining frequencies correspond to "out-of-plane" torsions, where the two molecules leave the preferred parallel configuration.

4.3.2.2 Dispersed Fluorescence Spectra

(a) Excitation of the 0_0^0*- Transition*

The dispersed fluorescence spectra of the A- and C-isomer of stilbene-(hexane) (1:1) complexes recorded for 0_0^0-excitation are displayed in Fig. 4.2. Both spectra have the same general features. The most prominent feature of both spectra is a four-member (A-isomer) and five-member (C-isomer) progression of the low-frequency cluster mode *X*, already observed in the fluorescence excitation spectrum. The spacing of this progression is 17.2 ± 0.5 cm^{-1} for the A-isomer and 14.8 ± 0.5 cm^{-1} for the C-isomer. This progression is found to be repeated in intervals of 205 ± 1 cm^{-1} (A) and 204±1 cm^{-1} (C). The dispersed fluorescence spectrum of the 0_0^0-transition of the bare *trans*-stilbene molecule, given in Fig. 4.3 for comparison, shows that this repetition of the low-frequency pattern is due to the combined excitation of overtones of the cluster mode *X* and overtones of the symmetric in-plane ethylene bend mode υ_{25} of stilbene [43] in the ground electronic state of the cluster. Therefore the vast majority of bands detected in the dispersed fluorescence spectrum can be assigned to the transitions $25_m^0 X_n^0$ (see Table (1)).

The frequency spacing between overtones of stilbene-type mode (υ_{25}: 205 cm^{-1}) as well as the relative intensity of these bands in the bare molecule, are found to be almost the same as in the cluster, indicating that this symmetric in-plane mode is only weakly affected by complexation. A much stronger perturbation of all out-of-plane stilbene-type modes can be expected in the complex. Neither the C_e-C_{ph} out-of-plane bending mode (υ_{36}), nor the very anharmonic very low frequency C_e-C_{ph} out-of-plane twisting mode (υ_{37}) [43-46], or combinations thereof, can be found in the dispersed fluorescence spectra of the complexes.

Several low intensity bands can be resolved in the low-energy region of the dispersed fluorescence spectra of the A-isomer (see Table (1) and Fig. 4.3). These bands can be tentatively assigned to a second cluster mode Y (υ=76 cm^{-1}), and combinations of this mode with the cluster mode X and υ_{25} $25^0_m X^0_n Y^0_1$, although a conclusive assignment cannot be given without a normal mode analysis of the cluster [42].

(b) Excitation of Higher Vibrational Levels

Dispersed fluorescence spectra for nineteen vibrational levels in the S_1-state of the A- and C-isomer of *trans*-stilbene-(hexane) (1:1) complexes have been recorded. Excitation energy wavelength, and assignment of the excited bands are given in Table (1). For all of these cluster levels, the excitation wavelength was red-shifted with respect to the origin of the bare stilbene molecule. Consequently, the fluorescence of the bare molecule is eliminated, but, the possibility of detecting fluorescence from larger clusters ($n \geq 2$) should not be ruled out. A careful look at both the excitation (Fig. 4.2) and dispersed (Fig. 4.3) fluorescence spectra reveals a trace of spectral congestion even at zero excess-vibrational energy (compare the background before and after the excitation laser).

(i) A-Isomer.

The fluorescence spectra recorded for excitation of the overtones X_0^k ($0 \leq k \leq 4$) of the low frequency cluster mode X are shown in Fig. 4.4. In all cases a clear line spectrum was observed with some spectral congestion. This congestion is larger for higher overtones. One prominent feature of these spectra is a long low-frequency progression, which is repeated over a 200 cm^{-1} period. All bands of the progression are assigned to the transitions $A25_m^0 X_n^k$ ($0 \leq k \leq 4$, $0 \leq m \leq 1$, $0 \leq n \leq 9$).

Several low-intensity bands are found between 100 cm^{-1} and 200 cm^{-1} and above 300 cm^{-1}. As noted previously for the fluorescence spectrum of the 0_0^0-transition, these bands are tentatively assigned as $25_m X_n^k Y_1^0$, where Y denotes a second low-frequency cluster mode with υ= 76 cm^{-1}. At this low energy, no band that can be assigned for a nascent *trans*-stilbene transition was observed. An assignment cannot be given for two bands found in the AX_0^2 (at 46 and 250 cm^{-1}) and AX_0^3 spectrum (at 59 and 263 cm^{-1}). The dispersed fluorescence spectrum for an excitation energy of 200 cm^{-1} ($A25_0^1$) once again shows a structured spectrum, with the progression at low energies assigned to $A25_0^1 X_n^0$ transitions. Transitions of the combination type $A25_1^1 X_n^0$ are not detected, since the relative intensity of the transition 25_1^1 for the bare stilbene molecule is very low, as found in the fluorescence spectrum for this transition, Fig. 4.5. However, $A25_2^1 X_n^0$ transitions, shifted by 408 cm^{-1} relative to the $A25_0^1 X_n^0$ progression, are observed, in agreement with the Franck-Condon analysis for this mode [3,4]. Some congestion of the spectrum is found in the energy range between 100 and 400 cm^{-1}, indicating a possible onset of fast IVR or severe mixing of the optically active modes.

A strikingly different fluorescence spectrum is found upon excitation of the first combination band $A25_0^1 X_0^1$, see Fig. 4.6. Although the amount of excess energy is raised by only 20 cm^{-1} compared to $A25_0^1$, the dispersed fluorescence spectrum shows almost complete congestion at this transition. Only one of the $A25_0^1 X_n^1$ progressions remain, albeit strongly reduced in intensity compared to the broadband relaxed fluorescence. This spectrum indicates that IVR is presumably faster than the fluorescence rate even at this very low excess energy of 220 cm^{-1} in the S_1-state of the cluster. This point is examined below using time-resolved fluorescence measurements.

The fluorescence spectra for excitation of the next overtone of the low-frequency cluster mode, $25_0^1 X_0^2$, is even more congested; only two very weak isolated bands can be observed at this energy. The excitation of all higher overtones $25_0^1 X_0^n$, $3 \leq n \leq 5$, leads to completely congested spectra without isolated bands. This onset of congested spectra for the excitation of combination bands $25_0^1 X_0^n$ at excitation energies between 220 cm^{-1} and 300 cm^{-1} above the origin of the A-isomer has to be compared with that of the bare stilbene molecule. For the latter, completely congested spectra are not observed at energies below the threshold for photoisomerization (~1250 cm^{-1} [3,47,48]). In all spectra recorded at lower energies, well-resolved lines are present. The amount of spectral congestion in these spectra is generally found to increase with excess energy [3-5].

(ii) *C-Isomer.*

The dispersed fluorescence spectra of the C-isomer at low energies (excitation of CX_0^n, $0 \leq n \leq 2$) are similar to those for the A-isomer at corresponding excess energies. The spectral congestion (background) is ~50% larger than that for the A-isomer at the same excess energy. The prominent features in the dispersed fluorescence spectra, of the C-isomer, are two low frequency progressions CX_m^k and $C25_1^0 X_m^k$. More members of these progressions are detectable than for the A-Isomer, indicating a slightly larger displacement between the ground and excited state potential energy surfaces in the C-isomer (see below).

The excitation of a higher overtone of the cluster mode, CX_0^3, does not lead to a sharp line spectrum, but to an almost completely congested one (see Fig. 4.6). Some sharp features are still observable, but their intensities are very weak. The absorption band of the next higher overtone, CX_0^4, overlaps with a hot band of the A-isomer ($A25_0^1X_1^0$) and therefore the fluorescence spectrum for the CX_0^4 transition, shown in Fig. 4.6, is a combination of the dispersed fluorescence of $A25_0^1$ and CX_0^4. The three distinct bands around 0.0 cm^{-1} in this spectrum are assigned as transitions $A25_0^1X_n^0$, $0 \leq n \leq 2$, and are found at the same wavelength as in the $A25_0^1$ spectrum (Fig. 4.6). The rest of the spectrum can be assigned to the emission from CX_0^4 and is found to be slightly more congested than that for CX_0^3.

At higher excitation energies all measured dispersed fluorescence spectra are congested without any sharp fluorescence bands. Attention is drawn to the fact that excitation of the in-plane stilbene mode υ_{25} yields a congested spectrum, indicating very rapid IVR for the C-isomer, whereas for the A-isomer the corresponding spectrum is only slightly congested, and for the bare stilbene molecule a clear line spectrum is observed.

4.3.2.3 Franck-Condon Analysis

The intensity pattern of the dispersed fluorescence spectra, at low-excitation energies, may be examined using a Franck-Condon analysis. Following the approach by Coon *et al.* [49] and Ansbacher [50], it is assumed that the s normal coordinates of a polyatomic molecule in the electronically excited state q_i' are given by a linear displacement d_i of the corresponding ground-state normal coordinate q_i'': $q_i' = q_i'' + d_i$. The Franck-Condon overlap integral then separates into a product of one-dimensional overlap integrals, assuming harmonic oscillator wave functions in the ground and excited states [50]:

$$R(m,n) = (m!n!)^{1/2} 2^{-(m+n-1)/2} \left(\frac{\beta}{1+\beta^2} \right)^{1/2} \left(\frac{1-\beta^2}{1+\beta^2} \right)^{(m+n)/2} \exp\left(-\frac{1}{2} \frac{\gamma^2 \beta^2}{1+\beta^2} \right)$$

$$\sum_{l=0}^{\min(m,n)} \left[\left(\frac{4\beta}{1-\beta^2} \right)^{l} \frac{(-i)^{m-l}}{l!(m-l)!(n-l)!} H_{m-l}\left\{ i\beta^2 \gamma \left(1-\beta^4\right)^{-1/2} \right\} H_{m-l}\left\{ -\beta\gamma\left(1-\beta^4\right)^{-1/2} \right\} \right]. \tag{3}$$

Here, m and n denote the vibrational quantum number in the excited and ground states, respectively, and H_{m-l} and H_{n-l} are Hermite polynominals. Furthermore,

$$\alpha^2 = \frac{4\pi^2 c \nu}{h}, \qquad \beta = \frac{\alpha''}{\alpha'}, \qquad \gamma = -\alpha' d, \tag{4}$$

where ν is the vibrational frequency, given in cm^{-1}. The parameter d corresponds to the displacement between the minima in the electronic and excited state of the cuts through the potential energy surfaces along the mass-weighted normal coordinate q and is defined such that $a.d$, and therefore g, are dimensionless. A distortion factor $\gamma = 2\sqrt{2\ln 2}$ then corresponds to a displacement d which is equal to the width (FWHM) of the wave function in the vibrationless excited state $\Delta q'$: $d = -\gamma \Delta q' / \left(2\sqrt{2\ln 2}\right)$.

The relative spectral intensities are proportional to the square of the overlap integrals $|R(m,n)|^2$. The relative intensities for the bands of the low frequency progression AX_n^m and CX_n^m calculated on the basis of this model are in qualitative but not quantitative agreement with the measured dispersed fluorescence. For better agreement, anharmonic potentials for the ground and excited state were used:

$$V(x) = \frac{1}{2} m\omega^2 x^2 + \frac{1}{2\pi} \sigma h \omega x^3. \tag{5}$$

Using first-order perturbation theory, the anharmonic oscillator wave function in the eigenstate k is given as a sum of harmonic oscillator wave functions [51]:

$$|\psi_k\rangle = \sum_{i=-3}^{3} c_i |\Phi_{k+i}\rangle$$

with

$$c_0 = 1,\quad c_1 = -3\sigma\left(\frac{k+1}{2}\right)^{3/2},\quad c_2 = 0,\quad c_3 = -\frac{\sigma}{3}\left[\frac{(k+3)(k+2)(k+1)}{8}\right]^{1/2},$$

$$c_{-1} = 3\sigma\left(\frac{k}{2}\right)^{3/2},\quad c_{-2} = 0,\quad c_{-3} = \frac{\sigma}{3}\left[\frac{k(k-1)(k-2)}{8}\right]^{1/2}. \tag{6}$$

To second order in the perturbation expansion, the energy of the eigenstate k is obtained:

$$E_k = \frac{1}{2\pi}\left(k+\frac{1}{2}\right)h\omega - \frac{15}{8\pi}\sigma^2\left(k+\frac{1}{2}\right)^2 h\omega - \frac{7}{32\pi}\sigma^2 h\omega. \tag{7}$$

The relative spectral intensity is proportional to $|R_{anh}(m,n)|^2$, with $R_{anh}(m,n)$ given by:

$$R_{anh}(m,n) = \sum_{i=-3}^{3}\sum_{j=-3}^{3} c_i^e c_j^g R(m+i, n+j), \tag{8}$$

where c_i^e and c_j^g are the coefficients in the expansion for the wave function of the excited and ground state (eq. (6)), and $R(m+i, n+j)$ is given by eq.(3), with $R(m,n) = 0$ for $m \leq 0$ or $n \leq 0$. Figures 4.7 and 4.8 show the low-frequency part of the measured spectra together with the model calculations for the A- and C-isomer, respectively. The displayed simulations have been performed with the parameters shown in Table (2), which gave the best agreement between experiment and calculations. The errors quoted above give a conservative estimate of the range over which each parameter has to be varied to give a significantly worse fit to the experimental data.

In general, the calculated band intensities are in good agreement with the experimentally observed ones. For some bands, minor deviations between theory and experiment exist (see for example the intensity ratio of AX_3^1/AX_0^1 or the intensity of CX_3^2) and it is found that these deviations become larger for higher vibrational quantum numbers in the ground and excited states, where the anharmonic model potential becomes a less accurate approximation of the real potential. It is also found that the relative band intensities in the A and C-isomer for the progression AX_m^k are slightly different from those for the progression $25_0^1 AX_m^k$, which is due to an anharmonic coupling between the υ_{25} and X modes.

The Franck-Condon analysis presented above allows us to determine the parameters of an accurate anharmonic oscillator model potential for the low-frequency cluster mode X in both the ground and excited states. In the (presumably less strongly bound) C-isomer, the X normal coordinate shows a significantly larger displacement between the ground and excited states than in the A-isomer, implying that the cluster excitation to its S_1-state induces a larger structural change in the C- than in the A-isomer.

4.3.3 Dynamics

4.3.3.1 Fluorescence Rates: Wide-Band Detection

The fluorescence lifetime (τ_f) for the vibrationless S_1-state of bare stilbene has been measured [3,4,17,47,52] to be 2.65±0.02 ns. Fluorescence lifetimes for all absorption bands in the excitation spectrum of the A- and C-isomer are reported in Table. (3). The detection of the "total" fluorescence has been achieved by opening the monochromator slits completely and setting the detection wavelength far to the red of the excitation wavelength. The measured lifetimes of the hexane cluster are in excellent agreement with those recently reported by the Troe group [30]. As shown in Fig. 4.9, a slight decrease in the fluorescence lifetime can be observed as the vibrational energy in the S_1-state of the cluster is increased. Assuming that the fluorescence quantum yield in the cluster is equal to unity (as it is for the isolated molecule [53,54]), the fluorescence lifetimes of the vibrationless excited state are equal to the inverse of the radiative rate, which are then:

k_{rad} (A-isomer) = $(0.358 \pm 0.003) \times 10^9$ s^{-1}

k_{rad} (C-isomer) = $(0.357 \pm 0.003) \times 10^9$ s^{-1}.

Thus, the radiative rate of the $S_1 \rightarrow S_0$ transition in the cluster is slightly smaller than that of the isolated molecule, k_{rad} (bare *trans*-stilbene) = 0.377×10^9 s^{-1}. As has been pointed out by Strickler and Berg [55], and by Birk and Dyson [56,57], the radiative rate of the $S_1 \rightarrow S_0$ transition is approximately given by:

$$k_{rad} = \frac{1.8424x10^4 \pi}{c^2 N_A} \frac{n_f^3}{n_a} \left\langle \upsilon_f^{-3} \right\rangle_{Av}^{-1} \int \frac{\varepsilon}{\upsilon} d\upsilon, \qquad (9)$$

where n_f and n_a are the mean refractive indices of the solvent over the fluorescence and absorption spectrum, respectively. In eq. (9), υ denotes the frequency of the optical transition in s^{-1}, and $\left\langle \upsilon_f^{-3} \right\rangle_{Av}$ is the mean υ^{-3} over the fluorescence spectrum. Furthermore, ε is the molar extinction coefficient in $l.mol^{-1}.cm^{-1}$.
For isolated molecules and small clusters, $nf = 1$ and $n_a = 1$, and thus the ~5% decrease in k_{rad} of the A-isomer can be attributed in part to a solvation effect on $\left\langle \upsilon_f^{-3} \right\rangle_{Av}^{-1}$ and to the effect of the electrostatic interaction between the solute and the

solvent molecule on the fluorescence spectrum. Knowing the red-shift of 380 cm^{-1} for the A-isomer, the first factor will decrease k_{rad}, in the cluster, by 3.5 %. The effect of the solvent on the fluorescence spectrum in small clusters can, in principle, be calculated by an extension of the model suggested by Shalev and Jortner for solute rare-gas heteroclusters [58]. It should be mentioned that the effect of the refractive index on the radiative lifetime becomes important in solution as well as in clusters with dimensions much larger than the wavelength of the absorbed light.
The radiative rate of the *trans*-stilbene in (3:2)-methylcyclohexane-(iso-hexane) solvent has been found by Sumitami *et al.* to be 6.0×10^8 s^{-1} [59], which agrees closely with the value of 5.9×10^8 s^{-1} in -pentane at 30 °C calculated by Saltiel *et al.* using eq. (7) [60]. The refractive index of the solvent ($n = 1.36$ at 30 °C and 403 nm [63]) thus induces an increase in the radiative rate by approximately a factor of $n^2 = 1.85$ and counteracts the decrease in the radiative rate due to the solvent effect on the fluorescence spectrum.

In the gas-phase measurements (390 K) of the Hochstrasser group [58,59], the lifetime of *trans*-stilbene was found to be 15 ps at 265 nm and 55 ps at 287 nm excitation wavelength. In this case, the refractive index is one, but the laser excitation together with the thermal excitation induces a large excess energy in the molecule, and the lifetime represents an average value over the energy distribution including isomerization at higher energies [64].

4.3.3.2 Fluorescence Rates: Narrow-Band Detection

(a) $AX_0^n, 0 \leq n \leq 5$:

In an attempt to characterize the IVR behavior of stilbene-$(hexane)_1$ clusters, time- and frequency-resolved fluorescence detection has been performed for all ten transitions observed in the fluorescence excitation spectrum of the A-isomer at excess energies ranging from 0 to 300 cm^{-1}. Considering the signal-to-background ratio in the fluorescence excitation spectrum (Fig. 4.2), the excitation of a single vibronic level (SVL) in the S_1-state will be difficult especially at higher excess-energies. The fluorescence of large clusters in the supersonic-jet might contaminate the SVL fluorescence of 1:1 complex. As will be shown in Chapter 4, the absorption spectra of cluster with different sizes overlap and collective excitation becomes possible.

For excitation of all overtones of the low-frequency cluster mode X (AX_0^n, $0 \leq n \leq 5$), single exponential decays have been observed (Fig. 4.10), independent of detection wavelength and resolution. This indicates that vibrational energy redistribution is essentially *absent* at these low excitation energies. A closer look at the experimental data (shown in Table (4)) reveals that for all excited overtones, the decay rates measured with single vibrational level detection are slightly lower than for total fluorescence detection. This indicates that energy redistribution between different cluster modes occurs on a time scale significantly longer than the radiative lifetime.

(b) $A25_0^1$:

Excitation of the symmetric in-plane stilbene-type mode $A25_0^1$ leads to a biexponential decay with SVL detection. The fast decay component has a time constant (τ_1) of ~670 ps while ~2.7 ns was measured for the second component (τ_2) (Fig. 4.11 and Table (6)). In contrast to the biexponential decays observed for the bare stilbene molecule at energies above 1200 cm^{-1}, the relative amplitude of the slow component is much larger than one (a_s / a_f = 3.6). This large amount of long-lived fluorescence is probably not due to detection of redistributed fluorescence since the dispersed fluorescence spectrum is slightly congested in this region and the detection resolution was good enough for single vibronic level detection.

Biexponential decays are characteristic of dissipative IVR; one optically-active zero order level $|s\rangle$ couples strongly with a manifold of N ($N >> 1$) optically dark levels $\{|l\rangle\}$. If all these levels decay radiatively to the electronic ground state with a rate k_{rad}, the fluorescence decay for single vibrational level detection of the optically active state $|s\rangle$ is given by:

$$I_s(t) \propto (N-1)\exp[-(k_{rad}+\Delta)t] + \exp(-k_{rad}t), \tag{10}$$

where Δ corresponds to the rate of dissipative IVR. The above equation can be obtained quantum mechanically; an analogous kinetic description is also possible [65] if we consider the coupling in the N levels as reversible and the system decaying by k_{rad}. In this case, Δ is simply the sum of the forward and backward rate constants. Based on the above assumptions, the amplitude ratio of slow-to-fast component is $a_s / a_f = 1/(N-1)$, thus being smaller than unity.

In the case of the biexponential transient observed for excitation of $A25_0^1$, however, $a_s / a_f = 3.6$. Thus, the above IVR model (dissipative regime) does not account for the observed decay. In the $A25_0^1$ case, IVR can only occur by partitioning one high-energy, 200 cm^{-1} vibrational quantum of the stilbene mode υ_{25} into several quanta of low-frequency intermolecular vibrations. Once the energy has been transferred into the intermolecular modes, IVR is relatively more efficient within the manifold of intermolecular dark states $|c\rangle$. The low-frequency modes can exchange energy without large changes in the number of quanta involved. This is a sequential IVR process, where level coupling occurs between an optically active vibrational level $|a\rangle$ and an optically inactive state $|b\rangle$, which in turn couples to $|c\rangle$, etc. This state $|b\rangle$ differs in energy by $\Delta E = h\omega$ (ω may be negative), and $|a\rangle$ and $|b\rangle$ are coupled via an interaction matrix element V_{ab}. Both levels can fluoresce to the ground state with a radiative rate k_{rad}. The strong coupling of $|b\rangle$ to a manifold of energetically accessible vibrational levels $\{|l\rangle\}$ is introduced phenomenologically by a nonradiative decay of $|b\rangle$ with a rate constant Γ (Fig. 4.12). Such sequential IVR mechanisms were first observed in anthracene [1,2,6] and have found a number of applications (see *e.g.* refs. [22,66]). The equations of time-dependent perturbation theory in the interaction picture are then [51,67,68]:

$$iha = 2\pi V_{ab}\exp(-i\omega t).\, b - \frac{1}{2}ihk_{rad}.\, a$$
$$ihb = 2\pi V_{ab}\exp(i\omega t).\, a - \frac{1}{2}ih(k_{rad} + \Gamma).\, b, \qquad (11)$$

where a and b denote the probability amplitude in states $|a\rangle$ and $|b\rangle$, respectively. The general solutions of eq. (11) are

$$a = A_1\exp(\mu_1 t) + A_2\exp(\mu_2 t),$$

$$b = \frac{ih}{2\pi V_{ab}}\left\{\left(\mu_1 + \frac{1}{2}k_{rad}\right)A_1\exp[(\mu_1 + i\omega)t] + \left(\mu_2 + \frac{1}{2}k_{rad}\right)A_2\exp[(\mu_2 + i\omega)t]\right\}, \qquad (12)$$

with

$$\mu_{1,2} = -\frac{1}{4}\left[-(2k_{rad} + \Gamma + 2i\omega) \pm \left(\sqrt{\Gamma^2 - 4\omega^2} + 4i\Gamma\omega - 16V_{ab}^2\right)\right]. \qquad (13)$$

The excitation of the optically active $|a\rangle$ state is represented by the initial conditions

$a = 1,$

$b = 0$, at $t = 0$, and this gives

$$A_1 = \left(\mu_2 + \frac{1}{2}k_{rad}\right) / \left(\mu_2 - \mu_1\right), \qquad A_2 = -\left(\mu_1 + \frac{1}{2}k_{rad}\right) / \left(\mu_2 - \mu_1\right). \tag{14}$$

The fluorescence intensity for single-level detection of the optically active state $|a\rangle$ is proportional to

$$|a|^2 = \left|A_1 \exp(\mu_1 t) + A_2 \exp(\mu_2 t)\right|^2 \ . \tag{15}$$

Using this simplified picture, we can successfully model the observed decay for excitation of $A25_0^1$ if we choose the parameters $k_{rad} = 0.358 \times 10^9$ s^{-1} (known), V_{ab} = 0.6 GHz, $\omega = 2\pi\left(E_b - E_a\right)/h$ = 2.5 GHz, and $\Gamma = 1.0 \times 10^9$ s^{-1} (Fig. 4.13). To reproduce quasi-biexponential decays with the above model, the damping, introduced by the nonradiative decay rate Γ, has to be stronger than the effective vibrational coupling V_{ab} between states $|a\rangle$ and $|b\rangle$. This is consistent with the suggested physical picture in which the coupling between the intermolecular modes is enhanced compared to the coupling between the stilbene modes υ_{25} and the cluster modes due to a large change in the number of vibrational quanta involved and/or the mismatch in energy. The quantum mechanical treatment, mentioned above, has a kinetic analog assuming a sequential process with reversibility in the first step. This analog will proceed with the final rate being faster than the equilibrium rate in the first step. Under this condition, the fast component would essentially be given by Γ and the slow one by the vibration rate, with the amplitude ratio of fast to slow now being less than one. It should be noted, however, that the quantum treatment is more appropriate, as these limits of extreme kinetic parameters are not exact and do not include the coherence in the system.

(c) $A25_0^1 X_0^n, 0 \leq n \leq 5$:

As shown in Fig. 4.14, excitation of a combination band of the stilbene-type mode υ_{25} with the low-frequency cluster mode, $A25_0^1X_0^1$, leads to a decay with strong quantum-beat modulation. Fourier analysis [2] of the signal reveals at least three frequencies, the most prominent of which has a frequency of 1.73 GHz, corresponding to a recurrence period of ~580 ps. A somewhat less modulated decay is observed for excitation of the next overtone $A25_0^1X_0^2$ (see Fig. 4.14 and Table (5)). Again, at least three beat frequencies can be identified by Fourier transformation, indicating that a number of modes are involved in the energy exchange.

The fluorescence decay underlying the modulation can not be described by a single exponential with a lifetime equal to the inverse of the radiative rate. In both cases, for $A25_0^1X_0^1$ and $A25_0^1X_0^2$, the underlying decay is clearly multiexponential and fits well to a sum of two exponentials with lifetimes of 0.7 and 2.7 ns (fast/slow amplitude ratio (a_f / a_s) = 0.3), as found in the analysis of the decay of $A25_0^1$. This leads us to the conclusion that in the case of all three excited levels, the underlying biexponential decay is due to the energy flow out of the stilbene-type mode υ_{25} into the cluster vibrations and can be described in terms of the simple model (Fig. 4.12) described above.

The quantum beat monitored for $A25_0^1X_0^3$ (see Fig. 4.14 and Table (5)) is different in that only one frequency is prominent in the Fourier spectrum with υ = 2.02 GHz, equivalent to a recurrence period of 492 ps. It is worth mentioning that more than ten recurrences have been monitored in this perfect example of quantum beats in clusters, indicating a coherent and reversible energy flow involving t-stilbene-(hexane) cluster modes.

The dynamics of $A25_0^1$ and $A25_0^1X_0^3$ vibrational modes might exhibit mode selectivity. This could be examined by fitting the quantum-beats modulated fluorescence decay of the $A25_0^1X_0^3$ combination band using eq. (15). A reasonable fit, especially of the first 3 ns, was obtained using the following parameters: k_{rad} = 0.358x10^{9}s^{-1}, V_{ab} = 4.9 GHz, $\omega = 2\pi(E_b - E_a)/h$ = 8.0 GHz, and Γ = 1.6x10^9 s^{-1} (see Fig. 4.13 and Table (5)). The main difference between this fit and that of $A25_0^1$ is the considerably larger coupling matrix element V_{ab}. This increase corresponds to a largely accelerated IVR rate. The IVR acceleration in the $A25_0^1X_0^3$ vibrational mode might occur because four vibrational quanta are excited and more pathways for energy redistribution are possible (with no or relatively little change in the total number of vibrational quanta). The effective coupling is enhanced when cluster and solute modes are matched.

By increasing the excitation energy further ($A25_0^1X_0^4$ and $A25_0^1X_0^5$), one monitors biexponential decays corresponding to dissipative energy redistribution (Fig. 4.15 and Table (6)). In both cases, the fast component of the decay was less than 100 ps (50 and 80 ps), indicating very rapid vibrational dynamics. From the amplitude ratio (a_f/a_s) of 5.5 for $A25_0^1X_0^4$, it can be inferred that the number of coupled levels (N) is at least 6. Unlike the situation for lower quanta of X, the fast component, in this dissipative regime, is the dominant one. The important point here is the dissipative regime and, unlike lower quanta of X, the dominance of the fast component. The slight modulation which remains on the decay of $A25_0^1X_0^4$ is typical for excitation energies just high enough to observe dissipative behavior, as has been demonstrated in the case of the isolated stilbene and anthracene molecules [1-6].

The cluster and the bare molecule have both similarities and striking differences in their IVR dynamics. Both exhibit the general regimes of IVR: *absent* IVR at low excess energies, manifested by single exponential decays, *restricted* IVR in an intermediate energy region with quantum-beat modulated decays, and *dissipative* IVR at high excess energies, identified by strongly biexponential decays.

4.3.3.3 Density of States Calculations

Estimates of the frequencies (76, 9, 15, 18, 108, and 78 cm^{-1}) of the six van der Waals modes of this complex, based on an atom-atom pair-potential calculation of the intermolecular potential, have recently been given by Mangle *et al.* [31]. Using these frequencies, we find that the density of states exceeds 60 per cm^{-1} at an excess energy of 200 cm^{-1} (Fig. 4.16). For the isolated stilbene molecule, restricted IVR is observed (in the energy range 789-1170 cm^{-1}) for a density of states between 10 and 150 per cm^{-1}. Since IVR is shown to be dissipative for higher values, the increase in the density of states through complexation seems more than enough to account for the observed dissipative IVR above 260 cm^{-1}. This assumes that the mean coupling elements between optically active and dark states in the cluster are at least comparable to those in the bare stilbene molecule. Even for intermolecular vibrational frequencies 50% higher than those used in the above estimation, the density of states would exceed 20 per cm^{-1} at excess energy of 200 cm^{-1} and 100 per cm^{-1} at 300 cm^{-1}.

4.3.3.4 IVR in Stilbene-(Hexane)$_1$ Complex: A-Isomer

The excitation energies, at which the three regimes were observed, is very different between the cluster and the isolated molecule. The bare stilbene molecule needs more than 600 cm^{-1} of vibrational energy to show quantum beats and more than 1200 cm^{-1} to reach the dissipative regime, whereas the corresponding energies are vastly decreased in the cluster. Quantum beats are found for energies between

220 cm^{-1} and 260 cm^{-1}, and at higher energies IVR is dissipative. One important factor for this lies in the large number of low-frequency vibrations (*i.e.* large density of states) provided by the complexation. Currently, a normal mode analysis of the intermolecular vibrations of stilbene-(hexane) complexes is not available and so a precise count of the density-of-states cannot be presented. To estimate the increase in the density-of-states on complexation, we calculated the density-of-states for stilbene-hexane complexes under the assumption that the frequencies of the intermolecular vibrations are the same as for a fairly similar complex, 2,5-diphenylfuran-(*n*-hexane) [31].

Out-of-phase quantum-beats have been observed in the case of anthracene and *trans*-stilbene [1-6] through detection of relaxed fluorescence. However, our attempts to observe similar out-of-phase quantum-beats in stilbene-(hexane)$_1$ cluster have not been successful. Furthermore, unlike bare trans-stilbene and anthracene molecules, the dispersed fluorescence spectra of the stilbene-(hexane) complex shows no sharp bands in the relaxed fluorescence. For two excitation bands, $A25_0^1$ and $A25_0^1X_0^2$, a slight rise was found in the time-resolved decays when detecting relaxed fluorescence, but the relative amplitude of the rising component was not large enough to allow an unambiguous determination of the corresponding time constant.

4.3.3.4 IVR in Stilbene-(Hexane)$_1$ Complex: C-Isomer

A similar investigation of the IVR behavior in the C-isomer was performed by detecting the time- and frequency- resolved fluorescence for the transitions CX_0^n ($0 \leq n \leq 4$) and $C25_0^1X_0^n$ ($0 \leq n \leq 2$). At very low excitation energies (CX_0^n, $n \leq 2$) single exponential decays are observed as in the case of the A-isomer (Fig. 4.10). Interestingly, excitation of the next two overtones of this low frequency cluster mode, CX_0^3 and CX_0^4, reveals beat-modulated decays, although the modulation is far less pronounced than in the case of the A-isomer. These quantum-beats represent a unique example for restricted energy redistribution between different cluster modes without a molecular mode of each one of the two cluster partners being excited.

Excitation of the symmetric stilbene vibration $C25_0^1$ shows dissipative energy flow into the intermolecular vibrations on a time scale of less than 100 ps, thus being far more rapid than observed for the A-isomer. This dissipative energy relaxation seems to become slightly more rapid for excitation of the combination bands $C25_0^1X_0^1$ and $C25_0^1X_0^2$ (Fig. 4.17). We thus conclude that vibrational energy redistribution in the C-isomer again proceeds via the three distinguishable regimes, *i.e.* absent, restricted, and dissipative. In comparison to the A-isomer, IVR is accelerated in the C-isomer. This is, at least in part, due to a lowering of the frequencies of intermolecular vibrations, as shown for the *X*-mode which has a frequency of 17 cm^{-1} in the C-isomer compared to 20 cm^{-1} in the excited state of isomer A. Even a small decrease in the low-frequency intermolecular vibrational frequencies raises the density of states significantly, leading to faster IVR. The less rigid structure of the C-isomer, as revealed by a smaller red-shift and a larger displacement of the *X* normal coordinate between ground and excited state, should lead to larger amplitude motions, and hence larger anharmonicities for the coupling.

4.4 CONCLUSION

In this work, the picosecond dynamics of IVR in "solute-solvent"-complexes of *trans*-stilbene and *n*-hexane was investigated using time- and frequency-resolved picosecond fluorescence spectroscopy. Due to the large binding energy and number of transitions in the fluorescence excitation spectrum, *trans*-stilbene-(hexane) clusters provide a unique opportunity to follow the energy redistribution from the solute molecule into the intermolecular solute-solvent vibrations without vibrational predissociation.

As in the bare *trans*-stilbene molecule, we identified and studied three different IVR regimes in this cluster. At low energies, no apparent vibrational redistribution of the optically excited level occurs on the time scale of the fluorescence lifetime. At intermediate energies, restricted IVR manifests itself through quantum-beat fluorescence decays, whereas quasi-biexponential decays at higher energy indicate a dissipative character of IVR. The mechanism of IVR involves sequential steps with an effective coupling, which is dependent on the excited vibrational mode in either the solute or cluster.

The striking difference between the IVR behavior in the isolated molecule and in the complex is the extreme lowering of the amount of excess energy necessary for rapid energy redistribution. While the bare stilbene molecule must be excited to vibrational energies of at least 600 cm^{-1} to observe restricted IVR, quantum beats in the A-isomer of the complex were observed at energies between 200 cm^{-1} and 240 cm^{-1} and between 60 cm^{-1} and 80 cm^{-1} in the case of the C-isomer. At all higher energies, vibrational energy redistributes dissipatively on a time scale of tens of picoseconds. This factor of five decrease in the amount of energy needed for IVR to occur dissipatively compared to the bare stilbene molecule, where dissipative IVR sets in at 1200 cm^{-1}, is related to the enormous increase in the density of states provided by the six low-frequency intermolecular cluster vibrations. The coherent transfer of energy between the solute and cluster modes becomes evident in a quantum-beat pattern (up to ten recurrences) with a redistribution time of ~ 500 ps. There is an interplay between the structure and the dynamics of IVR in the two isomers studied. Further studies of the dynamics are planned for larger members of the cluster family.

Table (1): Assignment of the dispersed fluorescence spectrum of 0_0^0-transition in both A- and C-isomers of *trans*-stilbene-(hexane)$_1$ complex.

A-Isomer			C-Isomer		
Frequency[a] [cm^{-1}]	Relative Intensity	Assignment[b]	Frequency [cm^{-1}]	Relative Intensity	Assignment
0.0	0.67	A 0_0^0	0.0	0.34	C 0_0^0
17.5	1.00	A X_1^0	15	0.86	C X_1^0
35	0.59	A X_2^0	30	1.00	C X_2^0
52	0.18	A X_3^0	45	0.67	C X_3^0
76.5	0.07	A Y_1^0 (?)	59.5	0.24	C X_4^0
92.5	0.06	A $Y_1^0 X_1^0$	204	0.24	C 25_1^0
205	0.57	A 25_1^0	219	0.66	C $25_1^0 X_1^0$
221.5	0.95	A $25_1^0 X_1^0$	234	0.94	C $25_1^0 X_2^0$
239	0.66	A $25_1^0 X_2^0$	248	0.79	C $25_1^0 X_3^0$
256.5	0.19	A $25_1^0 X_3^0$	262	0.36	C $25_1^0 X_4^0$
279.5	0.07	A $25_1^0 Y_1^0$	282	0.18	?
297	0.12	A $25_1^0 Y_1^0 X_1^0$	407	0.09	C 25_2^0
314	0.05	A $25_1^0 Y_1^0 X_2^0$	421	0.29	C $25_2^0 X_1^0$
409	0.27	A 25_2^0	436	0.47	C $25_2^0 X_2^0$
426	0.55	A $25_2^0 X_1^0$	453	0.53	C $25_2^0 X_3^0$
443.5	0.42	A $25_2^0 X_2^0$	467	0.25	C $25_2^0 X_4^0$
460.5	0.14	A $25_2^0 X_3^0$	625	0.06	C $25_3^0 X_1^0$
485	0.02	A $25_2^0 Y_1^0$	639	0.18	C $25_3^0 X_2^0$
503	0.08	A $25_2^0 Y_1^0 X_1^0$	654	0.22	C $25_3^0 X_3^0$
519	0.05	A $25_2^0 Y_2^0 X_1^0$	668	0.15	C $25_3^0 X_4^0$

Table (1) (continue): Assignment of the dispersed fluorescence spectrum of 0_0^0-transition in both A- and C-isomers of *trans*-stilbene-(hexane)$_1$ complex.

A-Isomer			C-Isomer		
Frequency [a] [cm^{-1}]	Relative Intensity	Assignment [b]	Frequency [cm^{-1}]	Relative Intensity	Assignment
616	0.09	$A25_3^0$			
632.5	0.22	$A25_3^0X_1^0$			
649	0.19	$A25_3^0X_2^0$			
665	0.10	$A25_3^0X_3^0$			

[a] Frequencies are reported relative to the 0_0^0-transition of each isomer: $\upsilon(A\,0_0^0) = 31855$ cm^{-1}, $\upsilon(C\,0_0^0) = 31970$ cm^{-1}[30].

[b] $IY_k^lZ_m^n$, where I denotes the isomer (A or C), and Y and Z the vibrational modes. The sub- and superscripts indicate the number of vibrational quanta in the ground and excited state, respectively.

Table (2): Fitting parameters which gave the best aggreement between the experimental and Franck-Condon factor calculations (see text).

Isomer A		Isomer C	
$\upsilon_g = 17.2 \pm 0.5$ cm^{-1}	$\upsilon_e = 20.0 + 0.5$ cm^{-1}	$\upsilon_g = 14.7 \pm 0.5$ cm^{-1}	$\upsilon_e = 17.8 + 0.5$ cm^{-1}
$\sigma_g = 0.028 \pm 0.005$	$\sigma_e = 0.025 + 0.005$	$\sigma_g = 0.025 \pm 0.008$	$\sigma_e = 0.020 + 0.005$
$\gamma = 1.60 + 0.05$		$\gamma = 2.25 \pm 0.05$	

Table (3): The excess energy dependence of the fluorescence decay times (τ_f) of *trans*-stilbene-hexane (1:1) complex with wide-band detection.

Transition	Energy [cm^{-1}] [a]	τ [ns]
$A0_0^0$	0	2.79
AX_0^1	20	2.79
AX_0^2	40	2.79
AX_0^3	60	2.80
AX_0^4	80	2.78
AX_0^5	100	2.78
$C0_0^0$	115	2.80
CX_0^1	132	2.78
CX_0^2	149	2.78
CX_0^3	166	2.76
CX_0^4	183	2.78
$A25_0^1$	200	2.78
$A25_0^1X_0^1$	220	2.77
$A25_0^1X_0^2$	240	2.77
$A25_0^1X_0^3$	260	2.77
$A25_0^1X_0^4$	280	2.76
$A25_0^1X_0^5$	300	2.76
$C25_0^1$	315	2.76
$C25_0^1X_0^1$	332	2.76
$C25_0^1X_0^2$	349	2.75

[a] Energy relative to (A 0_0^0) = 31855 cm^{-1}.

Table (4): Fluorescence decay times (τ_f) of *trans*-stilbene-hexane (1:1) complex for single vibronic level (narrow-band) detection in the intermediate energy domain (*i.e.* restricted IVR).

Transition	Energy [a] [cm^{-1}]	Detection Band [b] [cm^{-1}]	Resolution [cm^{-1}]	τ_f [ns]
A 0^0_0	0	17	33	2.772
A 0^0_0	0	222	33	2.779
AX^1_0	20	51	33	2.733
AX^2_0	40	68	33	2.714
AX^3_0	60	0	33	2.716
AX^4_0	80	48	33	2.654
AX^4_0	80	97	33	2.672
C 0^0_0	115	231	25	2.756
C 0^0_0	115	1850	33	2.786
CX^1_0	132	49	25	2.668
CX^2_0	149	90	33	2.731

[a] Energy relative to (A 0^0_0) = 31855 cm^{-1}.

[b] Detection wavelength given in cm^{-1} to the red of the excitation laser.

Table (5): Prominent beat frequencies modulating the decays of *trans*-stilbene-hexane (1:1) complexes shown in Figs. 4.10 and 4.14.

Transition	Energy [cm^{-1}] [a]	Detection Band [cm^{-1}] [b]	Resolution [cm^{-1}]	Frequencies $\omega/2\pi$ [cm^{-1}]
C X^{3}	166	20	33	0.77, 1.50
C X^{4}	183	20	18	0.76, 1.52
A $25^{1}X^{1}$	220	52	17	0.77, 1.71, 2.35
A $25^{1}X^{1}$	220	52	17	0.74, 1.75, 2.35
A $25^{1}X^{2}$	240	68	65	2.97, 1.29, 3.84
A $25^{1}X^{3}$	260	68	17	2.02

Energy relative to (A 0_0^0) = 31855 cm^{-1}.

Detection wavelength given in cm^{-1} to the red of the excitation laser.

Table (6): Decay parameters of the biexponential fluorescence (Figs. 4.11, 4.15, and 4.17) decay profiles observed for *trans*-stilbene-hexane (1:1)-complex.

Transition	Energy	Detection	Resolution	Decay parameters		
	[cm^{-1}]	Band [cm^{-1}]	[cm^{-1}]	τ_1[ns]	τ_2[ns]	a_s/a_f
A25^1	200	18	8	2.73	0.67	0.28
A25^1	220	18	11	2.80	0.56	0.35
A25^1	240	18	25	2.76	0.57	0.33
A$25^1 X^4$	260	100	80	0.05	2.44	0.18
A$25^1 X^5$	280	64	65	0.08	2.35	0.25
C25^1	315	87	80	0.07	2.40	0.15
C$25^1 X^1$	332	76	80	0.06	2.03	0.12
C$25^1 X^2$	349	76	80	0.04	2.45	0.23

[a] Energy relative to $\upsilon(A\,0_0^0) = 31855$ cm^{-1}.

4.5 REFERENCES

1. W. R. Lambert, P. M. Felker, and A. H. Zewail, *J. Chem. Phys.* **81**, 2217 (1984).
2. P. M. Felker and A. H. Zewail, *J. Chem. Phys.* **82**, 2961, 2975, 2994 (1985).
3. J. A. Syage, W. R. Lambert, P. M. Felker, and A. H. Zewail, and R. M. Hochstrasser, *Chem. Phys. Lett.* **88,** 266 (1982).
4. J. A. Syage, P. M. Felker, and A. H. Zewail, *J. Chem. Phys.* **81**, 4685, 4706 (1984).
5. P. M. Felker, W. R. Lambert, and A. H. Zewail, *J. Chem. Phys.* **82**, 3003 (1985).
6. P.M. Felker and A. H. Zewail, *Adv. Chem. Phys.* **70**, 265 (1988).
7. A. J. Kaziska, S. A. Wittmeyer, A. L. Motyka, and M. R. Topp, *Chem. Phys. Lett.* **136**, 199 (1987).
8. J. F. Kaufmann, M. J. Côté, P. G. Smith, and J. D. McDonald, *J. Chem. Phys.* **90**, 2874 (1989).
9. D. R. Demmer, J. W. Hager, G. W. Leach, and S. C. Wallace, *Chem. Phys. Lett.* **136**, 329 (1987).
10. J. S. Baskin, M. Dantus, and A. H. Zewail, *Chem. Phys. Letters* **130**, 473 (1986).
11. G. A. Bickel, D. R. Demmer, G. W. Leach, and S. C. Wallace, *Chem. Phys. Lett.* **145**, 423 (1988).
12. C. Lakshminarayan and J. L. Knee, *J. Phys. Chem.* **94**, 2637 (1990).
13. P. G. Smith and J. D. McDonald, *J. Chem. Phys.* **92**, 1004 (1990).
14. P. G. Smith and J. D. McDonald, *J. Chem. Phys.* **96**, 7344 (1992).
15. A. J. Kaziska and M. R. Topp, *Chem. Phys. Lett.* **180**, 423 (1991).

16. L. W. Peng, B. W. Keelan, D. H. Semmes and A. H. Zewail, *J. Phys. Chem.* **92**, 5540 (1988).

17. L. Bañares, A. A. Heikal, and A. H. Zewail, *J. Phys. Chem.* **96**, 4127 (1992).

18. D. M. Willberg, M. Gutmann, E. E. Nikitin, and A. H. Zewail, *Chem. Phys. Lett.* **201**, 506 (1993).

19. M. Gutmann, D. M. Willberg, and A. H. Zewail, *J. Chem. Phys.* **97**, 8048 (1992).

20. M. Gutmann, D. M. Willberg, and A. H. Zewail, *J. Chem. Phys.* **97**, 8037 (1992).

21. D. M. Willberg, M. Gutmann, J. J. Breen, and A. H. Zewail, *J. Chem. Phys.* **96**, 198 (1992).

22. D. H. Semmes, J. S. Baskin, and A. H. Zewail, *J. Chem. Phys.* **92**, 3359 (1990).

23. A. Heikal, L. Bañares, D. H. Semmes, and A. H. Zewail, *Chem. Phys.* **157**, 231 (1990).

24. M. R. Nimlos, M. A. Young, E. R. Bernstein, and D. F. Kelley, *J. Chem. Phys.***91** , 5268 (1989).

25. J. J. F. Ramackers, H. K. van Dijk, J. Langelaar, and R. P. H. Rettschnick, *Faraday Disc. Chem. Soc.* **75**, 183 (1983).

26. M. Heppner and R.P.H. Rettschnick, in: *Structure and Dynamics of Weakly Bound Complexes*, ed. A. Weber (Reider, Dordtrecht 1987), p. 553.

27. P. M. Weber and S. A. Rice, *J. Chem. Phys.* **88**, 6120 (1988).

28. A. J. Kaziska, S. A. Wittmeyer, and M. R. Topp, *J. Phys. Chem.* **95**, 3663 (1991).

29. M. Topp, *Inter. Rev. Phys. Chem.* **12**, 149 (1993).

30. C. Lienau, Ph. D. Dissertation, Gottingen (1992).

31. E. A. Mangle, A. L. Motyka, P. Salvi, and M. R. Topp, *Chem. Phys.* **112**, 443 (1987).

32. A. J. Kaziska, M. I. Shchuka, and M. R. Topp, *Chem. Phys. Lett.* **183**, 552 (1991).

33. D. E. Williams and T. L. Starr, *Comput. Chem.* **1**, 173 (1977).

34. D. E. Williams, *Acta Cryst.* **A31**, 56 (1975); **36**, 715 (1980).

35. G. Nemethy, M. S. Pottle, and H. A. Scheraga, *J. Phys. Chem.* **87**, 1883 (1983).

36 F. A. Momany, L. M. Carruthers, R. F. McGuire, and H. A. Scheraga, *J. Phys. Chem.* **78**, 1595 (1974).

37. K. S. Law and E. R. Bernstein, *J. Chem. Phys.* **82**, 2856 (1985).

38. F. Negri, G. Orlandi and F. Zerbetto, *J. Phys. Chem.* **93**, 5124 (1989).

39. Landolt-Bornstein, *Zahlenwerte und Funktionen aus Naturwissenschaften und Technik*, Neue Serie, Vol. **II**, p. 7 (Springer, Berlin, 1976).

40. J. S. Baskin and A. H. Zewail, *J. Phys. Chem.* **93**, 5701 (1989).

41. D. H. Waldeck, *Chem. Rev.* **91**, 415 (1991).

42. S. Li and E. R. Berstein, *J. Chem. Phys.* **95**, 1577 (1991).

43. A. Warshel, *J. Chem. Phys.* **62**, 214 (1975).

44. L. H. Spangler, R. van Zee, and T. S. Zwier, *J. Phys. Chem.* **91**, 2782 (1987).

45. T. Urano, H. Hamaguchi, M. Tasumi, K. Yamanouchi, S. Tsuchiya, and T. L. Gustafson, *J. Chem. Phys.* **91**, 3884 (1989).

46. T. Suzuki, N. Mikami, and M. Ito, *J. Phys. Chem.* **90**, 6431 (1986).

47. T. J. Majors, U. Even, and J. Jortner, *J. Chem. Phys.* **81**, 2330 (1984).

48. J. Troe, *Chem. Phys. Lett.* **114**, 241 (1985).

49. J. B. Coon, R. E. DeWames and C. M. Loyd, *J. Mol. Spectrosc.* **8**, 285 (1962).

50. F. Ansbacher, *Z. Naturforschung Teil A*, **14**, 889 (1959).

51. C. Cohen-Tannoudji, B. Diu and F. Laloë, *Quantum Mechanics* Vol. I and II (Wiley, NewYork, 1977).

52. P. M. Felker and A. H. Zewail, *J. Phys. Chem.* **89**, 5402 (1985).

53. M. Sonnenschein, A. Amirav, and J. Jortner, *J. Phys. Chem.* **88**, 4214 (1984).

54. A. Amirav and J. Jortner, *Chem. Phys. Lett.* **95**, 295 (1983).

55. S. J. Strickler and R. A. Berg, *J. Chem. Phys.* **37**, 814 (1962).

56. J. B. Birks and D. J. Dyson, *Proc. Roy. Soc.* **A 275**, 135 (1963).

57. J. B. Birks, in: *Photophysics of Aromatic Molecules* (Wiley-Interscience, New York, 1970).

58. E. Shalev and J.Jortner, *Chem. Phys. Lett.* **178**, 31 (1991).

59. M. Sumitani, N. Nakashima, K. Yoshihara and S. Nagakura, *Chem. Phys. Lett.* **51**, 183 (1977).

60. A. Marinari and J. Saltiel, *Mole. Photochem.* **7**, 225 (1976).

61. Landolt-Bornstein, *Zahlenwerte und Funktionen aus Naturwissenschaften und Technik*, Neue Serie, Vol II, pt. 8 (Springer, Berlin, 1961).

62. B. I. Greene, R. M. Hochstrasser and R. B. Weisman, *Chem. Phys.* **48**, 289 (1980).

63. R. M. Hochstrasser, *Pure Appl. Chem.* **52**, 2683 (1980).

64. J. W. Perry, N. F. Scherer and A. H. Zewail, *Chem. Phys. Lett.* **103** (1983) 1.

65. A. Frad, F. Lahmani, A. Tramer and C. Tric, *J. Chem. Phys.* **60**, 4419 (1974).

66. A. A. Stuchebrukhov and R. A. Marcus, in: *Proceedings of the Berlin Conference on Femtosecond Chemistry*, Berlin, 1993.

67. W. E. Lamb Jr. and R. C. Retherfor, *Phys. Rev.* **79**, 549 (1950).

68. T. E. Orlowski and A. H. Zewail, *J. Chem. Phys.* **70**, 1390 (1979).

69. T. Beyer and D. F. Swinehart, *Commun. Assoc. Comput. Mach.* **16**, 379 (1973).

4.6 FIGURE CAPTIONS

4.1 The minimum energy structure of *trans*-stilbene-hexane$_1$ (top views) based on Lennard-Jones atom-atom potential energy calculations. Three isomers were preidcted and only the more stable ones (A (top) and C (bottom) iosmers) are shown, see text.

4.2 Fluorescence excitation spectrum of *trans*-stilbene-(hexane) complex as reported by Lienau *et al.* [30]. The red-energy shift is given in cm^{-1} relative to the 0_0^0-transition of *trans*-stilbene, which has intensity of 1.0. The progressions AX_0^n and $A25_0^1X_0^n$ for the A-isomer and CX_0^n and $C25_0^1X_0^n$ for the C-isomer are high-lighted in the spectrum.

4.3 Dispersed fluorescence spectra of (top) *trans*-stilbene, (middle) A-isomer and (bottom) C-isomer of *trans*-stilbene-(hexane)$_1$ complex, excited to the transitions. The energy is given in cm^{-1} relative to the 0_0^0 band in *trans*-stilbene (32235 cm^{-1}), the A-isomer (31855 cm^{-1}), and C-isomer (31970 cm^{-1}), respectively. All three spectra have been recorded under the same experimental conditions: trans-stilbene temperature $T = 100\ ^\circ$C, helium backing pressure *(P)* = 60 psi, *x/d* ~30 (where *x* = laser-to-nozzle distance, and *d* = the nozzle diameter ~70 μm), and spectral resolution R = 8 cm^{-1}.

4.4 Low-energy region (0 to 400 cm^{-1}) of the dispersed fluorescence spectra following excitation of the 0_0^0 band and overtones X_0^n, $1 \leq n \leq 4$, of the low-frequency cluster mode X in the A- and C-isomer of stilbene-(hexane)$_1$

complexes. All spectra have been recorded under the same experimental conditions: $T = 100\ ^{\circ}\text{C}$, $P = 60$ psi, $x/d \sim 30$, and $R = 8\ \text{cm}^{-1}$.

4.5 Dispersed fluorescence spectra of 25_0^1 transition in *trans*-stilbene (top), A-isomer (middle), and C-isomer (bottom) of stilbene-(hexane)$_1$ complex.

4.6 Dispersed fluorescence spectra (0 to 500 cm^{-1}) following the excitation of symmetric in-plane ethylene bend mode (υ_{25}) and its combination bands $25_0^1 X_0^n$, $1 \leq n \leq 4$, for the A- and C-isomer of stilbene-(hexane)$_1$ complexes. Experimental conditions as those in Fig. 4.3.

4.7 Comparison of the dispersed fluorescence spectra AX_0^n, $n = 0, 1, 2$ (left), with simulations (right) based on a Franck-Condon analysis (see text for details). The following parameters were used in the simulation: $\upsilon_g = 17.2 \pm 0.5\ \text{cm}^{-1}$, $\upsilon_e = 20.0 \pm 0.5\ \text{cm}^{-1}$, $\sigma_g = 0.028 \pm 0.005$, $\sigma_e = 0.025 \pm 0.005$, $\gamma = 1.60 \pm 0.05$.

4.8. Comparison of the dispersed fluorescence spectra CX_0^n, $n = 0, 1, 2$ (left),with simulations (right) based on a Franck-Condon analysis (see text). The following parameters were used in the simulation: $\upsilon_g = 14.7 \pm 0.5\ \text{cm}^{-1}$, $\upsilon_e = 17.8 \pm 0.5\ \text{cm}^{-1}$, $\sigma_g = 0.025 \pm 0.008$, $\sigma_e = 0.020 \pm 0.005$, $\gamma = 2.25 \pm 0.05$.

4.9. Excess-energy dependence of the fluorescence lifetime τ_f of the electronically excited configuration S_1 of stilbene-(hexane)$_1$ complexes. Filled circles denote the A-isomer, and open circles C-isomer transtions. Total fluorescence detection has been achieved by completely opening the monochromator slits and setting the detection wavelength far to the red of excitation wavelength (see text).

4.10 Time- and frequency resolved fluorescence decay profiles following excitation of the electronic origin 0_0^0 and overtones X_0^n, $1 \leq n \leq 4$, of the low-frequency cluster mode X in the A- and C-isomer of *trans*-stilbene-(hexane) complexes. For all measurements the experimental conditions were the same as given in Fig. 4.3. The detection wavelength (relative to the respective origin) and spectral resolution from top to bottom are: A-isomer: 17 and 33 cm^{-1}, 51 and 33 cm^{-1}, 68 and 33 cm^{-1}, 0 and 33 cm^{-1}, 48 and 33 cm^{-1}. C-isomer: 231 and 25 cm^{-1}, 49 and 25 cm^{-1}, 90 and 33 cm^{-1}, 20 and 33 cm^{-1}, 20 and 33 cm^{-1}. The fitting parameters for these decays are given in Table (4) and (5).

4.11 A biexponential fluorescence decay following the excitation of 1:1 complex (A-isomer) to the $A25_0^1$ vibrational transition in the S$_1$-state. The fitting parameters are: $\tau_1 = 0.67$ ns, $\tau_2 = 2.73$ ns, and $a_s / a_f = 3.6$). The detection wavelength and spectral resolution are 18 cm^{-1} and 8 cm^{-1}, respectively. The residuals of both single and double exponential fit are shown to reflect the goodness of the fit.

4.12 A sequential model for IVR mechanism in 1:1 complex. The optically active level $|a\rangle$ is coupled via an interaction matrix element V_{ab} to an optically dark state $|b\rangle$. Both states can fluoresce to the electronic ground state $|g\rangle$ with a radiative rate k_{rad}. The strong coupling of $|b\rangle$ to a manifold of energetically nearby vibrational levels $\{|l\rangle\}$ is phenomenologically described by a nonradiative decay of $|b\rangle$ with a rate constant Γ.

4.13. Top: Comparison of the observed biexponential decay for the excitation of $A25^1_0$ (dotted line) to model calculations (solid line) using the sequential IVR model with k_{rad} = 0.358x10^9 s^{-1}, V_{ab} = 0.6 GHz, ω= $2\pi\left(E_b - E_a\right)/h$ = 2.5 GHz, and Γ= 1.0x10^9 s^{-1}. This corresponds to a coupling between the optically excited level $|a\rangle$ ($A25^1_0$) to the dark state $|b\rangle$ (intermolecular vibrational level), which is weak relative to the subsequent damping of $|b\rangle$ by vibronic coupling to the manifold of dark states $\{|l\rangle\}$.

Bottom: Comparison of the observed quantum beats for the excitation of $A25^1_0X^3_0$ (filled circles) to model calculations (solid line) using the sequential IVR model. The transitory behavior was obtained with k_{rad} = 0.358x10^9 s^{-1}, V_{ab} = 4.9 GHz, $\omega = 2\pi\left(E_b - E_a\right)/h$ = 8.0 GHz, and Γ = 1.6x10^9 s^{-1}. This corresponds to a coupling between the optically excited level $|a\rangle$ ($A25^1_0X^3_0$) to the dark state $|b\rangle$, which is strong relative to the subsequent damping of $|b\rangle$ by vibronic coupling to the manifold of dark states $\{|l\rangle\}$.

4.14. Fluorescence decays of the combination bands $A25^1_0X^n_0$, n = 1, 2, and 3 in A-isomer complex. Fourier analysis of the quantum-beat modulated decay of $A25^1_0X^1_0$ (top) reveals at least three modulation frequencies: υ_1 = 0.77 GHz, υ_2 = 1.71 GHz, υ_3 = 2.35 GHz. Detection wavelength and spectral resolution for this decay measurement were 52 cm^{-1}, spectral resolution 17 cm^{-1}, respectively. For $A25^1_0X^2_0$ (middle), three beat frequencies are distinguished by Fourier analysis: υ_1 = 2.97 GHz, υ_2 = 1.29 GHz, υ_3 = 3.84 GHz. The detection wavelength and resolution are 68 cm^{-1}, 65 cm^{-1}, respectively. The fluorescence decay of $A25_0^1 X_0^3$ combination (bottom) in the A-isomer shows quantum beats with a large modulation depth. The frequency of the modulation is 2.02 GHz which is equivalent to a recurrence period of 495 ps. Fluorescence was detected at 68 cm^{-1} to the red of the excitation laser wavelength. The spectral resolution was 17 cm^{-1} and the other experimental conditions are similar to those of Fig. 4.3.

4.15. Biexponential fluorescence decays for excitation of the A-isomer at excess energies of 280 cm^{-1} and 300 cm^{-1}. $A25_0^1 X_0^4$ (top): The decay is shown together with the best biexponential fit ($\tau_1 = 50$ ps, $\tau_2 = 2.44$ ns, $a_s / a_f =$ 0.18). The slight modulation observed is characteristic for excitation energies just high enough to observe dissipative IVR behavior. Detection wavelength: 100 cm^{-1}, resolution: 80 cm^{-1}. $A25_0^1 X_0^5$ (bottom): Parameters of the best biexponential fit are $\tau_1 = 80$ ps, $\tau_2 = 2.35$ ns, $a_s / a_f = 0.25$. The detection wavelength and the spectral resolution were 100 cm^{-1}, and 80 cm^{-1}. Experimental conditions are similar to those in Fig. 4.4.

4.16. Density of states for stilbene-(hexane)$_1$ complexes and bare *trans*-stilbene obtained by direct count [69]. For the vibrational modes of *trans*-stilbene, the frequency set, given by Negri *et al.* [38],were used. For the six intermolecular cluster modes, in stilbene-(hexane)$_1$, the calculated frequencies (see the text) were used. The dashed line represents the density of states obtained by using the frequencies estimated by Mangle *et al.* [31] for 2,5-diphenylfuran-(hexane)$_1$ complexes. Anharmonicity corrections were neglected. The energy is given with respect to the origin of bare stilbene and stilbene-(hexane)$_1$ complex, respectively.

4.17. The observed fluorescence decay profiles for excitation of $C25^1_0X^n_0$, $n = 0$, 1, 2 at excess energies of 200, 217 and 234 cm^{-1} relative to the origin of the C-isomer. The data are shown together with the best biexponential fit with the following parameters: $C25^1_0$ (top): $\tau_1 = 0.07$ ns, $\tau_2 = 2.40$ ns, $a_s / a_f = 0.15$. $C25^1_0X^1_0$ (middle): $\tau_1 = 0.06$ ns, $\tau_2 = 2.03$ ns, $a_s / a_f = 0.12$. $C25^1_0X^2_0$ (bottom): $\tau_1 = 0.04$ ns, $\tau_2 = 2.45$ ns, $a_s / a_f = 0.23$. All experiments have been performed with a spectral resolution of 80 cm^{-1} and the detection wavelength 87 cm^{-1} (top) and 76 cm^{-1} (middle and bottom) to the red of the excitation laser wavelength.

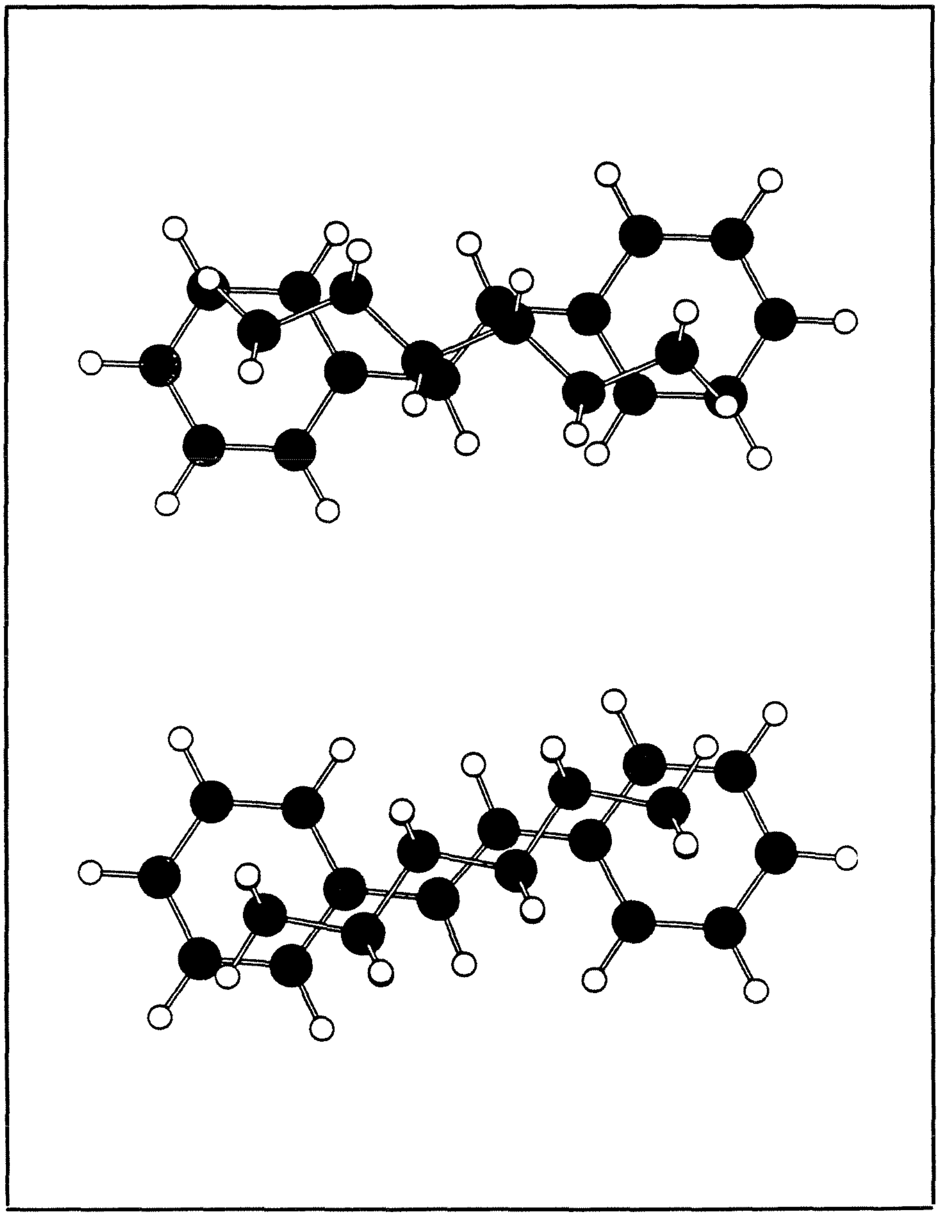

Fig. 4.1

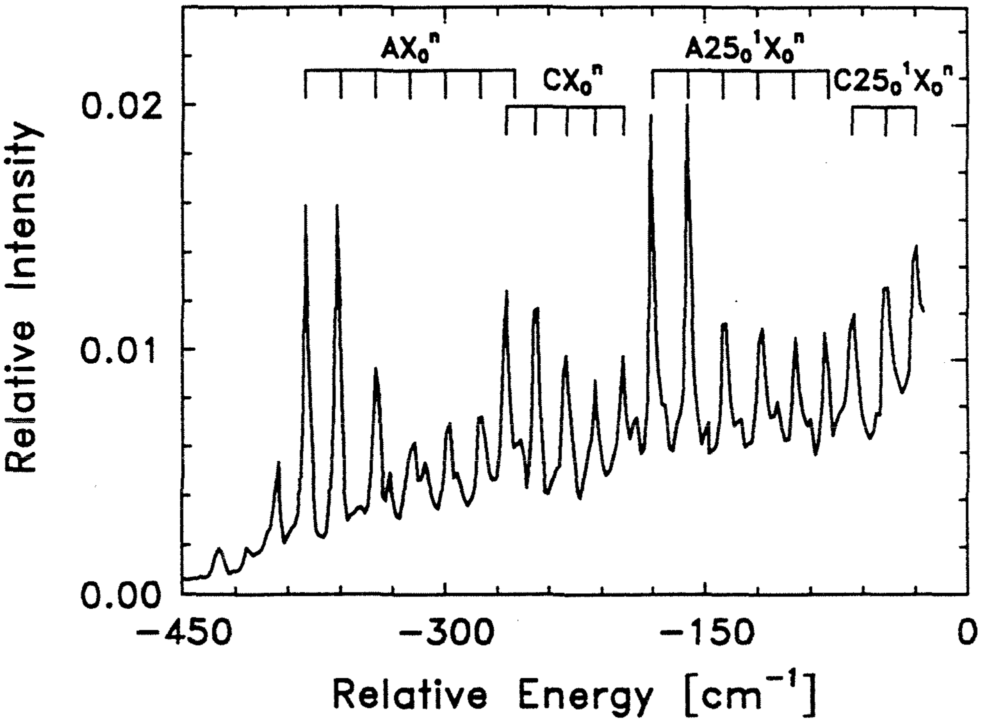
AX_0^n
CX_0^n
$A25_0^1X_0^n$
$C25_0^1X_0^n$
0.02
0.01
0.00
Relative Intensity
−450
−300
−150
0
Relative Energy [cm^{-1}]

Fig. 4.2

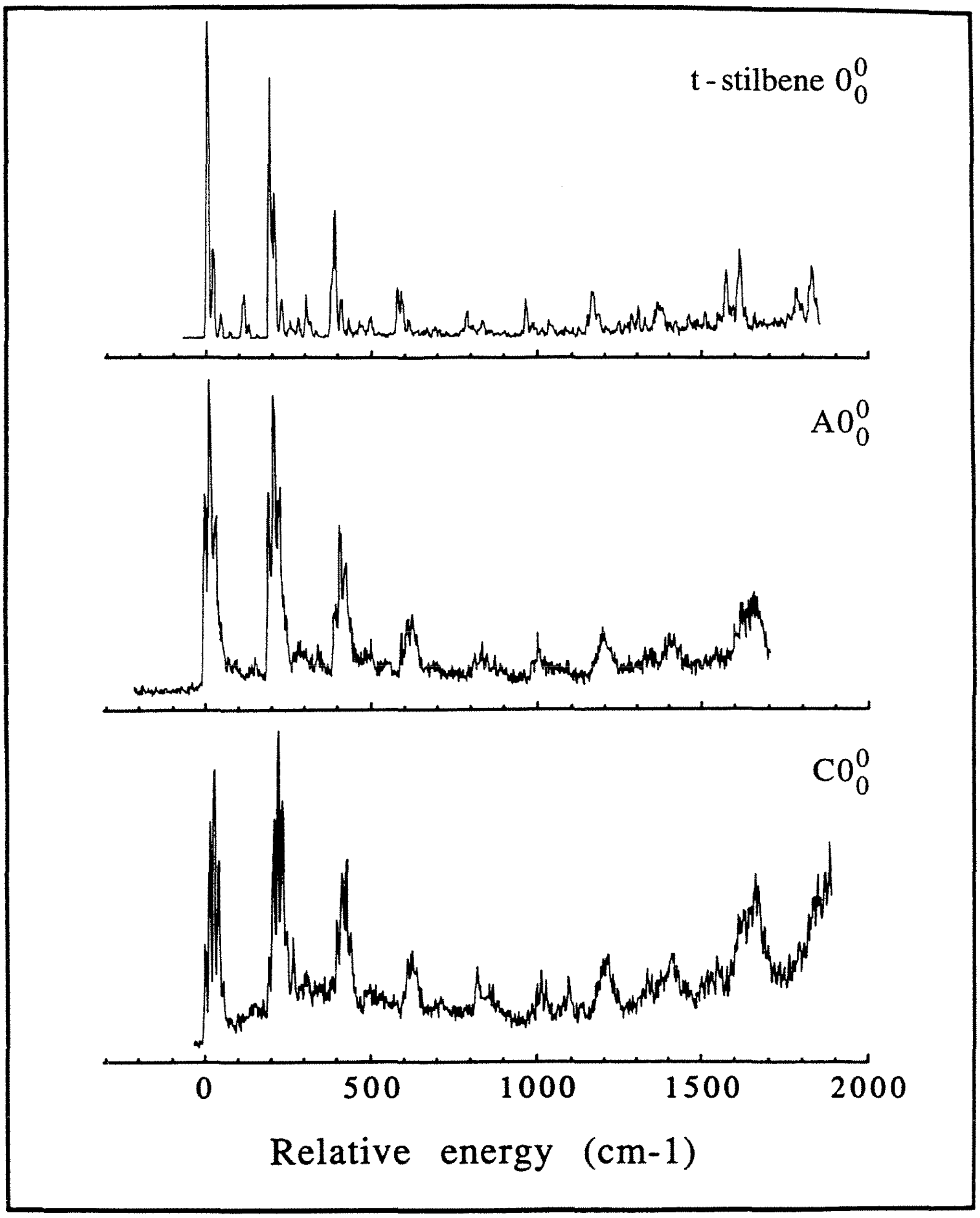
t-stilbene 0_0^0
$A0_0^0$
$C0_0^0$
0
500
1000
1500
2000
Relative energy (cm-1)

Fig. 4.3

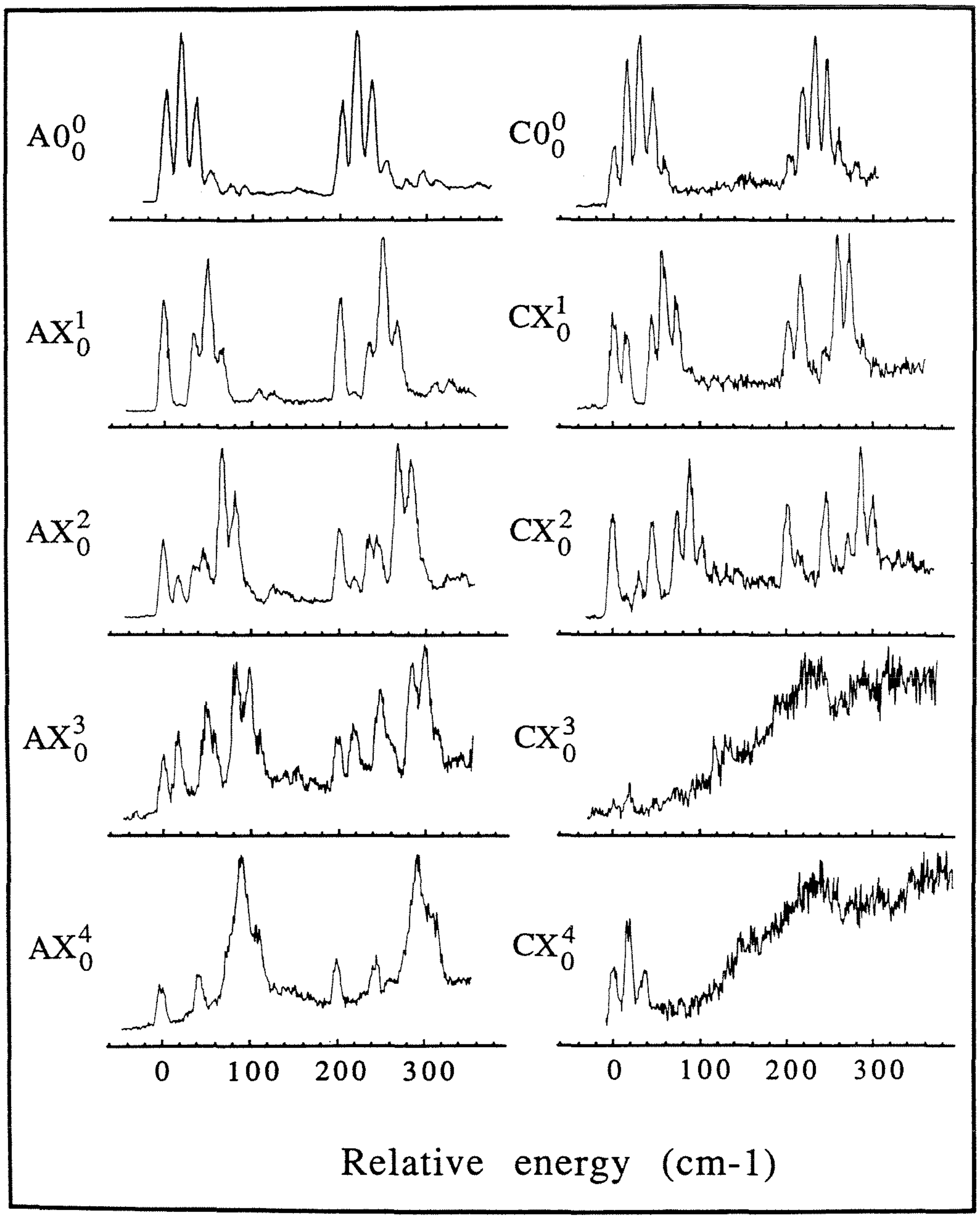
$A0_0^0$
$C0_0^0$
AX_0^1
CX_0^1
AX_0^2
CX_0^2
AX_0^3
CX_0^3
AX_0^4
CX_0^4
0
100
200
300
0
100
200
300
Relative energy (cm-1)

Fig. 4.4

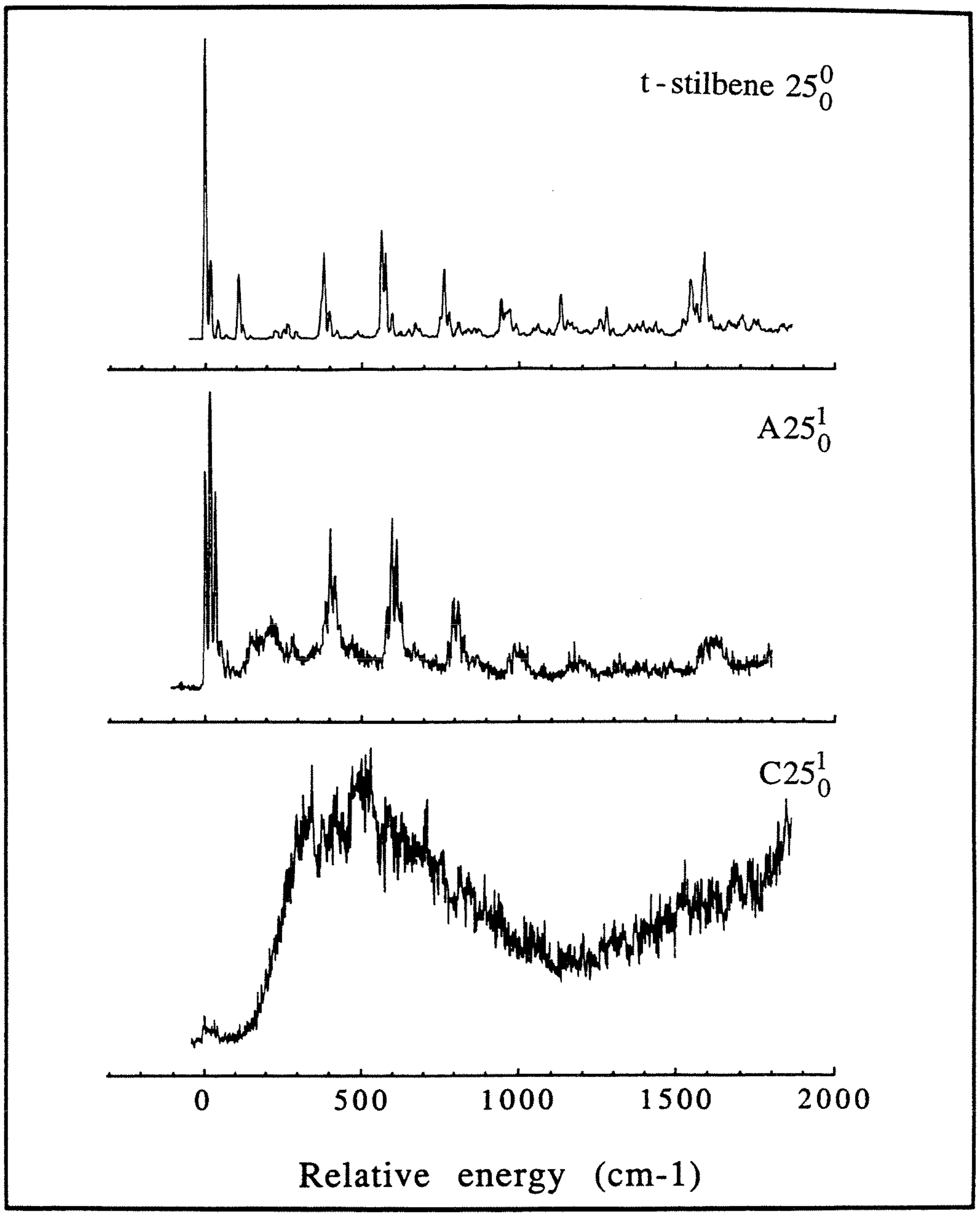
t-stilbene 25_0^0
$A25_0^1$
$C25_0^1$
0
500
1000
1500
2000
Relative energy (cm-1)

Fig. 4.5

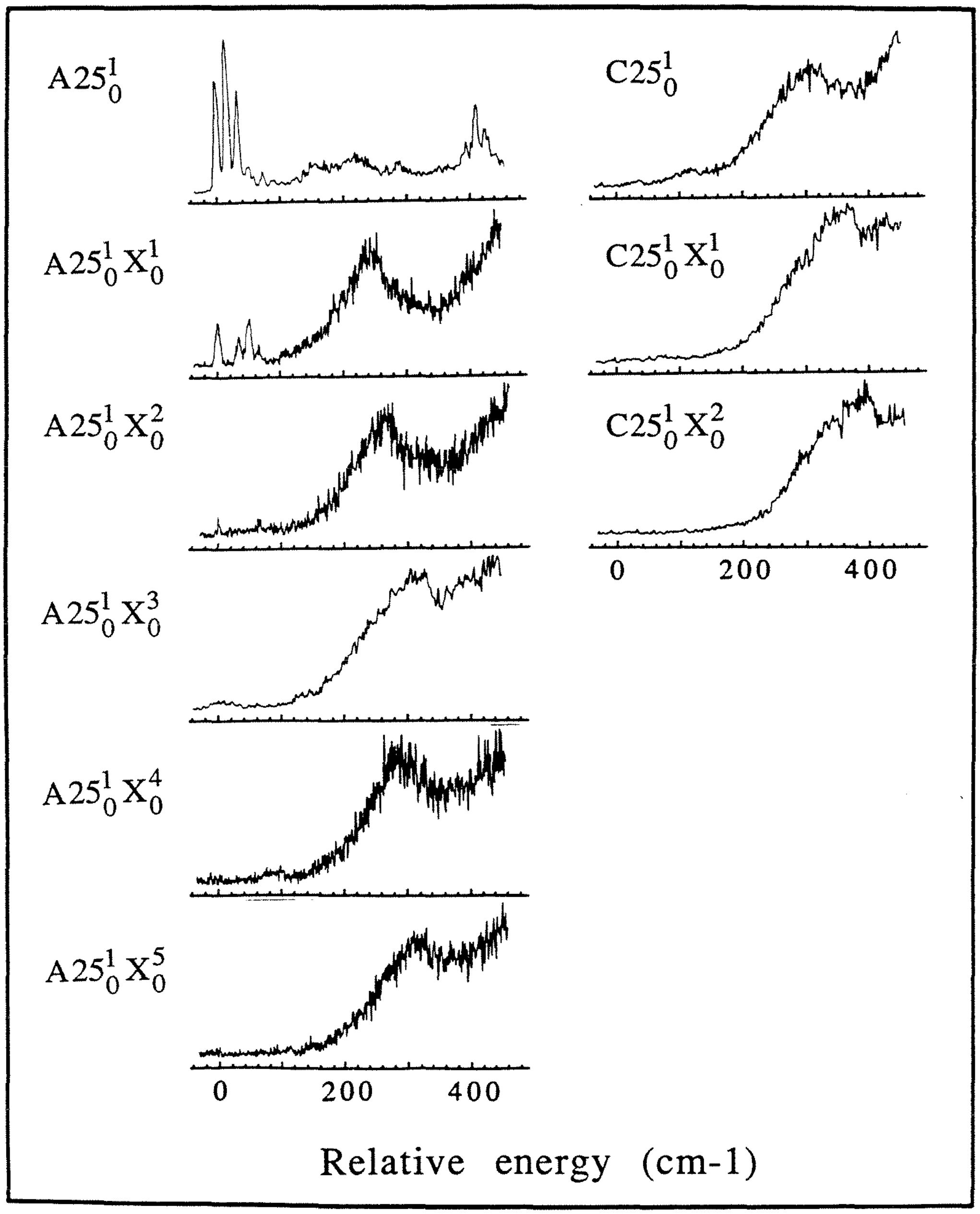
$A25^1_0$
$C25^1_0$
$A25^1_0X^1_0$
$C25^1_0X^1_0$
$A25^1_0X^2_0$
$C25^1_0X^2_0$
0
200
400
$A25^1_0X^3_0$
$A25^1_0X^4_0$
$A25^1_0X^5_0$
0
200
400
Relative energy (cm-1)

Fig. 4.6

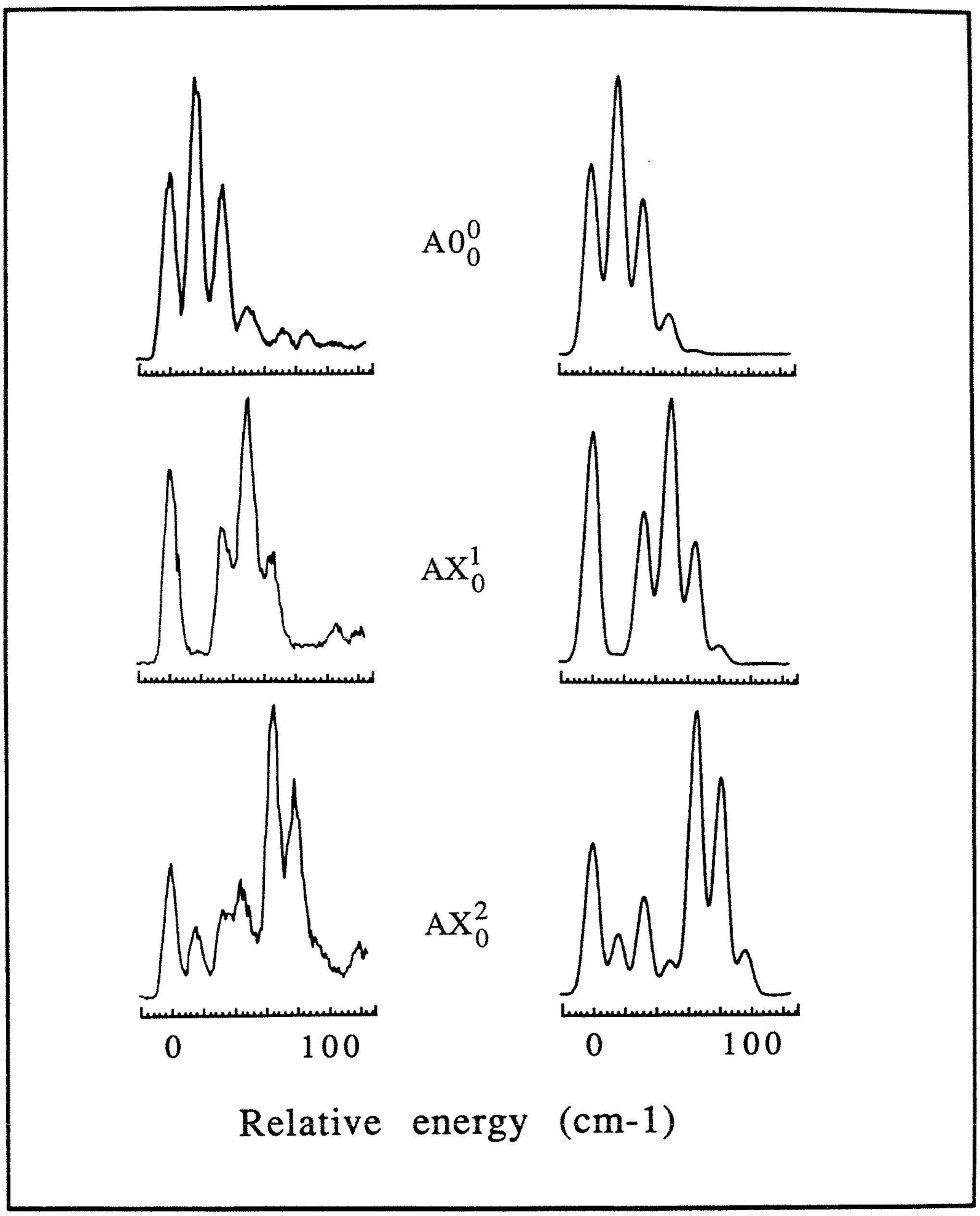

Fig. 4.7

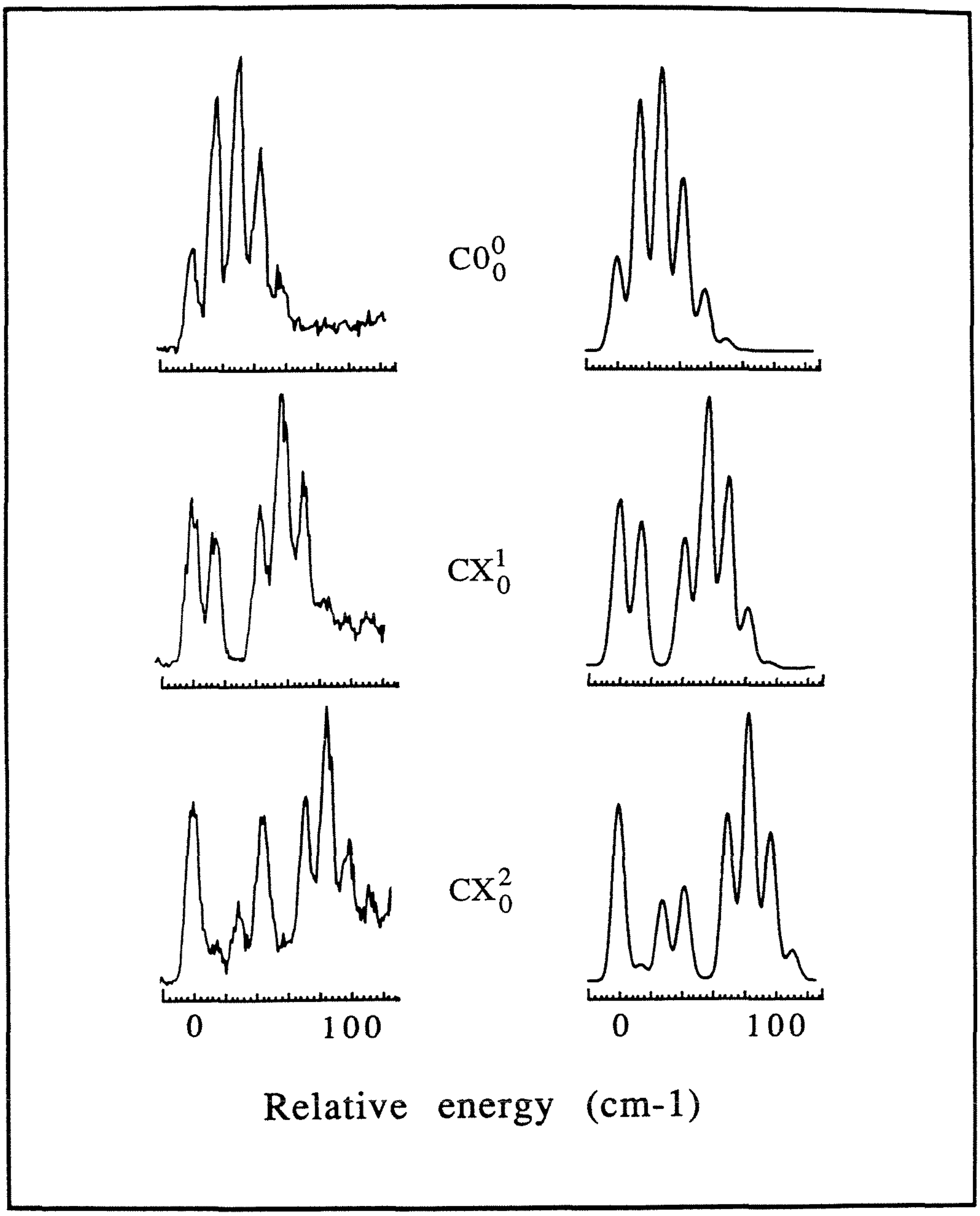

Fig. 4.8

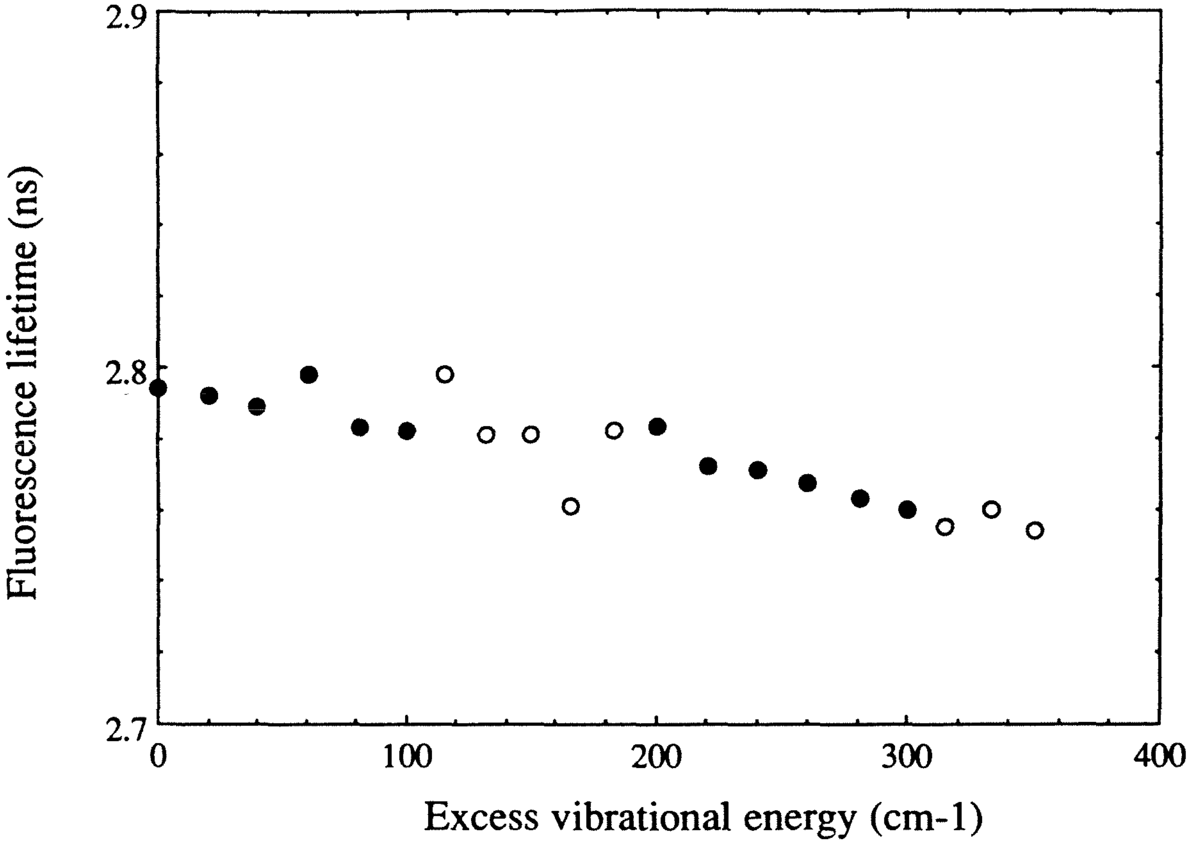
2.9
2.8
2.7
0
100
200
300
400
Fluorescence lifetime (ns)
Excess vibrational energy (cm-1)

Fig. 4.9

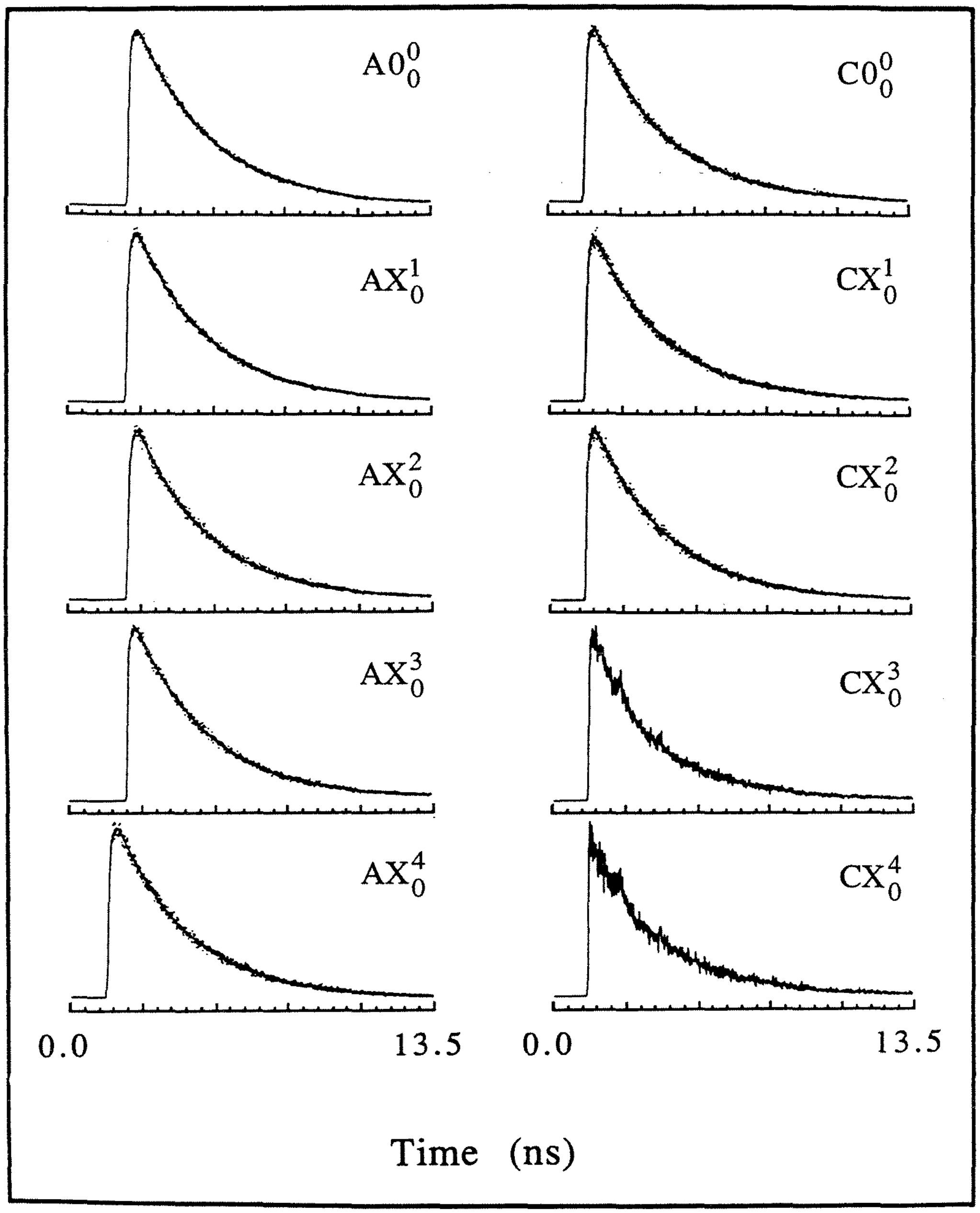
$A0_0^0$
$C0_0^0$
AX_0^1
CX_0^1
AX_0^2
CX_0^2
AX_0^3
CX_0^3
AX_0^4
CX_0^4
0.0
13.5
0.0
13.5
Time (ns)

Fig. 4.10

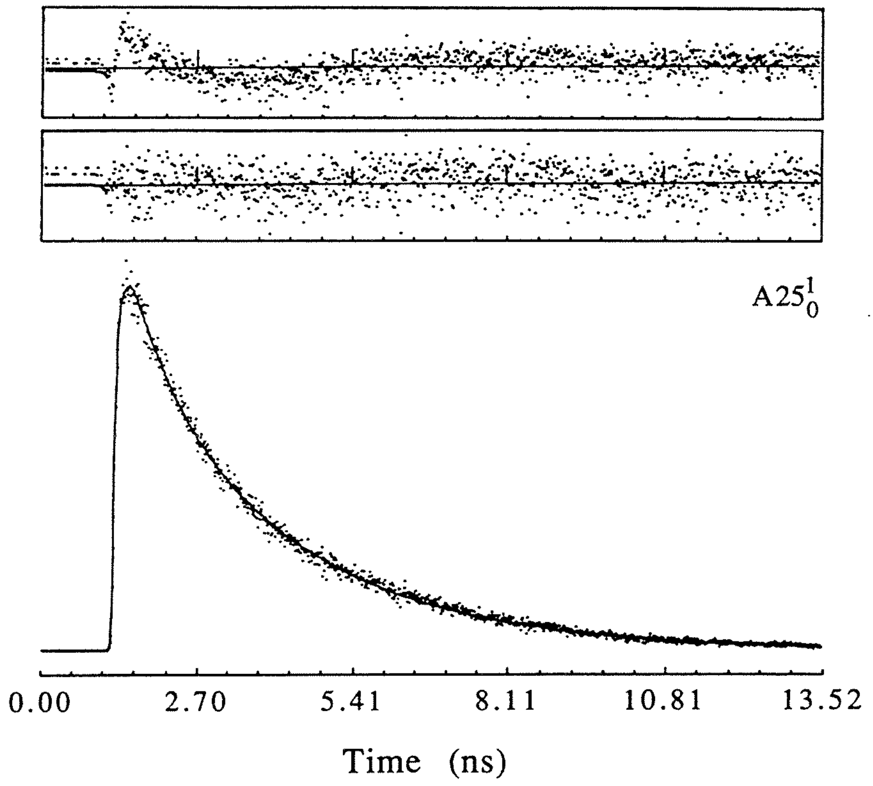

Fig. 4.11

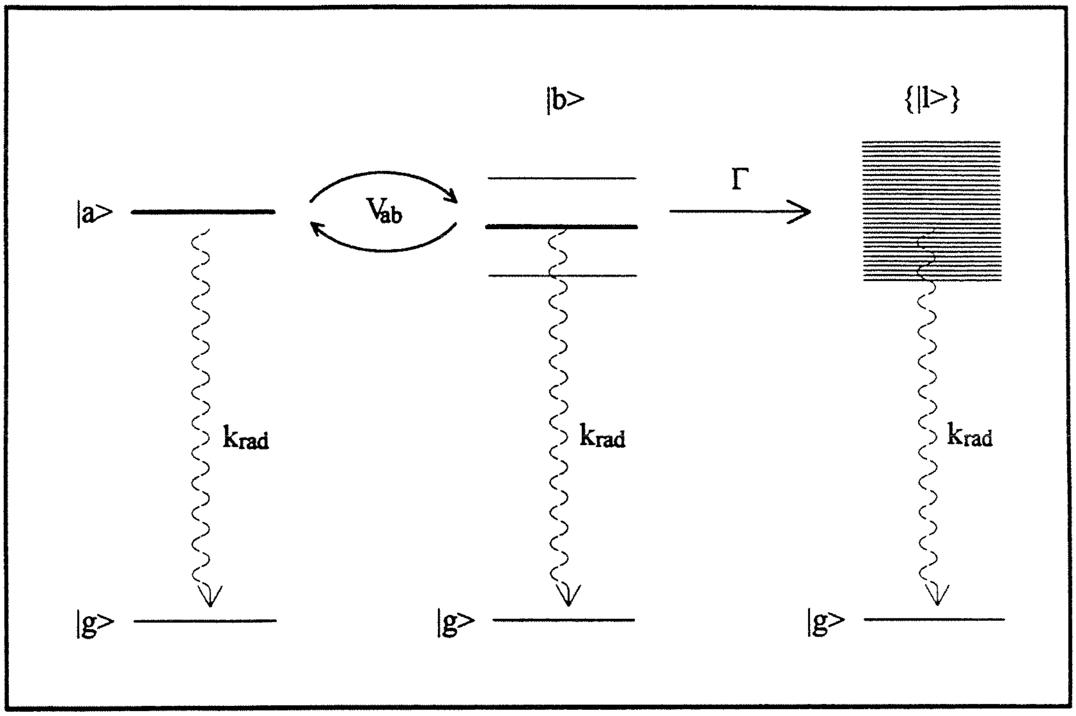

Fig. 4.12

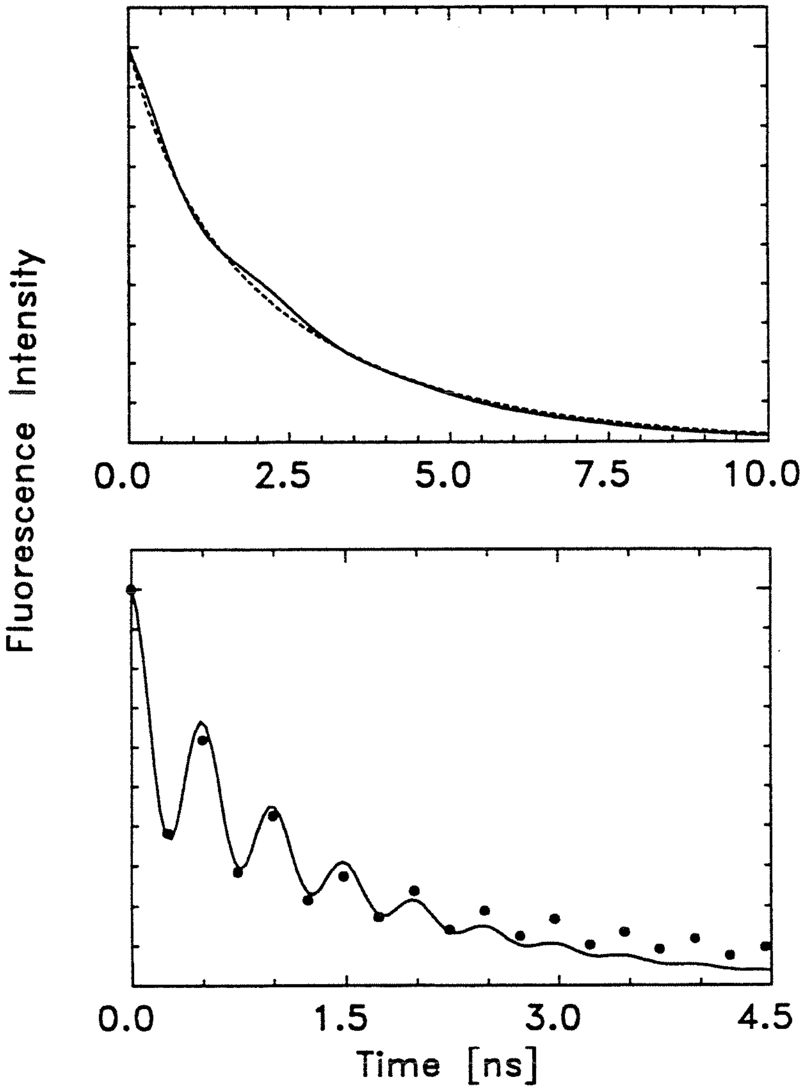

Fig. 4.13

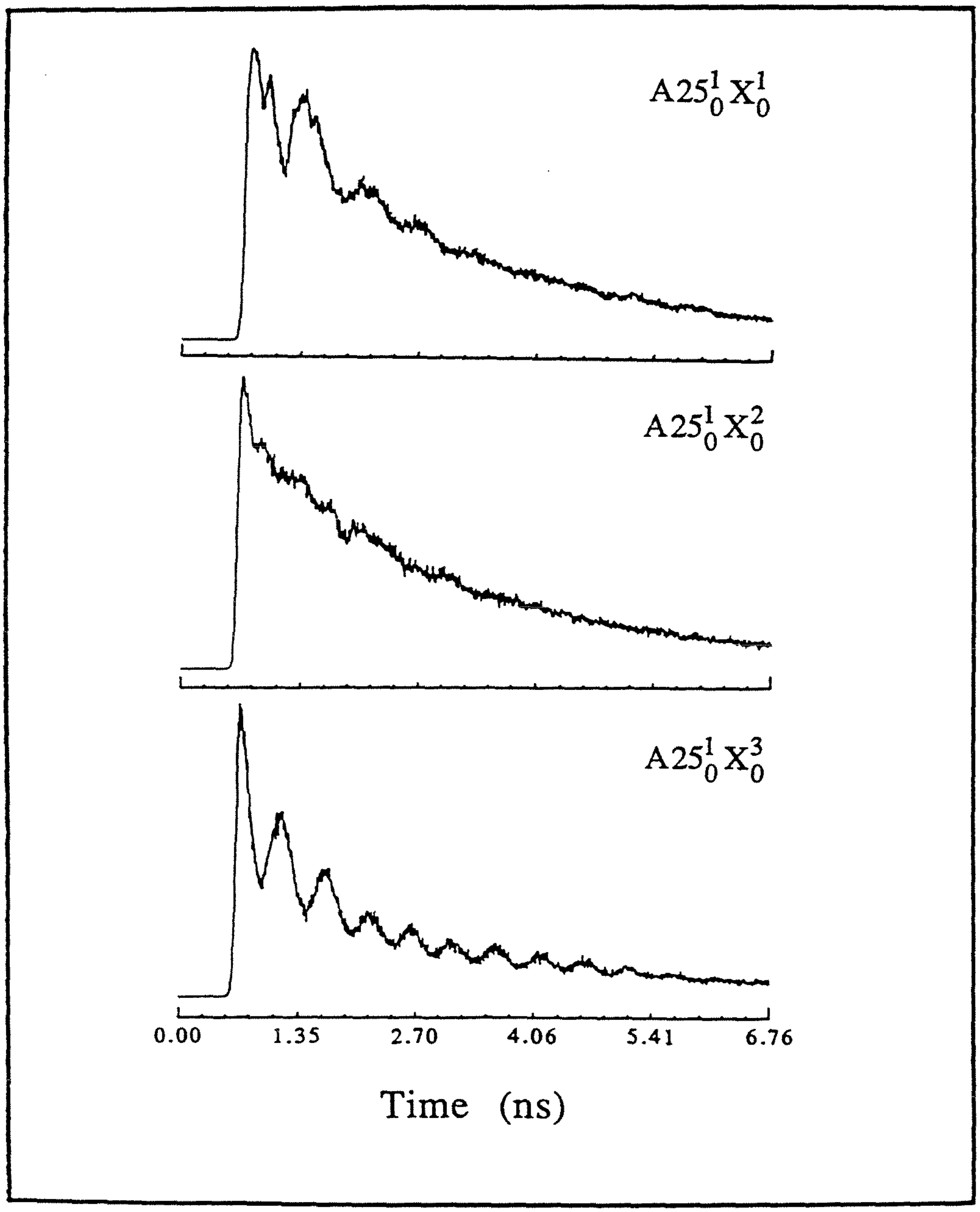

Fig. 4.14

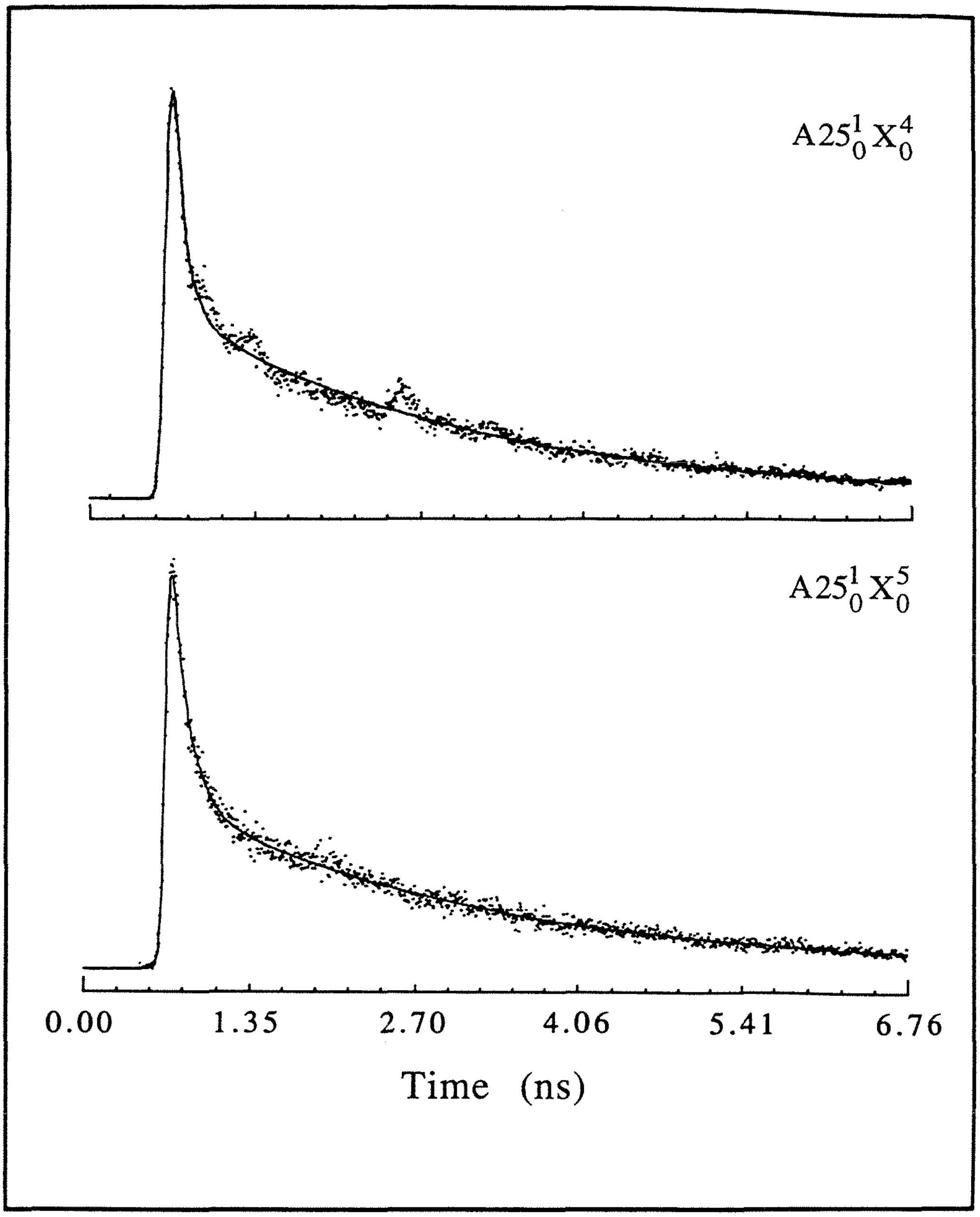

Fig. 4.15

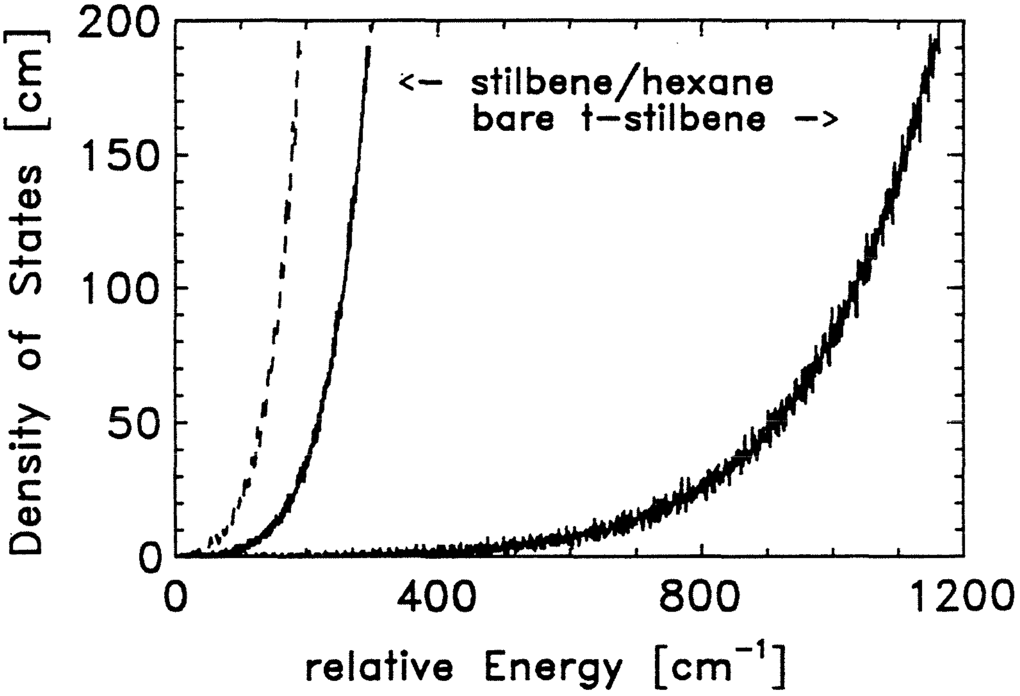

Density of States [cm]
0
50
100
150
200
0
400
800
1200
relative Energy [cm^{-1}]
<- stilbene/hexane
bare t-stilbene ->

Fig. 4.16

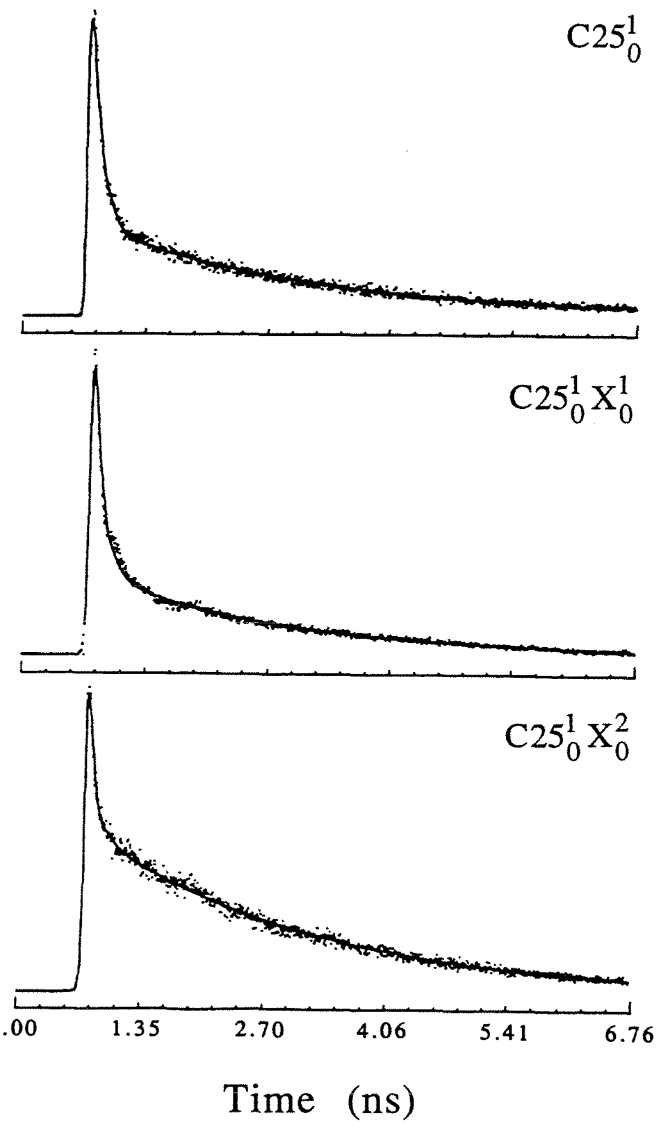

Fig. 4.17

Chapter 5

SOLVATION EFFECTS ON PICOSECOND MOLECULAR DYNAMICS (II): ISOMERIZATION OF *TRANS*-STILBENE SOLVATED IN SIZE-SELECTED HEXANE CLUSTERS

A portion of this chapter has been accepted for the following publication:

"Microscopic Friction and Solvation in Barrier Crossing: Isomerization of Stilbene in Size-Selected Hexane Clusters," by A. A. Heikal, S. H. Chong, J. B. Baskin, and A. H. Zewail, submitted to *Chem. Phys. Lett.*

5.1 INTRODUCTION

Solvation effects on a chemical reaction can be distinguished by measuring and comparing the chemical rates (at equivalent energies) of a prototype reaction both with (*e.g.* solution) and without (*e.g.* gas-phase or supersonic-jet) solvent. These studies represent two limiting phases of matter and may not directly connect the molecular and bulk properties. One way to bridge this gap is to study clusters of molecules as a function of cluster size such that the transition from molecular properties to bulk properties can be examined. The dynamics are compared as the cluster-size increases *one molecule at a time* so that the role of individual solvent molecules can be discerned [1].

A prototype unimolecular reaction, which has drawn the attention of so many groups in the last two decades, is photoisomerization of *trans*-stilbene. Time-resolved fluorescence measurements of the isomerization rate in solution and in gas phase at thermal energies were reported by Hochstrasser's group [2]. Isomerization rates in jet-cooled isolated *trans*-stilbene molecules were subsequently measured by picosecond time-resolved fluorescence spectroscopy [3-9].

The isomerization reaction in *trans*-stilbene involves large-amplitude motions such as the twisting of phenyl groups around the $C_e{=}C_e$ central double-bond. Intuitively one would expect that the reaction rate should be decreased by solvent molecules in solution. In contrast, the *trans*-stilbene isomerization rate was *accelerated in solution in comparison with the isolated-molecule rate at comparable energies* [1-10]. Considering the wealth of information on the reaction in the jet-cooled molecule, solvation effects must be responsible for this unexpected behavior [2].

Even though several research groups [11-21] investigated the solvation effects on the isomerization dynamics in a variety of environments, a definitive explanation for the accelerated isomerization rate in solution is far from being understood. However, Troe and coworkers [11,12,13] suggest that solvent molecules exert an unusually strong effect on the reactive potential energy surface and significantly lower the barrier. This lowering of the barrier, which is due to the formation of solute-solvent cluster, accelerate the isomerization rates [11-14]. Alternatively, it was suggested that since the reaction barrier may be due to a surface crossing, then the crossing probability could be strongly affected by the presence of the solvent [3,4,5,22]. In either case, solvent perturbations on the potential energy curve are predicted and should be evident for no more than a few solvent molecules. If so, a definitive answer might be obtained by measuring the rates in stilbene-solvent clusters as a function of the cluster-size and the excess-energy [1].

Following this line of reasoning, solvation effects on the isomerization reaction have been studied in *trans*-stilbene solvated in size-selected alkane clusters. In a series of experiments, the reaction rates were measured as a function of excess-energy in the S_1-state and cluster size. Among stilbene-alkane$_n$ complexes, stilbene-hexane$_1$ (t-S-H_1) is the only species which has been the subject of previous investigation [23]. In those studies, IVR dynamics in t-S-H_1 were characterized and compared with that in the parent molecule, (see Chapter 4). The relatively high binding energy of this cluster (~2100 cm^{-1}) provides an excellent opportunity to investigate the solvation effects on the isomerization reaction at high excess-energies without the complications of vibrational predissociation. Meanwhile, the IVR and spectroscopy of this cluster [22] provides a firm basis for analyzing the results presented in this chapter.

In this chapter, the excess-energy and cluster-size dependence of the isomerization rate in *trans*-stilbene-(hexane)$_n$ clusters are reported. Complementary experiments were also carried out on deuterated hexane (d_{14}) and hexanenitrile (as a polar solvent) complexes with *trans*-stilbene. Pump-probe methodology in a molecular beam [24] is utilized for measuring the rates as a function of both cluster-size *(n)* and the excess-energy in the S_1-state manifold. Extensive and careful measurements are performed to obtain a clear picture of the energy dependence of isomerization reaction rate, the reaction barrier, and vibrational predissociation dynamics.

5.2 EXPERIMENTAL

The experimental technique used in the following studies has been described in detail in Chapter 2. The pump-laser dyes used in these experiments were SR640, Kiton Red, and R6G to cover wavelength range of 580-620 nm depending on the excess vibrational energy, in the S_1-state, of interest. For the probe laser (650 nm), only DCM dye, in methanol, was used.

The rising edge of the transients were well fit by a system response of 60-70 ps corresponding to the measured cross correlation between our pump and probe laser pulses. Rotational coherence effects on the measured transients should not be overheld because the polarization of both pump and probe lasers was parallel. Rotation of the pump or probe polarization was not done to avoid reductions in the laser intensity upon using a half-wave plate.

The solute molecule (*trans*-stilbene, Aldrich, 96% purity, used without further purification) was placed in a sample compartment of stainless steel attached to the back of the pulsed nozzle and heated to approximately 100 °C. The nozzle was kept about 10 °C warmer than the sample reservoir in order to prevent clogging. The carrier gas (helium) pressure was maintained in the range of 14-100 psi. Solvents such as *n*-hexane-h_{14} (Aldrich, UV spectroscopy grade, 99% purity), *n*-hexane-d_{14} (Aldrich, UV spectroscopy grade, 99% purity), and *n*-hexanenitrile (Aldrich, 98% purity) were used without further purification. The solvent was seeded in the carrier rare-gas by connecting the solvent reservoir (made from stainless steel and kept outside the molecular beam chamber) to the carrier-gas line. To create enough population of large clusters, helium (~14 psi) was bubbled through the hexane liquid (kept at room temperature) before reaching the stilbene compartment. The amount of *n*-hexane vapor was controlled by the backing pressure of carrier gas. To test the cooling effects on the measured rates, helium with high backing pressure (~100 psi) was passed over the surface of hot hexane (~60 °C) carrying out the hexane vapor to the stilbene reservoir. The experimental conditions were set to maximize the signal of a size-selected cluster under study.

The reaction of interest (*e.g.* isomerization in clusters) was initiated by a UV laser-pulse (pump laser). Since the ionization potential of *trans*-stilbene is 7.7 eV [25], a second UV probing laser pulse is required to sample (by photoionization) the reactants population in the S_1 state. Alternatively, two visible photons were used in gas phase studies of IVR and rotational coherence in *trans*-stilbene [26]. In that approach, the ionization efficiency is quite high due to a resonant intermediate (S_4) which is strongly electric-dipole coupled to the S_1 state [26]. A transient profile of the reaction dynamics in size-selected clusters in its S_1-state is obtained by monitoring the ion signal as the delay time between the pump and probe lasers varies. Zewail and coworkers [26] studied the excited state rotational constants and rotational coherence of *trans*-stilbene in the gas phase using picosecond multiphoton ionization (MPI) mass spectrometry. From the shape and the waveform of the rotational recurrences, information on the direction of the transition moments was provided. The good agreement between the experimental and theoretical results implied that the transition moments for fluorescence ($S_1 \rightarrow S_0$) and MPI ($S^+ \leftarrow S_4 \leftarrow S_1$) are both parallel. However, those authors conducted preliminary UV-pump/UV-probe experiments and concluded that the transition moment for the ion$\leftarrow S_1$ excitation is somewhat different from that of $S^+ \leftarrow S_4 \leftarrow S_1$ (i.*e.* $S_1 \leftarrow S_0$) [26].

5.3 RESULTS

5.3.1 Bare Trans-Stilbene

5.3.1.1 Electronic Origin

A typical transient for bare *trans*-stilbene, excited to its S_1-state origin, is shown in Fig. 5.1. This transient was measured with pump- and probe-laser wavelengths were 310 nm and 327 nm, respectively. The estimated decay time constant (τ) is 2.6 ± 0.2 ns which is in a good agreement with the lifetime measurement using the time-correlated single photon counting technique [3-9].

Several control experiments were conducted to test all the experimental parameters that might affect the measured decay time of bare *trans*-stilbene. Since the pump laser wavelength was selected for the 0_0^0 transition of the bare molecule, the probe laser wavelength (327 nm) was chosen such that pump- plus probe-photons will ionize the molecule near the ionization threshold. The pump laser intensity was adjusted such that the multiphoton ionization (MPI) signal due to the pump laser alone was minimal. The maximum signal enhancement due to pump plus probe photons was up to ten times greater than the time-independent background in bare *trans*-stilbene detection. However, this ratio was less for cluster-ion detection and decreased as the cluster size increased. Second, the time-constant of the bare molecule, excited to the S_1 origin, was measured as a function of the probe laser wavelength (318-327 nm). The measured time constant was independent of the probe laser wavelength in that range. Third, as an indication of the approximate linearity of the total signal in these experiments, the rise of the transients could be fitted nicely to the cross-correlation (~70 ps) of both pump and probe lasers. All the experiments reported here were performed several times under different experimental conditions to ensure reproducibility.

5.3.1.2 Excess-Energy Dependence of the Time-Constant (τ)

The excess-vibrational energy dependence of τ in the S_1-state of jet-cooled *trans*-stilbene is well documented using laser-induced fluorescence and time-correlated single photon counting (TCSPC) techniques [3-9]. To estimate the uncertainty level in our measurements as well as testing cooling effects on measured rates, the excess energy dependence of the rate constants were reproduced by R2PI-TOF technique under two different experimental conditions. Backing pressures of ~14 psi and 100 psi of pure helium were used in this control experiment. The measured rates under these two conditions are shown in Fig. 5.1 with the TCSPC results for comparison. Figure 5.1 shows an excellent agreement between R2PI (100 psi backing pressure) and TCSPC [27] results. However, the effective residual thermal energy in the 14 psi experiments is estimated to be 250 ± 150 cm^{-1} from the energy shift. The initial increase in rate is especially sensitive to cooling, and at 14 psi begins at ~1000 cm^{-1} instead of the known 1200 cm^{-1} threshold. However, under the experimental conditions at which large clusters were created (backing pressure ~14 psi), the measured rates in bare t-S, particularly at high energies, are faster than those of TCSPC studies due to cooling effects. It is worth mentioning that in the non-steady state conditions of the gas pulse [28], faster rates above the isomerization threshold were also measured for the same reason. Furthermore, backing-pressure dependence of the time-constant, at excess energy of ~ 2000 cm^{-1} in the S_1-state of *trans*-stilbene, was studied to test the cooling effects. These measurements show that the molecular-beam cooling improves as the carrier-gas pressure increases (see Fig. 5.2). All the transients measured for bare *trans*-stilbene excited to different vibronic levels in the S_1-state decay as a single exponential.

5.3.2 Time-of-Flight Mass Spectrum

A typical time-of-flight mass spectrum (TOFMS) for *trans*-stilbene-(hexane)$_n$ clusters is shown in Fig. 5.3. The ion signal is due to two-color resonant two-photon ionization (two-color R2PI). The pump-laser wavelength (314 nm) corresponds to the vibrationless $S_1 \leftarrow S_0$ electronic transition in t-S and excites bare *trans*-stilbene-(hexane)$_n$ clusters to different vibrational energies in their S_1 state (depending on the shift in the S_1-state origin). This excess vibrational-energy depends on the red-shift of the electronic S_1-origin upon hexane complexation. The probe laser (325 nm) was set at a delay time of ~11 ps with respect to the pump laser pulse. Figure 5.3. also shows the TOFMS with the probe laser blocked. On the other hand, there is no signal due to two probe-photons as shown in Fig. 5.3. Clusters as large as n = 7 were formed in the molecular beam as shown in the mass spectrum. The intensity distribution of cluster bands can be controlled, to some extent, using the following parameters: the voltages on the repeller, extractor, and the lens in the ion optics, and the delay time (DT2) between the nozzle-opening and the laser pulses. The general features are the same with different pump-laser wavelengths (i.e. excess vibrational energy in the S_1 state) except that the relative contribution of the probe laser to the ion signal becomes larger (2cR2PI). Stilbene dimers were formed in the molecular beam (see Fig. 5.3) but their population was small.

5.3.3 *Trans*-Stilbene-(Hexane)$_1$ cluster

5.3.3.1 Electronic Origin

The electronic origin of the S_1-state in the stilbene-hexane$_1$ complex (isomer A) is 380 cm^{-1} to the red of that in bare *trans*-stilbene [23]. Using the time-correlated single photon counting (TCSPC) techniques, the radiative lifetime of the origin was measured to be 2.79 ns [23]. Furthermore, a similar fluorescence lifetime was measured (2.80 ns) for isomer C, excited to its origin at 265 cm^{-1} to the red of the bare molecule.

Utilizing the pump-probe technique with TOF mass-selectivity, a transient for the $n = 1$ complex was measured several times under different experimental conditions using pump- (probe-) laser wavelength of 313.8 (327.0) nm (see Fig. 5.7). The decay time of that transient was estimated as 2.7 ± 0.2 ns. With this technique, it is difficult to differentiate between different conformers of the same cluster. The time constant seems to be slightly dependent on the probe-laser intensity. The small difference in τ between pump-probe and TCSPC techniques can be attributed, in part, to the detection of large-cluster fluorescence along with that of the $n = 1$ complex in TCSPC experiments.

5.3.3.2 Excess-Energy Dependence of the Time-Constant

The energy dependence of the time constant (τ) in stilbene-hexane$_1$ complexes following excitation to the S_1-state has been studied. The molecular beam parameters were optimized for the cluster of interest. All transients measured at different excess-energies were satisfactorily fit as single exponentials except ~1600-2400 cm^{-1} range where single exponential fit was inadequate). Furthermore, a control experiment was carried out to test cooling effects on the measured rate in the low-energy domain of the S_1-manifold in t-S-H_1. A high backing pressure (100 psi) of helium was passed over the surface of heated hexane (instead of bubbling through), mixing with the hexane vapor before reaching the stilbene compartment. Under these conditions, cooling in the molecular beam is expected to improve, and the measured rates were slightly slower compared to the "bubbling-through" experiments (with ~14 psi). The measured rate constant as a function of the excess-energy is shown in Fig. 5.4.

Using the TCSPC technique, the fluorescence lifetime of stilbene-hexane$_1$ complex was found to be independent of excess-energy up to 380 cm^{-1} above the S_1-origin [22]. However, this is not the case for the same system using the R2PI-TOFMS technique; the time constant decreased monotonically as the excess energy increases up to ~1400 cm^{-1} in the S_1-manifold (Fig. 5.4). Interestingly, in the excess-energy range of ~1600-2400 cm^{-1} the rate becomes less dependent on energy and a plateau could be identified. Above 2500 cm^{-1}, the rate constant increases slowly as the energy increases.

The estimated uncertainty in residual thermal energy plus the spectral distribution of isomeric forms is ~± 300 cm^{-1}. This must be considered as the uncertainty with which the excess energy in the S_1-state could be specified for a given cluster size. Values of the excess energy in Fig. 5.4 have not been adjusted to reflect the residual thermal contribution. However, the energy was adjusted for the spectral spread of the electronic origin from the multiple isomers that could be identified at a given cluster size using potential energy calculations.

5.3.4 Stilbene-(Hexane-d_{14})$_1$ Complex

Similar measurements the rate constant in stilbene-(hexane-d_{14})$_1$ complex were carried out as a function of the excess energy in the range of ~1600-3020 cm^{-1} (see Fig. 5.5). Similar measurements were conducted for hexane-h_{14} clusters under the same experimental conditions for comparison. Across the transition region from 1600 to 2400 cm^{-1}, where a plateau was identified for $k^{(n=1)}(E_x)$, the rates for hexane-d_{14} and hexane-h_{14} clusters were indistinguishable. However, at two higher excitation energies (~3200 and 3400 cm^{-1} in t-S-H_1) the measured rates for *trans*-stilbene-hexane-d_{14} cluster was 15% lower than those of *trans*-stilbene-hexane-h_{14} (see Fig. 5.10) for the TOFMS).

5.3.5 *Trans*-Stilbene-(Hexane)$_2$ cluster

A similar excess-energy dependence of the rate constant in stilbene-(hexane)$_2$ cluster was measured (see Fig. 5.6). The excess energy extended over approximately 3700 cm^{-1} above the electronic origin of the S_1-state in the $n = 2$ cluster. Over this energy range, the probe-laser wavelength was kept at 325.5 nm for experimental reasons and the time constant changed from 2.9 ± 0.2 ns to 670 ps in that energy range. Unlike the $n = 1$ complex, the rate constant increases very slowly as the excess-energy increases (Fig. 5.6). All the molecular beam parameters were fixed for this series of experiments in which t-S, t-S-H_1, and t-S-H_2 rates were measured.

5.3.6 Clusters-Size and Excess-Energy Dependence

Collective vibronic excitation of large stilbene-(hexane)$_n$ clusters to the S_1 manifold was possible due to the overlap of absorption profiles of these clusters (pump-laser band width was ~18 cm^{-1}). Characterization of the cluster-size and excess-energy dependence of the rate constant in these clusters was conducted as outlined below using selected pump/probe laser wavelengths (see Table (1)). A general trend could be identified at all the excess-energy reported here: the time constant increases as the number of the solvent molecules in the cluster increases.

(a) 313.8 nm/324.6 nm:

In the vicinity of the electronic origin of the $S_1 \leftarrow S_0$ transition in n=1 complex (31867.4 cm^{-1} [23]), cluster-size dependence (n = 5) of the time constant was studied using pump/probe wavelengths of 313.8 nm/3224.6 nm. All the transients were measured more than once and fit as single exponentials. Representative transients are shown in Fig. 5.7.

(b) 310.1 nm/324.6 nm:

Similar measurements for stilbene-hexane$_n$ (n = 0-5) clusters were carried out at the pump-laser wavelength 310.1 nm, which corresponds to the electronic origin of the $S_1 \leftarrow S_0$ transition in bare *trans*-stilbene (Fig. 5.8). The probe laser wavelength was fixed at 324.6 nm.

(c) 287.1 nm/324.6 nm:

At excess-energies of 2586 cm^{-1} in the S_1-electronic state of the bare molecule, similar measurements were carried out and the results are shown in Fig. 5.9.

(d) 282.5 nm/327.1 nm:

At an excess-energy of ~3150 cm^{-1} above the S_1-electronic origin of the parent *trans*-stilbene, the cluster-size dependence of the time (rate) constant was measured once. At this energy, the measured rate in the bare molecule (~13.3x10^9 s^{-1}) is faster than that measured with TCSPC technique (~10x10^9 s^{-1}) due to cooling effect.

5.3.7 *Trans*-Stilbene-(Hexanenitrile)$_n$ cluster

To estimate the impact of solvent polarity on the isomerization dynamics in *trans*-stilbene similar excess-energy dependent measurements of the S_1-state rate constant were carried out for t-S solvated in hexanenitrile$_n$ clusters (see Fig. 5.10 for TOFMS). These measurements were conducted for n = 0,1,2 complexes and were limited to four pump-laser wavelengths (310.1, 305.4, 296.4, and 287.2 nm) (Fig. 5.11 and 5.12 show transients for 310.1 and 287.2 nm, respectively). The probe-laser wavelength was fixed at 327.5 nm. Following the excitation of n=1 complex by the 310 nm pump laser, the ion signal decays as a biexponential with a fast component (τ_1) of 397±70 ps, a slow component (τ_2) of 2.65±0.03 ns, and a fast-to-slow amplitude ratio (a_f / a_s) of 0.6±0.2. The degree of non-exponentiality decreases with increasing energy. At high excess-energies above the S_1-state origin (287.2 nm pump which corresponds to an excess-energy of ~2580 cm^{-1} in the S_1-state of the bare molecule), single exponential transients were measured with an estimated decay time of 33±5 ps. Under the same experimental conditions, a single exponential transients for the $n = 2$ complex were measured at different excess-energies mentioned above. The decay time for these transients ranged from ~2.17 ns (310 nm pump-laser) to 250 ± 30 ps (287.2 nm pump laser).

5.4 DISCUSSION

5.4.1 Kinetic Model

5.4.1.1 S1-State Deactivation Channels

A simple kinetic model, which is taking into account isomerization and by vibrational predissociation in the S1-state, was developed to describe the time evolution of the initially excited cluster $A.B_n^*$. Following the kinetic scheme shown in Fig. 5.13, the time evolution of the parent $A.B_n^*$ signal ($S_t^{(n)}$), above the dissociation and isomerization threshold, is given by

$$S_t^{(n)} = S_{t=0}^n \exp\left\{-\left(k_{total}^n\right)t\right\} \tag{1}$$

where $k_{total}^n = k_{rad}^n + k_{iso}^n + k_{vp}^n \; k_{rad}^n ,$ is the total deactivation rate of the S1-state (radiative (k_{rad}^n), isomerization (k_{iso}^n), and vibrational predissociation k_{vp}^n rates) of the parent $A.B_n$ cluster. Following the vibrational predissociation of $A.B_n$, where m solvent molecules are evaporated, the population of the product $A.B_{n-m}^*$ will decay as:

$$S_{vp}^{(n-m)} = a_0^{n-m}\left\{\exp\left(-k_{total}^{n-m}(E_x^n - mD_0^n)t\right) - \exp\left(-\left(k_{rad}^n + k_{iso}^n + k_{vp}^n\right)t\right)\right\} \tag{2}$$

where k_{total}^{n-m} is the total rate of the product $A.B_{n-m}^*$, and

$$a_0^{n-m} = [A.B_n^*(t=0)]\left\{\frac{k_{vp}^n}{k_{total}^n(E_x^n) - k_{total}^{n-m}(E_x^n - mD_0^n)}\right\}. \tag{3}$$

This amplitude will be positive since that $k_{total}^n(E_x^n)$ is expected to be greater than $k_{total}^{n-m}(E_x^n - mD_0^n)$. The total ion signal for the $A.B_{n-m}$ cluster (including both reactant and product) will be described by

$$S_{total}^{(n-m)} = a_0 \exp\left(-k_{total}^{n-m}(E_x^{n-m})t\right) + a_t \exp\left(-k_{total}^{n-m}(E_x^n - D_0^n)t\right) - a_t \exp\left(-k_{total}^n t\right), \tag{4}$$

where,

$$a_0 = \left[A.B_{n-m}^*(t=0)\right], \tag{5}$$

and

$$a_t = \left[A.B_n^*(t=0)\right]\left\{\frac{k_{vp}^n}{k_{total}^n(E_x^n) - k_{total}^{n-m}(E_x^n - mD_0^n}\right\}. \tag{6}$$

A transient represented by eq. (4) will rise with a rate of $k_{total}^n(E_x)$ and decay with two components. The first component that transient will decay with a fast rate of $k_{total}^{n-m}(E_x) = k_{rad}^{n-m} + k_{iso}^{n-m} + k_{vp}^{n-m}$, whereas the second component will decay with a slow rate of $k_{total}^{n-m}\left(E - mD_0^{(n)}\right)$. Unless E is sufficiently greater than $D_0^{(n)}$, the second (slow) rate will be reduced to the radiative rate of the smaller cluster *(n-m)*, since $E - D_0^{(n)}$ is expected to be below the isomerization barrier. The amplitude ratio of the slow-to-fast decay component, in eq. (5) and (6), will be given by

$$a_0 / a_t = k_{vp}^n(E_x) / \left[k_{total}^n(E_x) - k_{total}^{n-m}(E_x - mD_0^n)\right], \tag{7}$$

which, to the first approximation, will equal $k_{vp}^n(E_x) / \left[k_{vp}^n(E_x) + k_{iso}^n(E_x)\right]$ since $k_{iso}^{n-m}\left(E - mD_0^{(n)}\right)$ is much smaller than $k_{iso}^n(E)$ and the radiative rates of the two clusters are approximately the same. The two limits which give rise to single exponential behavior are discussed below.

(i) $k_{vp}^n(E) >> k_{iso}^n(E)$:

Assuming that the vibrational predissociation rate, $k_{vp}^n(E)$, of the $A.B_n$ cluster initially excited to an excess-energy E_x in the S_1-state, is faster than all other pertinent rates. The microcanonical rate of the $A.B_n$ cluster isomerization, $k_{iso}^n(E)$, will then be virtually undetectable by the R2PI-TOF technique. Furthermore, a part of the detected ion-signal at the $A.B_{n-m}$ mass will be attributed to the nascent $A.B_{n-m}$ cluster with excess-energy $E - mD_0^{(n)}$.

(ii) $k_{iso}^n(E) >> k_{vp}^n(E)$:

If instead $k_{vp}^n(E)$ is very slow compared to the probe-pulse's delay time, the S_1-state dynamics of the $A.B_n$ cluster could be measured even when the excess energy E_x is larger than the dissociation energy $D_0^{(n)}$. In this limit, the signal detected at mass $A.B_{n-m}$ will be given by:

$$S_{total}^{(n-m)} \cong a_0^{n-m} \exp\left[-\left(k_{rad}^n + k_{iso}^n(E)\right)t\right]. \tag{8}$$

With pump-probe TOF detection, measured transients reflect the time dependence of mass-selected species within a certain time window (the boxcar gate width ~30-100 ns). At low excess energies in S_1 and ionization near threshold, no fragmentation of the excited clusters is expected, and each transient gives directly the dynamics of the cluster of detected ion-mass. However, when the $A.B_n$ cluster is excited to the S_1-state with an excess energy greater than $D^{(n)}{}_0$, fragmentation as well as isomerization must be considered.

5.4.1.2 Fragmentation of the Ionic Cluster

Our attempts to probe (*i.e.* ionize) high vibrationally-excited levels in the S_1 state of the clusters near the ionization threshold were not successful. This due to the insufficient ion signal levels, presumably due to unfavorable Franck-Condon overlap, and the unknown solvation effects on the ionization threshold in those clusters. However, the ionization thresholds and cross-sections in clusters have been studied by Castleman *et al.* [29], and Jortner [30]. The general finding is that the ionization energy of homogeneous systems tend to decrease with increasing cluster size. A linear dependence of the ionization energy as a function of the inverse of the cluster size has been observed for several systems. Trott *et al.* [31] justified this relationship on the basis of quantum mechanical calculations. An exception to this trend is expected for clusters of ionic salts; the removal of an electron results in a decrease in the madelung energy and the vertical ionization potential should therefore increase with increasing cluster size.

At high excess-energy in the ionic continuum, the fragmentation of $A.B_n$ cluster in the ionic state is expected and the time distribution of the TOF ion-signal becomes an important issue. Depending on the relation between the acceleration time (t_a) and the *piont in time* at which the fragmentation takes place (t_{frag}), in the TOF drift-tube, one of the following three situations may occur: First, if $t_{frag} \gg t_a$, the parent ($A.B_n$) will dissociate after the acceleration region (*i.e.*

in the field-free region). In this case, both the parent and fragment ($A.B_{n-m}$) will have the same TOF reaching the detector at about the same time. Second, if $t_{frag} \ll t_a$, the fragment will have TOF that is proportional to the root square of its mass, i.e. the parent and the fragment will arrive at the detector at different times. Third, if $t_{frag} \sim t_a$, then the ion signal of the fragment ($A.B_{n-m}$) in the TOF mass spectrum will spread over between the TOF of both the intact parent $A.B_n$ and the fragment $A.B_{n-m}$.

From the design parameters of two-stage time-of-flight mass spectrometer, the acceleration time (t_a) was estimated to be ~1 μs. To see which one of the above mentioned cases match our experimental conditions, the excess-energy dependence of the time-of-flight mass spectrum of stilbene-hexane$_n$ cluster were measured and shown in Fig. 5.14 for n = 1 mass only. Very slight broadening in the n=1 mass peak can be identified in the excess-energy range of ~1000-2300 cm^{-1}. Neither the residual thermal energy (~250 cm^{-1}) in the molecular beam nor the energy distribution due to different conformation are not accounted for in this estimate. This observation is consistent with $\tau_{frag} \leq 1$ μs (the acceleration time in our TOF mass spectrometer). However, our knowledge of van der Waals complex dissociation dynamics and this minor broadening suggest that τ_{frag} is much less than the acceleration time (~1 μs). Furthermore, $\tau_{frag} \leq 30$ ns (the time-of-flight mass resolution) appears reasonable. Consequently, signal from the $A.B_n$ cluster is detected at the $A.B_n$ mass position when initially excited below the dissociation threshold ($D_0^{(n)}$) and at the $A.B_{n-m}$ ion-mass when excited above that threshold. In this case, the total ion signal detected at $A.B_{n-m}$ mass will be given by,

$$\begin{aligned} S_{total}^{(n-m)} &= a_0 \exp\left(-k_{total}^{n-m}(E_x^{n-m})t\right) + a_t \exp\left(-k_{total}^{n-m}(E_x^n - D_0^n)t\right) \\ &\quad +(c_{ion} - a_t)\exp\left(-k_{total}^n t\right) \end{aligned} \tag{9}$$

where the constant c_{ion} depends on, $\left[A.B_n^+(t=0)\right]$, the fragmentation rate in the ionic state of the parent complex, and the ionization cross-section.

If above mentioned assumption is incorrect, the analysis and conclusions are basically the same except that the assignment of certain rates will be shifted by one step in cluster size. It should be noted that up to E_{ex} ~ 4000 cm^{-1} only one solvent molecule can evaporate since D_0^1 is ~2100 cm^{-1}.

5.4.2 Structures

Atom-atom pair-potential energy calculations, similar to those described in detail in Chapter 4, have been carried out to deduce the most energetically favorable configuration for the stilbene-hexane$_n$ clusters. For clusters of a specific size, multiple isomers with similar binding energies (but significantly different geometries) were predicted. The predicted red-shift of the S$_1$-origin (compared to that in bare *trans*-stilbene), the zero-energy, and the dissociation energy for stilbene-hexane$_n$ clusters are listed in Table (2).

(a) n=1 complex:

The minimum energy structure of the n = 1 cluster (isomer A) is characterized by the carbon atoms of the hexane molecule being located in a plane parallel to that of the bare stilbene plane. The long axis of hexane approximately parallel (~14° off) to the bare t-S long axis (see Fig. 5.15 or Fig. 4.1). The binding energy for this configuration ($D_e^{(1)}$) was estimated as -2132 cm^{-1}, where $D_e^{(n)}$ is the stilbene-(hexane)$_n$ cluster's dissociation energy in the S$_1$-state. The potential energy calculations predict a second stable configuration (labeled isomer C), with a binding energy of -2047 cm^{-1}. In this configuration, the hexane molecule is rotated by 180° around its long axis, and the long axes of both trans-stilbene and hexane are not parallel to each other. The distance between the center of mass of both molecules (3.78 Å) is slightly larger than in the A-isomer configuration (3.73 Å). The average red-shift of the S_1-origin, measured for the different isomers, is ~322 cm^{-1}.

(b) n=2 complex:

The most stable structure for the $n = 2$ cluster has both hexane molecules on the same side of the t-stilbene plane, see Fig. 5.15. Another isomer, within ~100 cm^{-1} in energy, has one hexane molecule on each side of the t-S plane. The dissociation energies of the most stable configurations of stilbene-(hexane)$_2$ are predicted to be ~100 cm^{-1} greater than that for the comparable trans-stilbene-(hexane)$_1$ isomers; *i.e.* $D_e^{(2)} = 2250$ cm^{-1}. Furthermore, the average red-shift of the S_1-origin, with respect to that in the bare molecule is estimated as ~645 cm^{-1}.

(c) n≥3 complexes:

Following the same type of potential energy calculations, the minimum energy structure found for stilbene-(hexane)$_3$ cluster combine, in a close approximation, the minimum energy structure for both $n = 2$ on one side of the t-stilbene plane and that of $n = 1$ on the other side (Fig. 5.15). The estimated red-shift of the S_1-origin is ~860 cm^{-1} with respect to that in the bare molecule. Two hexane molecules on each side of the bare-stilbene plane is the minimum energy structure for n=4. A similar configuration was found for the n=5 cluster with the addition of a fifth hexane molecule to the edge of the n=4 structure. The estimated red-shift of the S_1-origin is ~1060 and 1183 cm^{-1} with respect to that in the bare molecule for the $n = 4$ and $n = 5$ clusters, respectively.

5.4.3 Photoisomerization Reaction Dynamics in Clusters

5.4.3.1 Preliminaries

Solvent effects on the isomerization reaction rate reflect the alteration of the reaction potential, coupling of the reaction coordinate to the solvent, and the increase in the density of states (intermolecular and solvent vibrational modes). Since dissipative IVR was observed in t-S-H_1 complexes on a time scale of less than 80 ps below 300 cm^{-1} [23], IVR is expected to be complete, in the high energy domain, without limiting the isomerization reaction. The same conclusion could be adapted for the larger clusters as well.

In the isolated molecule (*i.e.* in the absence of a solvent), the barrier crossing rate during the isomerization reaction is determined by the excess energy above the electronic origin of the S_1- state. If this excess energy is lower than the isomerization barrier (E_0), no barrier crossing takes place and the fluorescence lifetime is essentially the radiative lifetime of the trans configuration (~2.65 ns). For an excess energy above the isomerization barrier, the fluorescence lifetime decreases with energy [3-9].

In a solution, the fluorescence lifetime of *trans*-stilbene no longer depends on the excess energy in the S_1-state and the fluorescence quantum yield in solution seems to be excess-energy independent [32]. It is likely that the excess energy is rapidly transferred to the solvent. The crossing of the barrier in solution is determined by *the strength of the coupling between the solute and the solvent.* First, in the case of very weak solute-solvent coupling, the isomerization-rate limiting step is the rate of collision between solute and solvent molecules which excites the former above the barrier. The isomerization rate is then expected to increase with the strength of the coupling. Second, if the coupling is very strong, a local equilibrium in energy is established for the intermediate species located at the top of the barrier. In this case, the rate is then limited by collisions of this species with the solvent molecules which cause a re-crossing of the barrier in the *trans* direction. Consequently, the rate decreases as the solute-solvent coupling increases. Third, between these two extremes there is an intermediate case where the isomerization rate reaches a maximum [15].

5.4.3.2 Stilbene-(Hexane)$_1$ Complex

Among all the clusters of different sizes presented here, the most interesting case is the stilbene-(hexane)$_1$ complex. As mentioned above, the excess-energy dependence of the rate constant shows the following features: First, the isomerization barrier has been reduced upon complexation with one solvent molecule in comparison to bare t-S. As mentioned above, the precision with which the excess-energy could be specified is ~± 300 cm^{-1}. Even with this uncertainty, the difference in the isomerization barrier in bare *trans*-stilbene and $n = 1$ complex appears to be significant (Fig. 5.4 and 5.16). The estimate for that barrier in stilbene-(hexane)$_1$ complex is ~700±100 cm^{-1}. Furthermore, the isomerization rate is slightly slower than that observed in the bare molecule above the isomerization barrier (and below ~1500 cm^{-1}) (see Fig. 4.16). The acceleration of the isomerization reaction in compressed-gas and solution studies has been reported by several groups, see ref. [11-14]. It was suggested that the solvent molecules strongly affect the potential energy surface of the reaction coordinate and significantly lower the isomerization barrier, *i.e.* enhance the isomerization rate. Alternatively, the reaction barrier may be due to a surface crossing, and the barrier-crossing probability is strongly affected by the solvent molecules [3,4,5,22].

For the first time, our direct experimental observation supports the barrier-shift predictions as an expanation for the acceleration of the isomerization reaction in the condensed phase. However, even though the barrier is reduced upon the solvation of *trans*-stilbene by *one* hexane molecule, the rate is still *slower* than the rate in *trans*-stilbene isolated in supersonic jet or solvated in solution (see Fig. 5.17). On the other hand, the observed retardation of the isomerization rate (as shown in Fig. 5.16 and 5.17) rules out the suggestion that solvation effects on the curve crossing (in the nonadiabatic mechanism) during the isomerization reaction could account for the observed acceleration of the reaction rate in solution [3,4,5,22].

Second, over the excess-energy range 1500-2400 cm^{-1} in the S_1-manifold of $n = 1$ complex, the rate (~$14.3x10^9$ s^{-1}) is energy-independent and a plateau in $k(E_x)$ could be identified. According to the potential energy calculations, the vibrational predissociation of clusters is expected to take place in this energy domain. This plateau is consistent with a gradual (due to the thermal and isomeric energy spread) transition from measuring $k_{iso}^{(n=1)}(E)+k_f^{(n=1)}(E)$ below dissociation to measuring a lower rate equal to $k_{iso}^{(n=2)}(E)+k_f^{(n=2)}(E)$ above dissociation, as expected in the second limit. On the other hand, the observed energy-independent rate is clearly inconsistent with the first limit, in which the slow radiative rate of t-S-H_1 should reappear at t-S-H_1 mass detection. The condition $k_{iso}^n(E)$ >> $k_{vp}^n(E)$ means that the dissociation lifetime of t-S-H_2 at the threshold is ≥ 7 ns. For this condition to be satisfied, a sensitivity of the exponential fit to the presence of a 10% or larger decay component must be assumed. The predicted dissociation lifetime of t-S-H_2 is reasonable considering the upper limit imposed by the TOF measurements (see the kinetic model). The excess energy of 1600 cm^{-1}, at which the rate measured at t-S-H$_1$ mass reaches a plateau, corresponds to ~1920 cm^{-1} in t-S-H$_2$. In this analysis, the plateau represents the energy where the contribution of nascent t-S-H$_1$ from t-S-H$_2$ dissociation begins to affect the transient measured by detecting the t-S-H$_1$ mass. Assuming a thermal energy of 250 cm^{-1}, this behavior is consistent with the predicted dissociation threshold energy. As the dissociation channel becomes accessible as another deactivation channel for the S$_1$-state population, the energy partitioning between these channels reduces the net energy in the isomerization reaction coordinate. This, in turn, slows down the isomerization barrier-crossing rate. The transition region ends at ~2400 cm^{-1} in t-S-H$_1$, at which all initial t-S-H$_1$ populations are dissociated, and only nascent t-S-H$_1$ from initial t-S-H$_2$ is detected. There is, however, another possibility that might account for this observed plateau in $k^{(n=1)}(E_x)$. As the *trans*-stilbene molecule isomerizes, a rearrangement of the solvent molecule could take place in search for the minimum-energy structure. In this case, talking of different isomers will be irrelevant at these high energies. Furthermore, as the isomerization reaction occurs in the solute molecule, the internal collision (or *internal friction*) between solute and solvent molecules will yield energy flow to the van der Waals (and probably the solvent) modes. This energy transfer (which takes place on a very short time scale [23]) will lead directly to the reduction of the excess-energy in the reactive mode, *i.e.* a slower isomerization rate.

Third, above S$_1$(n = 1)+2500 cm^{-1}, the rate increases as the excess energy increases. Meanwhile, the measured rate is obviously slower than in bare *trans*-stilbene at the same excess energy above the isomerization barrier (see Fig. 5.17). However, care must be taken when comparing the experimental results with the kinetic model prediction especially with the signal-to-noise in the intermediate energy range and the short time scale of the measured transients (< 4.0 ns).

5.4.3.3 Isotope Effects

The deuterium isotope effects on the isomerization rate in jet-cooled and deuterated *trans*-stilbene have been studied by Zewail and coworkers [3]. The measured isomerization rate in *trans*-stilbene-d_{12} is slower than that of non-deuterated stilbene. The experimental results and RRKM calculations suggest that the density of states plays a key role in the microcanonical rate. Furthermore, the role of IVR and the nonadiabatic influences on the reaction rates were considered. Fleming and coworkers [35] investigated the influence of the density of states on the isomerization dynamics in *trans*-stilbene and deuterated *trans*-stilbene in supersonic-jet gas-phase, and solution over a wide range of temperature. These authors reported that the density of states has very little or no role at all in the isomerization dynamics in the gas-phase or in solution.

In an attempt to test the effects of the state density on the isomerization rate in clusters, energy-dependent measurements on the S_1-rate were conducted for stilbene-(hexane-d_{14})$_1$ and compared with that of stilbene-(hexane-h_{14})$_1$ under the same experimental conditions. A lowering of the rate would be expected if the internal hexane modes play a significant role, in conjunction with stilbene-d_{14} and stilbene-h_{14} results [10] and in agreement with RRKM theory. The frequencies of the intermolecular modes are also lowered by the 17% change in hexane mass upon deuteration. As mentioned above, the measured rates for both deuterated and undeuterated hexane complexes are indistinguishable in the excess-energy range of ~ 1500-2400 cm^{-1}. Beyond the plateau region, the measured rate in stilbene-(hexane-d_{14})$_1$ complex seems to be slightly slower than that of stilbene-(hexane-h_{14})$_1$ complex (see Fig. 5.5. However, the experimental limitations dictate caution in the interpretation of these findings. The lack of substantial change may indicate a less important role for the density of states in the overall isomerization dynamics as observed in gas-phase and solution [33]. Furthermore, internal friction might play a key role in the reaction in clusters, as formulated by Marcus [34]. Theoretical treatment and density of states calculations are underway to quantify this trend.

5.4.3.4 Solvent Polarity Effects

The solvent polarity is expected to affect the transition-state energy, and the extraction of the isomerization barrier is much more complicated than in the alkane-solvents case[10,35,36]. In solution, the activation barrier for the isomerization reaction in a polar solvent decreases in comparison with that of a nonpolar (*e.g.* alkane) solvent. Waldeck and coworkers [35,36] have studied the isomerization reaction of *trans*-stilbene and symmetrically substituted *trans*-stilbene in *n*-alkanenitrile solvents. In the *n*-alkanenitrile solvents, including *n*-hexanenitrile, the isoviscosity plots yield constant slopes over a range of viscosity (0.7-5.0 cP). For *trans*-stilbene in these polar solvents, the activation energy for the isomerization is 2.4 kcal/mol which is significantly lower than the observed value in *n*-alkane solvents. However, studies in both solvents, polar and nonpolar, show that the hydrodynamic Kramers theory is inadequate for describing the isomerization rates [35,37,38]. Similar observations were reported for 4,4'-dimethoxystilbene and 4,4'-dihydroxystilbene in polar solvents. The reduction of the activation energy suggests that the transition state is polar and/or polarizable. This suggestion is in agreement with the importance of the doubly-excited ^1A_g-state configuration in the isomerization mechanism [39].

The excess-energy studies of the rate in *trans*-stilbene solvated in *n*-hexanenitrile complexes (see Fig. 5.11 and 5.12) show the same trends as observed in solution. As mentioned above, the rate increases very rapidly (in comparison with that in the bare stilbene) as the energy increases in the S_1-state of *trans*-stilbene-(hexanenitrile)$_1$ complex. The structure of this complex was investigated using the same type of potential energy calculations described above and in Chapter 4. The minimum energy configuration for (1:1) complex is very similar to that of stilbene-hexane (1:1) complex except that an extra isomer was found. In this isomer, the hexanenitrile molecule rests on the stilbene plane in a perpendicular configuration. However, in these calculations, the difference between the dipole moment in hexane and hexanenitrile molecules was not considered.

Even though the the polarity effects on the S_1-state origin is not known, these observations in stilbene-hexanenitrile$_n$ clusters are very significant. First, *one solvent molecule complexing with trans-stilbene is sufficient to show similar effects on the rate as those observed in solution.* Second, in contrast with *trans*-stilbene solvation in *n*-hexane clusters (see below), the second solvent molecule in stilbene-(hexanenitrile)$_2$ cluster counteracts the polarity effects observed in the n=1 complex. At an excess-energy of ~2580 cm^{-1} in the S_1-state of bare *trans*-stilbene, the rate for the $n = 2$ complex (~4.0x10^9 s^{-1}) is ~7.6 time *slower* than that measured rate for the $n = 1$ complex (~30.3x10^9 s^{-1}) and ~2.3 time *slower* than the rate in the bare *trans*-stilbene (~9.0x10^9 s^{-1}). Intuitively, one can expect that as the number of polar solvent molecules of stilbene-(hexanenitrile)$_n$ clusters increases, it is likely that the polarity effects will decrease.

5.4.3.5 Cluster-Size Dependence

The rates measured across the full energy range for t-S-H_2, including those above its dissociation energy (which are deduced from measurements at the t-S-

H_1 mass) show an even slower increase compared to both the bare-molecule and t-S-H_1 (see Fig. 5.6 and 5.18). The slower change in rate, with the excess-energy, makes an estimate of the barrier difficult for t-S-H_2, and RRKM calculations will be necessary for that purpose.

At any given energy, the rate decreases as the cluster-size (*i.e.* number of the solvent molecule) increases (see Fig. 5.17). More importantly, the S_1-rate becomes excess-energy independent for large clusters. These results are very consistent with the high-friction regime observed in solution as well as in compressed-gas studies. In this regime, the coupling between the solute and solvents becomes very strong, such that a local equilibrium in energy located at the top of the barrier is established for the intermediate species. In this case, the rate is then limited by collisions of this species with the solvent molecules, which cause a re-crossing of the barrier in the *trans* direction. Consequently, the rate decreases as the solute-solvent coupling increases [2].

In comparing bulk and isolated stilbene rates it was shown that $k(T)$ is larger than the averaged $k(E)$ at T (for more details see ref. [4]). The theoretical approach in ref. 10 indicates that the non-adiabatic effect decreases in the presence of the solvent. The increased adiabaticity of the reaction enhances the rates, as supported by the results of the isotope effect in ref. [3] and by recent theoretical calculations of the force field and rates [22]. In the cluster, the effective time the system spends in the transition state may be even longer since it is no longer determined by the translational collision time.

In general, the effect of solvent friction on the rates is to either increase them (through thermal fluctuations) by an energy-controlled process or to decrease them by forcing a back transition to the reactants (Kramer's two regimes) [44]. In the cluster, the thermal fluctuations of the solvent are negligible and the origin of the "internal friction" can be related to: (1) solute-to-solvent energy coupling, which we term "energy friction," and (2) intermolecular "motional friction" due to random forces of the solvent adsorbed on the solute. The solute-solvent system is now considered in its totality and the bath may exchange energy, not only dissipatively but also diffusively.

The observed decrease in k_{iso} with n therefore belongs to the high friction regime of bulk solutions, even though we have finite n (influence of the pre-exponential term in Kramers' theory). The effect of the exponential term is opposite: the lower the value of E_0, the higher the rates. Accordingly, the observed decrease in the rate reflects the dominance of frictional effects, as separated from the barrier-change effect. This separation of the static barrier solvent effect from the frictional dynamics of the crossing is a key to the reaction mechanism. The decrease in E_0 observed in the 1:1 solute-solvent species is consistent with the value deduced from careful studies of rate coefficients for different isoviscous Arrhenius fits in bulk hexane [41,33]; at viscosity ~10 cP, E_0 is ~850 cm^{-1}. It is interesting to note that the bulk rates measured in hexane show Kramers' behavior after the correction for solute-solvent interaction. Note that at room temperature and ambient pressure (~ 0.3 cP) $k_{iso} = 11.5x10^9$ s^{-1} [33].

5.5 CONCLUSION

The excess-energy and cluster-size dependence of the S_1-state rate constant in *trans*-stilbene-(hexane)$_n$ clusters have been studied using two color resonant two-photon ionization (2cR2PI) and time-of-flight mass spectrometry techniques. A large and progressive decrease in the total deactivation rate of the S_1-state in isolated stilbene-(hexane)$_n$ was observed as the cluster size *(n)* increases. These observations contradict the observed acceleration of the isomerization rates in solution. The binding energy of hexane and t-stilbene is sufficiently large to permit a separation of the time scales of vibrational predissociation and isomerization dynamics. However, all transients (measured for different cluster sizes) decay as single exponentials with rates defined essentially by the rate of isomerization for all clusters, even well above their dissociation thresholds.

The excess-energy, deuterium isotope, and polarity effects on the measured rates were also examined. In general, the rate increases as the excess-energy increases. However, as the cluster size increases, the rate becomes almost energy-independent. This behavior reflect a strong coupling between the solute and solvent molecules by which the excess-energy is drained from the reactive mode. Other similarities between solution and clusters were noticed. Isotope-effect experiments with stilbene-(hexane-d_{14})$_1$ suggest that the density of states plays little or no role in the isomerization dynamics in solute-solvent clusters which is similar to what was observed in solution and gas-phase studies. Meanwhile, these observations contradict RRKM predictions on the microcanonical rates in jet-cooled *trans*-stilbene-d_{12}. The measured rates in *trans*-stilbene solvated in polar solvent clusters (hexanenitrile) is much faster than that in either bare *trans*-stilbene or stilbene-(hexane)$_n$ clusters, where hexane is a nonpolar molecule. A similar trend was observed for trans-stilbene solvated in polar solvents in the liquid phase.

The microscopic picture which emerges from these studies separates the solvation and internal friction effects on both the barrier and the barrier-crossing, respectively. These effects are also present in the bulk, but difficult to separate from the collision due to translational motion. It is interesting to note that the results obtained here for a finite number of solvent molecules parallels the trend observed with the high friction regime in bulk liquids and at high solvent densities.

Table (1): Isomer-dependent energetic of *trans*-stilbene-(hexane)$_n$ clusters

Cluster Size (*n*)	Isomer Type[a]	Calculated D_e[b] (cm^{-1})	Red Shift ($\delta\mu$)[c] (cm^{-1})	Average Red Shift (cm^{-1})	Estimated $D_0(S_1)$[d] (cm^{-1})
$n = 1$	A	2132	380[e]	322	2150
	C	2047	265[e]		2010
$n = 2$	(2/0)	4359	530	645	2150
	(1/1)	4335	760		2220
$n = 3$	(2/1)	6621	860		
$n = 4$	(2/2)	9032	1060		
$n = 5$	(2/2/1)	11498	1183		

a: 1) The structure of isomer A and C are the same as described in ref. [4].
2) *(i/j/k)* refers to an *i* of the hexane molecules on the top of *trans*-stilbene molecule, *j* on the bottom, and *k* on the side.

b: L-J (6-12) parameters are similar to those in ref. [23].

c: The red shift ($\delta\mu$) with respect to the S_1-electronic origin in bare*trans*-stilbene (32243.5 cm^{-1}) (not corrected for Vacuum)

d: A zero-point energy of 170 cm^{-1} was assumed for van der Waal's modes based on the calculations of ref. [23].

e: See ref. [23].

Table (2): Cluster-size and pump/probe laser-wavelength dependent measurements of time-constant in *trans*-stilbene-(hexane)$_n$ clusters.

Pump-Laser Wavelength (nm)	Probe-Laser Wavelength (nm)	Detected Cluster (n)	Time Constant (ns)	Assignment [n; E_X (cm^{-1})]
313.8	324.6	0	-	-
		1	2.7 ± 0.3	1; 0000.
		2	2.9 ± 0.2	2; 0269
		3	3.2 ± 0.3	3; 0484
		4	3.6 ± 0.1	4; 0684
		5	3.8	5; -
310.1	324.6	0	2.7 ± 0.1	0; 0000.
		1	2.2 ± 0.2	1; 0322
		2	2.8 ± 0.1	2; 0645
		3	3.2 ± 0.3	3; 0860
		4	3.5 ± 0.1	4; 1060
		5	3.9 ± 0.1	5; -
287.1	324.6	0	0.15 ± 0.03	0; 2588
		1	0.35 ± 0.05	2; 3233
		2	0.91 ± 0.05	3; 3448
		3	1.3 ± 0.1	4; 3648
		4	2.3	5; -
282.5	327.1	0	0.07	0; 3155
		1	0.25	2; 3800
		2	0.67	3; 4015
		3	1.3	4; 4215
		4	2.3	5; -

5.6 REFERENCES

1. J. A. Syage, *Laser Focus World* vol. **30**, no. 10, 73 (1994).
2. R. M. Hochstrasser, *Pure & Appl. Chem.* **52**, 2683 (1980).
3. J. A. Syage, P. M. Felker, and A. H. Zewail, *J. Chem. Phys.* **81**, 4706 (1984).
4. P. M. Felker and A. H. Zewail, *J. Phys. Chem.* **89,** 5402 (1985).
5. J. A. Syage, W. R. Lambert, P. M. Felker, and A. H. Zewail, R. M. Hochstrasser, *Chem. Phys. Lett.* **88**, 266 (1982).
6. J. Troe and J. Schroeder, *J. Phys. Chem.* **90**, 4215 (1986).
7. J. Troe, *Chem. Phys. Lett.* **114**, 241 (1985).
8. T. J. Majors, U. Even, and J. Jortner, *J. Chem. Phys.* **81**, 2330 (1984).
9. A. Amirav, J. Jortner, *Chem. Phys. Lett.* **95**, 295 (1983).
10. D. H. Waldeck, *Chem. Rev.* **91**, 415 (1991).
11. J. Schroeder and J. Troe, *J. Chem. Phys. Lett.* **116**, 453 (1985).
12. G. Maneke, J. Schroeder, J. Troe, and F. Voss, *Ber. Bunsen-Ges. Phys. Chem.* **89**, 896 (1985).
13. J. Schroeder and J. Troe, *J. Annu. Rev. Phys. Chem* **38**, 163 (1987).
14. J. Schroeder, D. Schwarzer, J. Troe, and F. Voss, *J. Chem. Phys*. **93**, 2393 (1990).
15. M. Lee, G. R. Holtom, and R. M. Hochstrasser, *Chem. Phys. Lett.* **118**, 359 (1985).
16. G. R. Fleming, *Chemical Applications of Ultrafast Spectroscopy*; Oxford: New York, 1986.
17. G. R. Fleming, S. H. Courtney, and M. W. Balk, *J. Stat. Phys.* **42**, 83 (1986).
18. M. W. Balk and G. R. Fleming, *J. Phys. Chem.* 1986, **90**, 3975.

19. S. H. Courtney and G. H. Fleming, *Chem. Phys. Lett.* **103**, 443 (1984).

20. S. H. Courtney and G. R. Fleming, *J. Chem. Phys.* **83**, 215 (1985).

21. S. K. Kim and G. R. Fleming, *J. Phys. Chem.* **92**, 2168 (1988).

22. F. Negri and G. Orlandi, *J. Phys. Chem.* **95**, 748 (1981).

23. C. Lienau, A. A. Heikal, and A. H. Zewail, *Chem. Phys.* **175,** 171 (1993).

24. L. R. Khundkar and A. H. Zewail, *Ann. Rev. Phys. Chem.* **41**, 15 (1990).

25. J. P. Maier and D. W. Turner, *J. Chem. Soc. Far. Trans.* **2**, 69, 196 (1973).

26. N. F. Scherer, L. R. Khundkar, T. S. Rose, and A. H. Zewail *J. Phys. Chem.* **91**, 6478 (1987).

27. L. Bañares, A. A. Heikal and A. H. Zewail, *J. Phys. Chem.* **96** (1992) 4127.

28. M. Kappes, and S. Leutwyler, in *Atomic and Molecular Beam Methods* Vol.1, ed. By G. Scoles, (Oxford University Press, 1988) p.38].

29. T. D. Mark and A. W. Castleeman, *Adv. At. Mol. Phys.* **20**, 65 (1985).

30. J. Jortner, *Ber. Bunsenges. Phys. Chem.* **88**, 188 (1984).

31. W. M. Trott, N. C. Blais, and E. A. Walters, *J. Chem. Phys.* **69**, 3150 (1978).

32. R. M. Hochstrasser, *Can. J. Chem.* **39**, 459 (1961).

33. S. H. Courteny, M. W. Balk, L. A. Philips, S. P. Webb, D. Yang, D. H. Levy, and G. R. Fleming, *J. Chem. Phys.* **89**, 6697 (1988).

34. R. Marcus; to be published.

35. N. S. Park and D. H. Waldeck, *J. Phys. Chem.* **94**, 662 (1990).

36. N. Sivakumar, E. A. Hoburg, and D. H. Waldeck, *J. Chem. Phys.* **90**, 2305 (1989).

37. N. S. Park and D. H. Waldeck, *J. Chem. Phys.* **91(2)**, 943 (1989).

38. D. M. Zeglinski and D. H. Waldeck, *J. Phys. Chem.* **92**, 692 (1988).

39. G. Orlandi and W. Siebrand, *Chem. Phys.*, **30**, 352 (1975).

40. G. R. Fleming and P. Hanggi (eds.), *Activated Barrier Crossing*, World Scienfitic, Singapore (1993).

41. J. Schroeder, J. Troe, and P. Vohringer, *Chem. Phys. Lett.* **203**, 255 (1993).

5.7 FIGURE CAPTIONS

5.1. A typical transient for bare *trans*-stilbene 0_0^0-transition using 310 nm (pump)/325 nm (probe) wavelengths (top). The excess-energy dependence of the rate constant in bare trans-stilbene using 2cR2PI technique with 100 and 14 psi backing pressure of the carrier gas (helium) (bottom). Similar measurements using TCSPC technique are also shown for comparison (adapted from ref. [27]).

5.2. Backing pressure dependent measurements of the time constant in bare *trans*-stilbene excited to S_1+~2000 cm^{-1}. Using the TCSPC technique, a lifetime of ~400 ps was measured.

5.3. Time-of-flight mass spectrum of stilbene and stilbene-hexane$_n$ clusters using 2cR2PI technique (bottom). The same spectrum was recorded with the pump-laser acting alone while the probe laser was blocked (middle) and vice versa (top). Molecular beam conditions were: backing pressure of 56 psi He passed over hexane at 114 °C; 335 μs gas pulse width. λ_{pump} = 313.8 nm, λ_{probe} = 324.6 nm. The probe pulse was delayed ~67 ps with respect to the pump pulse.

5.4 The excess-energy dependence of the total rate constant in stilbene-hexane$_1$ complex using 2cR2PI technique under a backing pressure of ~14 psi. The zero energy corresponds to the 0_0^0transition in t-S-H_1 [23].

5.5 The excess-energy dependence of the rate constant in deuterated (d_{14}) and un-deuterated (h_{14}) hexane ($n = 1$) complexes with *trans*-stilbene.

5.6 The excess-energy dependence of the total rate constant in stilbene-hexane$_2$ complex using a backing pressure of ~14 psi.

5.7 Representative transients measured as a function of cluster size *(n)* at a fixed pump/probe laser wavelength of 314 nm/325 nm. The time zero corresponds to the maximum of the pump-probe cross-correlation profile (see Fig. 2.3 in Chapter 2), *i.e.* half the rise of each transient. The number of the solvent molecules *(n)* in a cluster and the time constant *(τ)* are shown in the upper left corner of each transient. The solid line is the best fit.

5.8 Representative transients measured as a function of cluster size at a fixed pump/probe laser wavelength of 310 nm/325 nm. The number of solvent molecules *(n)* in the cluster and the time constant are shown in the upper left corner of each transient.

5.9 Representative transients measured as a function of cluster size at a fixed pump/probe laser wavelength of 287 nm/327 nm. The number of solvent molecules *(n)* in the cluster and the time constant are shown in the upper left corner of each transient.

5.10 Time-of-flight mass spectrum of stilbene-M$_n$ clusters, where M = hexane-h$_{14}$ (bottom), hexanenitrile (middle), and hexane-d$_{14}$ (top). The TOFMS for hexane-h$_{12}$ and hexanenitrile clusters with *trans*-stilbene were recorded with pump/probe laser wavelength of 310/327 nm. Meanwhile, the mass spectrum of stilbene-hexane-d$_{14}$ were measured with 292 nm/327 nm which might explain the broadening in the bands due to possible fragmentation.

5.11. Representative transients for *trans*-stilbene-(hexanenitrile)$_n$ clusters (n = 0, 1, 2) at two excess-vibrational energies in the S$_1$-state that correspond to 310 nm. The probe laser was fixed at 327 nm. The number of solvent molecules *(n)* in the cluster and the time constant(s) are shown in the upper left corner of each transient. For n = 1 transient, τ_1 = 400 ps, τ_2 = 2.63 ns, $a_s / a_f = 0.71$.

5.12. Representative transients for trans-stilbene-(hexanenitrile)$_n$ clusters (n = 0, 1, 2) at two excess-vibrational energies in the S$_1$-state that correspond to 287 nm. The probe laser was fixed at 327 nm. The number of solvent molecules *(n)* in the cluster and the time constant are shown in the upper left corner of each transient.

5.13. A kinetic model for the time-evolution of the $A.B_n$ population in the S$_1$-state manifold. The fluorescence, isomerization, and vibrational predissociation are considered to be the deactivation channels of the S$_1$-state of the clusters with rates k_f^n, k_{iso}^n, and k_{vp}^n, respectively.

5.14 Time-of-flight mass spectra of stilbene-hexane (1:1) cluster as a function of excess energy in the S$_1$-state of the complex. The excess energies, shown in the upper left corners were calculated with respect to the 0_0^0-transition of stilbene-hexane$_1$ complex [23].

5.15. The minimum energy structure of stilbene-hexane$_3$ based on Lennard-Jones atom-atom potential energy calculations: ~45° angle view (top) and side view (bottom). The single hexane above the stilbene plane and the two below the plane also correspond closely to the minimum energy structures of stilbene-hexane$_1$ and stilbene-hexane$_2$, respectively. The structure for stilbene-hexane$_4$ has two solvent molecules above and two below the stilbene plane, while for stilbene-hexane$_5$, a fifth hexane lies in the plane, parallel to the other four.

5.16 The excess-energy dependence of the rate constant in stilbene-hexane$_n$ complexes ($n = 0, 1$). The experimental conditions were fixed during these measurements and the y-axis was expanded (top) to show the difference in the measured rates for $n = 0$ and $n = 1$ in the low energy region.

5.17 The excess-energy dependence of the rate constant in stilbene-hexane$_n$ complexes ($n = 0, 1$) above the energy threshold (barrier). The barrier in bare *trans*-stilbene is 1200 cm^{-1} (with a backing pressure of 100 psi) and 1000 cm^{-1} (with a backing pressure of 100 psi). Meanwhile, a barrier of 600 cm^{-1} was estimated (without considering the thermal energy which is ~200 cm^{-1}; see text).

5.18. The excess-energy dependence of the rate constant in *trans*-stilbene-(hexane)$_n$ clusters, $n = 0, 1, 2$ which was measured under the same experimental conditions for comparison.

5.19 Time and rate constants measurements in *trans*-stilbene-(hexane)$_n$ as a function of cluster size. These measurements were carried out at three different pump-laser wavelength (i.e. different excess energies): 314 nm (bottom), 310 nm (middle), and 283 nm (top). The probe laser wavelength is also shown. Notice the difference in the vertical-axis scales.

5.20 The excess energy dependence of the rate constant in *trans*-stilbene-(hexane)$_n$ clusters as a function of the cluster size. In this figure, the red shift in the 0_0^0-transitions in *trans*-stilbene-(hexane)$_n$ clusters of different size was considered when the excess energy was calculated (see Table (2)).

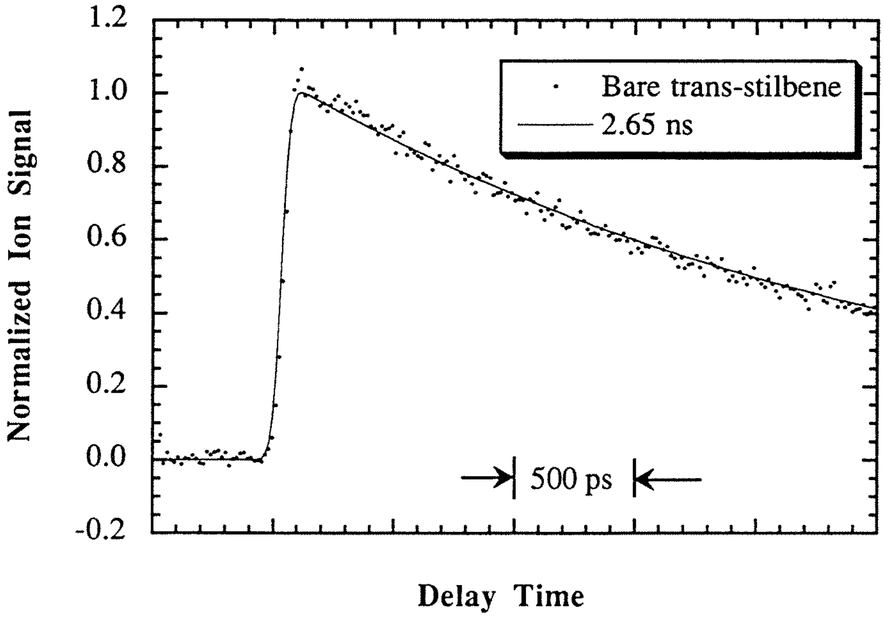
1.2
1.0
0.8
0.6
0.4
0.2
0.0
-0.2
Normalized Ion Signal
Delay Time
Bare trans-stilbene
2.65 ns
500 ps

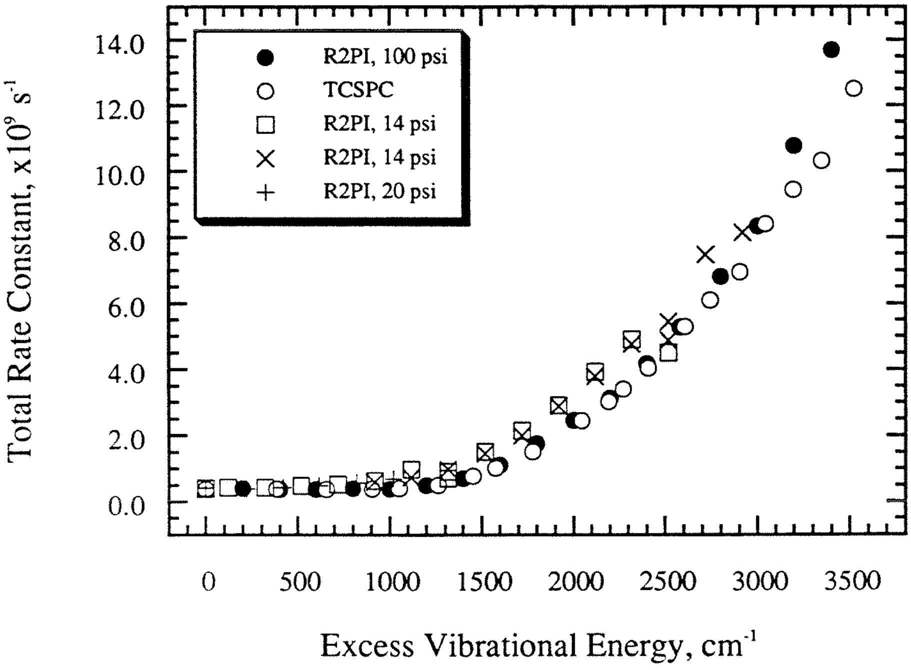
14.0
12.0
10.0
8.0
6.0
4.0
2.0
0.0
Total Rate Constant, x10⁹ s⁻¹
0
500
1000
1500
2000
2500
3000
3500
Excess Vibrational Energy, cm⁻¹
● R2PI, 100 psi
○ TCSPC
□ R2PI, 14 psi
× R2PI, 14 psi
+ R2PI, 20 psi

Fig. 5.1

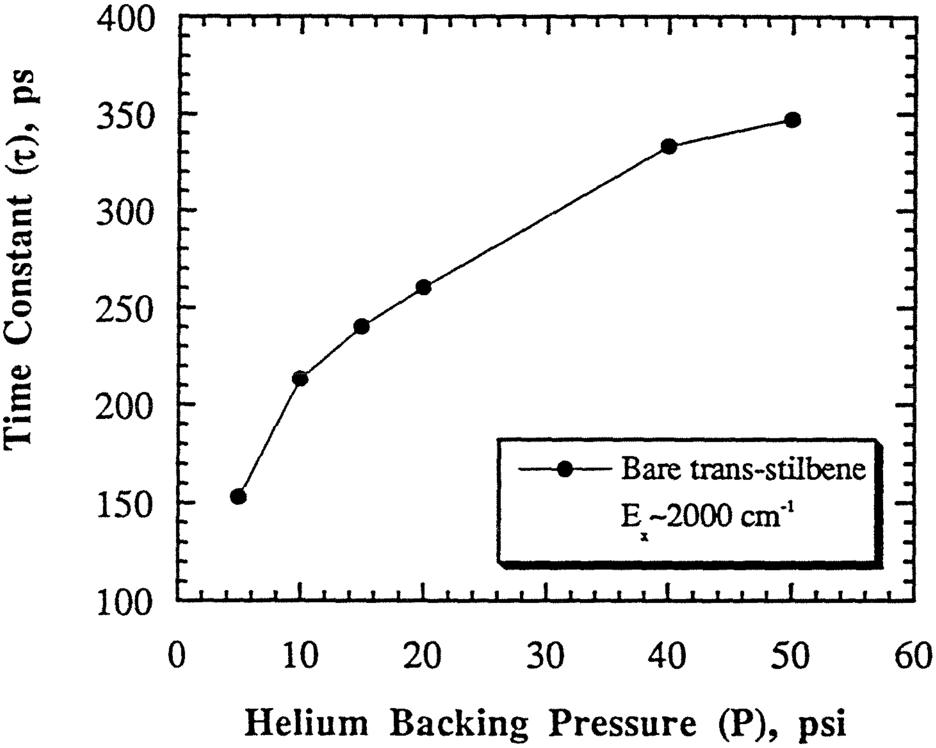
Time Constant (τ), ps
400
350
300
250
200
150
100
0
10
20
30
40
50
60
Helium Backing Pressure (P), psi
Bare trans-stilbene
E_x~2000 cm⁻¹

Fig. 5.2

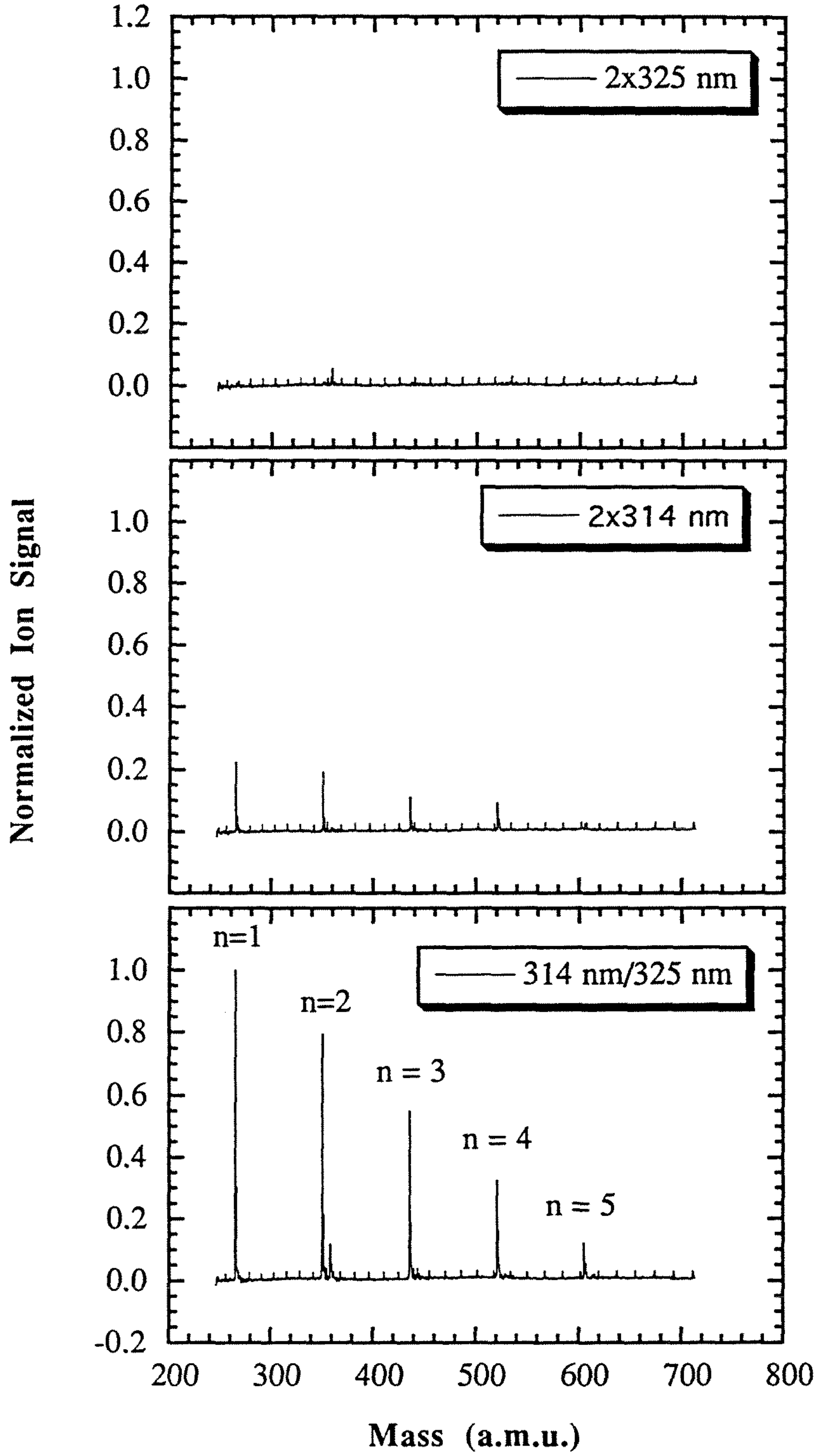
Normalized Ion Signal
Mass (a.m.u.)
2x325 nm
2x314 nm
314 nm/325 nm
n=1
n=2
n = 3
n = 4
n = 5
1.2
1.0
0.8
0.6
0.4
0.2
0.0
-0.2
200
300
400
500
600
700
800

Fig. 5.3

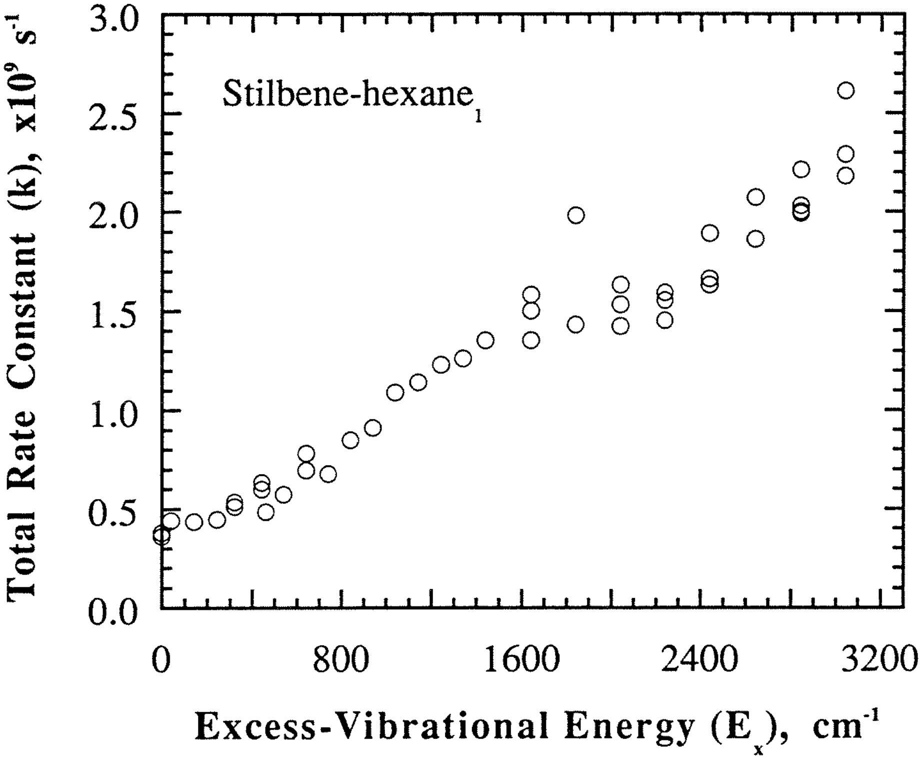
Stilbene-hexane₁
Total Rate Constant (k), x10⁹ s⁻¹
Excess-Vibrational Energy (Eₓ), cm⁻¹
0.0
0.5
1.0
1.5
2.0
2.5
3.0
0
800
1600
2400
3200

Fig. 5.4

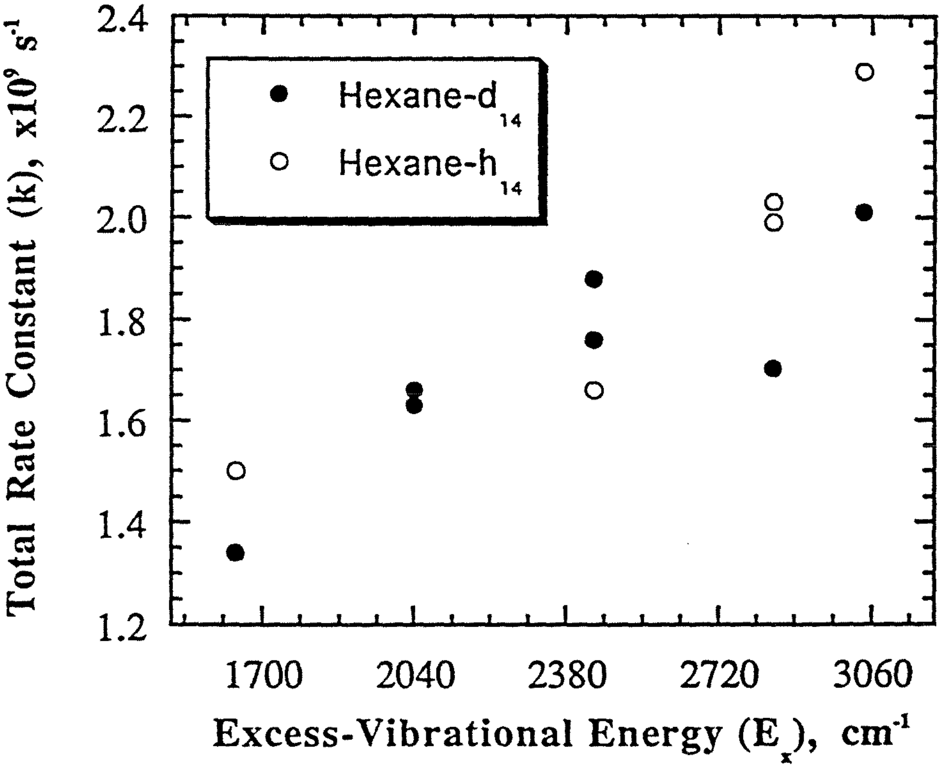

2.4
2.2
2.0
1.8
1.6
1.4
1.2
Total Rate Constant (k), x10^9 s^{-1}
● Hexane-d$_{14}$
○ Hexane-h$_{14}$
1700
2040
2380
2720
3060
Excess-Vibrational Energy (E$_x$), cm^{-1}

Fig. 5.5

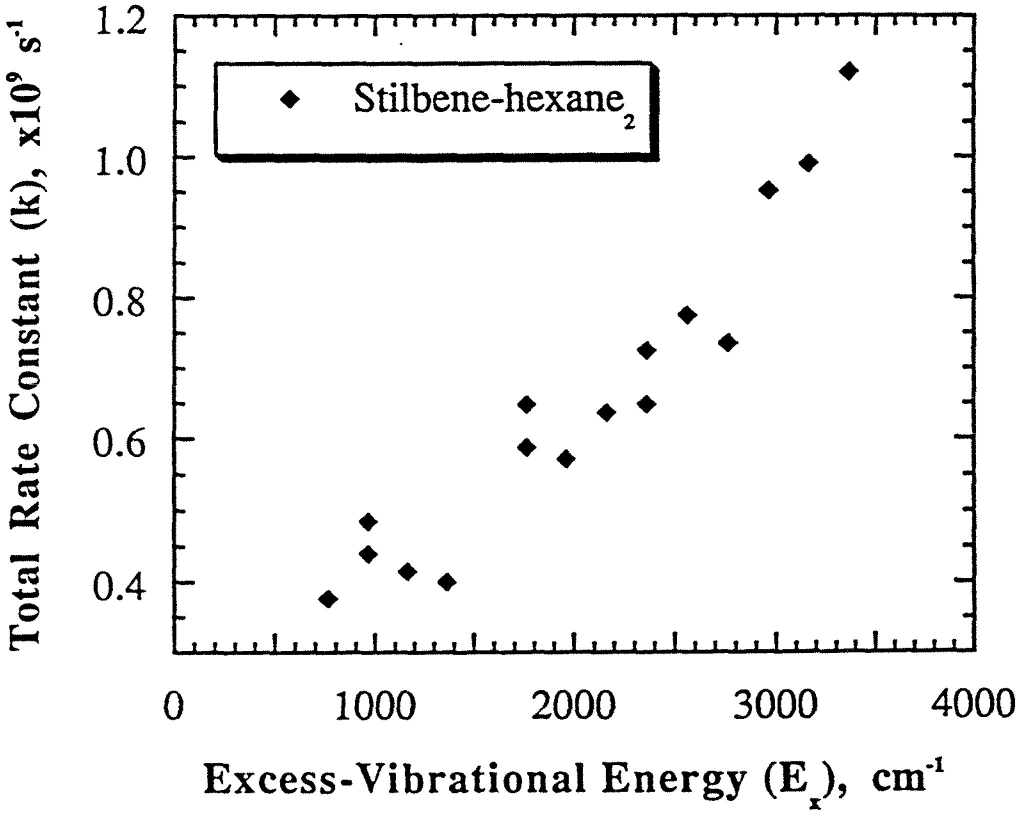
Total Rate Constant (k), x10^9 s^{-1}
1.2
1.0
0.8
0.6
0.4
Stilbene-hexane$_2$
0
1000
2000
3000
4000
Excess-Vibrational Energy (E$_x$), cm^{-1}

Fig. 5.6

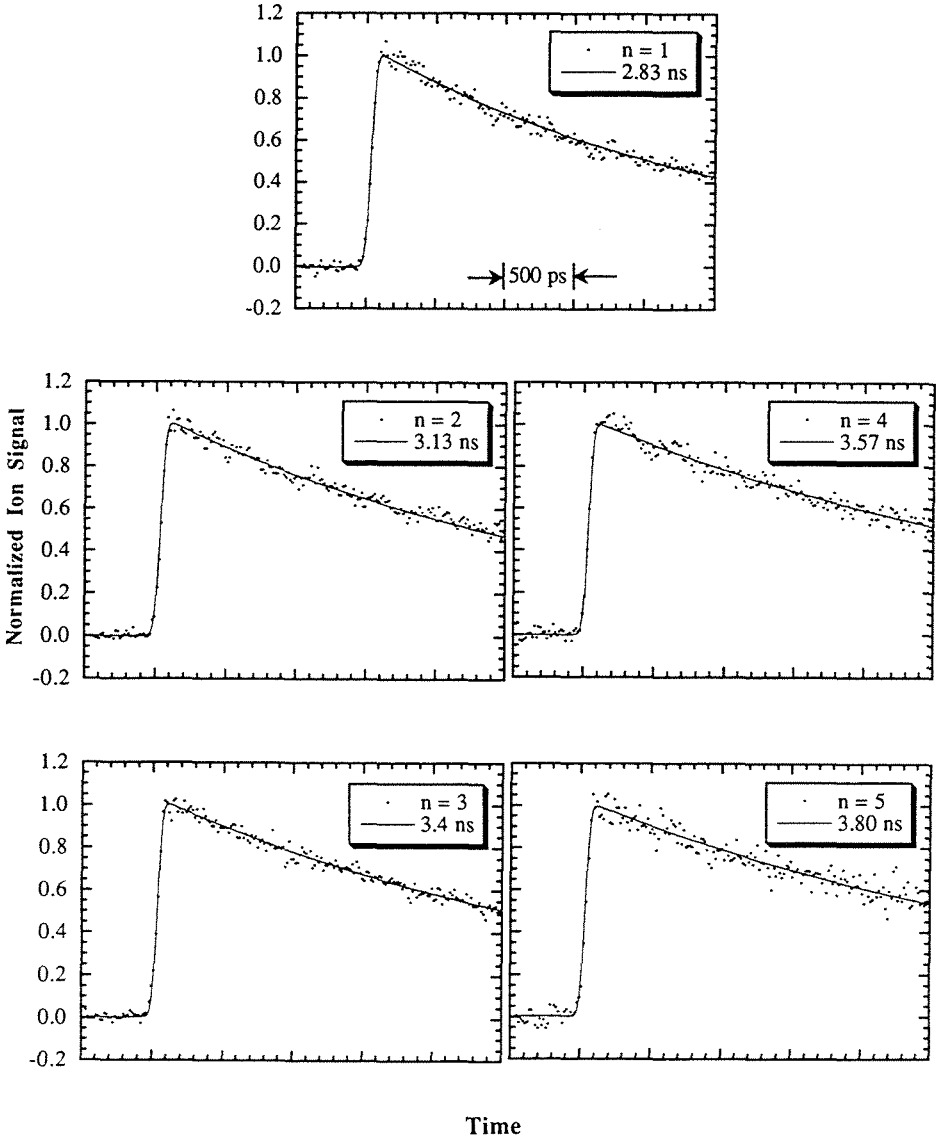
1.2
1.0
0.8
0.6
0.4
0.2
0.0
-0.2
n = 1
2.83 ns
500 ps
n = 2
3.13 ns
n = 4
3.57 ns
n = 3
3.4 ns
n = 5
3.80 ns
Normalized Ion Signal
Time

Fig. 5.7

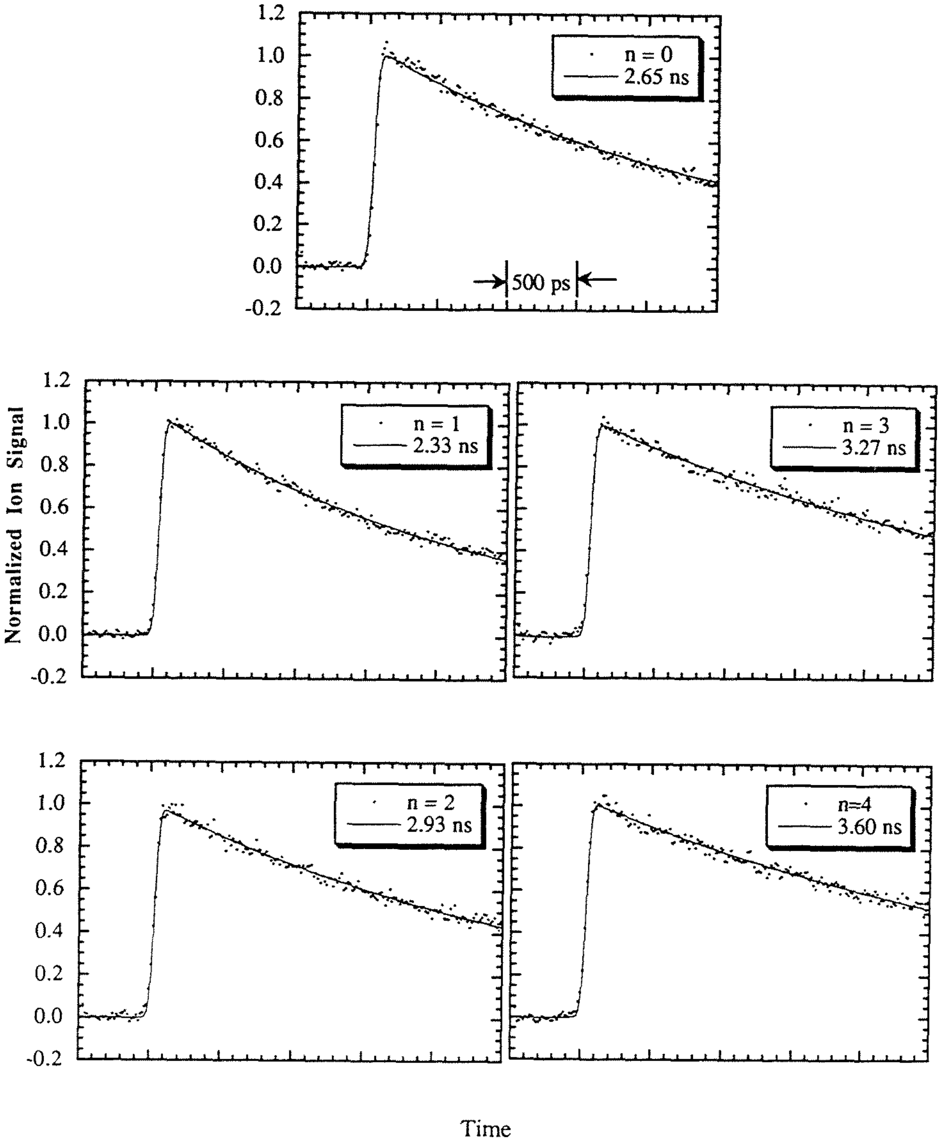
1.2
1.0
0.8
0.6
0.4
0.2
0.0
-0.2
n = 0
2.65 ns
500 ps
n = 1
2.33 ns
n = 3
3.27 ns
n = 2
2.93 ns
n=4
3.60 ns
Normalized Ion Signal
Time

Fig. 5.8

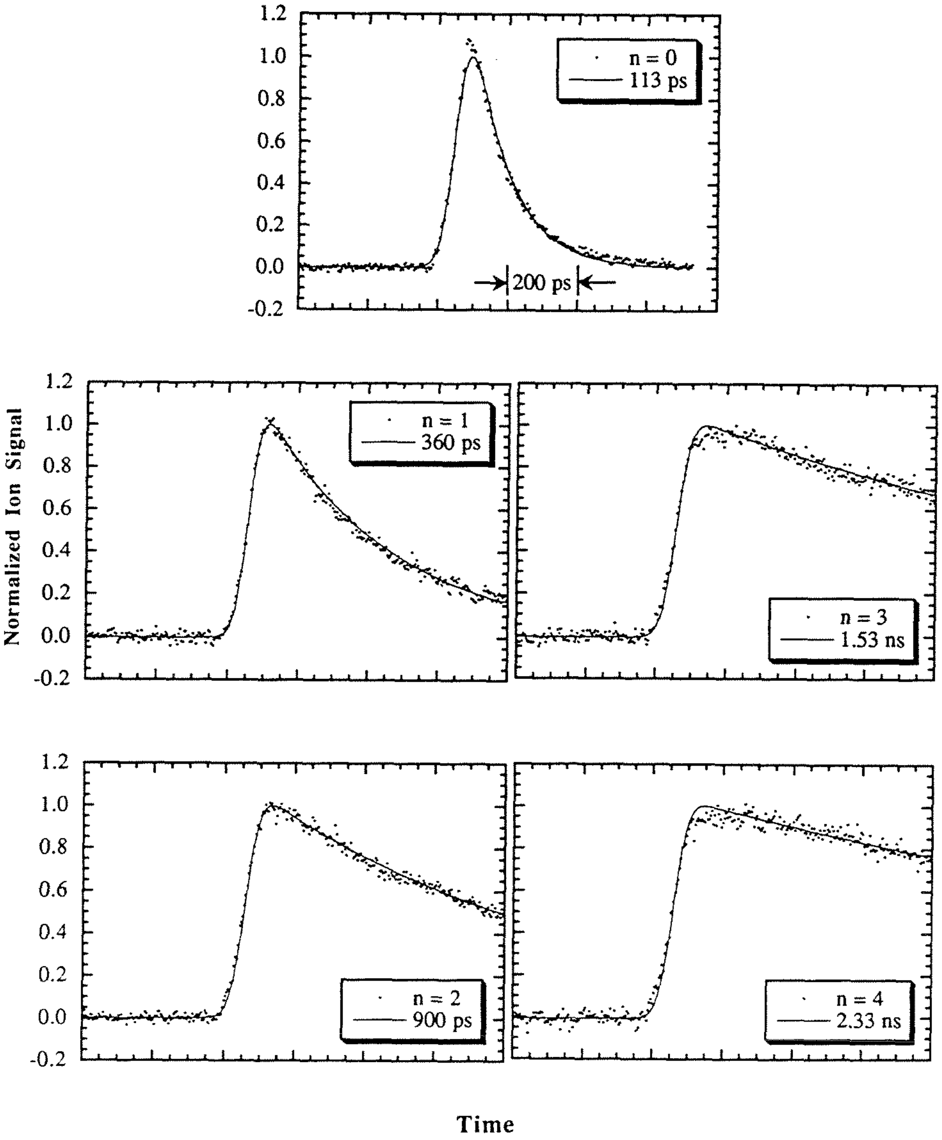
1.2
1.0
0.8
0.6
0.4
0.2
0.0
-0.2
n = 0
113 ps
200 ps
n = 1
360 ps
n = 3
1.53 ns
n = 2
900 ps
n = 4
2.33 ns
Normalized Ion Signal
Time

Fig. 5.9

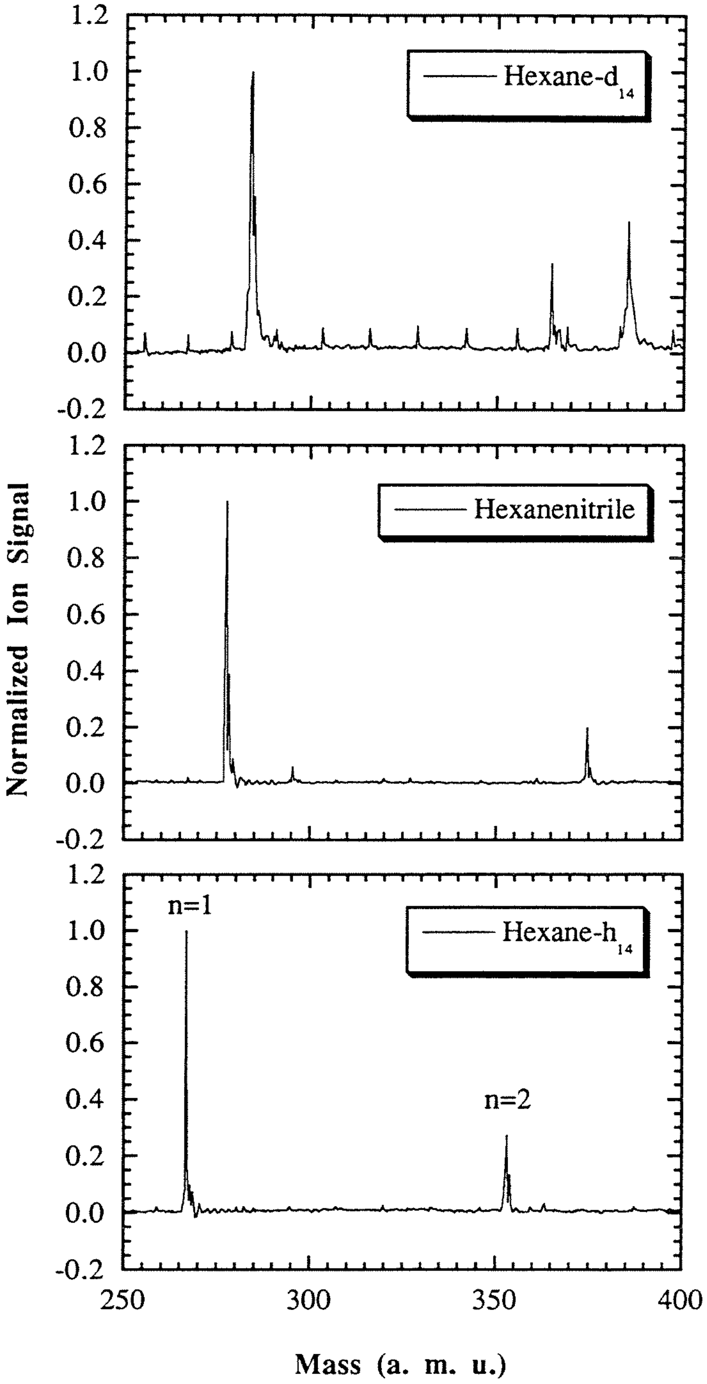
1.2
1.0
0.8
0.6
0.4
0.2
0.0
-0.2
Hexane-d_{14}
Hexanenitrile
Hexane-h_{14}
n=1
n=2
Normalized Ion Signal
250
300
350
400
Mass (a. m. u.)

Fig. 5.10

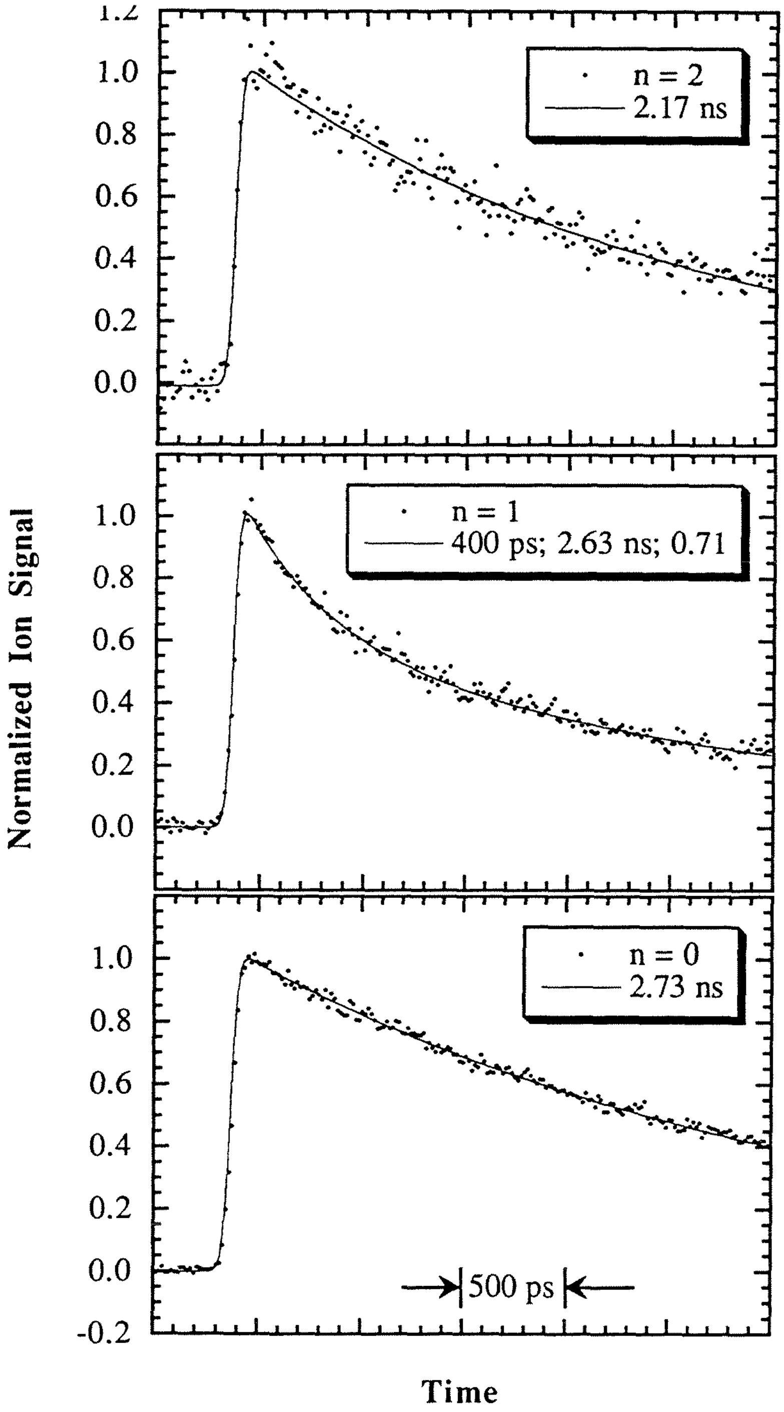
1.2
1.0
0.8
0.6
0.4
0.2
0.0
n = 2
2.17 ns
n = 1
400 ps; 2.63 ns; 0.71
n = 0
2.73 ns
-0.2
500 ps
Normalized Ion Signal
Time

Fig. 5.11

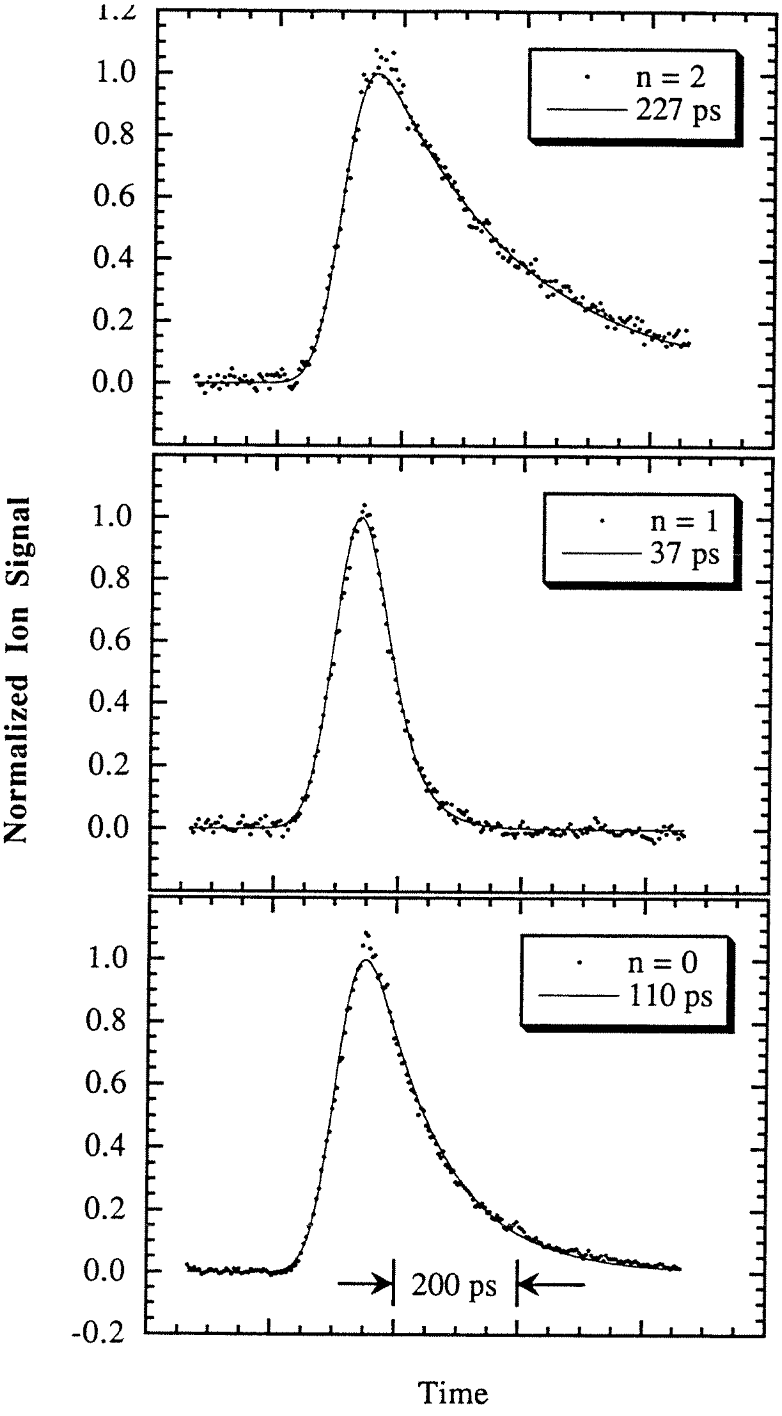
Normalized Ion Signal
Time
1.2
1.0
0.8
0.6
0.4
0.2
0.0
-0.2
n = 2
227 ps
n = 1
37 ps
n = 0
110 ps
200 ps

Fig. 5.12

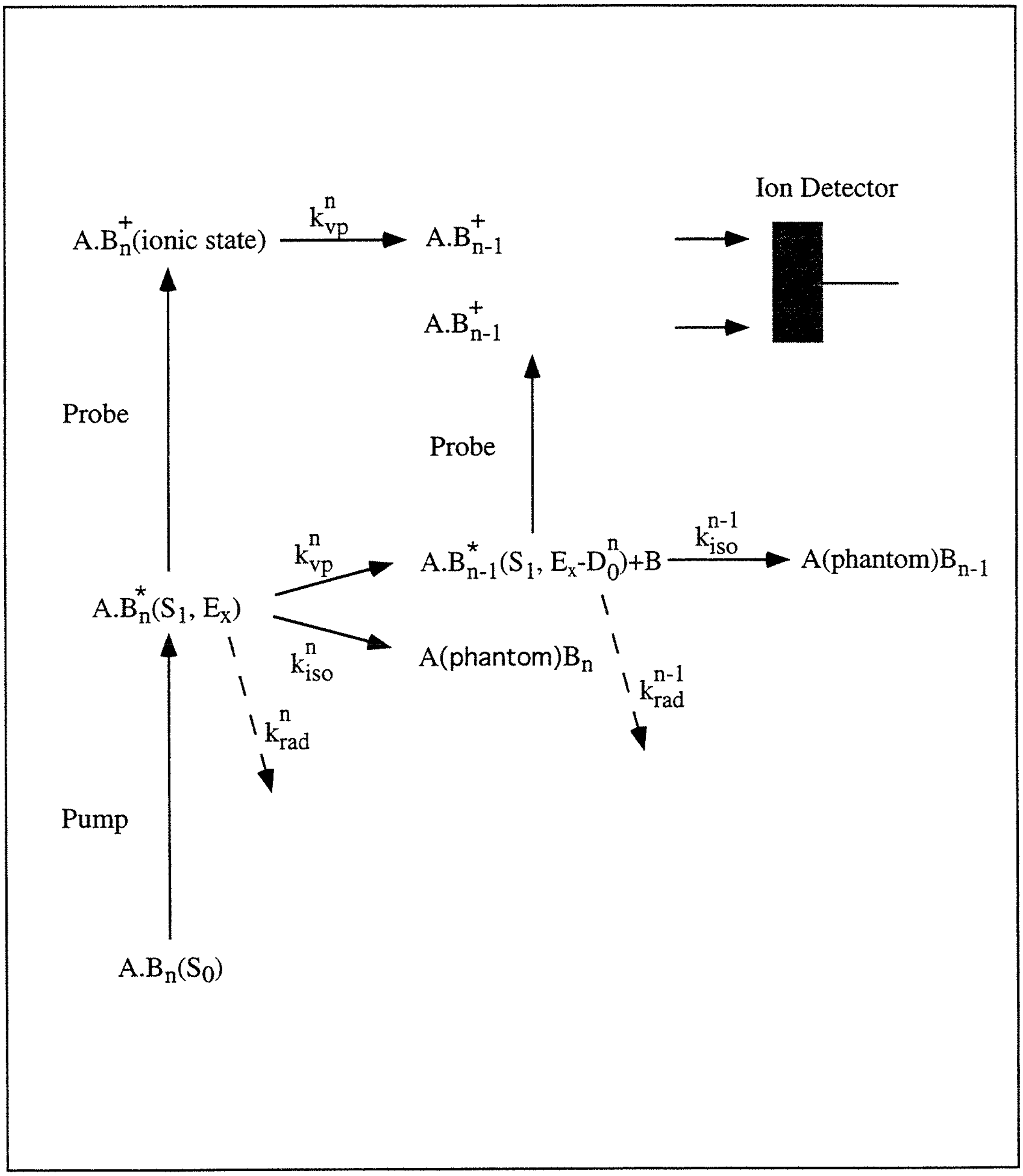
Ion Detector
$A.B_n^+$(ionic state)
k_{vp}^n
$A.B_{n-1}^+$
$A.B_{n-1}^+$
Probe
Probe
$A.B_{n-1}^*(S_1, E_x-D_0^n)$+B
k_{iso}^{n-1}
A(phantom)B_{n-1}
k_{vp}^n
$A.B_n^*(S_1, E_x)$
k_{iso}^n
A(phantom)B_n
k_{rad}^{n-1}
k_{rad}^n
Pump
$A.B_n(S_0)$

Fig. 5.13

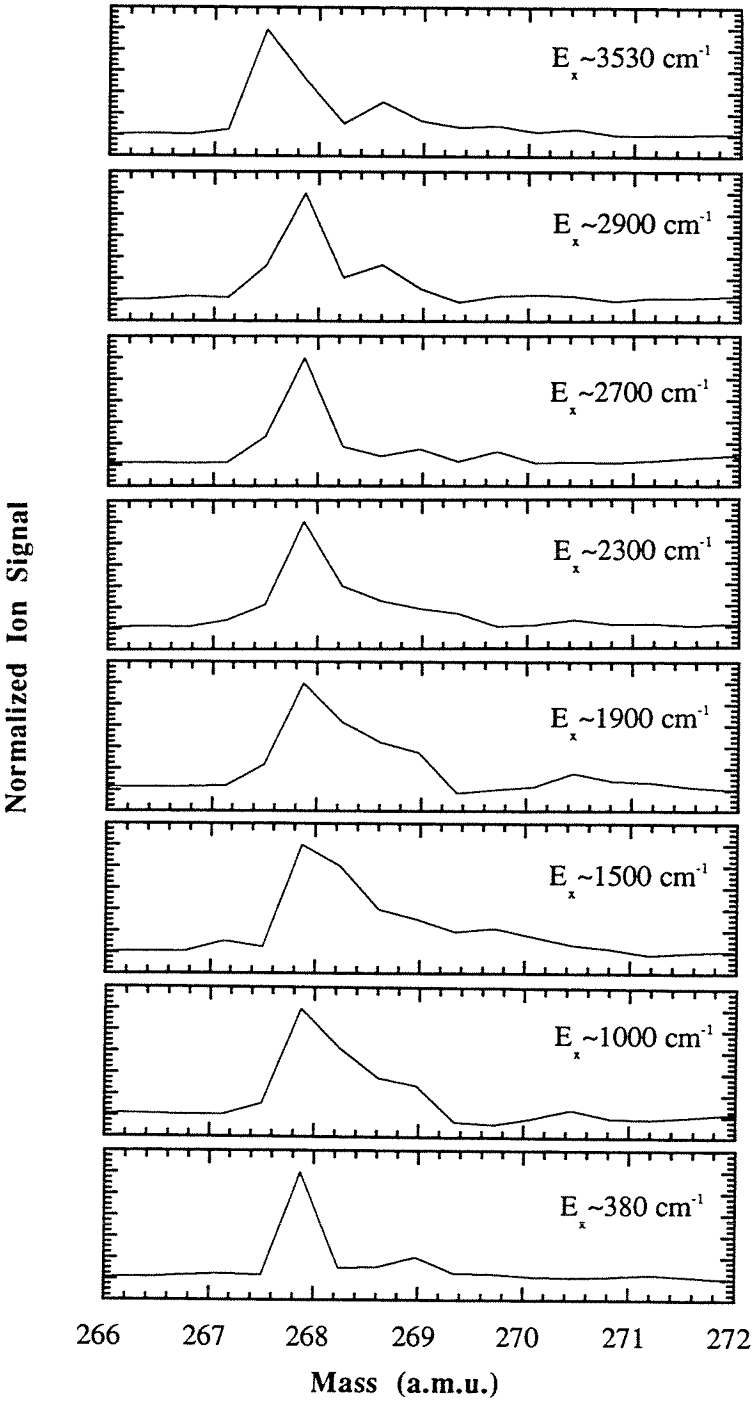
E_x~3530 cm^{-1}
E_x~2900 cm^{-1}
E_x~2700 cm^{-1}
E_x~2300 cm^{-1}
E_x~1900 cm^{-1}
E_x~1500 cm^{-1}
E_x~1000 cm^{-1}
E_x~380 cm^{-1}
Normalized Ion Signal
266
267
268
269
270
271
272
Mass (a.m.u.)

Fig. 5.14

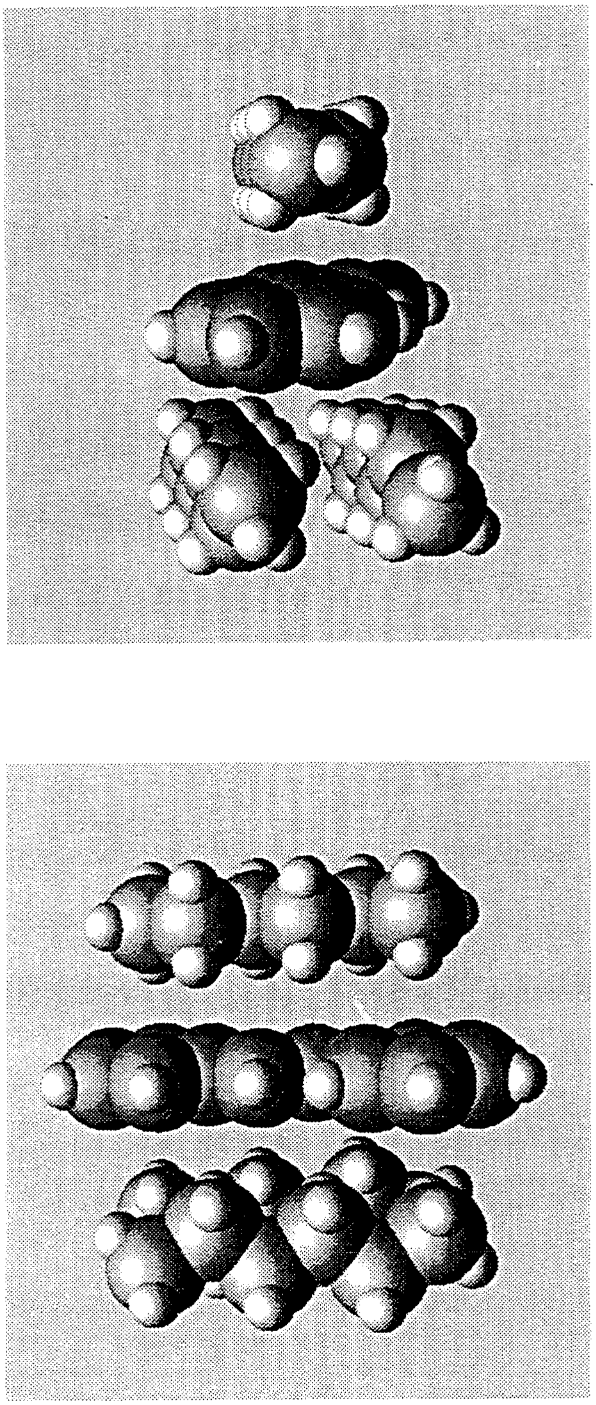

Fig. 5.15

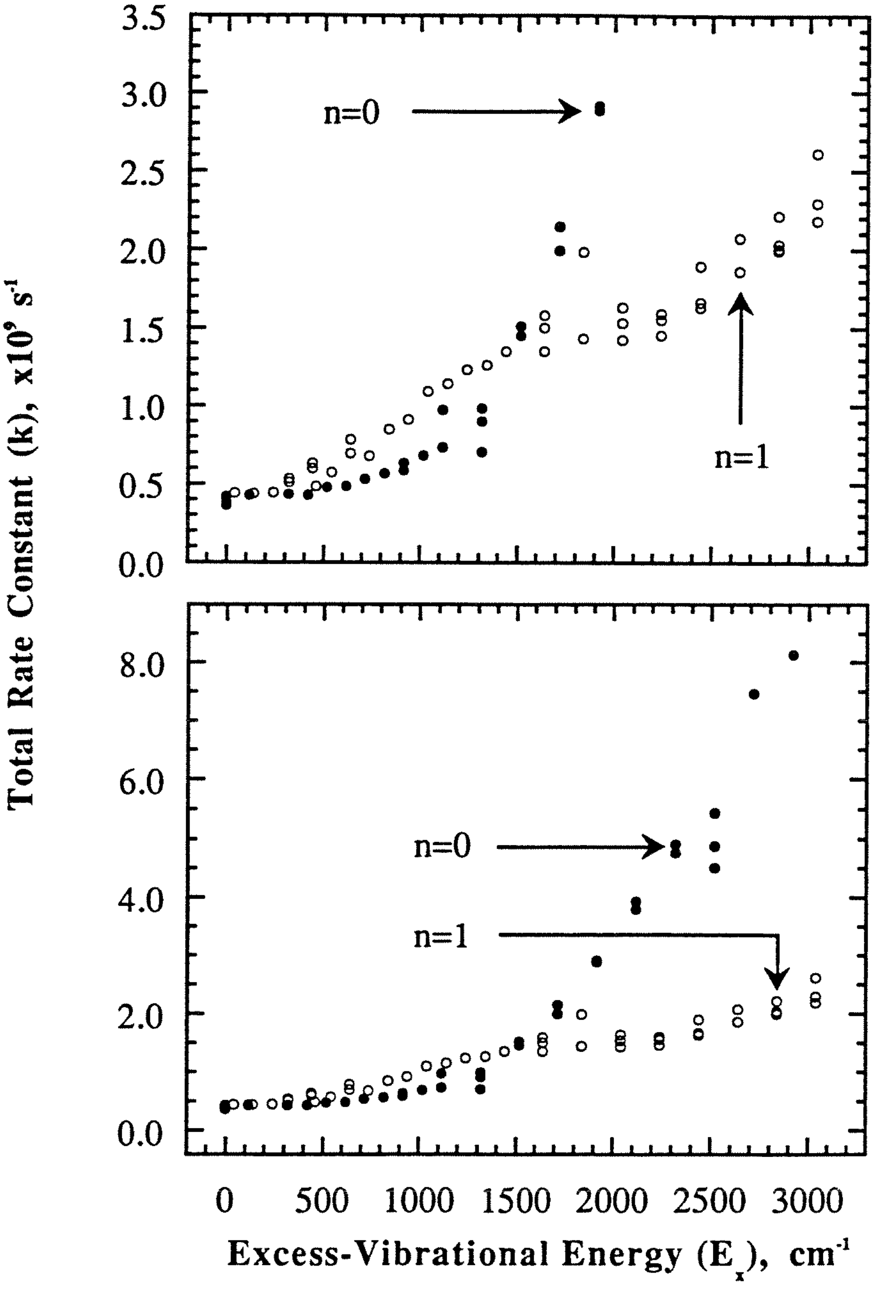
3.5
3.0
2.5
2.0
1.5
1.0
0.5
0.0
n=0
n=1
8.0
6.0
4.0
2.0
0.0
n=0
n=1
0
500
1000
1500
2000
2500
3000
Total Rate Constant (k), x10⁹ s⁻¹
Excess-Vibrational Energy (Eₓ), cm⁻¹

Fig. 5.16

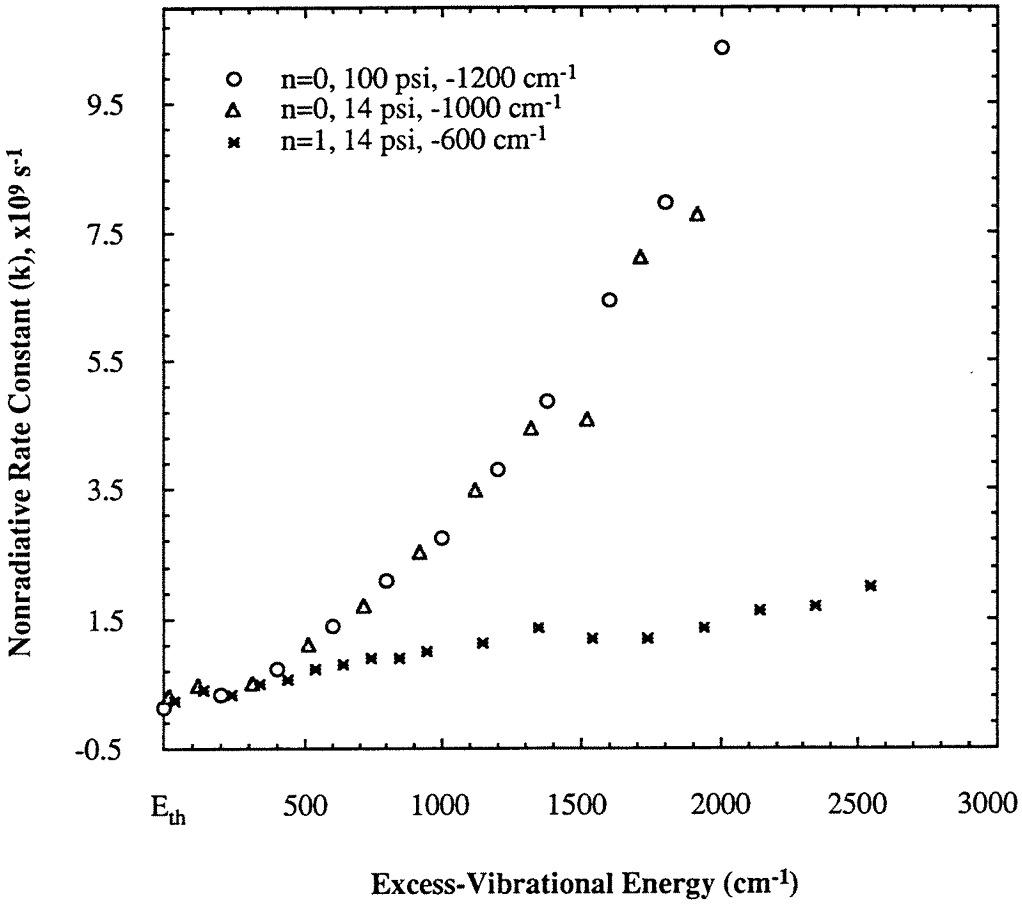
○ n=0, 100 psi, -1200 cm^{-1}
△ n=0, 14 psi, -1000 cm^{-1}
✖ n=1, 14 psi, -600 cm^{-1}
Nonradiative Rate Constant (k), x10^9 s^{-1}
9.5
7.5
5.5
3.5
1.5
-0.5
E$_{th}$
500
1000
1500
2000
2500
3000
Excess-Vibrational Energy (cm^{-1})

Fig. 5.17

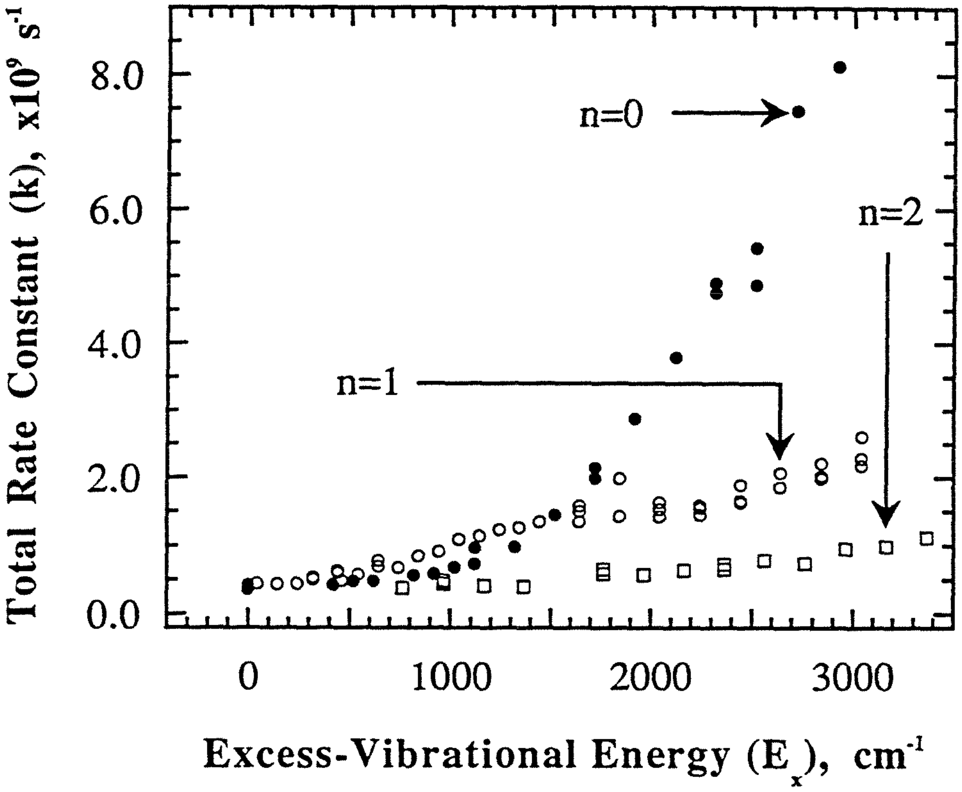
Total Rate Constant (k), x10^9 s^{-1}
0.0
2.0
4.0
6.0
8.0
0
1000
2000
3000
Excess-Vibrational Energy (E_x), cm^{-1}
n=0
n=1
n=2

Fig. 5.18

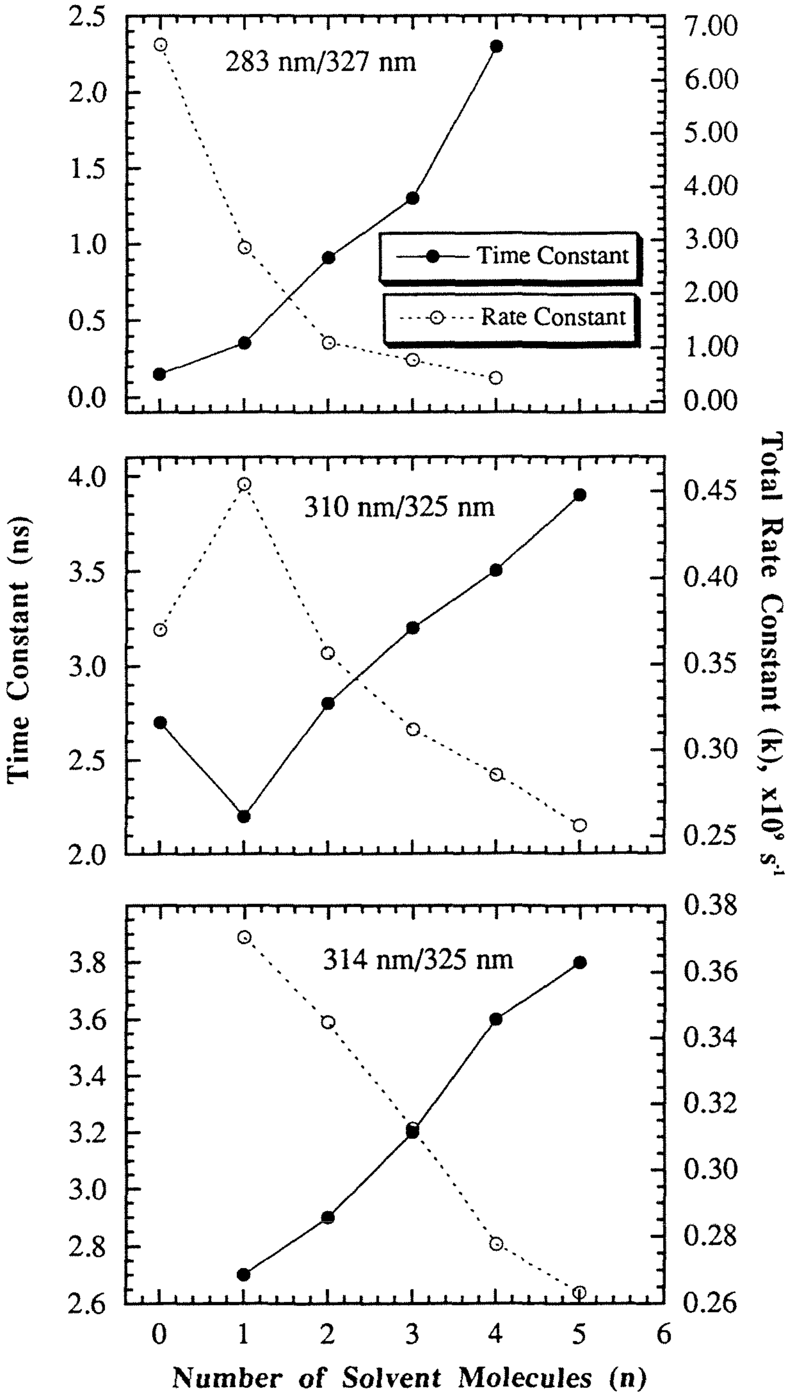
283 nm/327 nm
310 nm/325 nm
314 nm/325 nm
Time Constant
Rate Constant
Time Constant (ns)
Total Rate Constant (k), x10⁹ s⁻¹
Number of Solvent Molecules (n)
2.5
2.0
1.5
1.0
0.5
0.0
7.00
6.00
5.00
4.00
3.00
2.00
1.00
0.00
4.0
3.5
3.0
2.5
2.0
0.45
0.40
0.35
0.30
0.25
3.8
3.6
3.4
3.2
3.0
2.8
2.6
0.38
0.36
0.34
0.32
0.30
0.28
0.26
0
1
2
3
4
5
6

Fig. 5.19

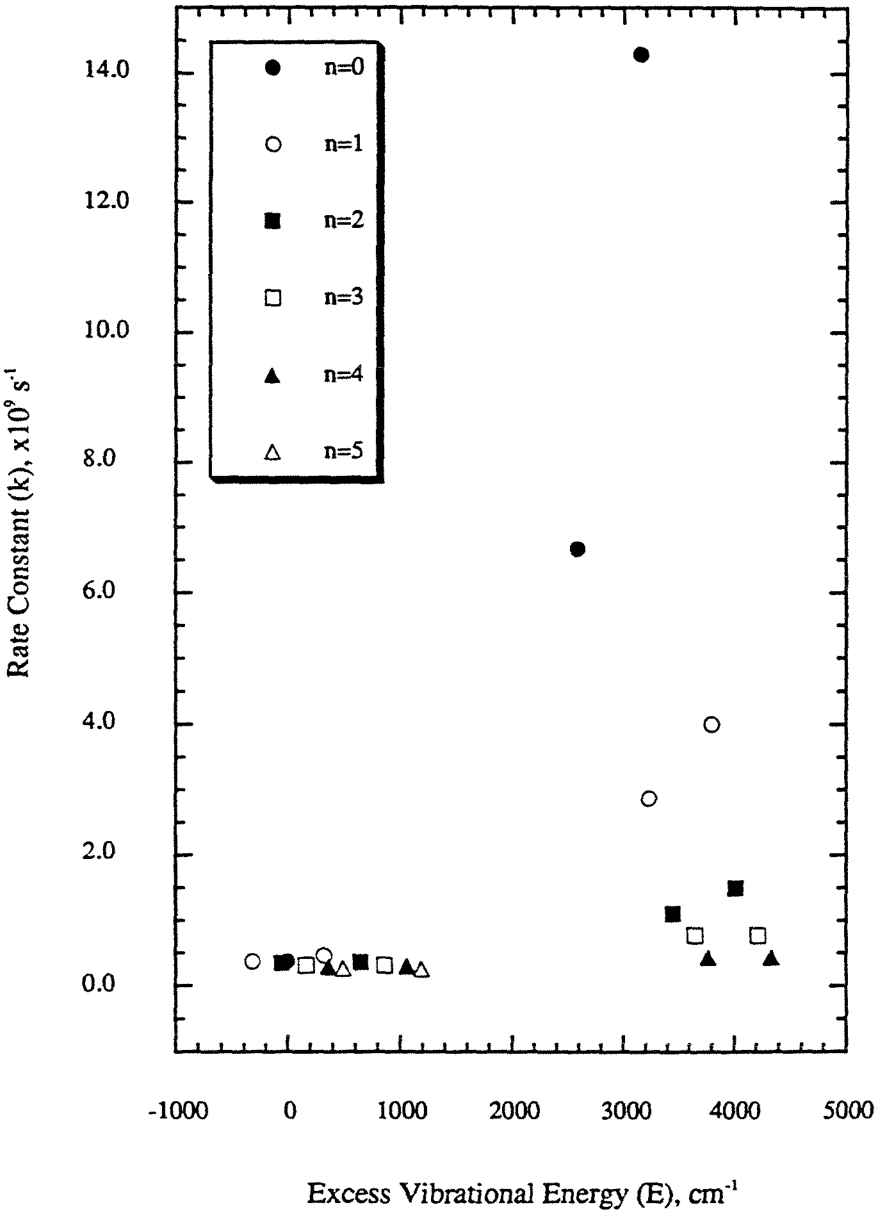
● n=0
○ n=1
■ n=2
□ n=3
▲ n=4
△ n=5
14.0
12.0
10.0
8.0
6.0
4.0
2.0
0.0
-1000
0
1000
2000
3000
4000
5000
Rate Constant (k), x10^9 s^{-1}
Excess Vibrational Energy (E), cm^{-1}

Fig. 5.20

Chapter 6

SOLVATION EFFECTS ON PICOSECOND MOLECULAR DYNAMICS (III): ISOMERIZATION REACTION IN SIZE-SELECTED *TRANS*-STILBENE-(ETHANE)$_n$ CLUSTERS

6.1 INTRODUCTION

In this chapter, we extend our investigation of solvation effects on the isomerization of *trans*-stilbene in size-selected ethane clusters. The *trans*-stilbene-(ethane)$_n$ model system has many interesting features. In particular, unlike stilbene-(hexane)$_n$ clusters, this system has a low binding energy, and the separation between the vibrational predissociation and isomerization rates should be very challenging. Furthermore, the kinetic model proposed in Chapter 5 should, in principle, account for the observed rates in the same fashion as in the stilbene-(hexane)$_n$ case. The size of the solvent molecule (relative to the solute size) and its effects on the overall isomerization dynamics could be understood by comparing the observed S_1-rates of *trans*-stilbene solvated in both hexane and ethane clusters with the jet-cooled bare *trans*-stilbene.

6.2 EXPERIMENTAL

Detailed description of the measurement technique is given in Chapter 2. The pump laser, SR640, R110, Kiton Red, and R6G were dissolved in methanol and used to cover the wavelength range of 570-630 nm. For the probe laser, DCM dye was used to generate 650 nm. Both laser beams were frequency-doubled using either a $LiIO_3$ or a KDP crystal.

To create stilbene-(ethane)$_n$ clusters in the molecular beam, *trans*-stilbene (Aldrich, 96% purity, used without further purification) was seeded into a mixture of helium and a small percentage of ethane (~5%, by volume, of ethane in helium). The backing pressure of the carrier gas was typically 30-60 psi. Ethane (Scott Specialty Gas, 99.0%) was used as purchased and the TOF mass spectra of *trans*-

stilbene-ethane clusters show the presence of water as impurities. The experimental conditions were set to maximize the signal of a size-selected cluster under study.

6.3 RESULTS AND DISCUSSION

6.3.1 Structures

Potential energy calculations were carried out to predict the most favorable structure for stilbene-(ethane)$_n$ clusters. The potential energy surface of stilbene-(ethane)$_1$ exhibits several minima, *i.e.* a number of cluster conformers are expected. At least five isomers could be identified for $n = 1$ complex. In one of the more stable configurations, the ethane molecule is displaced slightly from the phenyl ring center toward the ethylene moiety of *trans*-stilbene and inclined with respect to the plane of solute molecule, see Fig. 6.1. The binding energy of this isomer, as predicted by potential energy calculations, is ~885 cm^{-1}. However, for all other isomer, the binding energy range is 694-885 cm^{-1}, see Table (1). For stilbene-(ethane)$_2$ cluster, several possible geometries were predicted as well. The structure of stilbene-(ethane)$_2$ cluster is basically a combination of different minimum energy configurations of $n = 1$ complex, with the possibility of being localized on one or both sides of the stilbene plane. One of these geometries has an ethane molecule on each side of the stilbene molecule (see Table (1)). Another configuration involves both ethane molecules on the same side of the stilbene plane. Whenever the two ethane sites are equivalent, additive red-shift of the S$_1$-electronic origin is expected. As the cluster size increases, the number of isomers for each cluster increases. For stilbene-(ethane)$_3$ cluster, a favorable structure is that two of the ethane molecules rest on one side of the stilbene plane and the third ethane on the other side of the molecule. The site of each solvent molecule is about the same as that in stilbene-(ethane)$_1$ complex.

The above mentioned structures resemble some similarities to those predicted for toluene-(ethane)$_n$ complexes by Bernstein and coworkers [1]. The electronic origin of S_1-state in toluene molecule was red-shifted by ~50 cm^{-1} upon one-ethane complexation where only ~10 cm^{-1} red-shift was observed in toluene-(ethane)$_2$ cluster. Due to the fact that the polarizability of *trans*-stilbene is expected to be larger than that of toluene, the red-shift in stilbene S_1-origin will be larger upon ethane complexation. It will be reasonable to assume that the lower-limit for the S_1-origin red-shift, in $n = 1$ cluster, is ~50 cm^{-1} and the upper limit for that shift in stilbene-ethane$_1$ complex will be the shift observed for stilbene-hexane$_1$ complex (*i.e.* 265-380 cm^{-1} [2,3]).

6.3.2 Time-of-Flight Mass Spectrum

Using two-color resonant two photon ionization (2cR2PI), a typical time-of-flight mass spectrum (TOFMS) for *trans*-stilbene-(ethane)$_n$ clusters is shown in Fig. 6.2. This spectrum was measured using pump (probe) laser wavelength of 310 nm (327 nm). Clusters as large as $n = 8$ can be identified in the TOFMS with the most intense band for $n = 2$ mass. The excess vibrational energy depends on the red-shift of the electronic S_1-origin upon ethane complexation. The probe laser pulse was fixed at ~11 ps delay time with respect to the pump laser pulse. Figure 6.2 also shows the TOFMS with the pump laser alone (*i.e.* two pump-photon ionization) and exhibits a similar cluster-bands intensity distribution except for $n = 1$ band. It is interesting to compare the intensity of stilbene-(ethane)$_n$ band in these two cases (pump-probe and pump-pump ionization). With the two pump-photon ionization, the $n = 1$ band intensity in the TOFMS is ~30% weaker than that measured with 2cR2PI while the intensity distribution of all other cluster bands are about the same. This observation could be attributed to the fragmentation in the two pump-photon ionization case due to the large excess energy (~2387 cm^{-1}) compared with 724 cm^{-1} in 2cR2PI) above the ionization threshold (of the bare molecule). However, the difference in Franck-Condon factor in these two cases may contribute to this band intensity difference. There is no ion signal for clusters of any size in the TOFMS with two probe-photon ionization as shown in Fig. 6.2. The TOFMS was recorded under the same experimental conditions but with different delay times (11 ps to 2.45 ns) between the pump and probe laser pulses. Almost the same band-intensity distribution was observed. Due to water impurities in ethane, water complexes with stilbene and stilbene-ethane clusters were observed in the TOFMS as shown in Fig. 6.2.

6.3.3 Bare *Trans*-Stilbene

During the course of the excess-energy dependence of the rate constant in stilbene-(ethane)$_n$ clusters, similar measurements were carried out for the bare molecule for comparison (see Fig. 6.3). The only difference between these measurements and those outlined in Chapter 5 and the TCSPC results is the following. At excess-vibrational energy of ~2580 cm^{-1} in the S_1-state in *trans*-stilbene, clear biexponential transients were measured, see Fig. 6.3. These transients were recorded as a function of the delay time (DT2) between the laser pulses and the opening of the pulsed nozzle. The fast decay component ~(170 ps) match the measured fluorescence lifetime, at this excess-energy, using TCSPC technique [4-11]. The slow component is estimated to be ~2.1 ns on the average. As the gas pulse (~300 μs in width) was mapped out, the highest concentration of clusters was observed near the center of the gas pulse width (GPW), even though larger clusters were formed near the end of that pulse. The maximum of slow-to-fast amplitude ratio (a_s / a_f) (~51%) was measured near the middle of the gas pulse.

According to the kinetic model mentioned in Chapter 5, the fast component (~170 ps) represents $k_{total}^{n=0}(\sim 2580 cm^{-1})$. On the other hand, the slow component (~2.1 ns) represents $k_{total}^{n=m}(E_x^{n=m} - mD_0^{n=m})$, $m \leq 3$ where the excess-energy is large enough to dissociate at maximum three ethane molecules (see Table (1) for the calculated binding energies for stilbene-ethane$_n$ clusters).

6.3.4 Stilbene-(Ethane)$_1$ Complex

A typical transient of stilbene-(ethane)$_1$ cluster is shown in Fig. 6.5. The pump (probe) laser wavelength used for these representative transients was 310 nm (327 nm) and the time constant was estimated as 2.8 ± 0.1 ns. This time-constant is slightly longer than that measured for the bare molecule (2.67 ns) under the same experimental conditions. In comparison with hexane results, at this energy, this time constant is significantly slower than that measured for hexane clusters (Chapter 5). This transient was repeated with and without the presence of large-clusters in the molecular beam prior to the transient measurement. In our experimental error range, the same time-constant was measured under different experimental conditions at this low energy where the vibrational predissociation is unlikely. The pump-laser wavelength (310 nm) corresponds to the electronic origin of the S_1-state of the bare molecule and will be considered as our zero excess-energy point since the S_1-origin of $n = 1$ cluster is not known.

The excess-energy dependence of the S_1-state time constant (τ) of stilbene-ethane$_1$ complex was measured and is shown in Fig. 6.3. Under the same experimental conditions, similar measurements were carried out for bare *trans*-stilbene for comparison. Below E_x~800 cm^{-1} in the S_1-manifold of the bare molecule, the time constant decreases monotonically with energy and the transients fit well to a single exponential form. At E_X~800 cm^{-1} a lifetime of ~2.33 ns was measured for the $n = 1$ complex. The lifetime shows very slight or no change as the vibrational energy increases from ~800 cm^{-1} to ~1500 cm^{-1}.

In the neighborhood of ~1000 cm^{-1} excess energy in the S_1-state of bare *trans*-stilbene, the transient for stilbene-(ethane)$_1$ complex decays as a biexponential (not shown). The fast (τ_f) and slow (τ_s) decay components are 495±23 ps and 2.3±0.2 ns, respectively. The slow-to-fast amplitude ratio a_s / a_f is ~5.88. These transients were measured six times at different experimental conditions and single-exponential fit was never satisfactory. In this energy region, the measured time constant for stilbene-(ethane)$_2$ complex is ~2.75 ns which is larger than the slow component (2.3±0.2 ns) in the n=1 transient at the same energy. According to the kinetic model, developed in Chapter 5, the slow component (2.3±0.2 ns) is more likely to represent $k_{total}^{n=1}(E_x^{n=1} - D_0^2)$. Since an energy of ~800 cm^{-1} is required to dissociate one solvent molecule from $n = 2$ cluster (see Table (1)), 2.3±0.2 ns represents the time constant measured at an excess-energy of ~200 cm^{-1} in the S_1-state of the $n = 1$ complex. On the other hand, the rate of the fast decay component (2.02x10^9 s^{-1}) $\sim k_{rad}^{n=2} + k_{iso}^{n=2}(\sim 1000cm^{-1}) + k_{vp}^{n=2}(\sim 1000cm^{-1})$. The radiative rate for $n = 2$ complex is ~0.348x10^9 s^{-1} (as measured in the vicinity of the S_1-origin for the bare molecule), and therefore, $k_{iso}^{n=1} + k_{vp}^{n=1}$ ~1.67x10^9 s^{-1} at this energy. The amplitude ratio is not well defined due to the unknown portion of ion signal originated from ionic-state fragmentation. However, to the first approximation, this ratio is equal to $k_{vp}^{n=2} / k_{iso}^{n=2}$ [12]. Using the radiative rate for stilbene-(ethane)$_1$ complex, and (a_s / a_f) ~5.88, the isomerization and vibrational predissociation rates were estimated as ~0.24x10^9 s^{-1} and 1.43x10^9 s^{-1}, respectively. These rates suggest that, the vibrational predissociation is taking place on a time scale much shorter than that for the isomerization reaction to occur.

Similar behavior (*i.e.* a biexponential transient) was observed at an excess-energy of ~1500 cm^{-1}, and the fast decay component (~147 ps) is ~3.4 times faster than that measured at S_1(t-S)+1000 cm^{-1} (~495 ps) mentioned above. Meanwhile, the slow decay component is ~2.4 ns and the amplitude ratio a_s / a_f ~4.0. Using the same approach outlined above, the isomerization and vibrational predissociation rate constants are ~1.29x10^9 s^{-1} and 5.16x10^9 s^{-1}, respectively. Even though the energy red-shift of the S_1-state origin in stilbene-(ethane)$_1$ complex is not accounted for, this isomerization rate is slower than that for bare *trans*-stilbene at the same excess energy.

Above E_X~2000 cm^{-1}, a slight decrease in the lifetime was observed and a single exponential fit was adequate (see Fig. 6.6. The shortest lifetime (~2.1 ns) was measured at excess energy of ~3150 cm^{-1} (in the S_1-state of the bare molecule). This time is much longer compared to 467 ps measured for stilbene-(hexane)$_1$ complex at approximately the same excess energy.

6.3.5 Stilbene-(Ethane)$_2$ Complex

Under the same experimental conditions (mentioned above), similar excess-energy dependent measurements of the S_1-state lifetime (τ) in stilbene-ethane$_2$ complex were carried out, see Fig. 6.3 and 6.5. Following the excitation by a 310 nm photon, the time constant of 2.9 ± 0.1 ns was measured using 327 nm probe laser. This time constant is ~8% less than that measured for stilbene-hexane$_2$ complex at excess-energy of ~150 cm^{-1} (~3.1 ns). As the excess-energy increases, the time constant decreases slowly. All the measured transients for *n*=2 complex fit nicely to a single exponential form at any excess-energy in the range 0.0-3150 cm^{-1} in the S_1(t-S)-state.

At 3150 cm^{-1} above the S_1-origin in bare *trans*-stilbene, τ ~93 ps was measured for the bare molecule in comparison with ~2.22 ns for stilbene-ethane$_2$ complex. This time constant is much slower than the measured one in hexane cluster (~667 ps) of the same size (n = 2). Considering the excess-energy dependence of the time constant in n=2 complex, the energy difference due to the red-shift of the S_1-origin in both complexes is unlikely to account for the large decrease in the decay time upon hexane complexation. However, since the binding energy is approximately 876 cm^{-1}, the vibrational predissociation of stilbene-(ethane)$_2$ complex must be considered at high excess energy. In fact, the evaporation of more than one ethane molecule might be possible, at least energetically. According to the kinetic model, the detected ion signal at stilbene-(ethane)$_2$ mass could be created from the stilbene-(ethane)$_3$ dissociation. In this case, the above measured rate (0.45×10^9 s^{-1}) represent the rate of the nascent stilbene-(ethane)$_2$ complex at excess energy of approximately (3150 - 867xm) cm^{-1}, m is equal to the number of evaporated ethane molecules. According to our potential energy calculations, 3150 cm^{-1} excess energy is large enough to dissociate at least 3 ethane molecules in stilbene-(ethane)$_5$ leaving n = 2 complex with excess-energy of ~ 550 cm^{-1}.

6.3.6 Cluster-Size Dependence of the Rate Constant

In the vicinity of the electronic origin of 0_0^0-transition in bare stilbene (310 nm), cluster-size dependence of the time constant (τ) was studied. Representative transients for stilbene-(ethane)$_n$ (n = 0 - 5) were measured using 310 nm/327 nm and shown in Fig. 6.5. As the cluster-size increases, the time constant increases, see Table (2), Fig. 6.7, and Fig. 6.8. With the short delay-time range in these experiments and the excellent signal-to-noise, each one of these transients fit as a single exponential. The time constant increases from 2.76±0.04 ns to 3.4±0.1 ns as the cluster-size changes from $n = 1$ to $n = 5$. These measurements are reproducible within our experimental error range (~10%).

Similar measurements were conducted at higher energies in the S_1 state of stilbene-ethane$_n$ clusters of different sizes, typically, 2000, 2580 and 3150 cm^{-1} above the S_1-electronic origin of bare *trans*-stilbene, see Fig. 6.7, Fig. 6.8 and Table (2). The probe-laser wavelength (327 nm) was selected as far to the red as possible.

6.3.7 Stilbene Isomerization in Compressed Ethane-Gas

The isomerization rate of *trans*-stilbene as a function of collision frequency in ethane (at 350 K and the pressure < 120 atm) has been reported [13]. Three different regions were identified: rise, plateau, and decline of the isomerization rate with increasing friction. These observations are in quanlitative accord with Kramers' predicition. In the first region, the isomerization rate increases as the friction (or collision frequency) increases. Fleming and coworkers [14,15] and Troe and coworkers [16,17] reported similar observations. Schroeder *et al.* [17] extended these studies over a wide range of friction in different alkane solvents with an estimate of ~1.5-2.0 kcal/mol for the isomerization barrier. Furthermore, the turnover region of the isomerization rate shifts (along the friction axis) with the change of the solvent. It was argued that the observed shift is due to the modification of the potential energy surface upon cluster formation with the solvent [16,18].

Zewail and coworkers [4-6], and Negri and Orlandi [19] suggested that the acceleration of the isomerization rate in solvated *trans*-stilbene can be attributed to the reduction of the nonadiabaticity of the reaction due to the solvent (because more time is spent near the curve crossing) leading to higher rates. Restricted IVR in the gas phase and isolated molecule, and its role in reducing the isomerization rate, was also considered [20,21].

The time (rate) constant, at high energies (higher than the calculated binding energies), changes slowly with the excess-energy compared with that in *trans*-stilbene-hexane clusters (see Chapter 5). Furthermore, the cluster fragmentation is a serious problem in ethane clusters which stands in the way for investigating the isomerization rate at high excess-energies. Consequently, an enlightening comparison with either bare trans-stilbene, stilbene-hexane clusters, or high-pressure ethane gas studies will be hard to make. However, the value of ethane cluster results rests in showing how will a cluster with low-binding energy will be monitored by a pump/probe time-of-flight experimental technique like ours (especially if excited to higher excess-energies above its dissociation energy). Meanwhile, these observations are consistent with our understanding of stilbene-hexane cluster results which are invaluable.

6.4 CONCLUSION

Excess-energy dependence of the rate constant in *trans*-stilbene solvated in size-selected ethane clusters have been studied using two-color resonant two photon ionization and time-of-flight mass spectrometry techniques. The vibrational predissociation rate in stilbene-(ethane)$_n$ clusters is much faster than the isomerization rate, especially at excess energies higher than the dissociation threshold of these clusters. This is due to the low binding energy of stilbene-(ethane)$_n$ clusters compared with stilbene-(hexane)$_n$ clusters. Consequently, the isomerization dynamics could be studied up to ~900 cm^{-1} of excess-energy in the S$_1$-state manifold of these clusters (where the electronic origin is not known).

Table (1): The binding energy for the minimum-energy structures for *trans*-stilbene-(ethane)$_n$ clusters

Number of Solvent Molecules *(n)*	Isomer *	Binding Energy (D_e) cm^{-1}
1	A	-885.4
	B	-873.9
	C	-865.8
	D	-837.6
	E	-694.3
2	(C+C : 0)	-2040.6
	(B+E : 0)	-1818.2
	(A : A)$_S$	-1786.7
	(A : B)$_S$	-1774.9
	(B : B)$_S$	-1763.3
	(C : B)$_S$	-1754.7
	(C : C)$_S$	-1747.4
	(C : B)$_O$	-1747.3
	(B : D)$_S$	-1725.4
	(E : E)$_S$	-1399.0

* The subscript (s) and (o) means that the solvent molecules are on the same phenyl ring of the bare *trans*-stilbene or on opposit ones, respectively.

In stilbene-(ethane)$_2$ complex, either both ethane molecules can be on the same side of the stilbene plane (A+B : 0), or one solvent molecule on one side and the second on the other side (A : B).

Table (2): The time-constant measurements for the S_1-state of stilbene-(ethane)$_n$ clusters as a function of cluster size *(n)* and the pump/probe laser wavelengths.

Pump/Probe Wavelength (nm)	Cluster size (n)					
	n=0	n=1	n=2	n=3	n=4	n=5
310.1/326.7	2.65	2.7	2.9	3.0	3.2	3.4
292.0/327.0	0.29	2.2	2.3	2.5	2.8	3.0
287.3/327.0	0.14	2.1	2.2	2.3	2.6	2.7
282.5/327.0	0.09	1.95	2.2	2.3	2.5	2.8

6.5 REFERENCES

1. E. R. Bernstein, in: *Atomic and Molecular Clusters* (Plenum, New York, 1990) p 551.
2. C. Lienau, A. A. Heikal, and A. H. Zewail, *Chem. Phys.* **175**, 171 (1993).
3. C. Lienau, Ph. D. Dissertation, Gottingen (1992).
4. J. A. Syage, P. M. Felker, and A. H. Zewail, *J. Chem. Phys.* **81**, 4706 (1984).
5. P. M. Felker and A. H. Zewail, *J. Phys. Chem.* **89,** 5402 (1985).
6. J. A. Syage, W. R. Lambert, P. M. Felker, A. H. Zewail, and R. M. Hochstrasser, *Chem. Phys. Lett.* **88**, 266 (1982).
7. J. Troe and J. Schroeder, *J. Phys. Chem.* **90**, 4215 (1986).
8. J. Troe, *Chem. Phys. Lett.* **114**, 241 (1985).
9. T. J. Majors, U. Even, and J. Jortner, *J. Chem. Phys.*, **81**, 2330 (1984).
10. A. Amirav and J. Jortner, *Chem. Phys. Lett.* **95**, 295 (1983).
11. L. Bañares, A. A. Heikal, and A. H. Zewail, *J. Phys. Chem.* **96**, 4127 (1992).
12. A. A. Heikal, S. H. Chong, J. S. Baskin, and A. H. Zewail, Submitted to *Chem. Phys. Lett.* (1995).
13. M. Lee, G. R. Holtom, and R. M. Hochstrasser, *Chem. Phys. Lett.* **118**, 359 (1985).
14. S. H. Courtney and G. R. Fleming, *Chem. Phys. Lett.* **103**, 443 (1984).
15. S. H. Courtney and G. R. Fleming, *J. Chem. Phys.* **83**, 215 (1985).
16. G. Maneke, J. Schroeder, J. Troe, and F. Voss, *Ber. Bunsen-Ges. Phys. Chem.* **89**, 896 (1985).

17. J. Schroeder, D. Schwarzer, J. Troe, and F. Voss, *J. Chem. Phys.* **93**, 2393 (1990).

18. J. Schroeder and J. Troe, *Chem. Phys. Lett.* **116**, 453 (1985).

19. F. Negri and G. Orlandi, *J. Phys. Chem.* **95**, 748 (1981).

20. S. H. Courtney, M. W. Balk, L. A. Philips, S. P. Webb, D. Yang, D. H. Levy, and G. R. Fleming, *J. Chem. Phys.* **89**, 6697 (1988).

21. S. Nordholm, *Chem. Phys.* **137**, 109 (1989).

6.6 Figure Captions

6.1 Schematic diagram for the minimum-energy structure of stilbene-(ethane)$_1$ complex (top view). Different isomers were predicted by the potential energy calculations and labeled as A, B, C, D, and E in the figure. Isomer A and B have the most stable configuration compared with the others. The binding energy for each configuration is listed in Table (1). The intramolecular distance between the solute and solvent molecular plane is ~3.8±0.2 Å.

6.2 Time of flight mass spectra of stilbene-(ethane)$_n$ clusters using 310 nm (pump) and 327 nm (probe) lasers (bottom). The spectrum was recorded using one-color resonant two photon ionization, 2x310 nm (middle) and 2x327 nm (top). The ion signal in the three spectra was normalized to the maximum peak for $n = 3$ in 2cR2PI experiment (bottom). The small peaks are water complexes with stilbene and stilbene-(ethane)$_n$. The spectra were recorded under the following molecular beam conditions: backing pressure *(P)* = 40 psi, sample temperature *(T)* = 88 °C, and repetition rate *(RR)* = 90 Hz.

6.3 Typical transients for stilbene-(ethane)$_n$ clusters measured with 310.1 nm (pump) and 326.6 nm (probe) wavelengths. The cluster-size and the estimated decay time for each transient is also shown. These transients were recorded under the following experimental conditions: Backing pressure of helium (mixed with ~6% ethane) *(P)* = 4 0 psi, sample temperature *(T)* = 88 °C, and the boxcar gate width *(BGW)* = 60 ns.

6.4 Another set of representative transients for stilbene-(ethane)$_n$ clusters measured with 287.2 nm (pump) and 326.6 nm (probe) wavelengths. The cluster-size and the estimated decay time for each transient is also shown. These transients were recorded under the following experimental conditions: Backing pressure of helium (mixed with ~6% ethane)*(P)* = 40 psi, sample temperature *(T)* = 88 °C, and the boxcar gate width *(BGW)* = 60 ns.

6.5 The excess-energy dependence of the time constant in bare *trans*-stilbene, and stilbene-(ethane)$_n$, $n = 1$, and 2 clusters. The zero-excess energy corresponds to the S_1-origin in the bare molecule. These measurements were carried out under similar experimental conditions mentioned for Fig. 6.4.

6.6 Transients for the bare *trans*-stilbene excited to ~2580 cm^{-1} above the S_1-state origin as a function of the delay time (DT2) between the laser pulses and the opening of the pulsed nozzle. Notice the change in the time constant of the slow component (shown in the upper-left side of each transient) as DT2 changes.

6.7 Cluster-size and excess-energy dependence of the time constant in *trans*-stilbene-(ethane)$_n$ clusters. The zero-point for the excess-energies shown in the figure is the S_1-state origin of the bare molecule.

6.8 Cluster-size and excess-energy dependence of the time constant in trans-stilbene-(ethane)$_n$ clusters. The rate of bare *trans*-stilbene, at high excess-energies, is disregarded due to its large value compared to rates for $n \geq 1$ clusters. The zero-point for the excess-energies shown in the figure is the S_1-state origin of the bare molecule.

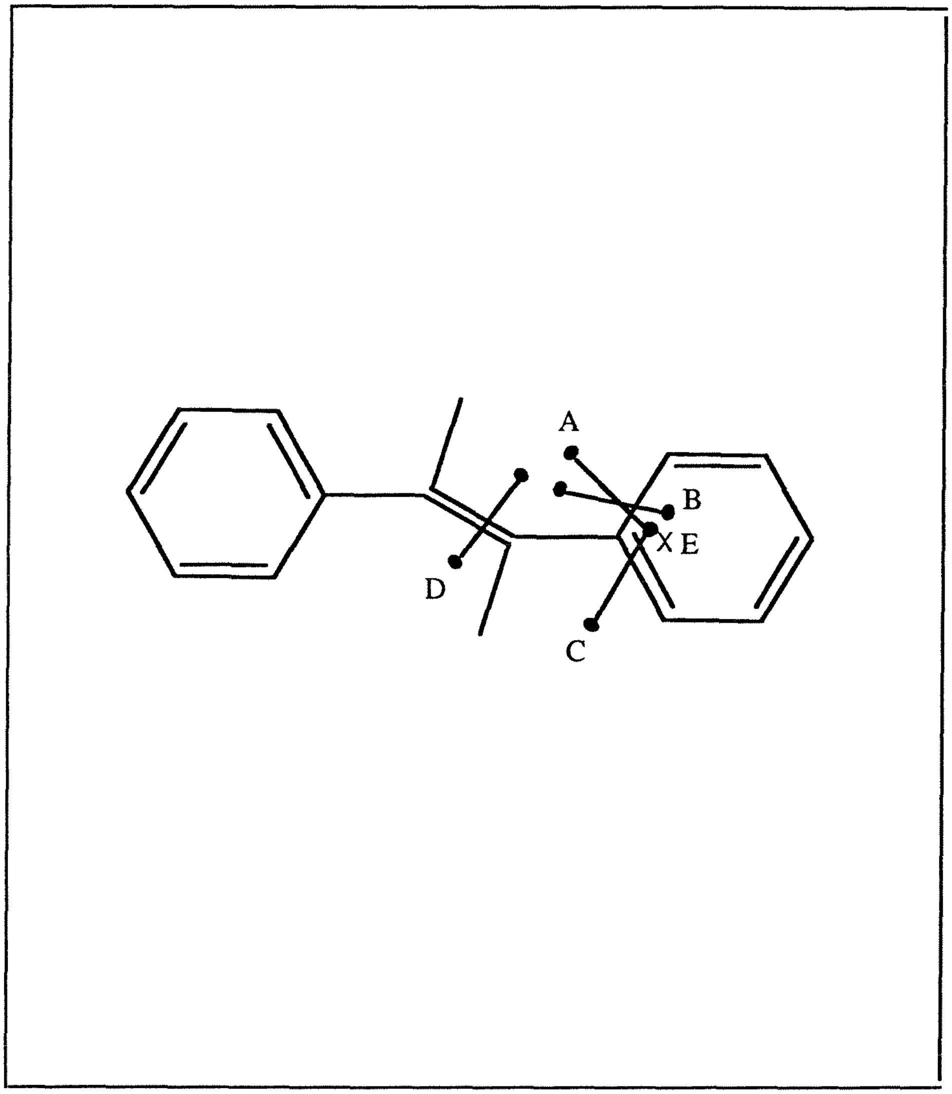

Fig. 6.1

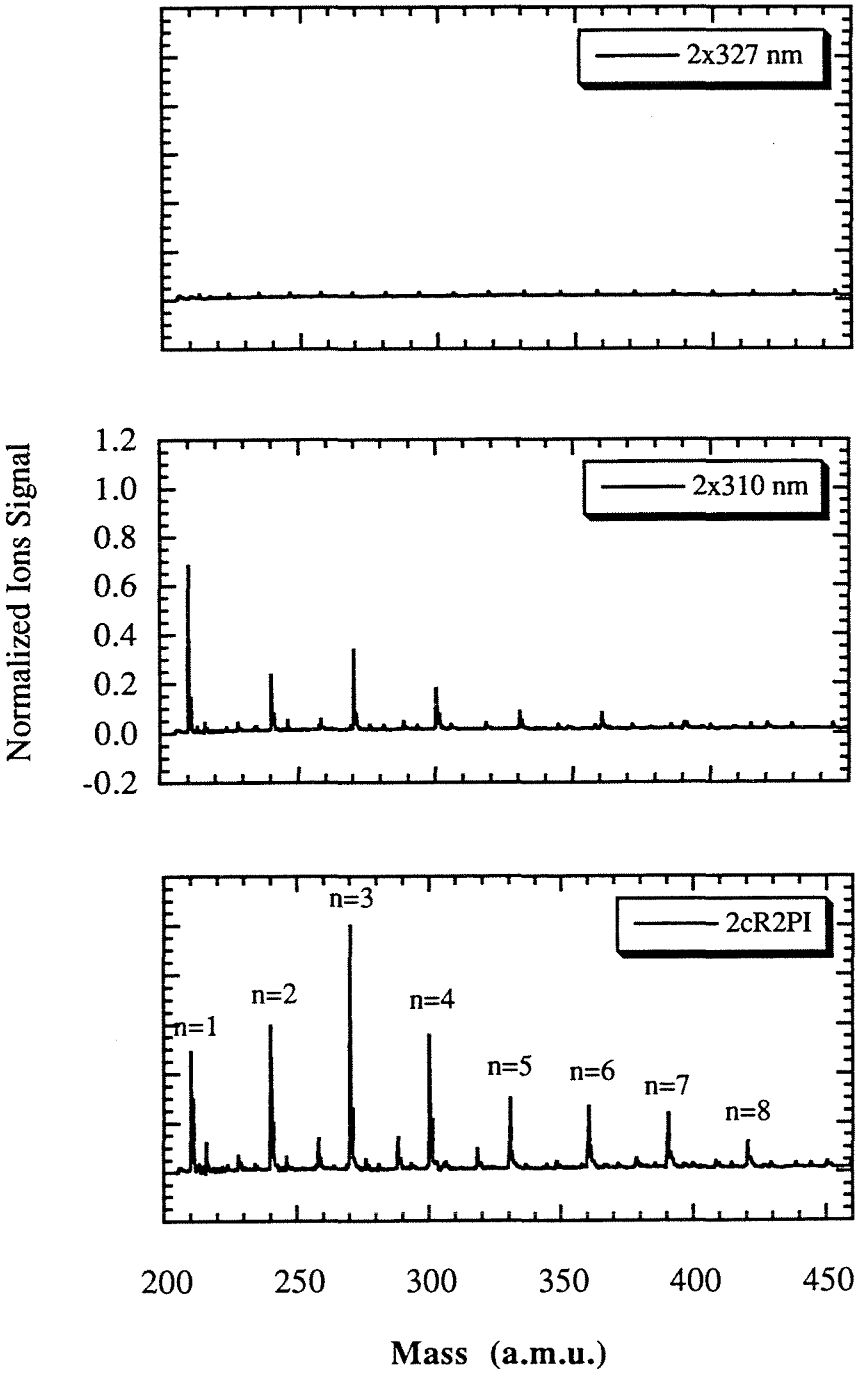
2x327 nm
Normalized Ions Signal
1.2
1.0
0.8
0.6
0.4
0.2
0.0
-0.2
2x310 nm
2cR2PI
n=1
n=2
n=3
n=4
n=5
n=6
n=7
n=8
200
250
300
350
400
450
Mass (a.m.u.)

Fig. 6.2

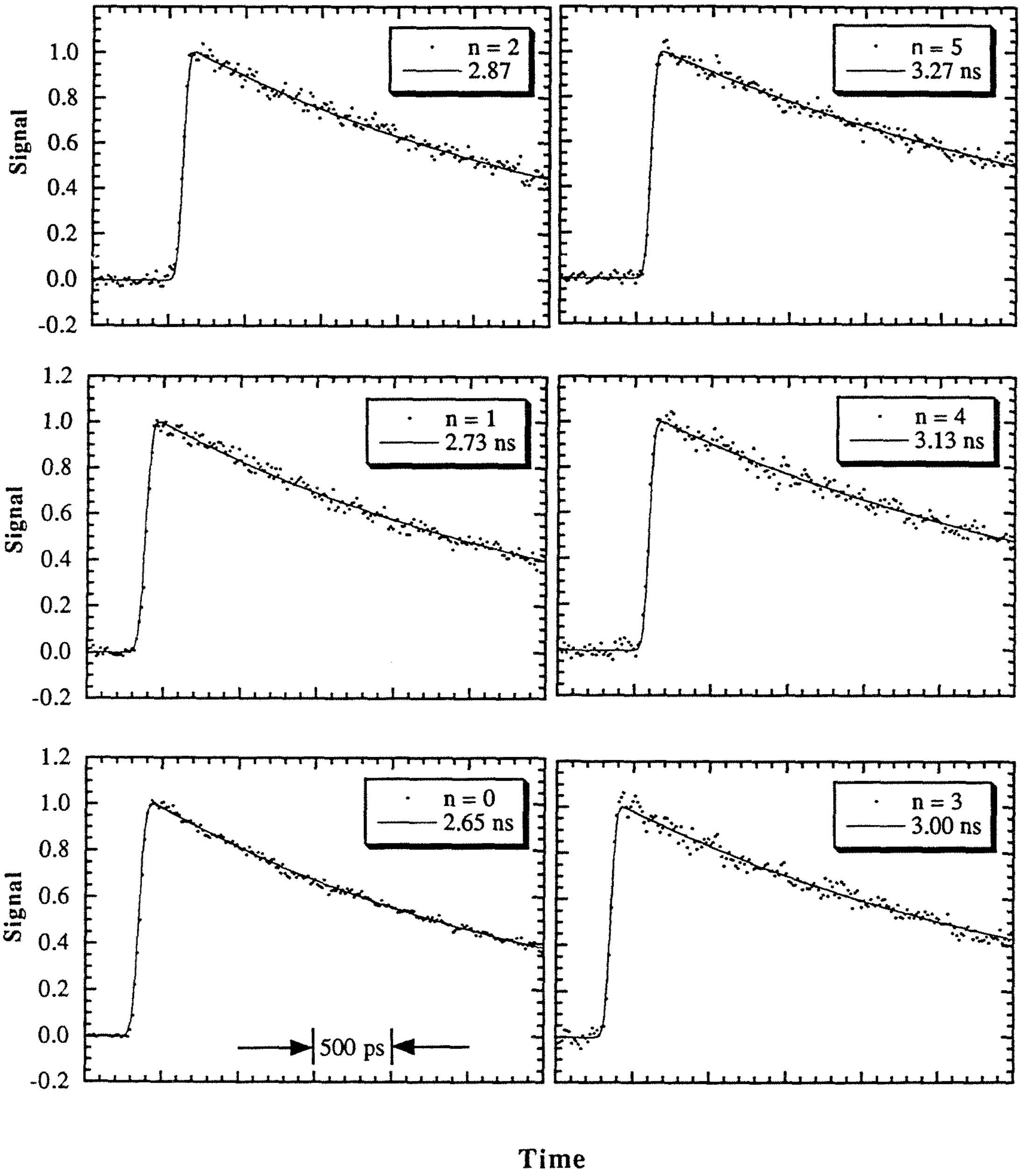
Signal
Time
1.2
1.0
0.8
0.6
0.4
0.2
0.0
-0.2
n = 2
2.87
n = 5
3.27 ns
n = 1
2.73 ns
n = 4
3.13 ns
n = 0
2.65 ns
n = 3
3.00 ns
500 ps

Fig. 6.3

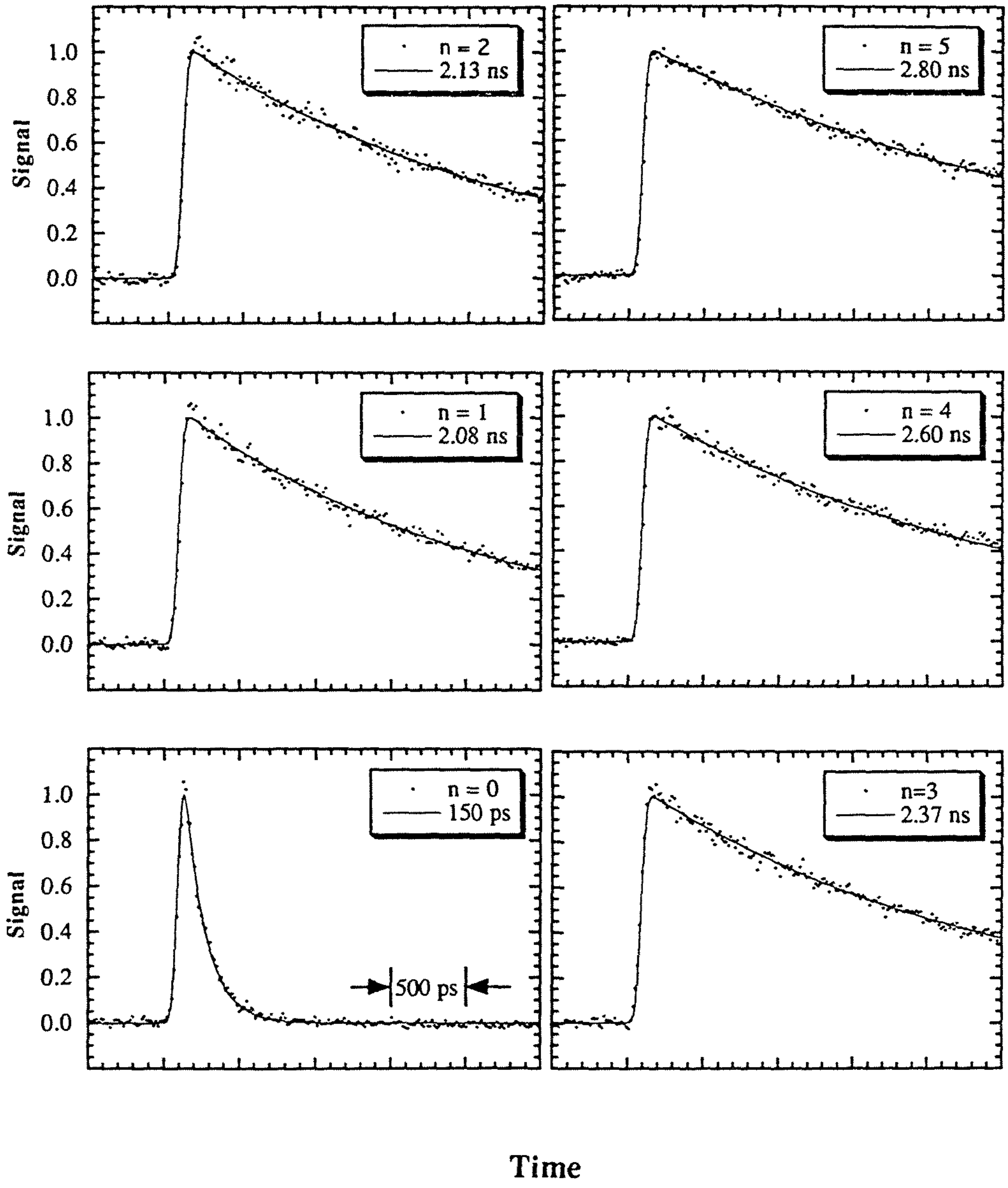
Signal
1.0
0.8
0.6
0.4
0.2
0.0
n = 2
2.13 ns
n = 5
2.80 ns
n = 1
2.08 ns
n = 4
2.60 ns
n = 0
150 ps
500 ps
n=3
2.37 ns
Time

Fig. 6.4

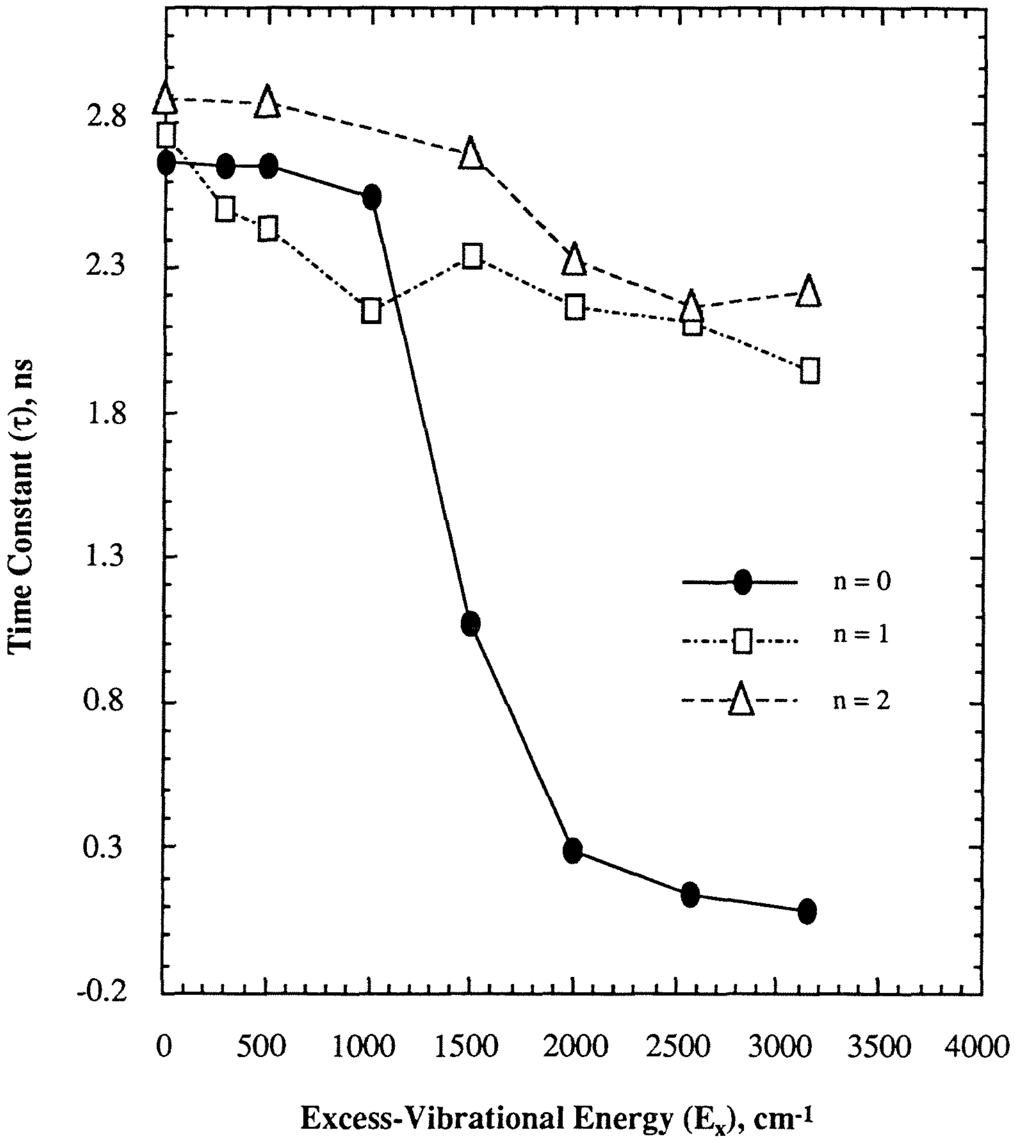
Time Constant (τ), ns
2.8
2.3
1.8
1.3
0.8
0.3
-0.2
0
500
1000
1500
2000
2500
3000
3500
4000
Excess-Vibrational Energy (E_x), cm-1
n = 0
n = 1
n = 2

Fig. 6.5

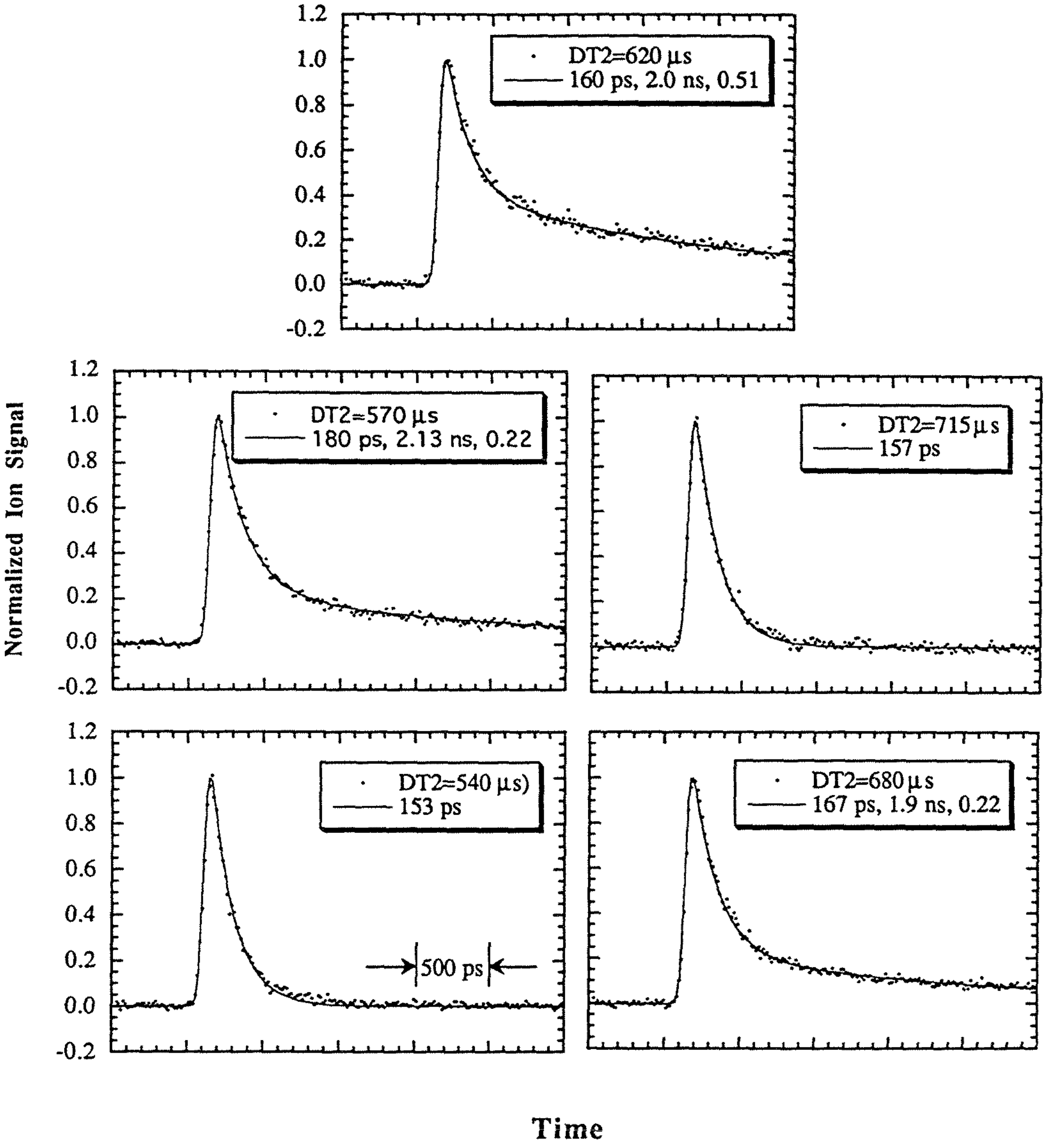
1.2
1.0
0.8
0.6
0.4
0.2
0.0
-0.2
DT2=620 µs
160 ps, 2.0 ns, 0.51
DT2=570 µs
180 ps, 2.13 ns, 0.22
DT2=715 µs
157 ps
DT2=540 µs)
153 ps
500 ps
DT2=680 µs
167 ps, 1.9 ns, 0.22
Normalized Ion Signal
Time

Fig. 6.6

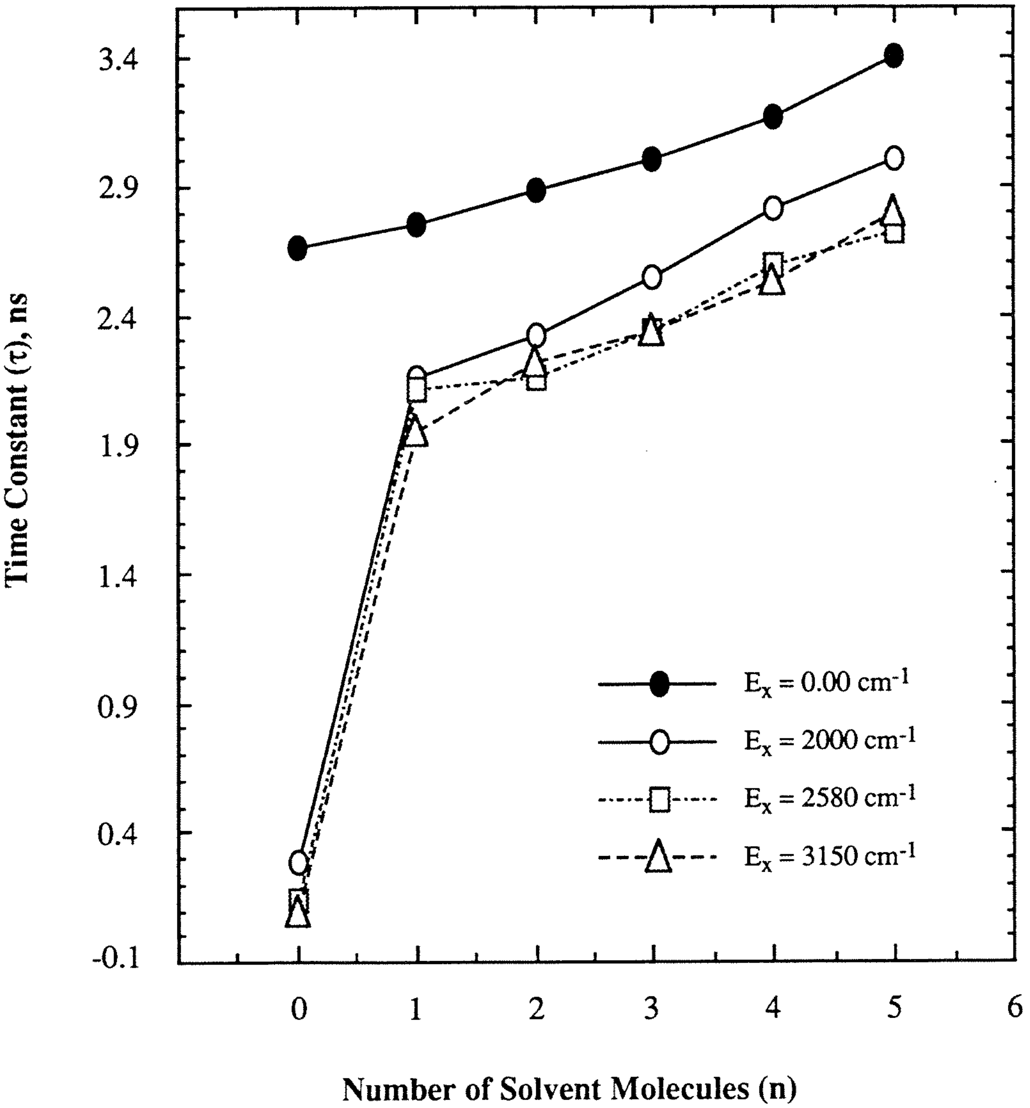
Time Constant (τ), ns
3.4
2.9
2.4
1.9
1.4
0.9
0.4
-0.1
0
1
2
3
4
5
6
Number of Solvent Molecules (n)
$E_x = 0.00\ cm^{-1}$
$E_x = 2000\ cm^{-1}$
$E_x = 2580\ cm^{-1}$
$E_x = 3150\ cm^{-1}$

Fig. 6.7

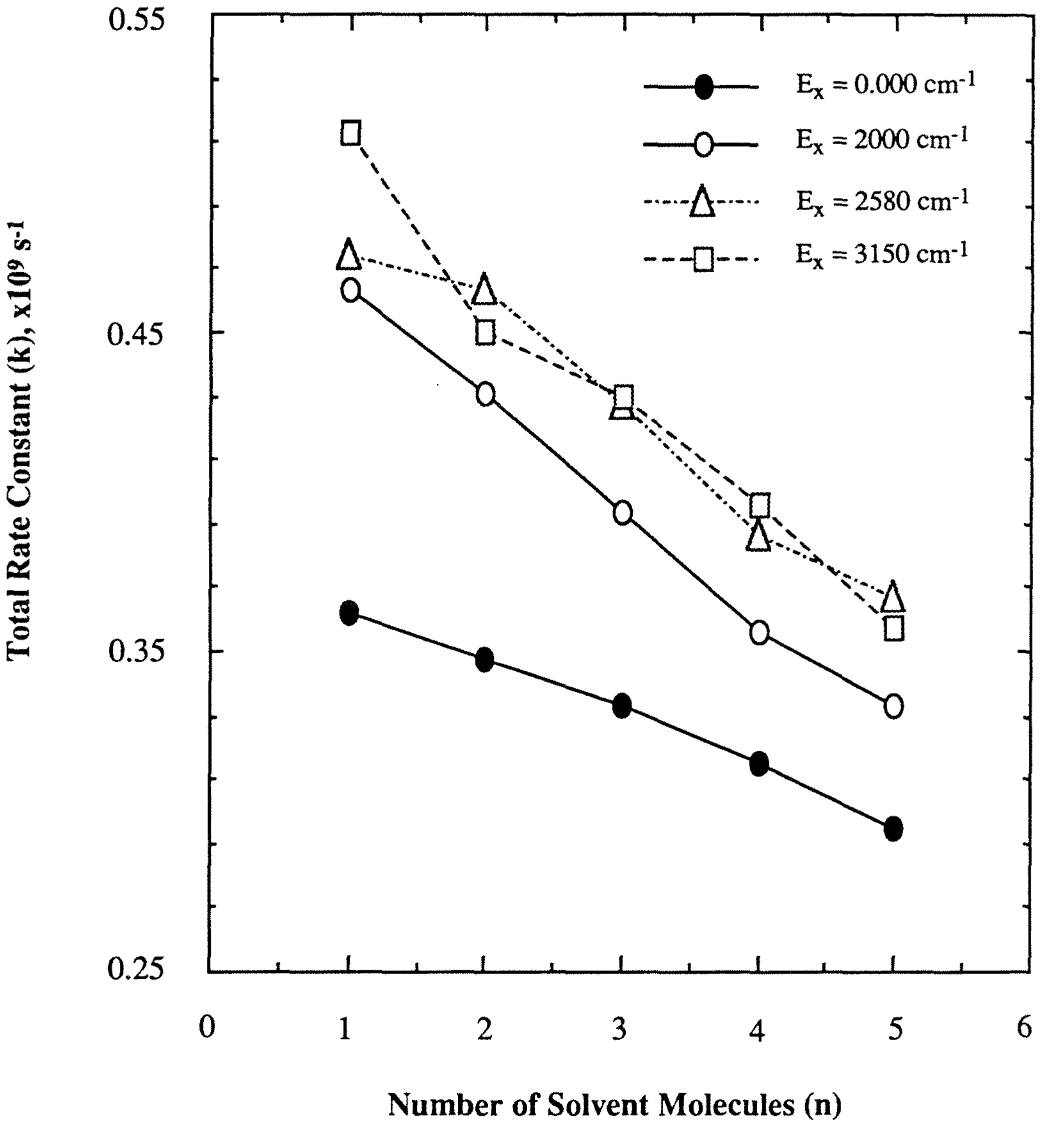
Total Rate Constant (k), x10⁹ s⁻¹
0.55
0.45
0.35
0.25
0
1
2
3
4
5
6
Number of Solvent Molecules (n)
Ex = 0.000 cm-1
Ex = 2000 cm-1
Ex = 2580 cm-1
Ex = 3150 cm-1

Fig. 6.8

PART TWO

Chapter 7

STRUCTURAL EFFECTS ON PICOSECOND MOLECULAR DYNAMICS (I): IVR IN SUBSTITUTED *TRANS*-STILBENES

Portions of this chapter are taken from the following published communication: "Ultrafast Dynamics of Isomerization Reactions: Structural Effects in Stilbene(s)," by L. Bañares, A. A. Heikal, and A. H. Zewail, *J. Phys. Chem.* 96, 4128 (1992).

7.1 INTRODUCTION

A corner stone in the photoisomerization reaction dynamics in isolated *trans*-stilbene is the intramolecular vibrational energy redistribution (IVR). The nonradiative rate increases smoothly as the energy increases above the isomerization barrier (~1250 cm^{-1}) in the S_1-state of jet-cooled *trans*-stilbene [1-4]. Furthermore, the $S_1 \leftarrow S_0$ absorption spectrum is congested. These observations indicate that the reaction rate is not mode specific due to an efficient IVR. However, the effects of IVR on the isomerization rate in the isolated molecule is still an open question concerning whether or not all vibrational modes are involved in IVR dynamics.

The RRKM calculations by Khundkar *et al.* [5] reveal that the experimental nonradiative rate values are lower by about an order of magnitude than the calculated rates. A reverse crossing of the barrier was suggested [1-3,6]. However, an optimized RRKM calculations by Troe and coworkers [7-13] account qualitatively for the isomerization rate and provide a necessary but by no means sufficient evidence for full energy redistribution among all vibrational modes in the jet-cooled *trans*-stilbene.

An alternative approach to elucidate the role of IVR in the isomerization dynamics is to study the effects of the total number of vibrational degrees of freedom on IVR dynamics in substituted *trans*-stilbene. Functional groups could be used as substituents to vary the vibrational space in the parent molecule. Majors *et al.* [14] studied the isomerization reaction in asymmetrically para-substituted *trans*-stilbenes cooled in supersonic-jet. 4-Chloro-stilbene (4CS) and 4-methyl-stilbene (4MeS) were used as model systems. The energy dependence of the nonradiative rate-constant in 4CS and 4MeS reveal that there is *no difference* in the isomerization barrier-height compared with the parent molecule. Furthermore, the isomerization rate in chlorine and methyl *p*-substituted stilbene is the same as that in *trans*-stilbene. This invariance of the isomerization rate has been attributed to *undemocratic* IVR in which all the vibrational modes are not involved [14]. In a similar attempt, Rademann *et.al.* [15] have re-examined the role of IVR in the overall isomerization dynamics of substituted *trans*-stilbene using different functional groups (typically, ethyl and *n*-propyl groups) in the para position of the phenyl moiety. An acceleration of the isomerization rate was observed in both 4-ethylstilbene (4ES) and 4-*n*-propylstilbene (4PS) molecules. Furthermore, the isomerization barrier-height in *trans*-stilbene (1300±50 cm^{-1}) decreases upon 4-ethyl (1100±100 cm^{-1}) and 4-propyl (1000±100 cm^{-1}) substitutions. The general arguments based on the role of IVR and the implications of statistical theories (*e.g.* RRKM theory) suggest that the isomerization rate should be retarded in those substituted stilbenes [15,13]. However, this argument contradicts the experimental observations by both Majors *et al.* [14] and Rademann *et al.* [15].

Herein, time- and frequency-resolved fluorescence measurements, as a function of the excess-vibrational energy in the S_1-state, of a designed set of jet-cooled substituted stilbenes are presented. 4-Methoxy-*trans*-stilbene (MS), 4,4'-dimethoxy-*trans*-stilbene (DMS), and 2-phenylindene (PI) are used as model systems for these studies. The role of symmetry, number of low-frequency modes, and the molecular rigidity in IVR dynamics in these molecules are studied. To isolate the structural effects on IVR, a comparison with IVR in the unsubstituted *trans*-stilbene was made.

This chapter is arranged as follow: The experimental set-up and the data-analysis technique are described in section (7.2) followed by the results and discussion presented in section (7.3). The conclusion and references are outlined in sections (7.4) and (7.5), respectively.

7.2 EXPERIMENTAL

Picosecond-laser induced fluorescence and time-correlated single photon counting were utilized to carry out the time- and frequency-resolved fluorescence measurements presented in this chapter. The dye solutions were prepared using DCM (1.5×10^{-3} M solution in a 3:2 (volume) mixture of ethylene glycol and benzyl alcohol), R6G, and R110 (both 2×10^{-3} M in ethylene glycol). For the frequency doubling, angle-tuned and appropriately cut 1 cm thick $LiIO_3$ (type I) and KDP (type I) crystals were used. *Trans*-stilbene (Aldrich, 96%), 4-methoxy-*trans*-stilbene (Parish) and 4,4'-dimethoxy-*trans*-stilbene (Aldrich, 97%) were used without further purification. 2-Phenylindene was synthesized following the method described by Greifenstein *et al.* [16]. NMR plus mass spectra were taken to test the purity of the synthesized compound and the results are in agreement with those of ref. [17]. The backing pressures of the carrier gas (helium) were typically in the range of 50-80 psi.

The vibrational levels in the S_1 electronic state in stilbene derivatives were localized by a manual scanning of the dye laser. During the scanning, the monochromator slit was completely open and the detection wavelength was fixed far to the red of the excitation-laser wavelength. In this way, the reddest excitation band was considered to be the electronic origin of the $S_1 \leftarrow S_0$ transition. Excitation bands with more than ~10% intensity relative to the 0_0^0 band were considered, specially in the region where the excitation spectrum shows sharp features. At higher energy (the continuum regime), the excitation wavelengths were selected randomly.

7.3 RESULTS AND DISCUSSION

7.3.1 Fluorescence Excitation Spectra

7.3.1.1 4-Methoxystilbene

The fluorescence excitation spectrum of jet-cooled 4-methoxystilbene has been reported recently by Siewert and Spangler [18]. Two planar conformers with *syn* (A-conformer) and *anti* (B-conformer) CH_3 group with respect to the $C_e{=}C_e$ double bond were identified (see Fig. 7.1 and Table (1)). The electronic origin of the $S_1 \leftarrow S_0$ transition in both conformers (A: 30744.1 cm^{-1}, and B: 31022.6 cm^{-1}) is separated by 278.5 cm^{-1}. The observed energy difference for the excited state in these isomers is greater than the calculated one for the ground state. This difference was attributed to greater π-electron delocalization in the S_1-state which, in turn, allows stronger interaction between the ethylene moiety, remote phenyl ring, and the methoxy substituent. The red-shifted origin of isomer (A) probably belongs to the conformer that is the better electron donor [18]. Furthermore, a higher υ_{37} ring torsion frequency (which is sensitive to the C_e-C_{ph} bond order) for the isomer (A) supports this reasoning. Further investigation of this issue was addressed by studying the spectroscopy of 4-methoxy-4'-methyl-*trans*-stilbene [18].

As mentioned before, the S_1-origin is located at 32234.7 cm^{-1} in *trans*-stilbene [1,2,19]. Many of the low-frequency bands were assigned by analogy to those in *trans*-stilbene. The comparison between the spectra of these two conformers reveals differences in the frequencies of the stilbene-type modes (*e.g.* υ_{36}, υ_{37}, υ_{25}, and υ_{24}), see ref. [18]. The red-shift of the 0^0_0 transition is quite large in comparison with that introduced by *p*-methyl, *p*-ethyl, *p*-propyl and *p*-chlorine mono-substitutions in *trans*-stilbene [14,15]. The large induced-stabilization in the S_1-electronic state of *trans*-stilbene upon mono-methoxy *p*-substitution can be attributed to the electron-donating capability of OCH_3 against methyl, ethyl, propyl and chlorine.

Topp and coworker [20] have also identified the same two conformers using rotational coherence spectroscopy. The measured rotational constant for A and B conformers were estimated as 334.4±0.3 and 329.8±0.3 MHz, respectively, which agrees with the assignment of Siewert and Spangler [18] (see Fig. 7.1).

In preliminary work on the MS molecule, Cable [21] has recorded the fluorescence excitation spectrum up to ~1900 cm^{-1} above the S_1-origin. The spectral congestion can be identified in the spectrum at excess-energy of ~650 cm^{-1} above the S_1-state origin. This energy can be considered as the threshold for IVR. No sharp vibrational bands were recorded above S_1+1360 cm^{-1}.

7.3.1.2 4,4'-Dimethoxystilbene

Two isomers were identified for jet-cooled 4,4'-dimethoxybenzene using one- and two-photon absorption spectra [22]. The relative orientation of the CH_3 is the main difference in the configuration of both isomers. In the *trans* (*cis*) conformer, the methyl groups are on opposite (same) side of the molecular axis. The electronic origin of the S_1-state in the *trans* and *cis* isomers is located at 33631 cm^{-1} and 33851 cm^{-1} respectively (*i.e.* 220 cm^{-1} shift, see table (1)). The cis-isomer is more stable than the *trans* one in the S_0 state.

The electronic origin of the $S_1 \leftarrow S_0$ transition in jet-cooled DMS is located at 29987.0 cm^{-1} which is 2247.7 cm^{-1} to the red of that in *trans*-stilbene. In comparison with MS (A: 1490.6 cm^{-1}, B: 1211.1 cm^{-1}), the observed red-shift in DMS is not additive and can be attributed to conformation differences of the CH_3 orientation (as in *p*-dimethoxybenzene [22]). Unfortunately, the fluorescence excitation spectrum of DMS and a complete assignment of the vibrational bands in the S_1-state are not available yet. However, Cable [21] recorded the excitation spectrum of DMS without vibrational assignment. The preliminary results show that the spectrum is congested above an excess energy of ~360 cm^{-1} in the S$_1$-state. The Franck-Condon factor of the 0_0^0-transition is less than that of most of the vibronic levels at higher energies. Furthermore, a progression of ~180 cm^{-1} could be distinguished.

7.3.1.3 2-Phenylindene

The electronic 0_0^0 transition in 2-phenylindene (31406.3 cm^{-1}) is shifted by ~828.4 cm^{-1} to the red with respect to that of *trans*-stilbene [21] (see Table (1). The most prominent feature of the excitation spectrum of PI is the 280 cm^{-1} progression and the absence of any spectral congestion up to ~1900 cm^{-1} above the S$_1$-state origin. Furthermore, the spectrum shows a limited number of low-frequency vibrational bands compared to *trans*-stilbene.

7.3.2 Dispersed Fluorescence Spectra

7.3.2.1 Electronic Origin

The assignments of the excitation and dispersed fluorescence spectra of t-S are well documented taking into account all the experimental and theoretical studies available [23-30]. Since the main interest here is how the structural changes in substituted stilbenes affect the photoisomerization dynamics, special attention will given to the low-frequency modes in these derivatives. However, due to the lack of experimental and theoretical studies on these substituted stilbenes, the low-frequency bands, in the dispersed fluorescence spectra, will be assigned tentatively by comparison with those in *trans*-stilbene (see Fig. 7.2, and 7.3).

In the ground state of trans-stilbene, the frequency of symmetric in-plane ethylene bend (25_1) mode is 199.5 cm^{-1}. The frequency of 37^0_2, 37^0_4, and 37^0_6 bands are 19, 43, and 70 cm^{-1}. These bands correspond to the even overtones of the fundamental C_e-C_e-C_{ph} out-of-plane twisting mode with a symmetry and a frequency of 8 cm^{-1} [27]. The 113 cm^{-1} band (36^0_2) is assigned as C_e-C_e-C_{ph} out-of-plane bend [25,26]. A complete assignment of the low-frequency vibrational bands in the S_0-state of t-S can be made using only these three modes (i.e. υ_{25}, υ_{36}, and υ_{37}).

Figure 7.2 shows the dispersed fluorescence spectrum of 4-methoxystilbene (isomer A) with an intense band at ~178 cm^{-1} assigned as 25_1 mode. Meanwhile, the same vibrational mode was identified in the dispersed fluorescence spectrum of isomer B at 193 cm^{-1} [18]. Other low frequency modes were identified in the dispersed fluorescence spectrum at 21, 82, and 258 cm^{-1} and were assigned as 37^0_2, 36^0_2, and 24^0_1 [18]. The same vibrational modes were observed for the B-isomer but at slightly different frequencies (37^0_2: 24 cm^{-1}, 36^0_2: 74 cm^{-1}, and 24^0_1: 222 cm^{-1} [18]). The vibrational bands at ~67 and 58 cm^{-1}, Fig. 7.2, have no analogs in the ground state manifold of *trans*-stilbene. The possibility of assigning these bands as the torsion of the methoxy, torsion of the methyl groups, or a methoxy bend was ruled out by Siewert and Spangler [18].

The 25_1 mode was observed at even lower frequency (~144 cm^{-1}) in the dispersed fluorescence spectrum of 4,4'-dimethoxystilbene (see Fig. 7.2). Furthermore, the spectrum reveals the presence of a progression of ~144 cm^{-1}. Another three low-frequency bands, located at ~14, 96, and 226 cm^{-1}, and their combination with the 144 cm^{-1} band can be identified in the dispersed fluorescence spectrum (see Fig. 7.2).

The number of low-frequency bands in the dispersed fluorescence spectrum of 2-phenylindene (Fig. 7.3) is less than that of *trans*-stilbene. The most prominent band in the PI spectrum is located at ~282 cm^{-1} and was assigned as the stilbene-type 25^0_1 band. The first low-frequency band appear at ~45 cm^{-1}, and its overtone (96 cm^{-1}), and was assigned as the equivalent of the 37^0_2 band in *trans*-stilbene. Furthermore, a 117 cm^{-1} band and its overtone (232 cm^{-1}) is also present in the spectrum. This band was assigned intuitively as 36^0_2-type band which is a C_e-C_e-C_{ph} out-of-plane bend.

Using the low-frequency modes in the dispersed fluorescence spectrum of the 0^0_0-transition in t-S, MS, DMS, and PI molecules, complete assignment of the bands in the low-frequency region can be done, see Table (2-5). The assignments and the frequencies given in those tables were intended to be considered as an approximation due to the uncertainty of our frequency measurements (± 10 cm^{-1}). Furthermore, since the vibrational bands are not well known, they will be assigned by their frequencies.

7.3.2.2 High Vibronic Levels

As in *trans*-stilbene, the dispersed fluorescence spectra of the higher vibronic levels in the S_1-state of jet-cooled substituted stilbenes could be classified into three categories depending on the excess-vibrational energy [31]. In the low-energy region (0.0-750 cm^{-1}) in S_1 *trans*-stilbene, the dispersed fluorescence spectrum shows sharp features with little or no spectral congestion. The *p*-methoxy substitution (as in MS) left these features unaltered except that the upper limit of the congestion-free region is decreased to ~540 cm^{-1} excess-energy. Similar features were observed in DMS where the dispersed fluorescence spectra, up to ~520 cm^{-1} in the S_1-state, show sharp features with no spectral congestion. This spectral congestion-free region in 2-phenylindene is expanded to ~ 930 cm-1 above the S_1-origin.

In the intermediate energy domain (~789-1170 cm^{-1}) in *trans*-stilbene, the dispersed fluorescence spectra show limited spectral congestion (to the red of the excitation bands) with minor sharp features. The dispersed fluorescence spectra from the vibronic levels in the range ~670-1126 cm^{-1} in 4-methoxystilbene, show similar features. Figure 7.4 shows representative spectra of this region. At a vibronic band as low as ~523 cm^{-1} above the S_1 electronic origin in 4,4'-dimethoxystilbene, the dispersed fluorescence spectrum shows some spectral congestion as well (Fig. 7.5). 2-Phenylindene is no exception and the dispersed fluorescence spectra of the vibrational bands in the S_1-state show the same general features as the other derivatives mentioned above in this intermediate-energy domain (Fig. 7.6). However, only three bands in the excess-energy range of ~560-1400 cm^{-1} show spectral congestion and some sharp features.

At high vibrational energies, the frequency-resolved fluorescence spectra of 4-methoxystilbene (above S_1+1150 cm^{-1}), show complete spectral congestion without any sharp features (compared to ~1230 cm^{-1} in *trans*-stilbene). Figure 7.7 shows representative spectra of 1247 and 1316 cm^{-1} excitation bands with complete congestion. The threshold of the complete spectral-congestion (in the dispersed fluorescence spectra) does not change upon the symmetrical *p*-methoxy substitution (as in DMS) (~1200 cm^{-1}) compared with unsubstituted *trans*-stilbene. In 2-phenylindene, excitation bands above ~1400 cm^{-1} in the S_1 manifold of 2-phenylindene show complete spectral congestion in their dispersed fluorescence spectra. Figures 7.8 shows the dispersed fluorescence spectra from high vibrational levels in the S_1-manifold of PI, respectively. Notice the sharp features in the spectrum even though the excess-energies are 1095 and 1193 cm^{-1} above the S_1-origin.

7.3.3 Time- Resolved Fluorescence: Narrow-Band Detection

7.3.3.1 Low-Energy Region

Following the excitation of 4-methoxystilbene to excess-energy below 540 cm^{-1} above the S$_1$-origin, the dispersed fluorescence decays as a single exponential with time constant equal to the radiative lifetime (A: 2.96 ns, B: 2.84 ns). 4,4'-Dimethoxystilbene (radiative lifetime ~2.96 ns) show the same features in the excess energy range of 0.0--~500 cm^{-1}. The dispersed fluorescence of the vibrational energy levels up to ~700 cm^{-1} in the S$_1$-electronic state of 2-phenylindene decays as a single exponential with radiative lifetime of 3.2 ns. The time-resolved fluorescence of the 0^0_0-transition in stilbene derivatives (such as MS, DMS, PI, and more) is shown in Chapter 8.

In jet-cooled *trans*-stilbene, this energy domain extends to ~750 cm^{-1} [31] where single exponential decays were measured with time constants equal to the radiative lifetime (2.67 ns) [1-15].

7.3.3.2 Intermediate-Energy Region

(a) 4-Methoxystilbene

In the excess-energy range of ~670-1126 cm^{-1} to in the S$_1$-state of 4-methoxystilbene, only two vibronic levels, exhibit quantum-beat modulated fluorescence (Fig. 7.9). These vibronic levels are located at S$_1$+ 670 and 905 cm^{-1}. The quantum beat-modulated fluorescence of the 670 cm^{-1} excitation band has recurrence time of ~470 ps while ~300 ps and 2.3 ns recurrences were observed following the 905 cm^{-1} excitation. Another excitation band (S$_1$+726 cm^{-1}) shows slow modulation (~2.9 ns), with very small modulation depth (not shown). In the S$_1$-state of trans-stilbene, the fluorescence of both 663 and 860 cm^{-1} vibrational levels exhibit quantum-beat modulations with the same recurrence times of 1.28 ns. It is worth mentioning that more than *eleven* beats can be seen in the fluorescence decay of the 670 cm^{-1} level in MS compared to *three* beats in the t-S fluorescence decay of a band with the about the same frequency (663 cm^{-1}) [31].

(b) 4, 4'-Dimethoxystilbene

At the 523 cm^{-1} vibrational band above the S_1 electronic origin in 4,4'-dimethoxystilbene, the dispersed fluorescence decay shows quantum beat-modulation of ~895 ps recurrence (see Fig. 7.10). The dispersed fluorescence decays of other excitation bands, S_1+990 and 1097 cm^{-1}, show quantum beats with ~1.97 ns and 468 ps recurrences, respectively. Slow modulation with a weak modulation-depth was observed in the fluorescence decay of another excitation band located at 1065 cm^{-1} above the S_1-origin in DMS (not shown). The vibrational bands 663, 987, and 1048 cm^{-1} in the S_1-state of *trans*-stilbene show similar fluorescence modulations even though the recurrence times and the modulation depth are different than these in DMS. The measured recurrence times in t-S fluorescence modulations are the following: 1.28 ns (663 cm^{-1}), 1.33 and 714 ps (987 cm^{-1}), and 303 ps, 256 ps, and 1.82 ns (1048 cm^{-1}). The modulation depth (which is related to the vibrational coupling matrix element) of t-S quantum beats, observed for these vibrational bands are significantly larger than those observed in DMS fluorescence decays.

(c) 2-Phenylindene

Two bands in the range S_1+560 to 1400 cm^{-1} in 2-phenylindene show quantum beats in the time-resolved fluorescence, see Fig. 7.11. The measured recurrence times for the quantum-beat modulated fluorescence of 929 cm^{-1} excitation band is ~335 ps. The vibrational band located at 989 cm^{-1} in the S$_1$-state of PI shows quantum beat modulation with recurrence time of 488 ps. These beats can be compared with those observed in t-S following the S$_1$+987 cm^{-1} excitation with 1.33 ns and 714 ps recurrence times [31]. Very small modulations could be distinguished in the dispersed fluorescence of the excitation bands located at S$_1$+703 cm^{-1} and 1095 cm^{-1} in PI (not shown) with nanosecond recurrence times.

7.3.3.3 High-Energy Region

(a) 4-Methoxystilbene

The time-resolved fluorescence following the excitations of S$_1$+1052 and 1125 cm^{-1} bands in 4-methoxystilbene, shows biexponential decay with fast components of approximately 115 and 70 ps, respectively (the figure is not shown, see Table (7)). Another biexponential fluorescence decays of higher vibrational bands (1247 and 1316 cm^{-1}) were measured with fast decay components of ~39 and 55 ps, respectively (see Fig. 7.12). The slow component is slightly shorter than the radiative lifetime (~2.5 ns). In the same energy region, similar behavior was observed in *trans*-stilbene [31] with 24-44 ps as fast decay component. The slow decay components was estimated as 1.7-1.9 ns [31]. The slow-to-fast amplitude ratio (a_s / a_f) in MS molecule (0.57-0.64) is significantly larger than those in t-S (0.08-0.10) [31].

(b) 4, 4'-Dimethoxystilbene

The dispersed fluorescence of S_1+1075 and 1123 cm^{-1} 4,4'-dimethoxystilbene fit as biexponential decay with fast components of ~386 and 320 ps, respectively (not shown, see Table (8) for more detail). The slow components, in these decays, are 2.84-2.97 ns with a_s / a_f~ 0.26-0.93. Another band (S_1+1197) cm^{-1}) shows similar behaviour (see Table (7)). As shown in Table (7), the fluorescence decays and their fit change slightly as the detection wavelength changes.

An interesting comparison can be made between DMS and t-S fluorescence decays in this energy region. Quantum-beat modulated fluorescence decays were observed when *trans*-stilbene was excited to S_1+1048 and 1170 cm^{-1}. The quantum-beat recurreneces were estimated to be 303, 256 ps, and 1.82 ns for the 1048 cm^{-1} band while 556 ps, 1.33, and 1.11 ns were measured for the 1170 cm^{-1} band in t-S molecule [31].

(c) 2-Phenylindene

In the S_1-state of 2-phenylindene, the time-resolved fluorescence of the excitation bands ~1095 and 1193 cm^{-1} shows biexponential decays with fast decay components of 179 and 286 ps, respectively (see Fig. 7.13 and Table (8)). The slow components were estimated as 2.96 ns with a_s / a_f~ 0.37 (1095 cm^{-1}) and 0.83 (1193 cm^{-1}). The fluorescence of another vibrational band (1373 cm^{-1}) decays as a biexponential with fast component of ~143 ps, slow component of 2.96 ns, and a_s / a_f ~0.02 .

A summary of the measured time constants in the intermediate and high energy regions in t-S, MS, DMS, and PI molecules are listed in Table (5).

7.3.4 IVR in Substituted *Trans*-Stilbenes

7.3.4.1 Preliminaries

Felker *at al.* [31] have probed the extent of intramolecular vibrational energy redistribution (IVR) in the regime between zero and an excess energy of ~ 1332 cm^{-1}. Three different regimes could be distinguished. In the low energy region (0.0-752 cm^{-1}), IVR is absent on the time scale of fluorescence (2.67 ns). The dispersed fluorescence spectra show sharp features with no congestion and the fluorescence decays as a single exponential. In the intermediate energy region (789-1170 cm^{-1}), IVR is restricted. Quantum-beat modulated fluorescence decays has been observed, in this intermediate energy regime, and minor congestion was observed in the dispersed fluorescence spectra. In the high-energy range (above ~1230 cm^{-1}), IVR is dissipative and the fluorescence decays in tens of picoseconds. The onset of dissipative IVR corresponds well to the threshold for isomerization, and may reflect a connection between these two processes.

No-, restricted- and dissipative-IVR were identified in a variety of large molecules, see ref. [33] for references. Density of states, symmetry, vibrational coupling, the number of the low-frequency modes and the anharmonicity are the key parameters in the intramolecular vibrational energy redistribution in large molecules. Unfortunately, there are no model systems in which these parameters and their effect on IVR can be tested separately. It is an interplay between these parameters which determine the general features of IVR that one can expect.

Since IVR is considered a determinant step for the photoisomerization process, it was important to characterize IVR in the stilbene derivatives presented in this work and compare it with that in *trans*-stilbene. The symmetry reduction in 4-methoxystilbene and 2-phenylindene in comparison with *trans*-stilbene is expected to reduce the restrictions on the vibrational coupling between different modes [31,32]. On the other hand, the number of the low-frequency modes will increase upon the para-methoxy substitutions in MS and DMS but decreases in PI due to the intramolecular bridging.

7.3.4.2 Asymmetric para-Methoxy Substitution

The symmetry reduction and the increase of the low-frequency modes upon *p*-mono-methoxy substitution in *trans*-stilbene (*i.e.* 4-methoxystilbene) are in favor of an efficient vibrational coupling and IVR. The congestion of the dispersed fluorescence spectra in the S_1-manifold of MS is observed at vibrational levels as low as ~540 cm^{-1} above the origin. However, the lowest vibrational level at which quantum beats is observed is the same (~670 cm^{-1}) as in *trans*-stilbene (~663 cm^{-1}). Regardless of the assignment of that band, the observed modulation in MS suggests a faster IVR (~469 ps) compared with that in *trans* stilbene (~1.28 ns); about 63% faster; see Fig. 7.9. Only two other vibrational bands in the S_1-state of MS show quantum beats (726 and 905 cm^{-1}) which represent ~23% of the investigated bands in the S_1+540 to S_1+1200 cm^{-1} region. In contrast, about 50% of the bands in the same region of stilbene [31,32] show quantum beats. On the other hand, the dispersed fluorescence of the vibronic transition 933 cm^{-1} has biexponential decay with fast component of ~54 ps and (a_s / a_f) ~1.2. The nearest vibronic transition in *trans*-stilbene is located at 987 cm^{-1} at which quantum-beat modulation of ~1.33 ns period is observed [31,32]. Another interesting comparison can be made between the kinetics of other two vibronic transitions 1052 and 1126 cm^{-1} in the 4-methoxystilbene and those at 1048 and 1170 cm^{-1} in trans stilbene. Biexponential decays are measured following 1052 and 1126 cm^{-1} excitations in the S_1-manifold of MS with fast components of 115 and 70 ps, respectively (see Fig. 7.12). However, quantum beats of 300 ps and 1.3 ns recurrence are observed at 1048 and 1170 cm^{-1}, respectively in *trans*-stilbene [31,32]. It is an unavoidable conclusion that *p*-methoxy mono-substitution not only accelerates the energy randomization, but also favor the dissipative-IVR mechanism more than the restricted one. This conclusion contradicts the argument that IVR in *p*-mono-alkyl-substituted stilbene does not involve the vibrational modes of the substituent and IVR is not democratic [14,15].

7.3.4.3 Symmetric para-Methoxy Substitution

In 4,4'-dimethoxystilbene, the symmetry reduction is not a factor, instead the increase of the density of states and the number of the low-frequency modes come into play. The symmetrical *p*-methoxy substitution in *trans*-stilbene has a profound effect on the dispersed fluorescence spectra in which spectral congestion has been observed for the excitation to very low vibrational energy (~523 cm^{-1}) (Fig. 7.5). However, no quantum beats were observed below ~523 cm^{-1} at which ~895 ps recurrence modulate the fluorescence decay. In comparison with *trans* stilbene, this IVR-time scale is about ~30% faster than that in *trans*-stilbene following the excitation of S_1+663 cm^{-1}. The time-resolved fluorescence of some other vibrational bands, such as 990 and 1097 cm^{-1}, show quantum beats of ~2.0 ns and 468 ps periods, respectively (see Fig. 7.10). In *trans*-stilbene, IVR of 1.33 ns and 300 ps time scales are measured at similar excess vibrational energies (987 and 1048 cm^{-1}) above the electronic S_1-origin. The modulation depth of the observed quantum beats in the intermediate energy regime of 4,4'-dimethoxystilbene is significantly smaller than that in *trans*-stilbene. Of course, the vibrational cooling and resolution may also contribute to small modulation-depth.

In the dissipative regime of the S_1-state in 4,4'-dimethoxystilbene, the dispersed fluorescence decay of the excitation band S_1+1075 and 1125 cm^{-1} are biexponential with fast decay components of ~178 and 320 ps. This dissipative behavior, which can be compared with restricted IVR in *trans*-stilbene excited to 1048 and 1170 cm^{-1} with 300 ps and 1.3, 1.8 and 1.3 ns time scales, respectively [31,32], sets another example of the structural effect on IVR dynamics in stilbene. Above S_1+1220 cm^{-1} in DMS, the dispersed fluorescence spectra are completely congested and show no sharp features, which is about the same as that in *trans*-stilbene.

7.3.4.4 Intramolecular Chemical Bridging

Anchoring the ethylene double-bond in *trans*-stilbene, 2-phenylindene, will decrease the number of the low-frequency modes and the rigidity of the molecule will be enhanced which might suggest a slow IVR rate. However, the symmetry reduction in 2-phenylindene will reduce the restrictions on the vibrational coupling, *i.e.* efficient IVR. Studying the IVR in 2-phenylindene might determine the dominant parameter in the IVR mechanism.

The congested dispersed fluorescence spectra with some sharp features have been observed in a wider range from ~560 to 1400 cm^{-1} in the S_1-manifold of 2-phenylindene. However, the dispersed fluorescence decays of only two vibrational levels show strong quantum-beat modulations (Fig. 7.11). The quantum-beats modulation in the dispersed fluorescence of the vibronic levels S_1+930 and 990 cm^{-1} suggests a time scale for a restricted IVR on the order of 335 and 488 ps, respectively. The IVR of isoenergetic vibronic level at S_1+987 cm^{-1} in *trans*-stilbene is restricted and taking place on a 1.33 ns time scale [31,32]. The dissipative IVR of the vibronic transitions at S_1+1097 cm^{-1} in 2-

phenylindene is taking place on a time scale of 178 ps. In this energy domain, the nearest vibrational level in the S_1-manifold of *trans*-stilbene, is located at 1048 cm^{-1}. The fluorescence of this vibrational level indicates a restricted IVR occurring on 0.26-1.82 ns time scale [31,32]. Furthermore, the time evolution of another vibronic level in the S_1-state of both 2-phenylindene (1194 cm^{-1}) and *trans*-stilbene (1170 cm^{-1}) could be compared. Although, IVR in 2-phenylindene (excited to S_1+1194 cm^{-1}) is dissipative in nature and taking place on ~320 ps time scale, the isoenergetic level in *trans*-stilbene (1170 cm^{-1}) shows a restricted IVR on a time scale of 0.556-1.33 ns (see Fig. 713). So far, the results indicate a faster IVR rate. However, the vibrational energy of the S_1+1332 cm^{-1} of bare *trans*-stilbene dissipates on a 24 ps time scale. This time scale is ~3.6 times faster than that measured at S_1+1373 cm^{-1} in 2-phenylindene.

Qian *et al.* [34] used picosecond resonance Raman spectroscopy to investigate IVR dynamics in the S_1-state of both *trans*-stilbene and 2-phenylindene in solution. The time-dependent spectral changes in the anti-stokes region, observed in 2-phenylindene, suggest that IVR is faster than that in *trans*-stilbene. The IVR acceleration was attributed to the rigid structure for 2-phenylindene which will alter the anharmonic couplings between the Franck-Condon active ethylenic mode and lower-frequency modes.

For visual comparison of *the overall IVR dynamics* in substituted and unsubstituted stilbenes, the measured IVR rates in both t-S (adapted from ref. [31]) and MS, DMS, and PI are plotted as a function of the excess energy in the S_1-state in each molecule (Fig. 7.14). To our surprise, the IVR rates are faster in the parent molecule (t-S) than in the substituted stilbenes. This results are counterintuitive especially for 4-methoxystilbene and 4,4'-dimethoxystilbene due to the following reasons. First, the density of states in MS and DMS molecules are expected to increase compared to t-S. Second, the lowering of the symmetry in MS (C_s) compared to t-S (C_{2h}) should, in principle, enhance the vibrational coupling between the low-frequency modes [35]. The same argument apply for PI molecule (C_s). However, the structural effects are pronounced in the following aspects of IVR dynamics in these substituted stilbenes. The nature of IVR in the substituted stilbenes (MS, DMS, and PI) is more dissipative than restricted. This conclusion is reached depending on the fact that a very limited number of vibrational modes (in the S_1-state) of MS, DMS, and PI show fluorescence decays with quantum beat modulations.

7.4 CONCLUSION

Time- and frequency-resolved fluorescence measurements of jet-cooled substituted *trans*-stilbenes have been presented and compared with those in trans-stilbene. Intramolecular vibrational energy redistribution (IVR) of 4-methoxystilbene, 4,4'-dimethoxystilbene and 2-phenylindene follow the same trend with excess-vibrational energy as does the parent *trans*-stilbene and other aromatic molecules. In the low-energy region, IVR was not present on the time scale of the fluorescence lifetime. Consequently, there is no apparent vibrational evolution of the optically active states prepared by the picosecond laser pulses. In the intermediate energy region, the fluorescence emission of a limited number of vibronic levels exhibit quantum-beat modulations, *i.e.* restricted IVR. The energy randomization could take place on a time scale of hundreds of picoseconds in this domain. At higher excitation energies, IVR becomes dissipative in nature and the fluorescence decays as biexponential. The IVR time scale in this domain is in the order of tens to a few hundred of picoseconds. The comparison between IVR in substituted and unsubstituted *trans*-stilbene suggests that the molecular structure could affect the *nature* of intramolecular dynamics (dissipative more than restricted IVR). The results of 4-methoxystilbene and 2-phenylindene suggest that symmetry, in particular, might play a significant role in IVR dynamics due to the enhancement of vibrational coupling upon symmetry reduction. However, the overall trend is that the highest IVR rate is measured for the unsubstituted *trans*-stilbene.

Table (1): The electronic origin of 0_0^0-transition in *trans*-stilbene (t-S), 4-methoxystilbene (MS), 4,4'-dimethoxystilbene (DMS), and 2-phenylindene (PI) and their radiative lifetimes.

Molecule	$\lambda(0_0^0)$ / Å	$\nu(0_0^0)$ / cm^{-1}	$\delta\nu$ * / cm^{-1}	τ_{rad} / ns
t-S	3101.4	32234.7	0.0	2.63
MS(A)	3252.7	30744.1	-1499.6	2.96
MS(B)	3223.6	31022.6	-1221.1	2.84
DMS	3334.8	29987.0	-2247.7	2.96
PI	3183.0	31416.9	-826.6	3.20

* The frequency shift ($\delta\nu$) was calculated with respect to the 0_0^0-transition in unsubstituted *trans*-stilbene.

Table (2). *Trans*-stilbene assignments in the low-frequency region.

Frequency (cm^{-1})	Intensity	Assignment
0.0	100.0	0^0_0
18.6	30.6	$(19)^0_1$
43.4	8.2	$(19)^0_2$
70.2	2.0	$(70)^0_1$
113.4	11.0	$(113)^0_1$
131.9	3.0	$(113)^0_1(19)^0_1$
156.6	1.6	$(113)^0_1(19)^0_2$
199.5	70.1	$(200)^0_1$
213.8	40.7	$(200)^0_1(19)^0_1$
234.3	13.4	$(200)^0_1(19)^0_2$
262.8	4.1	$(200)^0_1(19)^0_3$
273.0	3.3	$(200)^0_1(70)^0_1$
289.2	6.4	$(200)^0_1(70)^0_1(19)^0_1$
315.6	13.5	$(200)^0_1(113)^0_1$
327.8	6.4	$(200)^0_1(113)^0_1(19)^0_1$
348.1	1.7	$(200)^0_1(113)^0_1(19)^0_2$
410.7	36.6	$(200)^0_2$
428.9	13.4	$(200)^0_2(19)^0_1$
455.1	6.5	$(200)^0_2(19)^0_2$
489.2	5.5	
497.3	3.8	
525.3	7.4	
599.3	15.0	$(200)^0_3$

Table (3). Vibrational band assignment in the low-frequency range in the electronic ground state (S_0) of 4-methoxystilbene.

Frequency (cm^{-1})	Intensity	Assignment
0.0	100.0	0_0^0
18.8	31.0	$(19)_1^0$
41.4	9.1	$(19)_2^0$
58.3	4.8	$(19)_3^0$
69.6	9.0	$(70)_1^0$
92.1	4.7	$(19)_5^0$
118.3	4.7	$(118)_1^0$
140.7	2.7	
165.0	52.8	$(165)_1^0$
194.8	9.7	
235.6	41.5	$(118)_2^0$ or $(165)_1^0(70)_1^0$
282.0	7.5	
296.8	5.4	
311.5	5.4	
335.5	31.3	$(165)_2^0$
348.4	11.0	
383.4	3.9	
409.1	26.5	$(165)_2^0(70)_1^0$
427.4	7.7	$(165)_2^0(70)_1^0(19)_1^0$
454.9	6.3	
476.8	11.1	
498.7	12.2	$(165)_3^0$
518.8	9.8	
537.0	5.4	
571.5	15.7	$(165)_3^0(70)_1^0$

Table (4). Vibrational band assignment in the low-frequency range in the electronic ground state of 4,4'-dimethoxystilbene.

Frequency (cm^{-1})	Intensity	Assignment
0.0	100.0	0_0^0
14.3	39.4	$(14)_1^0$
35.8	11.9	$(14)_2^0$
59.0	4.4	$(59)_1^0$
96.4	3.2	$(96)_1^0$
142.6	79.4	$(143)_1^0$
153.3	52.1	$(143)_1^0(14)_1^0$
174.5	15.8	$(143)_1^0(14)_2^0$
195.8	6.0	$(143)_1^0(14)_3^0$
225.8	51.9	$(226)_1^0$
241.7	18.9	$(143)_1^0(96)_1^0$
266.3	6.2	
291.0	39.2	$(143)_2^0$
313.8	15.2	$(143)_2^0(14)_1^0$
336.6	6.2	
366.3	48.7	$(143)_1^0(226)_1^0$
382.0	24.4	$(143)_1^0(226)_1^0(14)_1^0$
403.0	7.6	
430.8	14.9	$(143)_3^0$
451.7	21.9	$(226)_2^0$
472.6	6.7	
508.9	20.3	$(143)_2^0(226)_1^0$
524.5	16.9	$(143)_2^0(226)_1^0(14)_1^0$
541.8	7.2	
571.1	6.8	$(143)_4^0$
593.6	17.8	$(143)_4^0(14)_1^0$

Table (5): The vibrational bands in the low-frequency range of the ground electronic state (S_0) of 2-phenylindene.

Frequency (cm^{-1})	Intensity	Assignment
0.0	100.0	0_0^0
45.1	19.1	$(45)_1^0$
96.0	6.2	$(45)_2^0$ or $(96)_1^0$
117.5	12.4	$(118)_1^0$
156.4	2.7	
232.1	1.2	$(118)_2^0$
282.3	54.6	$(282)_1^0$
324.7	13.3	$(282)_1^0(45)_1^0$
372.8	3.5	$(282)_1^0(96)_1^0$
398.0	5.2	$(282)_1^0(118)_1^0$
433.0	1.5	
512.2	1.1	
561.5	20.0	$(282)_2^0$
601.3	10.2	$(282)_2^0(45)_1^0$

Table (6): IVR time scale in substituted *trans*-stilbenes. The results of the unsubstituted stilbene were adapted from ref. [3].

		IVR Time Scale		
E_x / cm^{-1}	t-S	MS	DMS	PI
523	-	-	895	-
663	1.28 ns	-	-	-
670	-	470 ps	-	-
726	-	2.9 ns	-	-
789	790&571 ps	-	-	-
821	741&164 ps	-	-	-
852	625 ps	-	-	-
860	1.28 ns	-	-	-
905	-	300 ps	-	-
930	-	-	-	335 ps
987	1.33 ns& 714 ps	-	-	-
990	-	-	1.97 ns	488 ps
1048	300 &260 ps and 1.82 ns	-	-	-
1052	-	115 ps	-	-
1075	-	-	386 ps	-
1095	-	-	468 ps	179 ps
1126	-	70	241&320 ps	-
1170	1.33 &1.1 ns and 560 ps	-	-	-
1197	-	-	184	286 ps
1238	28 ps	39 ps	-	-
1241	33 ps	-	-	-
1247	27 ps	39 ps	-	-
1316	-	55 ps	-	-
1332	24 ps	-	-	-
1373	-	-	-	143 ps

Table (7): Dissipative IVR in 4-methoxystilbene.

E_x / cm^{-1}	υ_d / cm^{-1}	τ_2 / ns	τ_1 / ps	a_f / a_s
1052	636	2.60	115	0.7
1125	880	2.62	70	1.0
1247	320	2.44	39	2.2
1316	319	2.46	55	2.0

Table (8): Dissipative IVR in 4,4'-dimethoxystilbene.

E_x / cm^{-1}	υ_d / cm^{-1}	τ_2 / ns	τ_1 / ps	a_f / a_s
1075	159	2.84	386	1.2
	631	2.93	487	0.8
	790	2.91	519	0.5
1197	159	2.40	184	2.1
	324	2.41	223	1.8
1123	267	2.55	314	0.9
	440	2.56	226	1.1

Table (9): Dissipative IVR in 2-phenylindene.

E_x / cm^{-1}	υ_d / cm^{-1}	τ_2 / ns	τ_1/ps	a_f / a_s
1095	553	2.77	159	5.3
	834	2.84	167	4.2
	873	2.96	179	2.7
1193	868	2.86	286	1.9
	1191	2.89	282	1.9
	1464	2.96	288	1.2
1377	285	2.87	72	15.5
	844	2.96	143	5.5

7.5 REFERENCES

1. J. A. Syage, W. R. Lambert, P. M. Felker and A. H. Zewail and R. M. Hochstrasser, *Chem. Phys. Lett.* **88,** 266 (1982).
2. J. A. Syage, P. M. Felker, and A. H. Zewail, *J. Chem. Phys.* **81**, 4685, 4706 (1984).
3. P. M. Felker, W. R. Lambert, and A. H. Zewail, *J. Chem. Phys.* **82**, 3003 (1985).
4. P. M. Felker and A. H. Zewail, *Adv. Chem. Phys.* **70**, 265 (1988).
5. L. R. Khundkar, R. Marcus, and A. H. Zewail, *J. Phys. Chem.* **87**, 2473 (1983).
6. P. M. Felker and A. H. Zewail, *J. Phys. Chem.* **89,** 5402 (1985).
7. J. Schroeder and J. Troe, *Annu. Rev. Phys. Chem.* **38**, 163 (1987).
8. J. Troe, *J. Phys. Chem.* **90**, 357 (1986).
9. C. Gehrke, J. Schroeder, J. Troe, and F. Voss, *J. Chem. Phys.* **92**, 4805 (1990).
10. G. Maneke, J. Schroeder, J. Troe, and F. Voss, *Ber. Bunsen-Ges. Phys. Chem.* **89**, 896 (1985).
11. J. Schroeder, D. Schwarzer, J. Troe, and F.Voss, *J. Chem. Phys.* **93**, 2393 (1990).
12. J. Troe and J. Schroeder, *J. Phys. Chem.* **90**, 4215 (1986).
13. J. Troe, *Chem. Phys. Lett.* **114**, 241 (1985).
14. T. J. Majors, U. Even, and J. Jortner, *J. Chem. Phys.*, **81**, 2330 (1984).
15. K. Rademann, U. Even, S. Rozen, and J. Jortner, *Chem. Phys. Lett.* **125**, 5 (1986).
16. L. G. Greifenstein, J. B. Lambert, R. J. Nienhuis, H. E. Fried, and G. A. Pagani, *J. Org. Chem.* **46**, 5125 (1981).

17. D. A. Bors, M.J . Kaufman, and A. Streitweiser Jr., *J. Am. Chem. Soc.* **107**, 6975 (1985).

18. S. S. Stiewert and L. H. Spangler, *J. Phys. Chem.* **99**, 9316 (1995).

19. T. Zwier, M. E. Carrasquillo, and D. H. Levy, *J. Chem. Phys.* **78**, 5493 (1984).

20. T. Troxler, M. R. Topp, B. S. Metzger, and L. H. Spangler, *Chem. Phys. Lett.* **238**, 313 (1995).

21. J. R. Cable, Private communication.

22. A. Oikawa, H. Abe, N. Mikami, and M. Ito, *Chem. Phys. Lett.* **116**, 50 (1985).

23 A. Warshel, *J. Chem. Phys.* **62**, 214 (1975).

24. J. A. Syage, P. M. Felker, and A. H. Zewail, *J. Chem. Phys.* **81**, 4685 (1984).

25. L. H. Spangler, R. van Zee, and T. S. Zwier, *J. Phys. Chem.* **91**, 2782 (1987).

26. L. H. Spangler, R. D. van Zee, S. C. Blankespoor, and T. S. Zwier, *J. Phys. Chem.* **91**, 6077 (1987).

27. T. Suzuki, N. Mikami, and M. Ito, *J. Phys. Chem.* **90**, 6431 (1986).

28. T. Urano, H. Hamaguchi, M. Tasumi, K. Yamanouchi, and S. Tsuchiya, *Chem. Phys. Lett.* **137**, 559 (1987).

29. T. Urano, M. Maegawa, K. Yamanouchi, and S. Tsuchiya, *J. Phys. Chem.* **93**, 3459 (1989).

30. T. Urano, H. Hamaguchi, M. Tasumi, K. Yamanouchi, S. Tsuchiya, and T. L. Gustafson, *J. Phys. Chem.* **91**, 3884 (1989).

31. P. M. Felker, W. R. Lambert, and A. H. Zewail, *J. Chem. Phys.* **70**, 265 (1985).

32. P. M. Felker and A. H. Zewail, *Chem. Phys.* **88,** 6106 (1985).

33. C. Lienau, A. A. Heikal, and A. H. Zewail, *Chem. Phys*. **175**, 171 (1993) and reference therein.

34. J. Qian, S. L. Schultz, and J. M. Jean, *Chem. Phys. Lett*. **233**, 9 (1995).

35. P. M. Felker and A. H. Zewail, *Chem. Phys*. **82,** 2961 (1985).

7.6 FIGURE CAPTIONS

7.1 The molecular structures of *trans*-stilbene, 4-methoxystilbene, 4,4'-dimethoxy-stilbene, and 2-phenylindene. The two conformers of MS molecule are shown. Meanwhile, different conformers can be expected for DMS depending on the orientation of the methyl groups (not shown).

7.2 Dispersed fluorescence spectra of the vibrationless $S_1 \leftarrow S_0$ electronic transitions in *trans*-stilbene (bottom), 4-methoxystilbene (middle) and 4,4'-dimethoxystilbene (top). The expansion conditions are: Sample temperature *(T)* = 90, 100, and 240 °C for t-S, MS and DMS, respectively; *x/d* ~ 30 , Backing pressure *(P)* = 50 psi of Helium and slit width *(R)* = 30 μm. The relative frequency was calculated to reflect the red-shift of all vibrational bands in each spectrum with respect to the 0_0^0 transition.

7.3 Dispersed fluorescence spectrum of 2-phenylindene (top) excited to the S_1-origin. The dispersed fluorescence spectrum of *trans*-stilbene (bottom) is also shown for comparison. The experimental conditions are similar to those of Fig. 7.2.

7.4 The dispersed fluorescence spectra of 670 (bottom) and 905 cm^{-1} (top) (with respect to the origin of the S_1-state in) isomer A)excitation bands in 4-methoxy-stilbene show spectral congestion with some sharp features. The asterisks show the detection bands for the time-resolved fluorescence measurements (see the text). The expansion parameters are: T = 100 °C, P = 80 psi helium, *x/d* ~ 30 and R = 100 μm.

7.5 Representative dispersed fluorescence spectra of 4,4'-dimethoxystilbene excited to different vibronic levels (523, 990, and 1097 cm^{-1}) in the S_1-state. The experimental conditions are similar to those in Fig. 7.4. The asterisks show the detection bands for the time-resolved fluorescence measurements (see the text).

7.6 The dispersed fluorescence spectra of 2-phenylindene excited to S_1+929 (bottom) and 989 (top) cm^{-1}. The asterisks refer the detection bands for the time-resolved fluorescence measurements (see the text). The expansion parameters are similar to those mentioned for Fig. 7.4.

7.7 The frequency-resolved fluorescence spectra of MS excited to S_1+1247 (bottom) and 1316 cm^{-1} (top). The asterisks refer the detection bands for the time-resolved fluorescence measurements (see the text). The expansion parameters are similar to those mentioned for Fig. 7.4.

7.8 The frequency-resolved fluorescence spectra of PI excited to S_1+1095 (bottom) and 1193 cm^{-1} (top). The asterisks refer the detection bands for the time-resolved fluorescence measurements (see the text). The expansion parameters are similar to those mentioned for Fig. 7.4.

7.9 Quantum-beat modulated fluorescence decays following the excitation of 4-methoxystilbene to S_1+ 670 (bottom) and 905 cm^{-1} (top). The estimated recurrence times for 669 and 905 cm^{-1} bands are ~469 ps, and ~300 ps and 1.93 ns, respectively. The expansion parameter and the detection bands are mentioned in Fig. 7.4 caption.

7.10 The fluorescence decays of 523 (bottom), 990 (middle), and 1095 cm^{-1} (top) vibrational bands in the S_1-manifold of DMS, show quantum beats with small modulation depth. The estimated recurrence times are 895 ps, 1.97 ns, and 468 ps at the excess vibrational energies 523, 990, and 1095 cm^{-1}, respectively. Similar expansion parameters to those of Fig. 7.4 were used and the detection bands are shown in Fig. 7.5.

7.11 Quantum beats of 335 ps (bottom) and 488 ps (top) recurrences observed in time-resolved fluorescence of 2-phenylindene excited to S_1+929 and 989 cm^{-1}, respectively. The expansion parameters are similar to those in Fig. 7.4 and the detection wavelength are shown in Fig. 7.6.

7.12 In the high energy regime of 4-methoxystilbene (S_1+1247 and 1316 cm^{-1}), biexponential fluorescence decays were measured. The fitting parameters for the 1247 cm^{-1} decay are the following: $\tau_1 = 56$ ps, $\tau^2 = 2.45$ ns, slow-to-fast amplitude ratio (a_s / a_f) = 0.57, and $\chi^2 = 0.93$. Similar fitting parameters for the 1316 cm^{-1} decay were measured ($\tau_1 = 58$ ps, $\tau^2 = 2.46$ ns, $a_s / a_f = 0.57$, and $\chi^2 = 0.93$).

7.13 At higher excess-energy in the S_1-state of 2-phenylindene (1095 and 1193 cm^{-1}), biexponential fluorescence decays were measured. The fitting parameters for the 1095 cm^{-1} decay are the following: $\tau_1 = 178$ ps, $\tau^2 = 2.84$ ns, slow-to-fast amplitude ratio (a_s / a_f) = 0.27, and $\chi^2 = 1.72$. Similar fitting parameters for the 1193 cm^{-1} decay were measured ($\tau_1 = 320$ ps, $\tau_2 = 2.98$ ns, $a_s / a_f = 0.93$, and $\chi^2 = 0.98$).

7.14 For visual comparison, IVR rates in *trans*-stilbene, 4-methoxystilbene, 4,4'-dimethoxystilbene, and 2-phenylindene are plotted as a function of the excess-energy in the S_1-state of each molecule. In the restricted IVR domain, where quantum beats were observed, the reciprocal of the recurrence times were included in the graph as IVR rates [35].

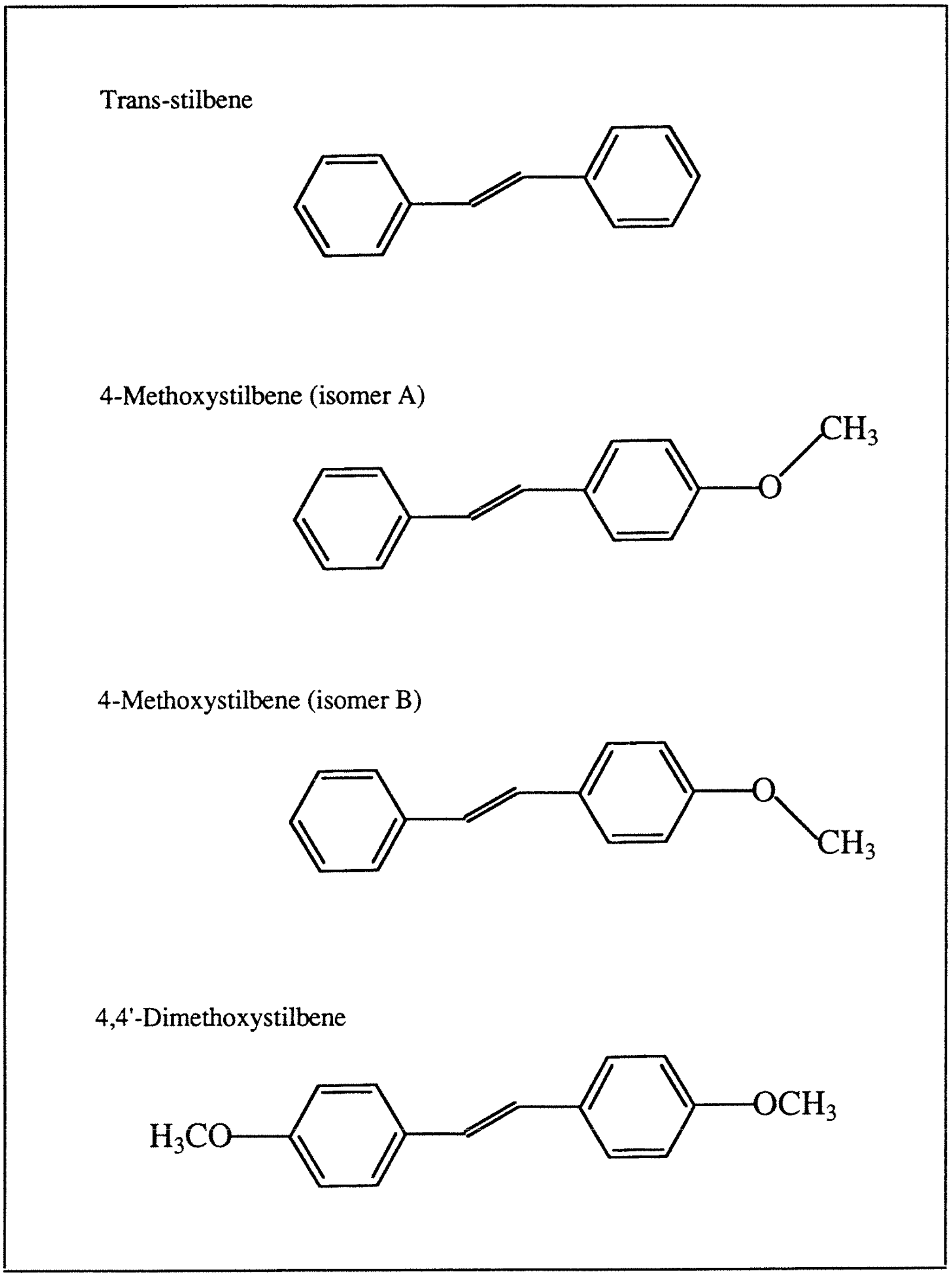
Trans-stilbene
4-Methoxystilbene (isomer A)
CH3
O
4-Methoxystilbene (isomer B)
O
CH3
4,4'-Dimethoxystilbene
H3CO
OCH3

Fig. 7.1

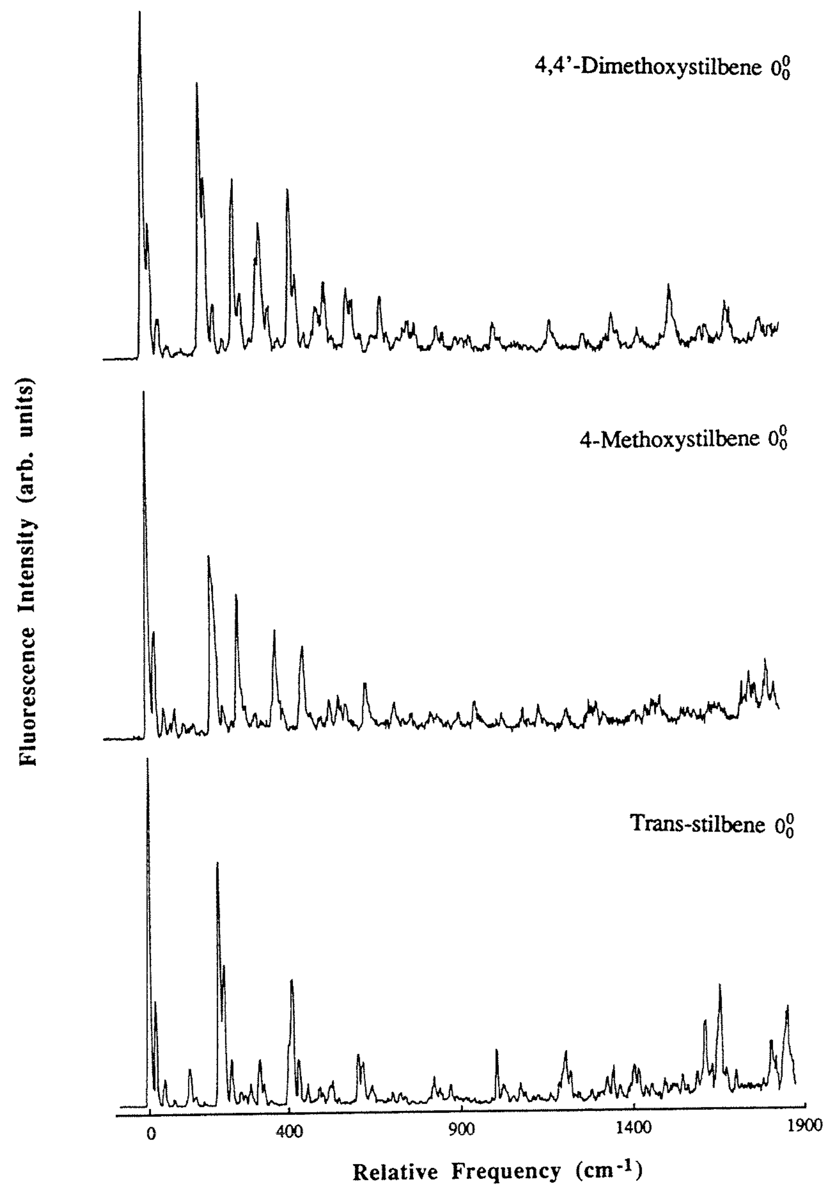
4,4'-Dimethoxystilbene 0_0^0
4-Methoxystilbene 0_0^0
Trans-stilbene 0_0^0
Fluorescence Intensity (arb. units)
0
400
900
1400
1900
Relative Frequency (cm^{-1})

Fig. 7.2

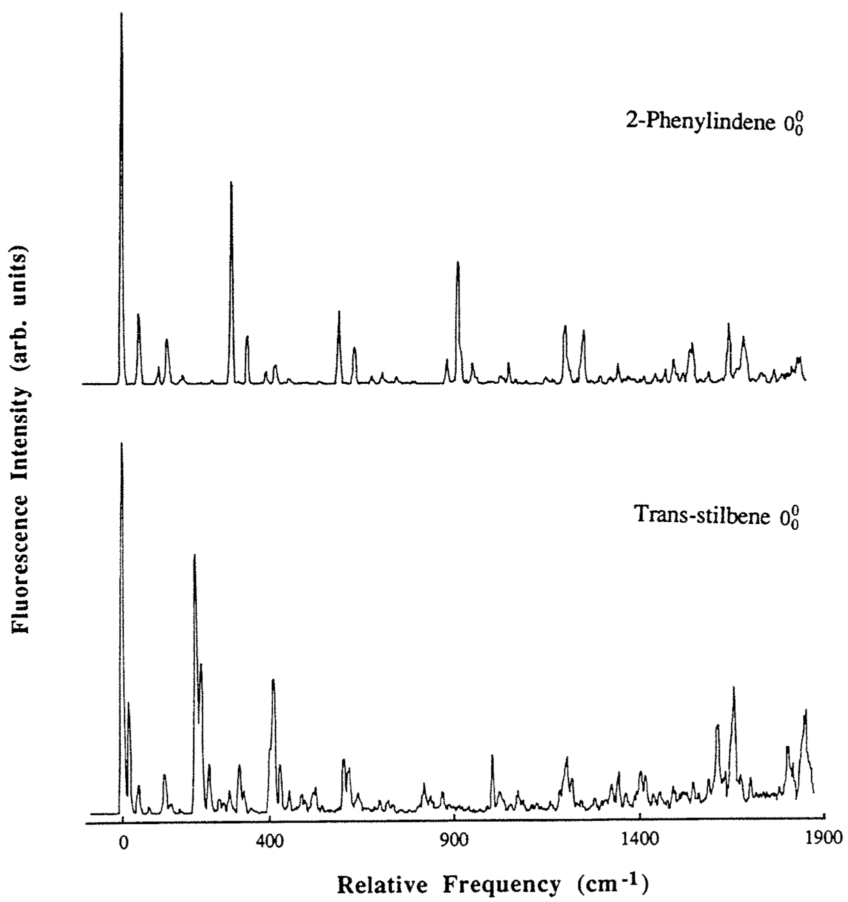
2-Phenylindene 0_0^0
Trans-stilbene 0_0^0
Fluorescence Intensity (arb. units)
0
400
900
1400
1900
Relative Frequency (cm^{-1})

Fig. 7.3

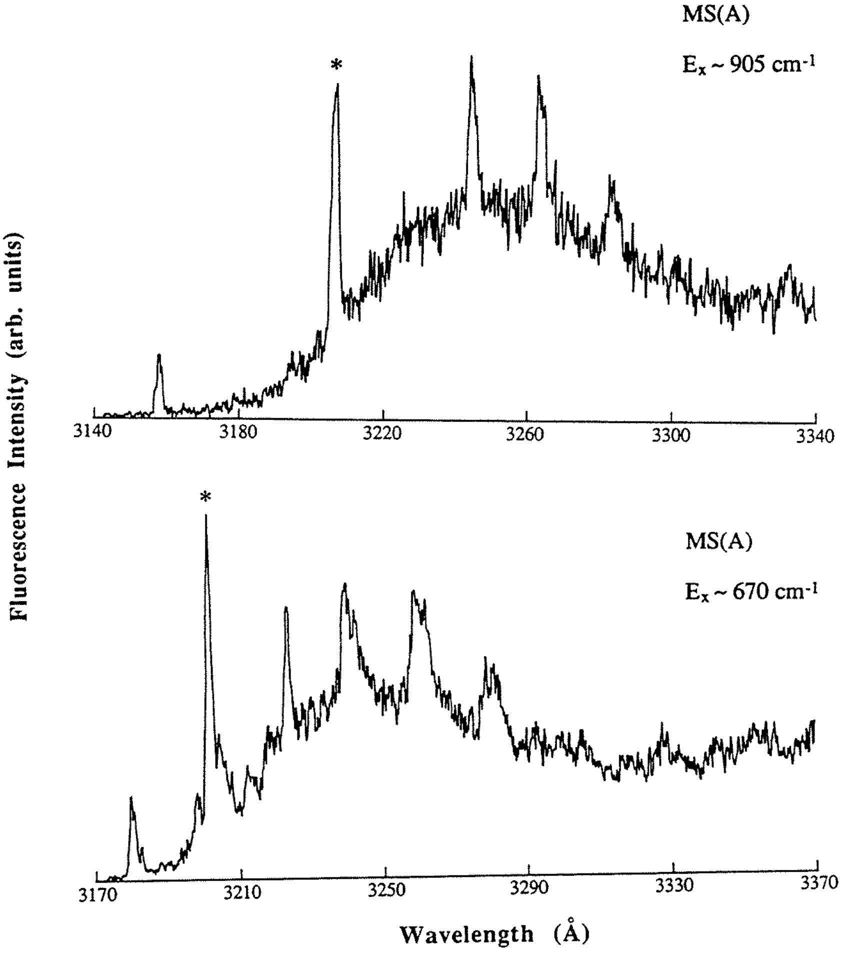
MS(A)
$E_x \sim 905$ cm^{-1}
*
3140
3180
3220
3260
3300
3340
MS(A)
$E_x \sim 670$ cm^{-1}
*
3170
3210
3250
3290
3330
3370
Fluorescence Intensity (arb. units)
Wavelength (Å)

Fig. 7.4

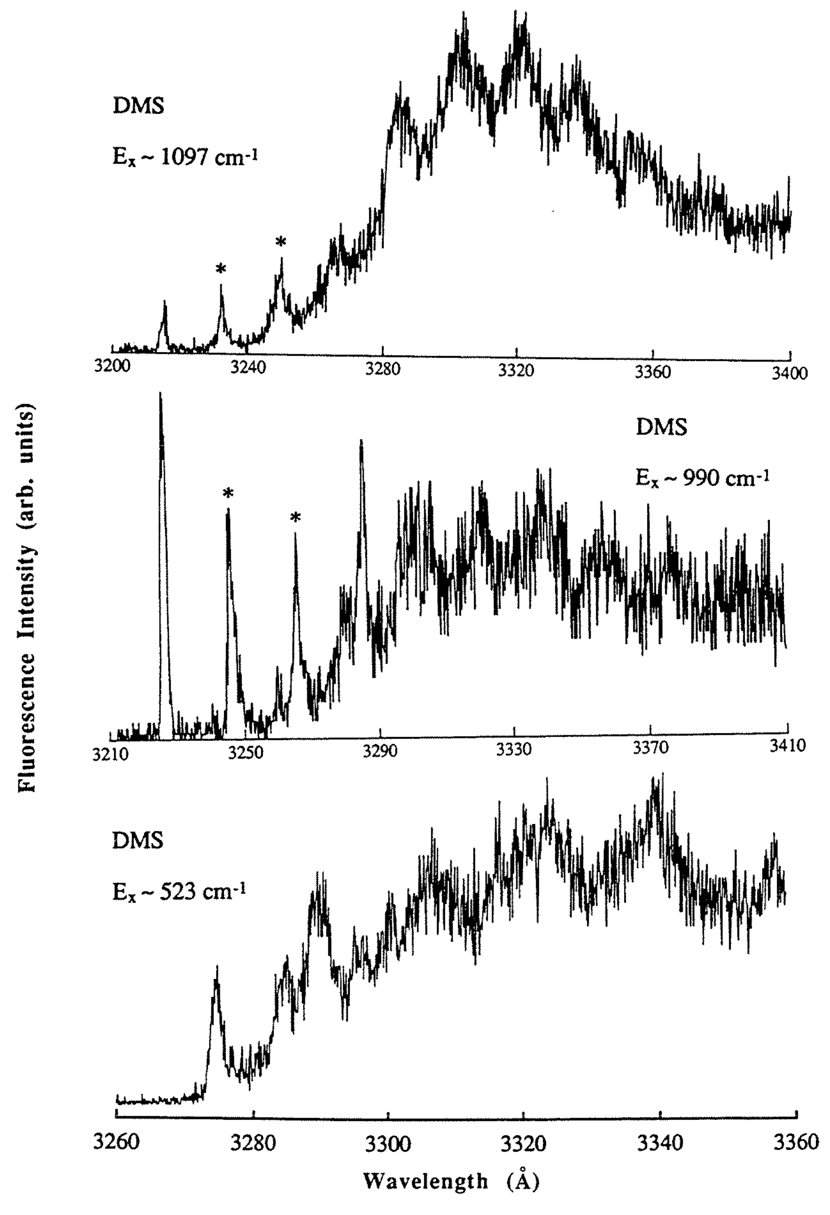
DMS
$E_x \sim 1097\ cm^{-1}$
*
*
3200
3240
3280
3320
3360
3400
DMS
$E_x \sim 990\ cm^{-1}$
*
*
3210
3250
3290
3330
3370
3410
DMS
$E_x \sim 523\ cm^{-1}$
3260
3280
3300
3320
3340
3360
Wavelength (Å)
Fluorescence Intensity (arb. units)

Fig. 7.5

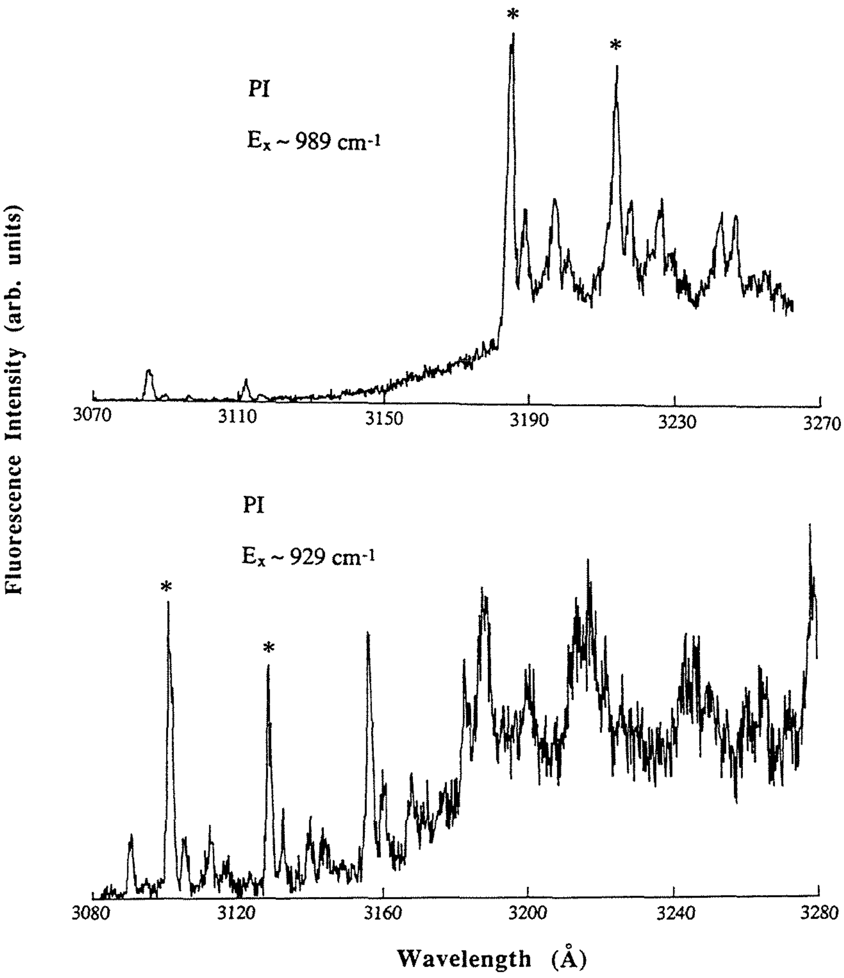
PI
$E_x \sim 989$ cm^{-1}
*
*
3070
3110
3150
3190
3230
3270
PI
$E_x \sim 929$ cm^{-1}
*
*
3080
3120
3160
3200
3240
3280
Fluorescence Intensity (arb. units)
Wavelength (Å)

Fig. 7.6

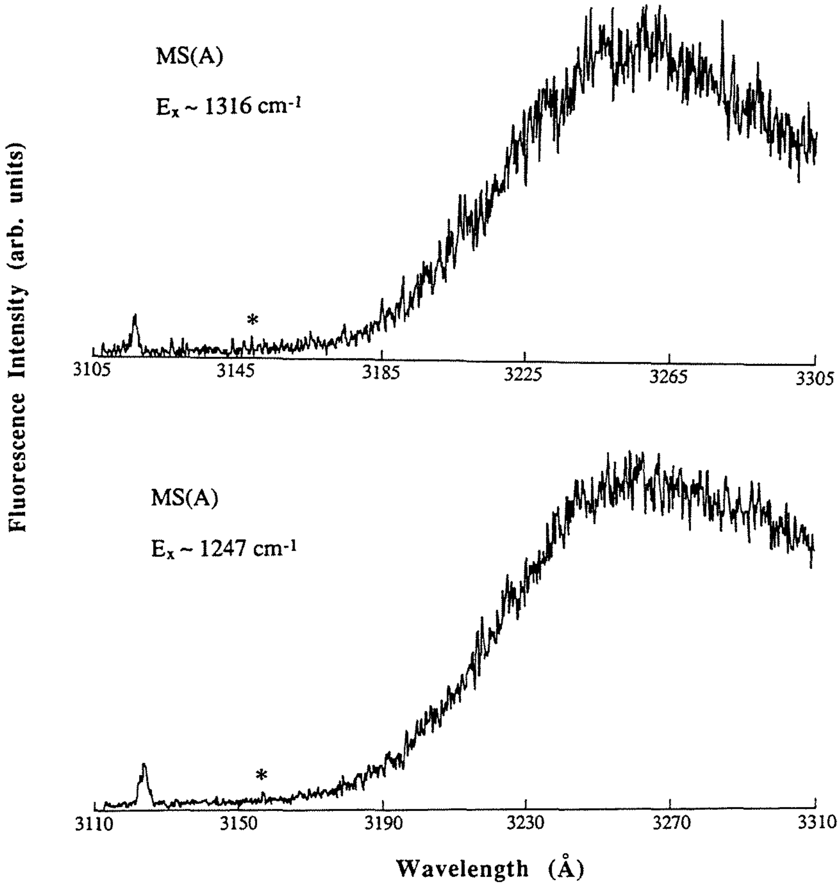
MS(A)
$E_x \sim 1316$ cm^{-1}
*
3105
3145
3185
3225
3265
3305
MS(A)
$E_x \sim 1247$ cm^{-1}
*
3110
3150
3190
3230
3270
3310
Fluorescence Intensity (arb. units)
Wavelength (Å)

Fig. 7.7

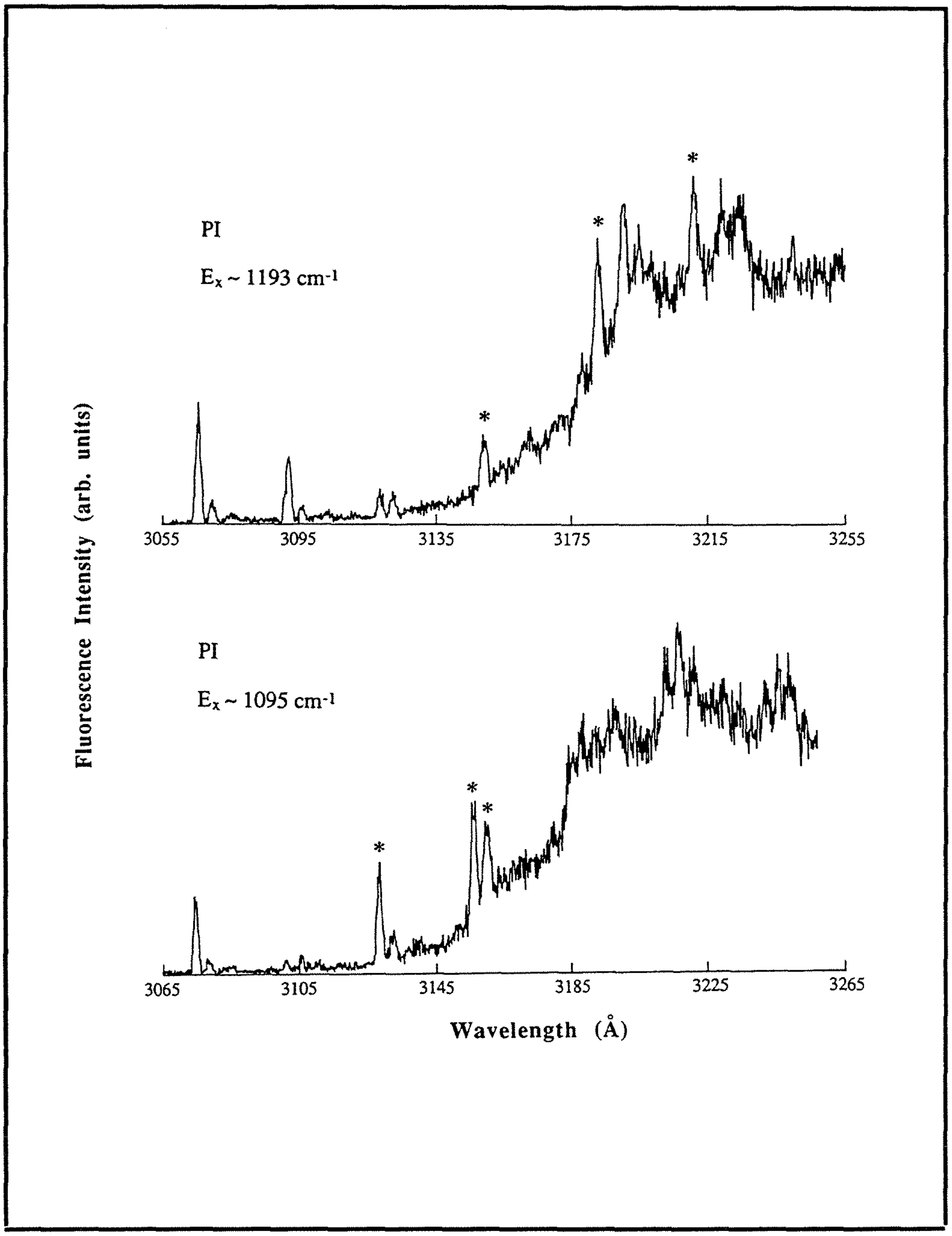
PI
$E_x \sim 1193\ cm^{-1}$
*
*
*
3055
3095
3135
3175
3215
3255
PI
$E_x \sim 1095\ cm^{-1}$
*
*
*
3065
3105
3145
3185
3225
3265
Fluorescence Intensity (arb. units)
Wavelength (Å)

Fig. 7.8

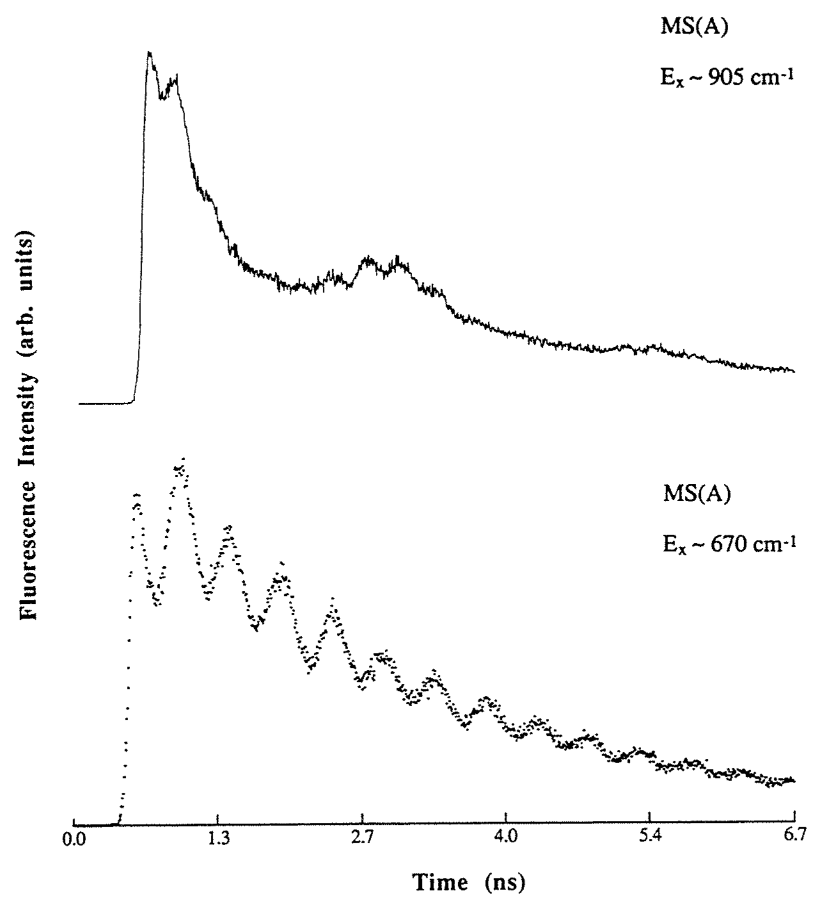
MS(A)
$E_x \sim 905$ cm^{-1}
MS(A)
$E_x \sim 670$ cm^{-1}
Fluorescence Intensity (arb. units)
0.0
1.3
2.7
4.0
5.4
6.7
Time (ns)

Fig. 7.9

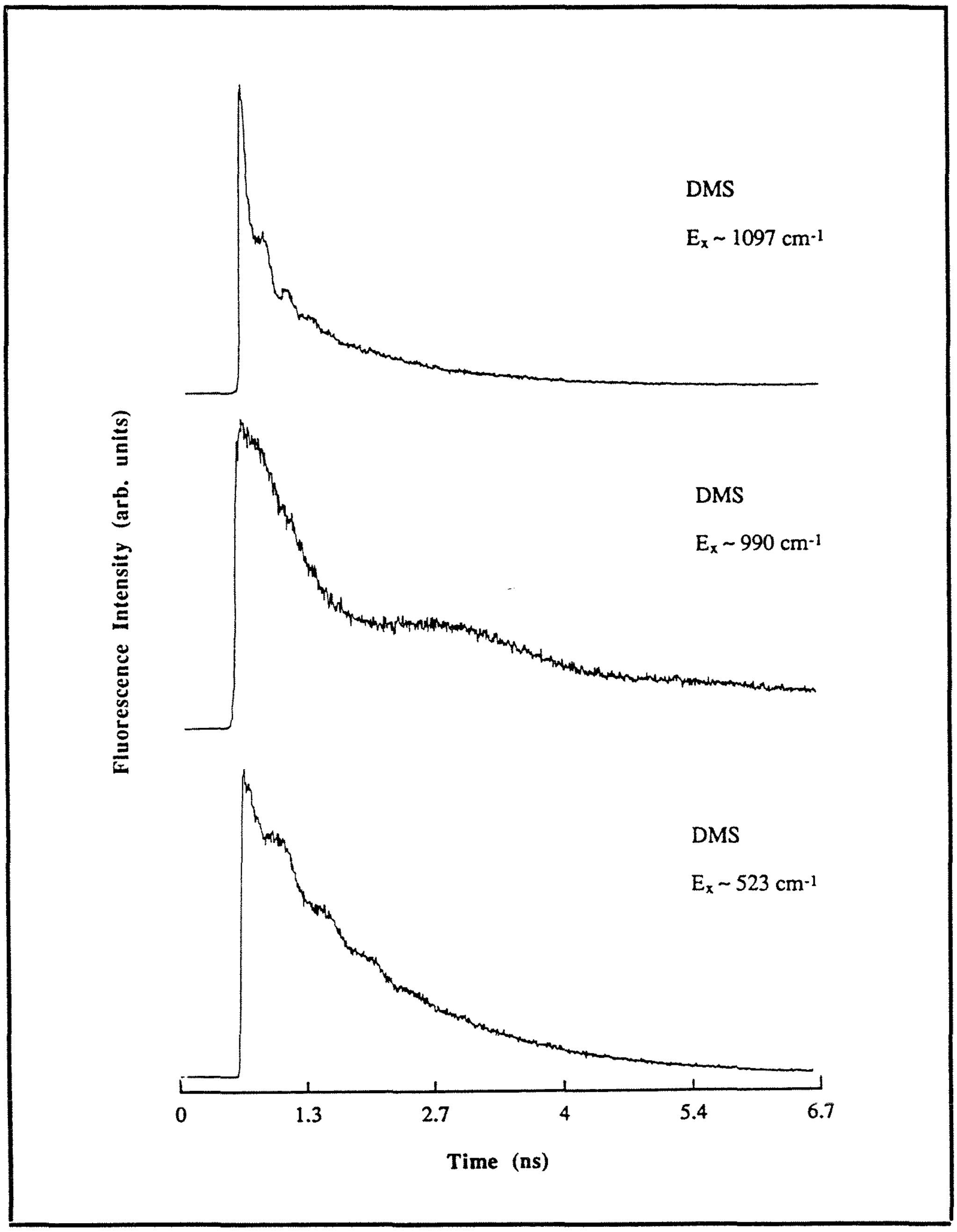
DMS
$E_x \sim 1097\ \mathrm{cm}^{-1}$
DMS
$E_x \sim 990\ \mathrm{cm}^{-1}$
DMS
$E_x \sim 523\ \mathrm{cm}^{-1}$
Fluorescence Intensity (arb. units)
0
1.3
2.7
4
5.4
6.7
Time (ns)

Fig. 7.10

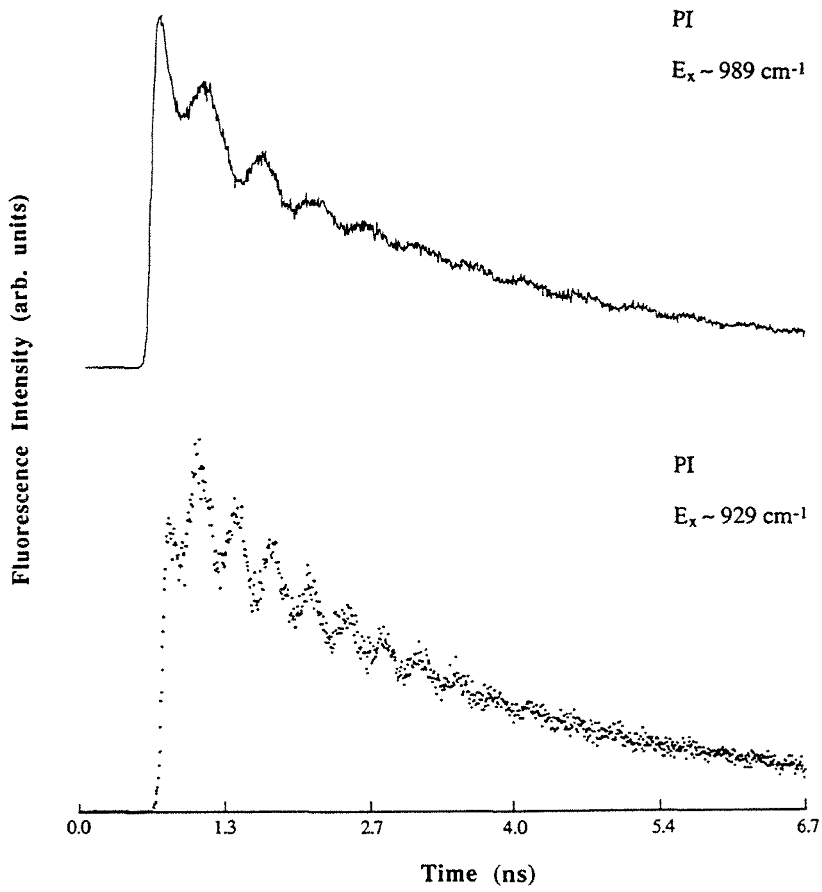
PI
$E_x \sim 989$ cm^{-1}
PI
$E_x \sim 929$ cm^{-1}
Fluorescence Intensity (arb. units)
0.0
1.3
2.7
4.0
5.4
6.7
Time (ns)

Fig. 7.11

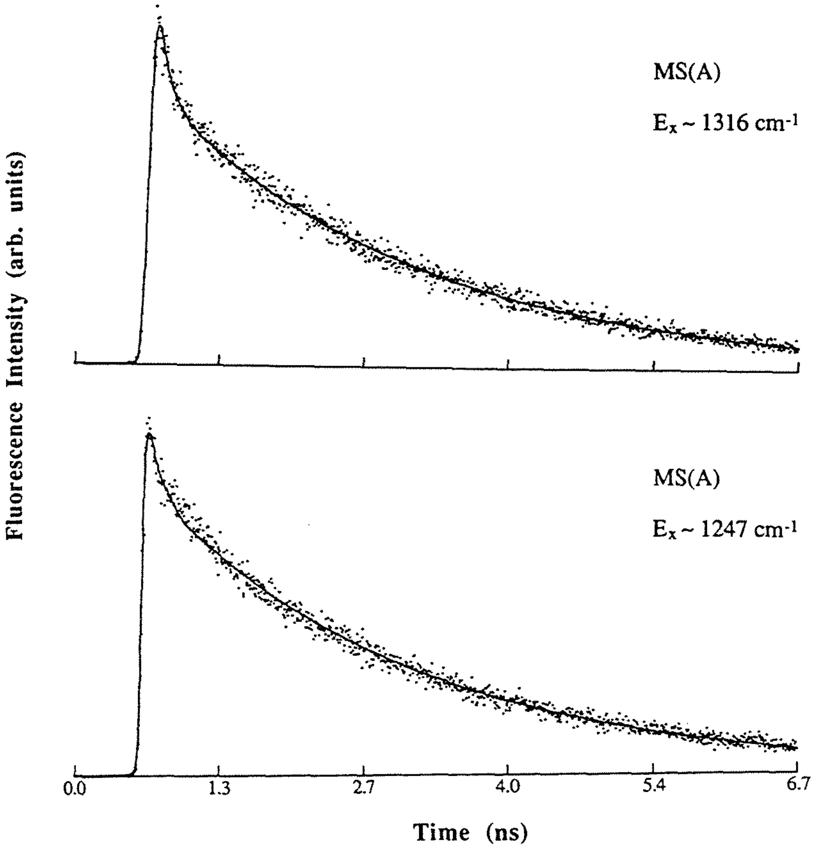
Fluorescence Intensity (arb. units)
MS(A)
$E_x \sim 1316\ \mathrm{cm^{-1}}$
MS(A)
$E_x \sim 1247\ \mathrm{cm^{-1}}$
0.0
1.3
2.7
4.0
5.4
6.7
Time (ns)

Fig. 7.12

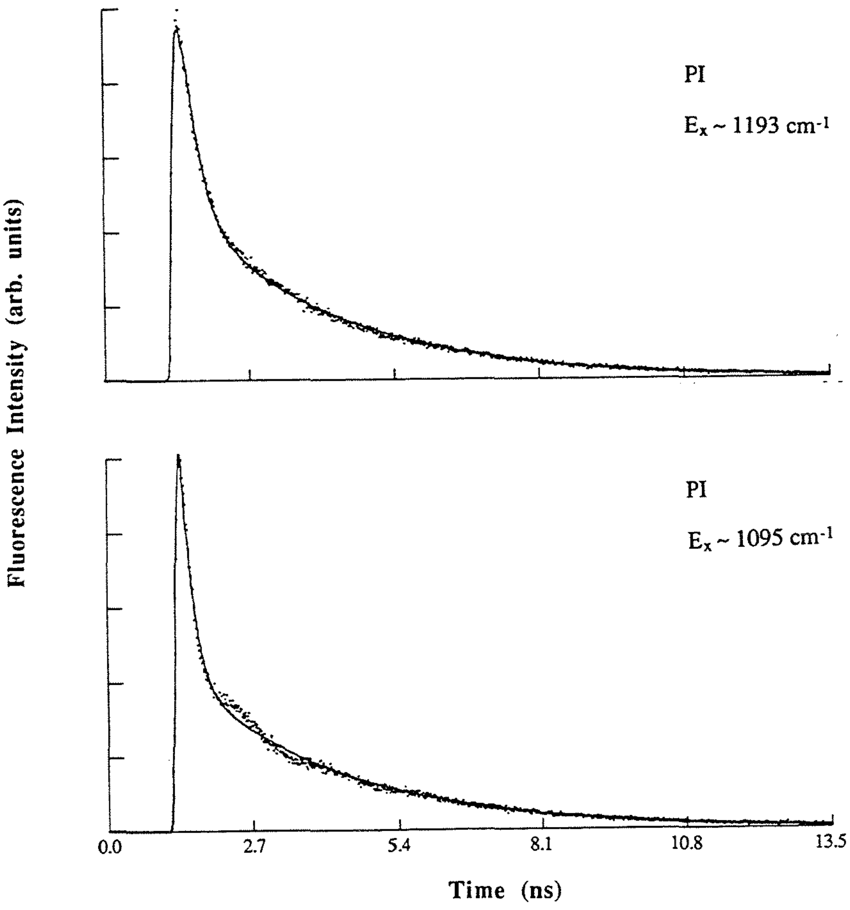
Fluorescence Intensity (arb. units)
PI
$E_x \sim 1193$ cm^{-1}
PI
$E_x \sim 1095$ cm^{-1}
0.0
2.7
5.4
8.1
10.8
13.5
Time (ns)

Fig. 7.13

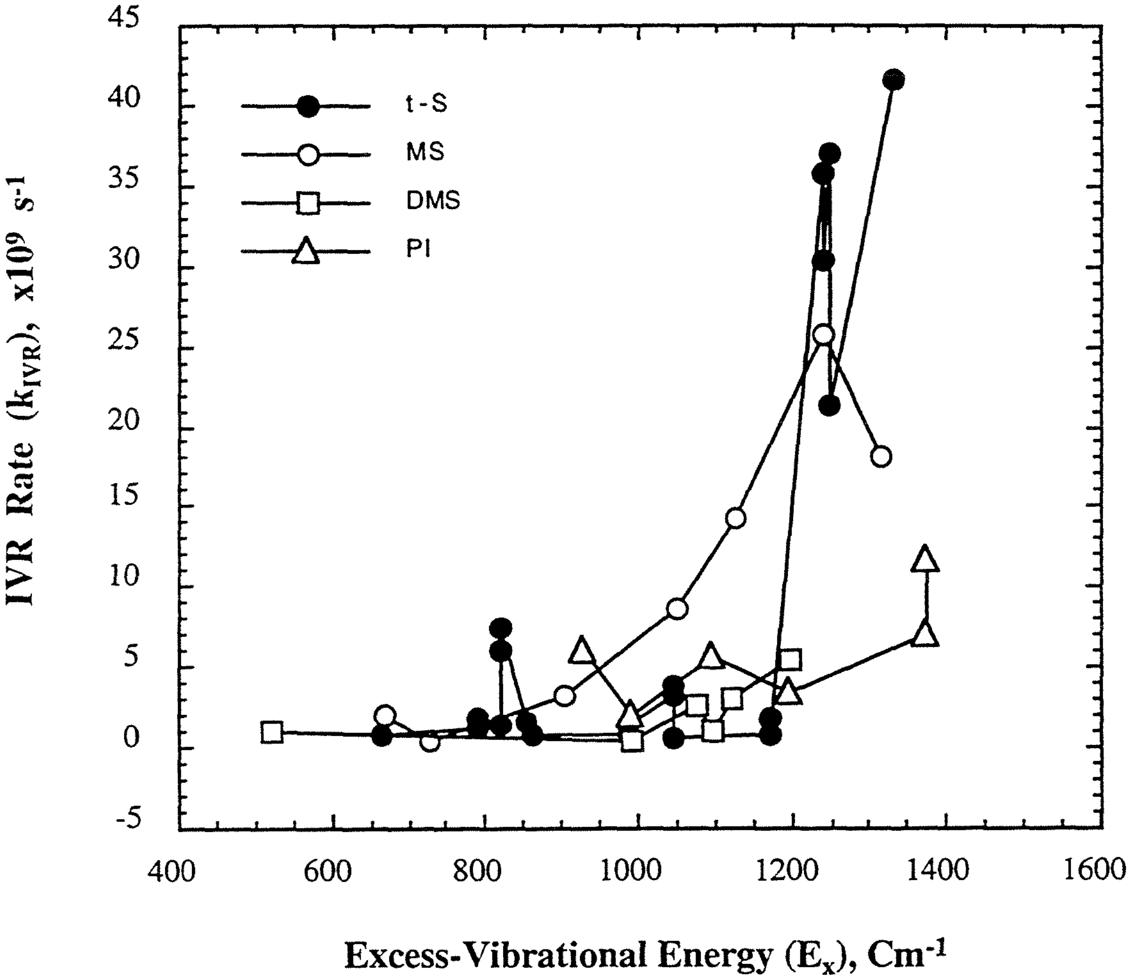
45
40
35
30
25
20
15
10
5
0
-5
400
600
800
1000
1200
1400
1600
t-S
MS
DMS
PI
IVR Rate (k_{IVR}), x10^9 s^{-1}
Excess-Vibrational Energy (E_x), Cm^{-1}

Fig. 7.14

CHAPTER 8

STRUCTURAL EFFECTS ON INTRAMOLECULAR VIBRATIONAL DYNAMICS (II): PHOTOISOMERIZATION REACTION IN SUBSTITUTED *TRANS*-STILBENES

Portions of this chapter are taken from the following published communication:
"Ultrafast Dynamics of Isomerization Reactions: Structural Effects in Stilbene(s),"
by L. Bañares, A. A. Heikal, and A. H. Zewail, *J. Phys. Chem.* 96, 4128 (1992).

8.1 INTRODUCTION

The photoisomerization of *trans*-stilbene (t-S) is one of the most extensively studied photochemical reactions, both theoretically and experimentally (for reviews see ref. [1,2]). It is known that photoisomerization reaction in t-S proceeds through a low-frequency large-amplitude motion of the phenyl rings and involves a large amount of the ethylenic torsion. Furthermore, steric repulsion, electron conjugation, and IVR play a major role in the isomerization dynamics in *trans*-stilbene.

Functional groups has been used as substituents to probe the nature of the potential energy surface and the reaction coordinate involved in the isomerization dynamics [1,2]. Steric constraints were used to probe the nuclear motions involved in the reaction coordinate. For example, the primary motion for isomerization is ethylenic torsion and that of the phenyl torsion is less important in the reaction as shown from studies on the isomerization of 1,1'-biindanylidene and 5,6,11,12-tetrahydrochrysene [3-7]. Similar conclusion has been reached by studying the isomerization dynamics of deuterated *trans*-stilbene in isolated-molecule and solution environments [8-15]. Furthermore, the influence of the functional groups on the isomerization pathway has been studied by directly monitoring the triplet state with transient-absorption method [16-23] and by triplet-quenching studies of the isomerization yields [23,24]. The nature of the substituent could have a profound effect on the excited-state mechanism through the coupling between the singlet and triplet manifolds. When the substituent enhances the singlet-triplet coupling (*e.g.* nitro-group), the triplet mechanism becomes more competitive. On the other hand, the alkyl substitution favors the singlet mechanism. However, in a few cases such as bromostilbene, a combination of both singlet and triplet mechanisms could be involved in the isomerization process [24].

Specific functional groups could be used to examine different influential parameters involved on intramolecular dynamics, such as IVR or the isomerization reaction in *trans*-stilbene molecule. Of particular interest is the contribution of the electronic conjugation throughout a molecule to the isomerization reaction in *trans*-stilbene as well as the number of atoms, symmetry, and constrained reaction-coordinate (*i.e.* C_e-C_e double-bond). In this chapter, a series of experimental studies on the isomerization dynamics in a designed set of molecules is described. For these studies, trans-stilbene (t-S), 4-methoxy-*trans*-stilbene (MS), 4,4'-dimethoxy-*trans*-stilbene (DMS), 4,4'-dihydroxystilbene, *trans*-β-1-cyclo-(hexane)-styrene (TCHS), and 2-phenylindene (PI) were used as model systems. The chemical structures of these molecules are shown in Fig. 7.1 and 8.1.

This chapter is arranged as follows: the experimental set-up and the data-analysis technique are described in section (8.2) followed by the results and discussion in section (8.3). The conclusion and references are outlined in sections (8.4) and (8.5), respectively.

8.2 EXPERIMENTAL

Time-resolved fluorescence measurements, presented in this chapter, were performed using an time-correlated single photon counting technique which has been described in Chapter 2. To generate dye-laser wavelengths in the range 550-667 nm, different dye solutions were prepared using DCM (1.5×10^{-3} M in mixture of ethylene glycol and benzyl alcohol with a ratio of 3:2 by volume), R6G, and R110 (both 2×10^{-3} M in ethylene glycol). For frequency doubling, angle-tuned and appropriately cut 1-cm thick $LiIO_3$ (type I) and KDP (type I) crystals were used.

Substituted *trans*-stilbenes were heated (typical temperatures, 90, 110, 180, 100, 90, 120 °C for t-S, MS, DMS, DHS, TCHS, and PI, respectively) in a glass nozzle with a pinhole diameter *(d)* of ~80 μm. The backing pressures of the carrier gas (helium) were in the range of 20-40 psi. The resulting free jet interacted with the laser pulses at a distance *(x)* ~2 mm from the nozzle orifice (*i.e. x/d*>30).

Trans-stilbene (Aldrich, 96%), 4-methoxy-trans-stilbene (Parish, unknown purity), and 4,4'-dimethoxy-*trans*-stilbene (Aldrich, 97%), and 4,4-dihydroxystilbene (ICN Biomedicals) were used without further purification. 2-Phenylindene was synthesized following the method described by Greifenstein *et al.* [25]. $_1$H NMR and mass spectra were recorded to examine the purity of the synthesized compound [26]. The results of $_1$H NMR are in agreement with those in ref.[26]. For *Trans*-β-1-cyclo-(hexane)-styrene, see ref. [27].

Since the excitation spectra of these stilbene derivatives were not known at the time of these experiments, the vibrational levels in the S_1 electronic state were localized by a manual scanning of the dye laser. During the scan, the monochromator slit was completely open and the detection wavelength was fixed at a value far to the red of the excitation-laser wavelength. The reddest excitation band was considered to be the electronic origin of the $S_1 \leftarrow S_0$ transition in substituted stilbenes. To rule out the possibility of assigning a hot band as the S_1-electronic origin, the dependence of the band intensity on the carrier-gas backing pressure has been investigated.

8.3 RESULTS AND DISCUSSION

8.3.1 Radiative Fluorescence Lifetime

Quantum yield measurements of the parent t-S molecule suggest that the fluorescence lifetime of the 0_0^0 transition represents the radiative lifetime and the intersystem crossing is negligible [28-30]. Unfortunately, similar quantum yield measurements for the substituted stilbenes are not available yet. Compared with the parent *trans*-stilbene, the fluorescence lifetime of the substituted stilbenes increases due to specific structural effects and therefore a similar conclusion will be adapted. Consequently, the fluorescence lifetime of the 0_0^0 transition in substituted stilbenes represents the radiative lifetimes and the intersystem-crossing channel will be considered closed [31]. The fluorescence decay of the S_1-state origin in t-S, MS (isomer A), DMS, DHS, TCHS, and PI molecules are shown in Fig. 8.2 and 8.3 and the measured radiative lifetimes are listed in Table (1).

(a) *Trans*-stilbene

The electronic origin of the $^1B_u \leftarrow {}^1A_g$ transition in jet-cooled *trans*-stilbene (t-S) is located at 32243 cm^{-1} (3101.4 Å) and has a fluorescence lifetime of 2.63±0.01 ns [8,28-35], Fig. 8.2. Absolute quantum yield measurements on *trans*-stilbene indicates that the 2.63 ns represents the pure radiative lifetime (τ_{rad}); and the intersystem-crossing or any other nonradiative channels are closed [28-30].

(b) 4-Methoxystilbene

The fluorescence excitation spectra and single vibronic level dispersed fluorescence spectra of 4-methoxystilbene (MS) reveal two stable conformers (A and B) [36]. The origins of the two S_1-states in these two conformers are shifted by ~278 cm^{-1}. Topp and coworkers [37] measured the rotational constant of both conformers in the S_1-state (A: 334.4 ± 0.3 and B: 329.8 ± 0.3 MHz) using rotational coherence measurements of this molecule. The S_1-state electronic origin (30765.5 cm^{-1}) in the first conformer (A) is red-shifted by 1478 cm^{-1} compared to that in *trans*-stilbene. The fluorescence lifetime of the vibrationless electronic

$S_1 \leftarrow S_0$ transition in isomer A increases by ~10% (2.96±0.01 ns) compared to that in t-S, Fig. 8.2. A slightly shorter lifetime (2.84 ± 0.01 ns, not shown) was measured for the second conformer (B) under the same experimental conditions.

(c) 4,4'-Dimethoxystilbene

The electronic origin of the $S_1 \leftarrow S_0$ transition in 4,4'-dimethoxystilbene is located at 29995.5 cm^{-1}, which is 2248 cm^{-1} to the red of that origin in *trans*-stilbene. The red shift due to *p*-di-methoxy substitutions (DMS) is not additive compared with that in *p*-mono-methoxy substitution (MS). This red shift represents a dramatic stabilization in the S_1-electronic state upon symmetric para-methoxy substitutions of t-S due to the electron-donating ability of the OCH_3 group. On the other hand, the fluorescence lifetime of the 0_0^0 transition is 2.96±0.06 ns, *i.e.* ~10% larger than that in the unsubstituted stilbene, see Fig. 8.2. This lifetime is about the same as that measured for MS (isomer A).

(d) 4,4'-Di-hydroxystilbene

The electronic origin of the $S_1 \leftarrow S_0$ transition in isolated 4,4'-di-hydroxystilbene (DHS) is not known. However, with manual scanning of the dye laser, the reddest excitation band (30451 cm^{-1}) was located at ~1793 cm^{-1} to the red of the electronic origin of the S_1-state in *trans*-stilbene and considered as the 0_0^0 transition in DHS. The fluorescence emission of this band and other vibrational bands in the S_1-state is very weak and show spectral congestion at low energies (see Fig. 8.4). The fluorescence lifetime of the 0_0^0-transition in DHS was measured as 3.6 ns (compared with 2.67 ns for t-S) (see Fig. 8.3).

(e) *Trans*-β-1-cyclo-(hexane)-styrene

The vibrationless electronic $S_1 \leftarrow S_0$ transition in *trans*-β-1-cyclo-(hexane)-styrene (TCHS) (can also be called *t*α-Phenyl-β-(1-cyclohexane)-ethylene) is located at 31417 cm^{-1} [38], which is 980 cm^{-1} to the red of that in *trans*-stilbene. Furthermore, the fluorescence lifetime of the S_1-origin in TCHS is ~8.9 ns (see Fig. 8.3) which is considerably larger than that of t-S (2.67 ns). The dispersed fluorescence spectrum of the 0_0^0-transition in TCHS is shown in Fig. 8.5.

(f) 2-Phenylindene

The electronic origin for the $S_1 \leftarrow S_0$ transition in 2-phenylindene (PI) is located at 31416.9 cm^{-1} (*i.e.* ~ 826.6 cm^{-1} to the red of that in t-S) [38]. The fluorescence lifetime of the S_1-electronic origin in PI is estimated as 3.20±0.02 ns and the fluorescnce decay is shown in Fig. 8.3.

8.3.2 Excess-Energy Dependence of Fluorescence Lifetime

The excess-energy dependence of the fluorescence lifetime in jet-cooled *trans*-stilbene has been studied previously by different groups [8,28,29,32,39,40] and reproduced here as a control experiment. Our measurements were extended to excess vibrational energies up to ~3500 cm^{-1} in the S_1-manifold and show excellent agreement with those previous studies; see Fig. 8.6.

Similar excess-energy dependent measurements of the fluorescence lifetime have been carried out for substituted stilbenes (*i.e.* MS, DMS, DHS, TCHS, and PI) in an attempt to study the nonradiative channel in these substituted stilbenes. Then by comparing the results with the substituted trans-stilbene, structural effects on the isomerization dynamics can be separated and better understanding of the key parameters in the reaction in t-S can be reached.

As observed in the parent *trans*-stilbene [8,28,29,32,39,40], the excess-energy dependence of the fluorescence lifetime (τ) in substituted stilbenes reveals the following three energy regions [see Figs. 8.6-8.11]. These regions are low-, threshold-, and high-energy regions and will be discussed below.

(a) Energy-Independent Region

Upon the excitation of a single vibronic level in the S_1-electronic state in *trans*-stilbene, up to S_1+1000 cm^{-1}, the fluorescence decays as a single exponential function with a decay time equals to the radiative lifetime (2.67 ns) [20]. The upper limit of this region has not changed upon *p*-methoxy substitution (MS). However, significant increase in this energy domain (up to ~2600 cm^{-1} above the S_1-electronic origin) was observed in DMS. Similar trend was observed in for DHS molecule where the fluorescence lifetime was independent of the excess-energy S_1+2200 cm^{-1}. The fluorescence lifetime in TCHS was energy-independent up to ~700 cm^{-1} above the S_1-origin. In 2-phenylindene, the upper limit of this region increases up to ~1600 cm^{-1}. Unlike *trans*-stilbene, the fluorescence lifetime of DMS and DHS show slight decrease in this region.

(b) The Threshold Energy

At a threshold energy in the S_1-manifold, the fluorescence lifetime starts to decrease, reflecting the onset of a nonradiative process which competes with the fluorescence channel in the S_1-state deactivation mechanism. In *trans*-stilbene, the threshold energy was estimated to be ~1250±50 cm^{-1} [8,28,29,32,39,40] and represents a barrier for the isomerization reaction in the parent t-S molecule. This threshold increases slightly to ~1330 cm^{-1} upon asymmetric para-methoxy substitution (MS isomer A) in comparison with ~3060 cm^{-1} due to symmetric para-methoxy substitution (DMS). For DHS, the threshold energy was estimated as ~2200 cm^{-1} above the S_1-origin. Similarly, the energy threshold in 2-phenylindene was estimated to be ~2460 cm^{-1}. A lower barrier (~800 cm^{-1}) was observed in the S_1-manifold of TCHS molecule. The uncertainty in the above estimates, especially in DMS, DHS, and PI, is mainly due to the slight changes in the fluorescence lifetime as the energy increases. More accurate values for the barriers in these molecules should be obtained by fitting these experimental results to RRKM calculations which must await the excitation spectra and vibrational-mode assignments in these derivatives.

(c) High-Energy Region

A significant decrease of the fluorescence lifetime of *trans*-stilbene has been observed at high excess vibrational energies, ranging from ~1200 to 3500 cm^{-1} above the S_1-state origin [31]. This observation suggests that a nonradiative process (namely, the photoisomerization reaction) is very efficient in that energy range, Fig. 8.6. The rate at which the fluorescence lifetime decreases with the excess-energy in MS is about the same as that in t-S even though the barriers are slightly different (see Fig. 8.7). However, the symmetric *p*-methoxy and *p*-hydroxy substitutions (DMS and DHS, respectively) change dramatically the excess-energy dependence of the nonradiative rate in comparison with t-S (see Fig. 8.8 and 8.9). The nonradiative rate increases very slowly with the excess energy in both DMS and DHS. Similar behavior was observed in the PI molecule, see Fig.

8.11. However, the nonradiative rate in TCHS is much faster than that observed in t-S or any other derivative used in these studies (Fig. 8.10).

8.3.3 Photoisomerization Reaction Dynamics in Substituted Stilbenes

8.3.3.1 Preliminaries

The influence of the functional groups on the isomerization pathway has been studied by directly monitoring the triplet state with the transient-absorption method [16-23] and by triplet-quenching studies of the isomerization yields [23,24]. The nature of the substituent could have a profound effect on the excited-state mechanism through the coupling between the singlet and triplet manifolds. When the substituent enhances the singlet-triplet coupling (*e.g.* nitro-group), the triplet mechanism becomes more competitive. On the other hand, the alkyl substitution favors the singlet mechanism [2]. However, in a few cases such as bromostilbene, a combination of both singlet and triplet mechanisms could be involved in the isomerization process [2].

Para-substitutions in *trans*-stilbene are not expected to affect the reaction coordinate of photoisomerization through steric interactions since the substituent is well separated from the ethylenic moiety. However, the substituents may still play an important role in the isomerization dynamics through the following three mechanisms. First, the electronic conjugation throughout the molecule is expected to change upon electron-donor group substitution, and consequently the C_e-C_e double-bond order will change. Intuitively, the higher the bond-order, the larger the barrier for the torsional motion (*i.e.*, isomerization reaction coordinate). The electron-donating capacity of the functional group will determine the significance of the electron conjugation in the overall isomerization dynamics. Second, the substituent contribution to the overall vibrational energy relaxation mechanism (IVR) could be significant. This contribution will be mainly due to the substitution effects on the density of states compared with that in the parent molecule. Third, the substitution can open another nonradiative channel to compete with isomerization and fluorescence in the deactivation process of the S_1-state. This possibility will be ruled out for the substituted stilbenes studied in this chapter due to the following reason. Quantum yield measurements of the parent t-S molecule suggest that the fluorescence lifetime of the 0^0_0-transition represents the radiative lifetime and the intersystem crossing is negligible [28-30]. Unfortunately, similar quantum yield measurements for the substituted stilbenes are not available yet. Compared with the parent *trans*-stilbene, the fluorescence lifetime of the substituted stilbenes increases due to specific structural effects, *i.e.*, a similar conclusion will be adapted. Consequently, the fluorescence lifetime of the 0^0_0 transition in substituted stilbenes represents the radiative lifetimes and the intersystem-crossing channel will be considered closed.

8.3.3.2 Asymmetric *p*-Methoxy Substitution

Structural effects on stilbene's spectra have been extensively investigated in solution [42-49]. Para substitutions introduce a red shift which increases with the polarizability/size of the substituent and is approximately additive in going from mono- to di-substituted stilbenes [44-46]. For *p*-methyl groups, the vibrational structure is slightly changed from that of the parent stilbene. It is important to realize that the methyl torsion could be coupled to the low-frequency modes of the stilbene. On the other hand, substitution in the meta-ring positions has little effect on the spectrum where the distinct conformers have similar spectra. Furthermore, ortho-substitution introduces significant steric hindrance, causing the phenyl rings to twist out of plane (about the ethylene/phenyl-ring bond) and impacts the absorption and fluorescence spectral features.

Asymmetrically substituted stilbenes, with electron-donating and -accepting groups in the two para positions, could display even more different behavior [50-52]. In these types of systems, twisted intramolecular charge transfer (TICT) becomes accessible and the charge-transfer state (which is a nonradiative state) can provide another relaxation pathway which competes with the isomerization channel(s) [2].

Recently, Troxler *et al.* [37] have identified two conformers, *syn* (isomer I) and *anti* (isomer II) rotamers, using rotational coherence spectroscopy. In both conformers, the methoxy groups are coplanar with the mean plane of the aromatic t-S molecule. The rotational constants (B+C) were estimated as 334.4±0.3 and 329.8±0.3 MHz for isomer A and B, respectively. These isomers were also distinguished by Siewert and Spangler [36] using the fluorescence excitation and dispersed fluorescence spectra of jet-cooled p-methoxy-trans-stilbene and p-methoxy-p'-methyl-trans-stilbene. The S_1-origins of these two conformers are shifted by 267 cm^{-1} [36,37].

Majors *et al.* [29] studied asymmetric substitution effects on photoisomerization dynamics in jet-cooled 4-chloro-stilbene (4CS) and 4-methyl-stilbene (4MeS). The energy dependence studies of the nonradiative rate-constant reveal that there is *no difference* in the isomerization barrier-height in substituted stilbenes (4CS and 4MeS) and the bare molecule. Furthermore, the isomerization rate is invariant upon para-chlorine and para-methyl substitutions in *trans*-stilbene. The invariance of the isomerization rate upon para-methyl substitution has been attributed to *undemocratic* vibrational energy redistribution in which all the vibrational modes are not involved. The intersystem crossing channel was found to be open with a quantum yield of 0.65±0.03 in 4-chloro-stilbene. However, the nonradiative decay rate was also invariant upon the para-chlorine substitution in *trans*-stilbene. The intersystem crossing in 4CS constitutes a separate decay channel which does not interfere with the nonradiative isomerization channel [29]. Rademann *et al.* [30] have examined the role that IVR might play in the overall isomerization dynamics of isolated *trans*-stilbene by studying alkyl substitutions in the para position of the phenyl moiety in *trans*-stilbene (*i.e.* 4-ethyl-*trans*-stilbene, and 4-*n*-propyl-*trans*-stilbene). These authors have reported that ethyl and propyl para-substitution of *trans*-stilbene enhances the photoisomerization rates. Furthermore, the isomerization barrier height in *trans*-stilbene (1300±50 cm^{-1}) has been reduced upon para-ethyl (1100±100 cm^{-1}) and para-propyl (1000±100 cm^{-1}) substitutions. The general arguments based on the role of IVR and the implications of statistical theories (*e.g.* RRKM theory) indicate that the isomerization rate should be retarded in those substituted stilbenes [29,30,41].

Our characterization of the isomerization dynamics in para-methoxy substituted *trans*-stilbene (MS, isomer A) shows a slightly different trend than that observed in p-M-trans-stilbenes (M = ethyl, methyl, propyl, and chlorine) [29,30]. The para-methoxy substitution in *trans*-stilbene (MS isomer A) enhances (by ~10%) the isomerization barrier height (~1330 cm^{-1}). However, above that energy barrier, the isomerization rates are about the same in both substituted and bare *trans*-stilbene.

Since a steric effect upon para-methoxy substitution in *trans* stilbene is unlikely, the observed difference in the isomerization barrier-height could be electronic in origin. The electron-donating capacity of the methoxy (OCH_3) is larger than that of methyl (CH_3), ethyl (CH_2CH_3), and propyl ($CH_2CH_2CH_3$) groups. In the S_1-electronic state, those additional delocalized electrons find their way to the ethylene moiety and enhance the double-bond order. Consequently, the electronic conjugation will contribute to the strong overlapping between the π-electrons and the double-bond order will increase. Simple Hückel molecular orbital calculations [53] support these arguments and predict an increase in the bond order of ethylenic double bond, in the excited state, upon para-methoxy substitution.

8.3.3.3 Para-Symmetric Substitution

Zeglinski and Waldeck [54] studied the multidimensionality of the isomerization potential energy surfaces and the solvent effects on overall dynamics using symmetrical para-substitutions of methyl (CH_3), methoxy (OCH_3), and hydroxy (OH) groups in *trans*-stilbene in solution. The activation barrier to isomerization for 4,4'-dimethylstilbene, in an homologous series of *n*-alkane solvents, agrees quite well with that of *trans*-stilbene in the same solvents [55]. This lack of change in the barrier heights comes in full agreement with the jet-cooled studies of 4-methylstilbene by Majors *et al.* [29]. In contrast, 4,4'-dimethoxystilbene (DMS) and 4,4'-dihydroxystilbene (DHS) in *n*-alkanes show a large barrier height (~5.7 kcal/mol) for the isomerization reaction in comparison with that of bare *trans*-stilbene. The increase in the barrier-height in both DMS and DHS were attributed to the increases of the double-bond order in the ethylene moiety caused by the presence of the oxygen atoms [55,56] and the electron-donating ability of the methoxy and hydroxy groups. Interesting enough, no significant effect on the barrier height (~3.5 kcal/mole) was observed when a weak electron-donor group (*e.g.* methyl) was used in symmetric *p*-substituted *trans*-stilbene (*i.e.* 4,4'-dimethylstilbene).

The energy dependence of the nonradiative rate-constant in isolated, jet-cooled 4,4'-dimethoxystilbene shows that the symmetric para-methoxy substitution has a profound effect on the isomerization dynamics in *trans*-stilbene; see Fig. 8.6. The isomerization threshold in DMS is ~2.4 times larger (~8.48 kcal/mol) than that in the parent molecule (~3.5 kcal/mol). The observed increase in the isomerization barrier-height in the isolated molecule agrees, in general, with the solution studies by Zeglinski and Waldeck [54]. Preliminary Hückel molecular orbital calculations [53] predict an increase of the double-bond order in DMS compared with that in both MS and t-S. Therefore, the observed increase in the isomerization barrier-height could be attributed to enhancement of the electron conjugation upon the methoxy (electron donor) substitution which, in turn, increases the C_e-C_e double-bond order. However, these simplified calculations failed to predict a larger increase in the double-bond order upon the symmetric *p*-dimethoxy substitution (DMS) in comparison with either *trans*-stilbene or asymmetric *p*-methoxy substituted stilbene (MS). Significant reduction in the isomerization rate above the barrier is observed in DMS in comparison with the parent molecule, Fig. 8.8. The large size of the methoxy group, in the para positions in *trans*-stilbene molecule (DMS) is expected to slow down the isomerization reaction rate due to the increase in the moiety involved in the reaction coordinate.

To examine the above mentioned arguments concerning the effects of electron conjugation and the size of the functional group on the isomerization barrier-height and rates, similar measurements were carried out on 4,4'-dihydroxystilbene (DHS). The functional group (OH) in this model system has a larger electron-donating ability and, at the meantime, smaller size than the methoxy group. The excess-energy dependence of the nonrdiative rate in DHS is shown in Fig. 8.9. Even though, the isomerization barrier-height in 4,4'-dihydroxystilbene (2200 cm^{-1}) is larger than that in *trans*-stilbene (1250 cm^{-1}), it is lower than that in 4,4'-dimethoxystilbene (3060 cm^{-1}). Above the barrier, the isomerization rate is much slower than that observed in the parent t-S molecule. However, this rate is the same as that in DMS molecule. The increase in the barrier height and the reduction of the isomerization rate above the barrier are consistent with our arguments regarding the role of the electron conjugation in the isomerization dynamics. However, the invariance of isomerization rate (above the barrier) in both DHS and DMS is unexpected considering the difference of the size of OH and OCH_3 groups. Furthermore, due to the increase of the electron-donating ability upon OH substitutions, one would expect a larger barrier for the isomerization reaction in comparison with OCH_3 substitution. However, the value of the barrier height given above for both DHS and DMS must be considered as an approximate since the exact S_1-origin in DHS and DMS is not exactly known.

8.3.3.4 Limited Electron Conjugation

The electronic resonance between the π-orbitals throughout *trans*-β-1-cyclo-(hexane)-styrene (TCHS) molecule is *limited* compared with that in the parent *trans*-stilbene (see Fig. 8.1). TCHS was used as a model system for further testing of the electron conjugation role in the isomerization reaction in *trans*-stilbene. Consequently, the rate constant of the S_1-state in jet-cooled TCHS was measured as a function of the excess-energy. Unlike DMS and DHS, the limited electronic resonance in TCSH molecule will reduce the electron conjugation, *i.e.* a reduction of the double-bond order is expected in comparison with that in the parent molecule.

The barrier height for the isomerization reaction in the S_1-state of TCHS is ~800 cm^{-1} which is ~34% lower than that in *trans*-stilbene (~1250 cm^{-1}) and ~26% of that in DMS molecule (~3060 cm^{-1}). Furthermore, above the isomerization barrier in TCHS, the rate is significantly faster than that in either t-S, DMS, or DHS (see Fig. 8.10). These experimental findings for TCHS, combined with those of DMS, DHS and t-S, support our arguments regarding to the key role of the electron conjugation in the isomerization dynamics.

8.3.3.5 C_e-C_e Torsionally Hindered Analog

The nature of the potential energy surfaces and the reaction coordinates involved in the isomerization dynamics, could be probed by using stilbene derivatives as model systems [2]. For example, the primary motion for isomerization is ethylenic torsion and that of the phenyl torsion is less important in the reaction as shown from studies on the isomerization of 1,1'-biindanylidene and 5,6,11,12-tetrahydrochrysene [3-7] (Figure 9 shows the chemical structure of these two molecules). A similar conclusion has been reached by studying the isomerization dynamics of deuterated *trans*-stilbene in isolated-molecule and solution environments [5-18].

The torsional motion around the ethylenic C_e-C_e double-bond is established to be the reaction coordinate of the isomerization dynamics in *trans*-stilbene [1,2]. However, studies on the temperature dependence of the isomerization dynamics of *m*-methyl-stilbenes in decane suggest that phenyl torsion around the C_e-C_{ph} single-bond can be competitive with the ethylenic torsion and must be considered as the second dimension of the potential energy surface [3]. The restriction of the phenyl torsion by intramolecular chemical bridging, as in 1,1'-biindanylindene molecule, increases the isomerization rate [4] in comparison with the parent *trans*-stilbene. Furthermore, the spectral features of 1,1'-biindanylindene are similar to that of *trans*-stilbene at very low temperature in a viscous environment [57,58]. On the other hand, when the torsional motion around both C_e-C_e double bond and C_e-C_{ph} single bond are restricted (as in 5,6,11,12-tetrahydrochrysene), the isomerization yield is zero and fluorescence quantum yield approaches unity [5]. Recently, quantum calculation on multidimensional isomerization-dynamics in *trans*-stilbene were carried out [59]. In these calculations, both C_e-C_e double-bond torsion and C_e-C_{ph} single-bond rotation (with higher energy) represent the reaction coordinates of the isomerization dynamics. The role of these reaction coordinates in the isomerization of stilbene in solution has been discussed [1,2].

To characterize the C_e-C_{ph} single-bond dynamics (as a possible second reaction coordinate in the isomerization dynamics), the central C_e-C_e double-bond in *trans*-stilbene must be constrained. As an electronic model system for these studies, 2-phenylindene (PI) offers a unique opportunity to isolate and characterize the rotation of the C_e-C_{ph} single-bond. However, this rotational motion around the $\mathrm{C_e}$-$\mathrm{C_{ph}}$ single-bond in both *trans*-stilbene and 2-phenylindene might not be exactly the same.

The energy dependence of the nonradiative rate-constant in 2-phenylindene reveals a threshold of ~2460 cm^{-1} at which an efficient nonradiative process is triggered. Above that barrier (which is ~40% larger than stilbene's), the nonradiative rate is very low compared to that in *trans*-stilbene (Fig. 8.11). The reaction coordinate involved in the nonradiative process in 2-phenylindene is most likely to be the rotational motion around the C_e-C_{ph} single-bond (see Fig. 8.1). The isomerization barrier in PI could be attributed to the steric interaction between the hydrogen atoms on both sides of the C_e-C_{ph} single-bond [60]. The C_e-C_{ph} single bond is expected to have some double-bond character in the excited state and the observed increase in the barrier height might explain the planarity of this molecule in its S_1-state.

8.3.3.6 Adiabatic vs. Non-adiabatic Reaction Meachanism

Orlandi and coworkers (fo reviews see ref.[1,2]) suggested a nonadiabatic potential energy surface for the isomerization reaction in *trans*-stilbene. In this model, the isomerization barrier in *trans*-stilbene is formed by the avoided (or possibly nonadiabatic) crossing of the ^1B_u and a doubly-excited ^1A_g-states. The

^1A_g state is believed to be localized on the phenyl rings with some delocalization and ionic character. Consequently, a red-shift of the $^1B_u(S_1) \rightarrow {}^1A_g(S_0)$ transition may signify that the barrier height *increases* as the red-shift of the S_1-state origin increases. Therefore, one might expect that the barrier will decrease in all the derivatives studied here (since the S_1-origin has been shifted to the red upon substitution, see Table (1)). This argument is consistent with the results of DMS, DHS, and PI molecules. On the other hand, the MS and TCHS results cannot be explained according to these arguments unless there are other factors that counteract the effect of the S_1-state stabilization on the barrier height. First, since the ^1A_g double excited state is believed to be polarized [1,2], the asymmetric *p*-methoxy substitution (MS) might stablize the ^1A_g state along with the S_1-state as well. Only in this case, the barrier height will not be affected by the substitution even though there is a significant red-shift of the S_1-state origin. Furthermore, this will be consistent with the work of Jortner's group [29,30]. However, studies on 275 nm absorption of anisole [21] and three deuterated derivatives (*e.g.* phenol [22], fluorobenzene [23], and chlorobenzene [24]) suggest that the changes on the electronic excitation (bonding and hence the vibrations) associated with the substituents are minor. This means that the electronic transition in anisole is localized to a large extent in the benzene ring and not strongly perturbed by the p-substituents. For TCHS molecule, the reduction of the electron delocalization between the two pheny rings (as argued above) might explain the lowering of the barrier height for isomerization.

8.4 CONCLUSION

Structural effects on photoisomerization reaction dynamics in jet-cooled substituted *trans*-stilbenes have been studied using picosecond time-resolved and laser-induced fluorescence spectroscopy. The excess-energy dependence of the nonradiative rate-constant reveals dramatic changes in the photoisomerization dynamics of symmetrically-substituted para-methoxystilbene (*i.e.* DMS) in comparison with the parent molecule (t-S) as well as the asymmetrical para-methoxystilbene (*i.e.* MS). The change in the photoisomerization parameters has been discussed in terms of the electron conjugation, IVR, and energy partitioning between vibrational subspaces. The excess-energy dependence of the nonradiative rate constant in DMS promoted a discussion about the adiabatic vs. nonadiabatic mechanism of photoisomerization reaction in *trans*-stilbene. In 2-phenylindene, a different reaction coordinate (rotational motion around the C_e-C_{ph} single-bond) was isolated and characterized. A dramatic change in the isomerization rate and barrier-height in PI were observed and compared with the parent molecule.

Table (1): The S_1-electronic origin and the radiative lifetime of *trans*-stilbene (t-S), 4-methoxystilbene (MS), 4,4'-dimethoxystilbene (DMS), 4,4'-dihydroxystilbene (DHS), *trans*-β-cyclo (hexane)styrene (TCHS), and 2-phenylindene (PI).

Molecule	$\lambda\ (0_0^0)$/ Å	$\nu\ (0_0^0)$ / cm^{-1}	$\delta\nu^*$ / cm^{-1}	τ_{rad} / ns
t-S	3101.4	32243.7	0.0	2.63
MS (A)	3252.7	30744.1	-1499.6	2.96
MS (B)	3223.6	31022.6	-1221.1	2.84
DMS	3334.8	29987.0	-2247.7	2.96
DHS	3283.9	30451	-1783.7	3.6
TCHS	3182.9	31417	-817.7	8.9
PI	3183.0	31416.9	-826.6	3.20

* The frequwncy shift ($\delta\nu$) was calculated with respect to the 0_0^0-transition in the unsubstituted *trans*-stilbene.

Table (2): Photoisomerization Barrier *(E_0)* for *trans*-stilbene (t-S), 4-methoxystilbene (MS), 4,4'-dimethoxystilbene (DMS), 4,4'-dihydroxystilbene (DHS), *trans*-β-1-cyclo-(hexane)-styrene (TCHS), and 2-phenylindene (PI).

Molecule	Barrier Height *(E_0)*
t-S	1250
MS (A)	1330
MS (B)	1051
DMS	3060
DHS	2200
TCHS	800
PI	2460

8.5 REFERENCES

1. J. Saltiel and Y. P. Sun, *Photochromism- Molecules and Systems*; H. Durr, and H. Bouas-Laurent, Eds. (Elsevier: Amsterdam 1990), p.64.
2. D. H. Waldeck, *Chem. Rev.* **91**, 415 (1991).
3. J. Saltiel and J. T. D'Agostino, *J. Am. Chem. Soc.* **94**, 6445 (1972).
4. M. Lee, A. J. Bain, P. J. McCarthy, C. H. Han, J. N. Haseltine, A. B. Smith III, and R. M. Hochstrasser, J. Chem. Phys. 85, 4341 (1986).
5. S. C. Shim, J. S. Chae, Bull. Chem. Soc. Jpn. 55, 1310 (1982).
6. J. Saltiel, O. C. Zifiriou, E. D. Megarity, and A. A. Lamola, *J. Am. Chem. Soc.* **90**, 4759 (1968).
7. C. Pyun, T. A. Lyle, G. H. Daub, and S. M. Park, *Chem. Phys. Lett.* **124**, 48 (1986).
8. P. M. Felker, and A. H. Zewail, *J. Phys. Chem.* **89,** 5402 (1985).
9. J. Saltiel, A. Waller, Y. P. Sun, and D. F. Sears Jr., *J. Am. Chem. Soc.* **112**, 4580 (1990).
10. J. Saltiel, J. T. D'Agostino, W. G. Herkstroeter, G. Saint-Ruf, and N. P. Buu- Hoi, *J. Am. Chem. Soc.* **95**, 2543 (1973).
11. W. G. Herkstroeter, and D. S. McClure, *J. Am. Chem. Soc.* **90**, 4522 (1968).
12. J. Saltiel, *J. Am. Chem. Soc.* **90**, 6394 (1968).
13. G. S. Hammond, J. Saltiel, A. A. Lamola, N. J. Turro, J. S. Bradshaw, D. O. Cowan, R. C. Counsell, V. Vogt, and C. Dalton, *J. Am. Chem. Soc.* **86**, 3197 (1964).
14. S. H. Courteny, M. W. Balk, L. A. Philips, S. P. Webb, D. Yang, D. H. Levy, and G. R. Fleming, *J. Chem. Phys.* **89**, 6697 (1988).
15. S. Nordholm, *Chem. Phys.* **137**, 109 (1989).

16. H. Gorner, *Ber. Bunsen.-Gas. Phys. Chem.* **88**, 1199 (1984); and references therein.
17. H. Gorner, and D. Schulte-Frohlinde, *Ber. Bunsen.-Gas. Phys. Chem.* **88**, 1208 (1984).
18. H. Gorner, and D. Schulte-Frohlinde, *Ber. Bunsen.-Gas. Phys. Chem.* **82**, 1102 (1978).
19. D. Schulte-Frohlinde, and H. Gorner, *Pure Appl. Chem.* **51**, 279 (1979); and references therein.
20. H. Gorner, *J. Photochem.* **13**, 269 (1980).
21. H. Gorner, *J. Photochem. Photobiol.* **A40**, 325 (1987).
22. H. Gorner, and D. Schulte-Frohlinde, *J. Phys. Chem.* **83**, 3107 (1979).
23. H. Gorner, and D. Schulte-Frohlinde, *J. Mol. Struct.* **84**, 227 (1982).
24. J. Saltiel, A. Marinari, D. W. L. Chang, J. C. Mitchener, and E. D. Megarity, *J. Am. Chem. Soc.* **101**, 2982 (1979).
25. L.G. Greifenstein, J.B. Lambert, R.J. Nienhuis, H.E. Fried, and G.A. Pagani, *J. Org. Chem.* **46**, 5125 (1981).
26. D. A. Bors, M.J. Kaufman and A. Streitweiser Jr., *J. Am. Chem. Soc.* **107**, 6975 (1985).
27. A few grams of TCHS was given to us as a gift from J. R. Cable.
28. A. Amirav, and J. Jortner, *Chem. Phys. Lett.* **95**, 295 (1983).
29. T. J. Majors, U. Even, and J. Jortner, *J. Chem. Phys.* **81**, 2330 (1984).
30. K. Rademann, U. Even, S. Rozen, and J. Jortner, *Chem. Phys. Lett.* **125**, 5 (1986).
31. L. Bañares, A. A. Heikal, and A. H. Zewail, *J. Phys. Chem.* **96**, 4127 (1992).
32. J. A. Syage, W. R. Lambert, P. M. Felker, and A. H. Zewail and R. M. Hochstrasser, *Chem. Phys. Letters* **88,** 266 (1982).;

33. J. A. Syage, P. M. Felker and A. H. Zewail, *J. Chem. Phys.* **81**, 4685, 4706 (1984).

34. T. Zwier, M. E. Carrasquillo, and D. H. Levy, *J. Chem. Phys.* **78**, 5493 (1984).

35. T. Suzuki, N. Mikami, M. Ito, *J. Phys. Chem.* **90**, 6431 (1986).

36. S. S. Stiewert and L. H. Spangler, *J. Phys. Chem.* **99**, 9316 (1995).

37. T. Troxler, M. R. Topp, B. S. Metzger, and L. H. Spangler, *Chem. Phys. Lett.* **238**, 313 (1995).

38. J. R. Cable, private communication.

39. Syage, J.A.; Felker, P.M.; Zewail, A.H. *J. Chem. Phys.* **81**, 4706 (1984).

40. Troe, J.; Schroeder, J. J. Phys. Chem. 1986, 90, 4215.

41. Troe, J. Chem. Phys. Lett. 1985, 114, 241.

42. *Theory and Applications of Ultraviolet Spectroscopy*, edited by H. H. Jaffe', and M. Orchin (Wiley, New York, 1962).

43. *Techniques of Chemistry III: Photochromism*, edited by G. H. Brown (Wiley, New York, 1971).

44. T. N. Bolotnikova, L. Y. Malkes, A. I. Nazarenko, and V. N. Yankovenko, *Opt. Spekt.* **25**, 621 (1968).

45. T. N. Bolotnikova, L. Y. Malkes, A. I. Nazarenko, and V. N. Yankovenko, *Opt. Spekt.* **26**, 132 (1969).

46. T. N. Bolotnikova, L. Y. Malkes, A. I. Nazarenko, and V. N. Yankovenko, *Opt. Spekt.* **26**, 649 (1969).

47. M. Oki, and H. Kunimoto, *Spectrochim. Acta* **19**, 1463 (1963).

48. W. H. Laarhoven, R. J. F. Nivard, and E. Havinga, *Rec. Trav. Chim. Pays-Bas* **79**, 1153 (1960).

49. R. N. Beale, and E. M. F. Roe, *J. Chem. Soc.* **74**, 2302 (1952).

50. W. Rettig, W. Majenz, *Chem. Phys. Lett.* **154**, 335 (1989).

51. E. Lippert, W. Rettig, V. Bonacic-Koutecky, F. Heisel, and J. A. Miehe, *Advances in Chemical Physics,* edited by S. A. Rice, and I. Prigogine (Wiley, New York, 1987), Vol.68.

52. H. Gruen, and H. Gorner, *J. Phys. Chem.* **93**, 7144 (1989).

53. D. H. Waldeck and D. Beratan, *Private Communication..*

54. D. M. Zeglinski, and D. H. Waldeck, *J. Phys. Chem.* **92**, 692 (1988).

55. N. S. Park, and D. H. Waldeck, *J. Chem. Phys.* **91(2)**, 943 (1989).

56. N. S. Park, and D. H. Waldeck, *J. Phys. Chem.* **94**, 662 (1990).

57. N. S. Park, and D. H. Waldeck, *Chem. Phys. Lett.* **168**, 379 (1990).

58. N. S. Park, and D. H. Waldeck, *Ultrafast Phenomena VII*, edited by C. B. Harris, E. P. Ippen, G. A. Mourou, and A. H. Zewail (Springer, New York, 1990).

59. J. Troe and K. M. Weitzel, *J. Chem. Phys.* **88**, 7030 (1988).

60. Y. Kawaguchi, *J. Chem. Phys.* **100**(12), 8856 (1994).

8.6 FIGURE CAPTIONS

8.1 The chemical structure of *trans*-stilbene (t-S) (top), 4-methoxystilbene (MS) (bottom), 4,4'-dimethoxystilbene (DMS) (middle), and *trans*-β-1-cyclo(hexane)-styrene (TCHS).

8.2 Time-resolved fluorescence decays following the excitation of the S_1-electronic origin in *trans*-stilbene (t-S, bottom), 4-methoxystilbene (MS, middle) and 4,4'-dimethoxystilbene (DMS, top). The estimated radiative lifetime of these origins are 2.65 ns (t-S), 2.96 ns (MS isomer A), and 2.95 ns (DMS).

8.3 Time-resolved fluorescence decays following the excitation of the S_1-electronic origin in *trans*-β-cyclo(hexane)styrene (TCHS, top), 4,4'-dihydroxy-stilbene (DHS, middle), and 2-phenylindene (PI, bottom). The estimated radiative lifetime of the molecules are 8.9 ns (TCHS), 3.6 ns (DHS), and 3.2 ns (PI).

8.4 Representative dispersed fluorescence spectra of DHS molecule excited to S_1+332 and 1173 cm^{-1}.

8.5 The dispersed fluorescence spectrum of the S_1-origin in TCHS molecule.

8.6 The excess-energy dependence of the time (dark circle) and rate constants in *trans*-stilbene.

Trans-stilbene

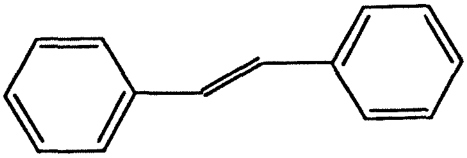

α-Phenyl-β-(1-cyclohexene)-ethylene

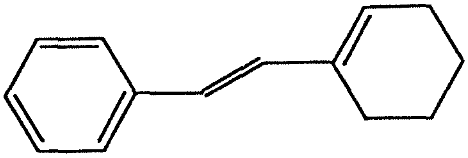

4,4'-Dihydroxystilbene

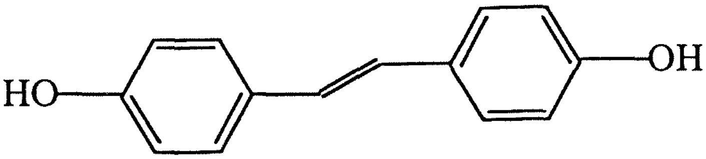

Fig. 8.1

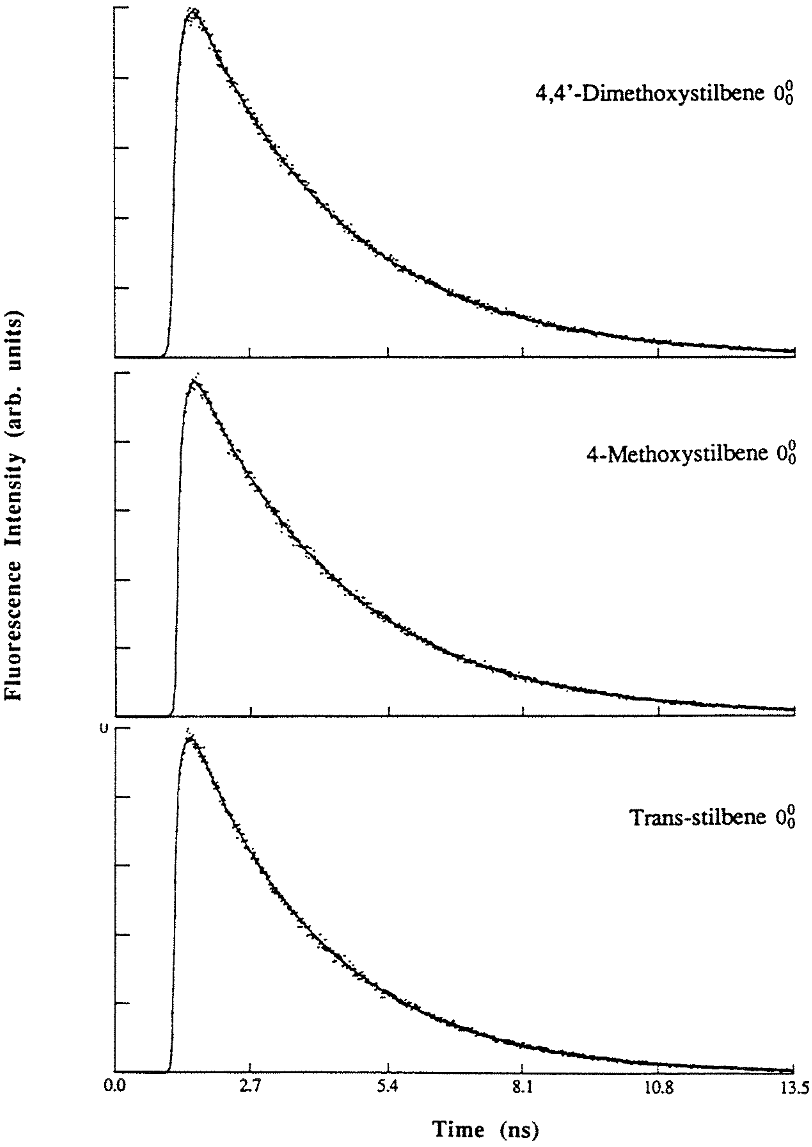
4,4'-Dimethoxystilbene 0_0^0
4-Methoxystilbene 0_0^0
Trans-stilbene 0_0^0
Fluorescence Intensity (arb. units)
0
0.0
2.7
5.4
8.1
10.8
13.5
Time (ns)

Fig. 8.2

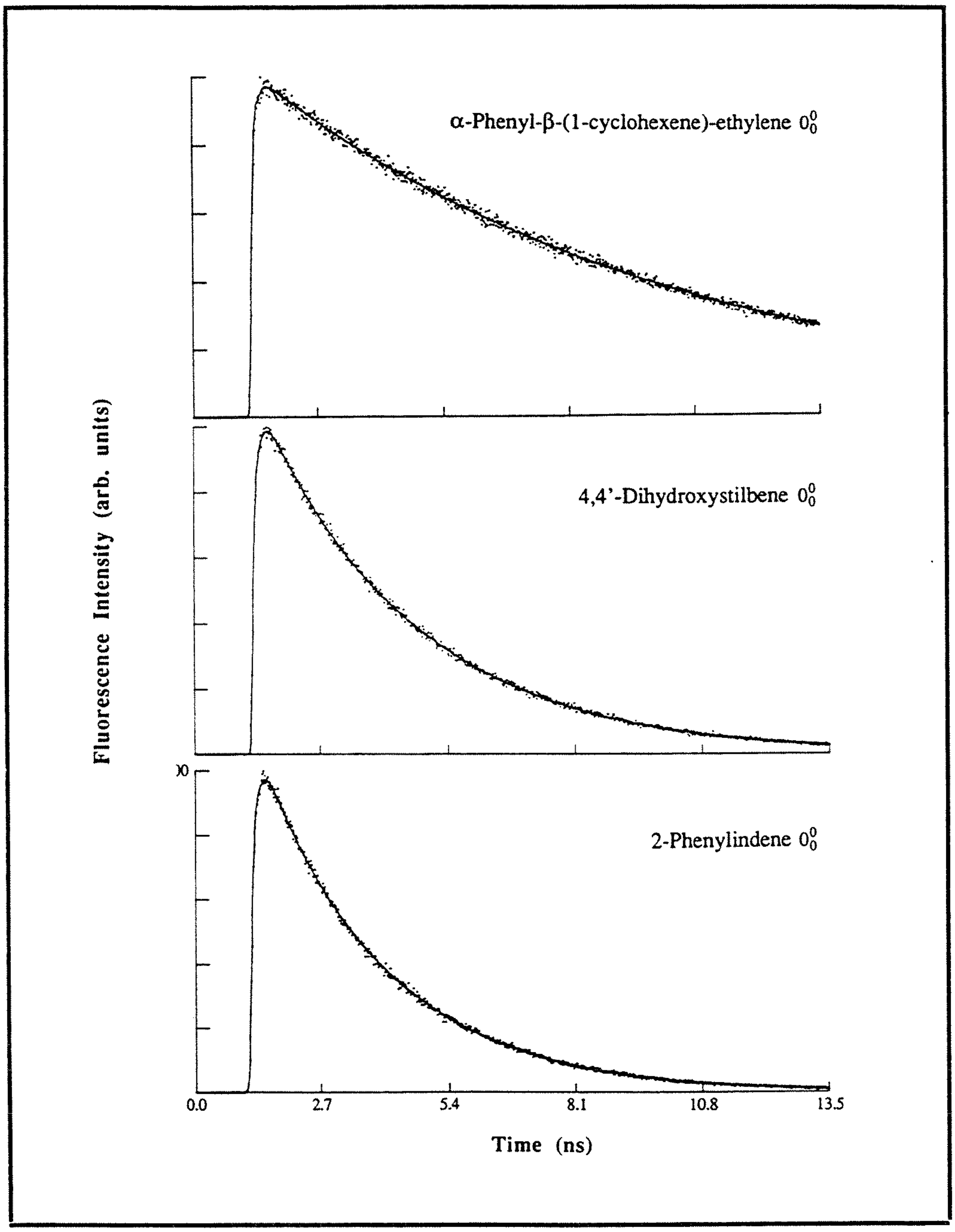
α-Phenyl-β-(1-cyclohexene)-ethylene 0^0_0
4,4'-Dihydroxystilbene 0^0_0
2-Phenylindene 0^0_0
Fluorescence Intensity (arb. units)
0.0
2.7
5.4
8.1
10.8
13.5
Time (ns)

Fig. 8.3

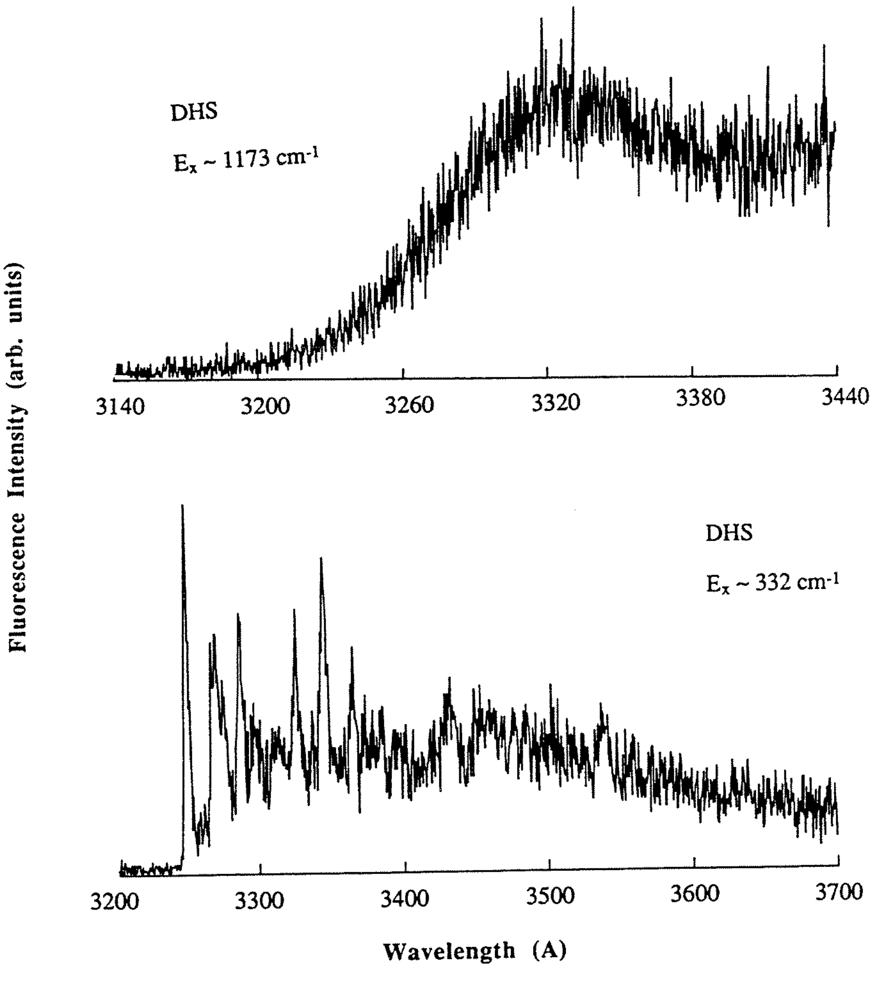
DHS
E$_x$ ~ 1173 cm^{-1}
3140
3200
3260
3320
3380
3440
Fluorescence Intensity (arb. units)
DHS
E$_x$ ~ 332 cm^{-1}
3200
3300
3400
3500
3600
3700
Wavelength (A)

Fig. 8.4

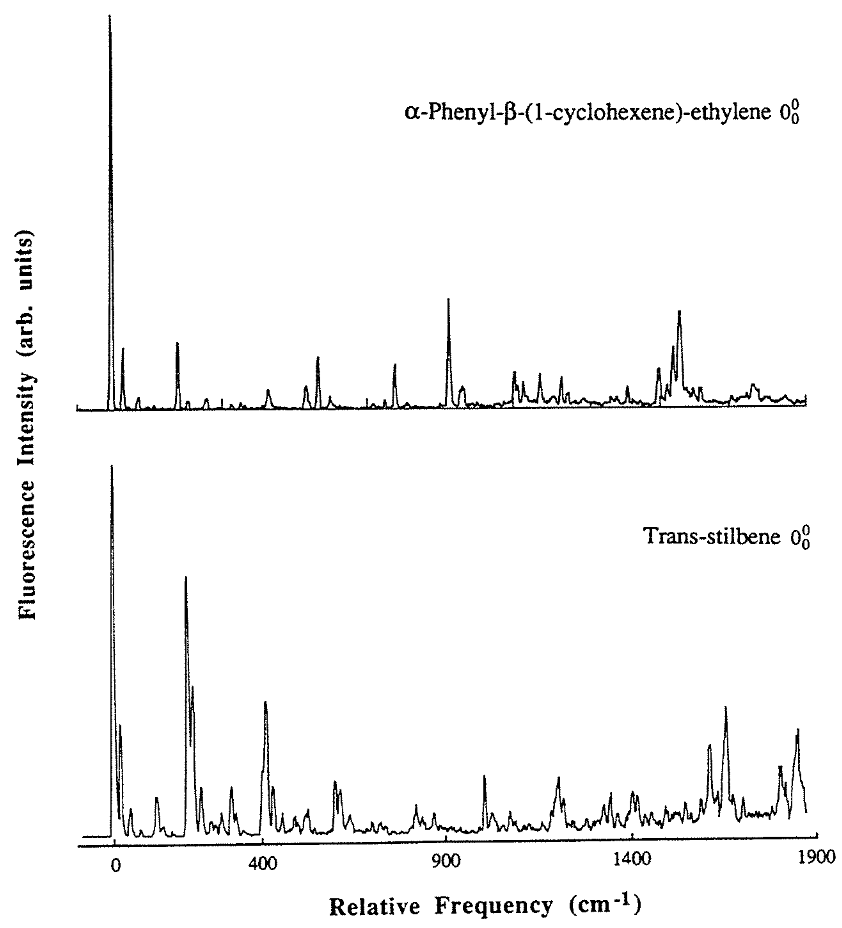
α-Phenyl-β-(1-cyclohexene)-ethylene 0_0^0
Trans-stilbene 0_0^0
Fluorescence Intensity (arb. units)
0
400
900
1400
1900
Relative Frequency (cm^{-1})

Fig. 8.5

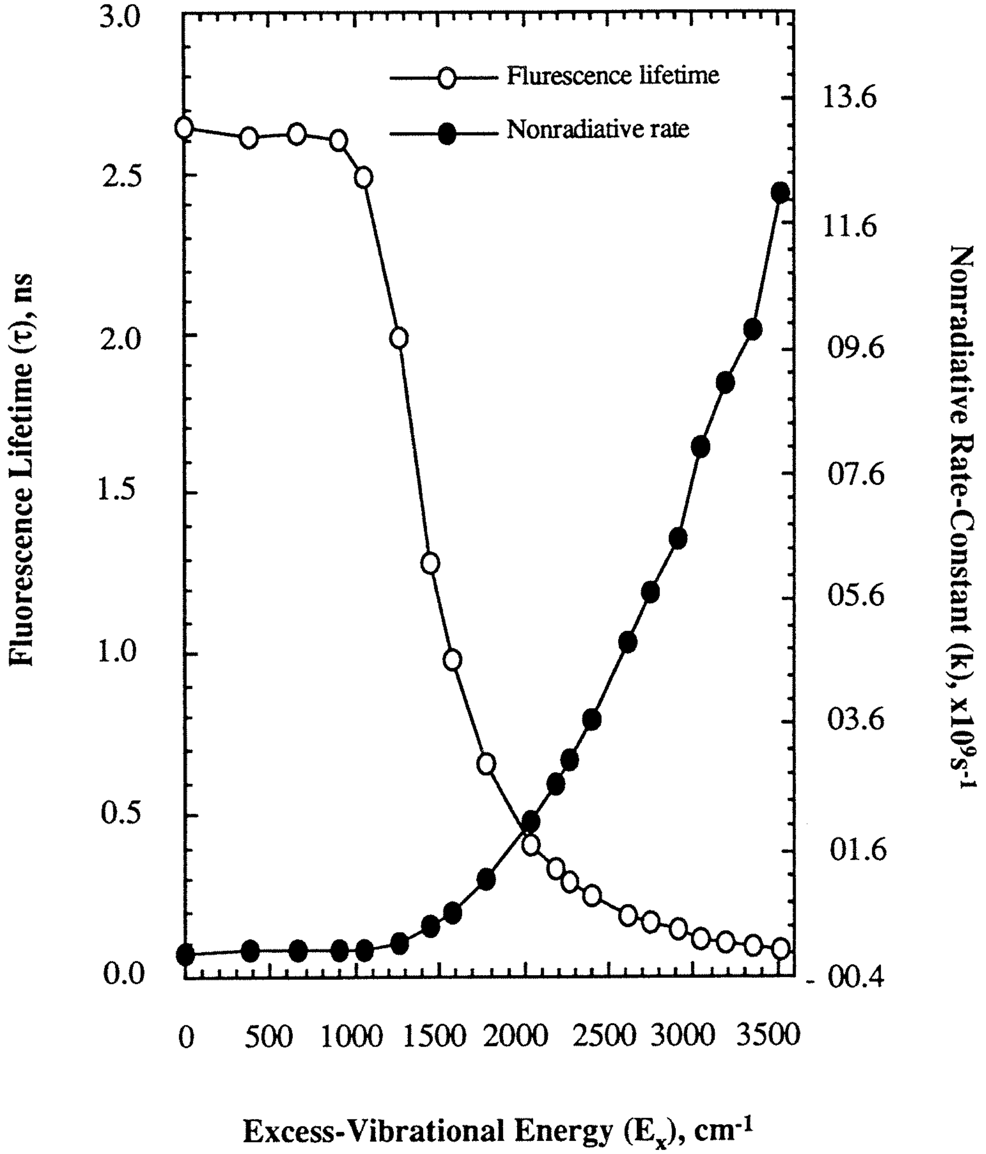
Flurescence lifetime
Nonradiative rate
3.0
2.5
2.0
1.5
1.0
0.5
0.0
13.6
11.6
09.6
07.6
05.6
03.6
01.6
- 00.4
0
500
1000
1500
2000
2500
3000
3500
Fluorescence Lifetime (τ), ns
Nonradiative Rate-Constant (k), x10⁹s⁻¹
Excess-Vibrational Energy (Eₓ), cm⁻¹

Fig. 8.6

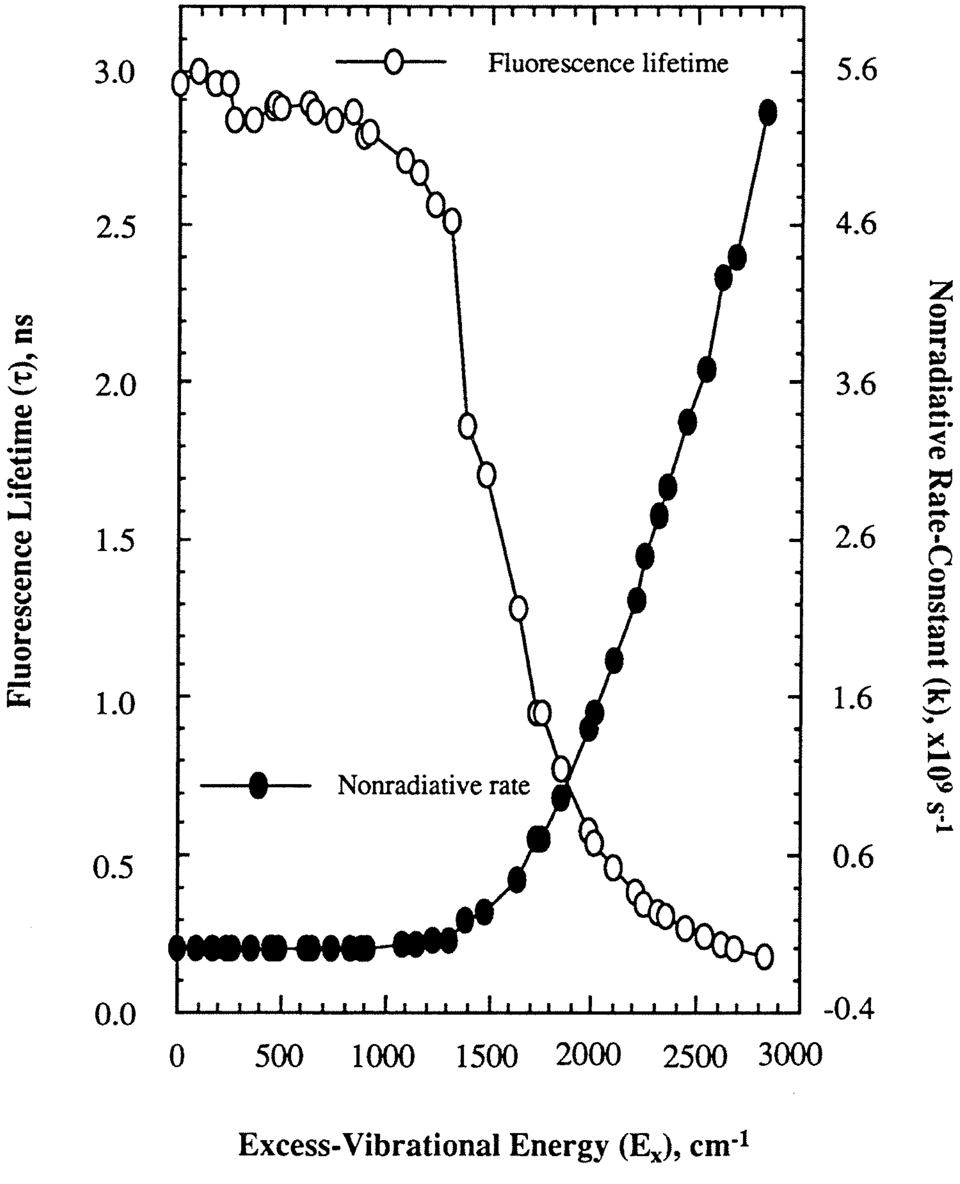
Fluorescence lifetime
Nonradiative rate
Fluorescence Lifetime (τ), ns
Nonradiative Rate-Constant (k), x10⁹ s⁻¹
Excess-Vibrational Energy (Eₓ), cm⁻¹
3.0
2.5
2.0
1.5
1.0
0.5
0.0
5.6
4.6
3.6
2.6
1.6
0.6
-0.4
0
500
1000
1500
2000
2500
3000

Fig. 8.7

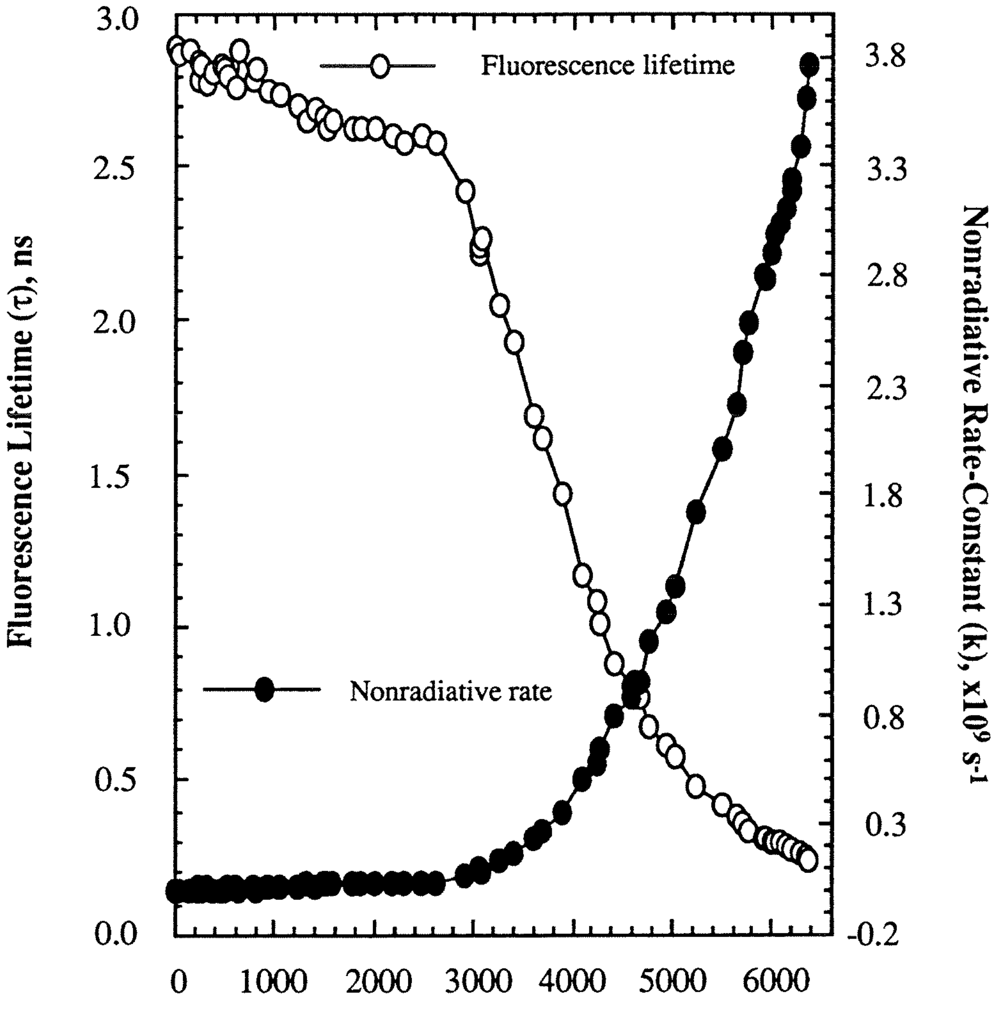
Fluorescence lifetime
Nonradiative rate
Fluorescence Lifetime (τ), ns
Nonradiative Rate-Constant (k), x10⁹ s⁻¹
Excess-Vibartional Energy (Eₓ), cm⁻¹
3.0
2.5
2.0
1.5
1.0
0.5
0.0
3.8
3.3
2.8
2.3
1.8
1.3
0.8
0.3
-0.2
0
1000
2000
3000
4000
5000
6000

Fig. 8.8

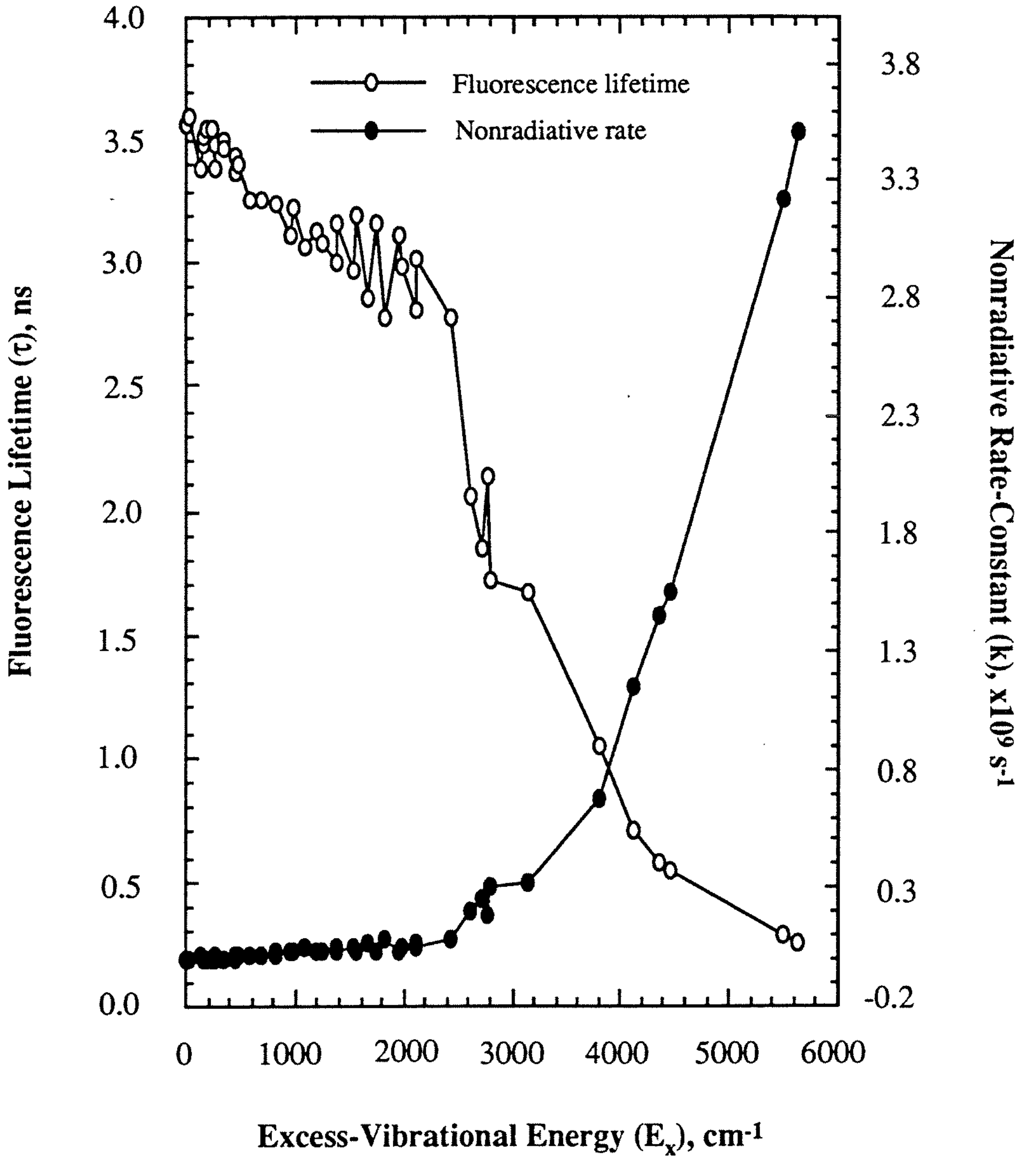
Fluorescence lifetime
Nonradiative rate
Fluorescence Lifetime (τ), ns
4.0
3.5
3.0
2.5
2.0
1.5
1.0
0.5
0.0
Nonradiative Rate-Constant (k), x10⁹ s⁻¹
3.8
3.3
2.8
2.3
1.8
1.3
0.8
0.3
-0.2
0
1000
2000
3000
4000
5000
6000
Excess-Vibrational Energy (Eₓ), cm⁻¹

Fig. 8.9

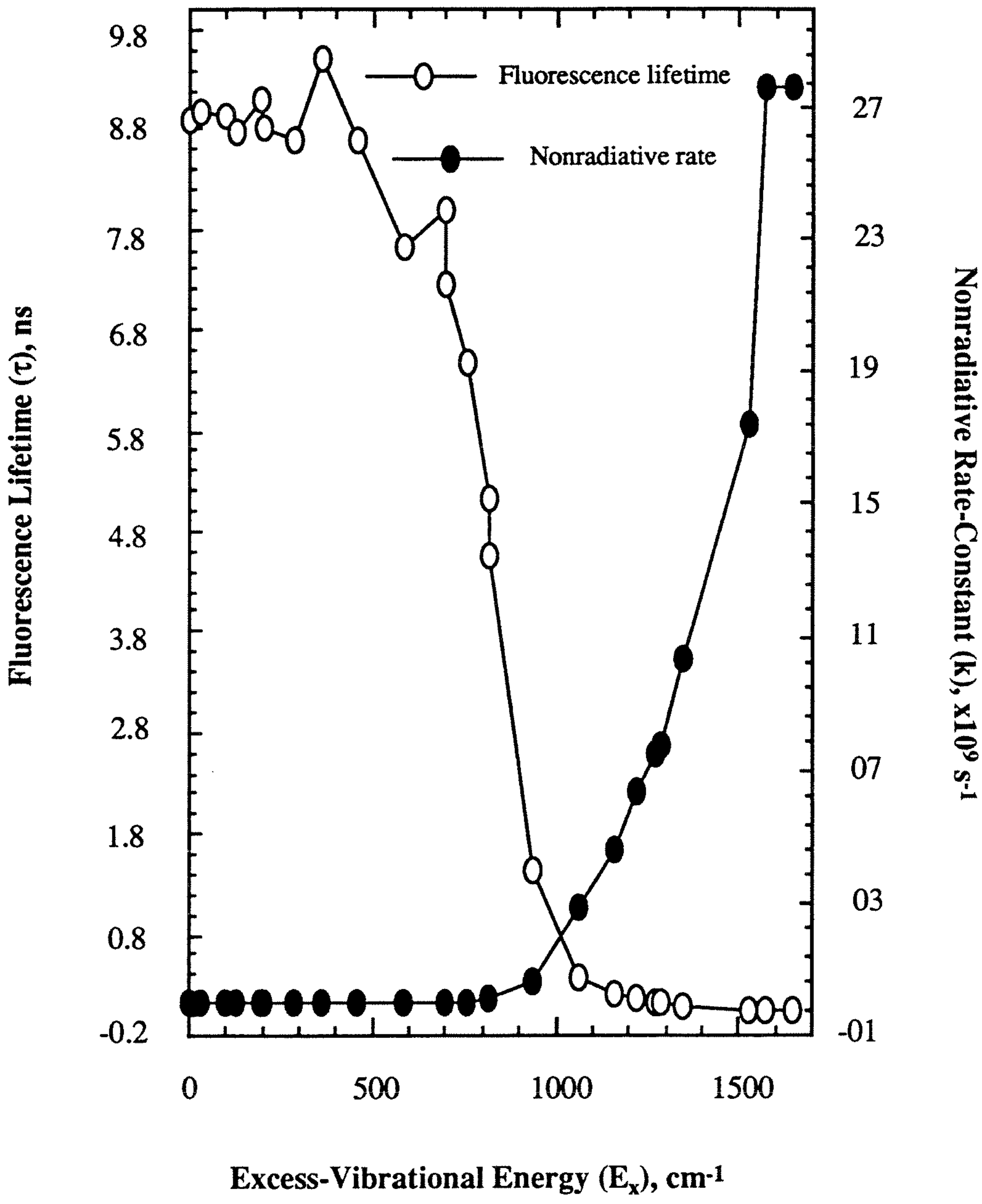
Fluorescence lifetime
Nonradiative rate
Fluorescence Lifetime (τ), ns
Nonradiative Rate-Constant (k), x10⁹ s-1
Excess-Vibrational Energy (Eₓ), cm-1
9.8
8.8
7.8
6.8
5.8
4.8
3.8
2.8
1.8
0.8
-0.2
27
23
19
15
11
07
03
-01
0
500
1000
1500

Fig. 8.10

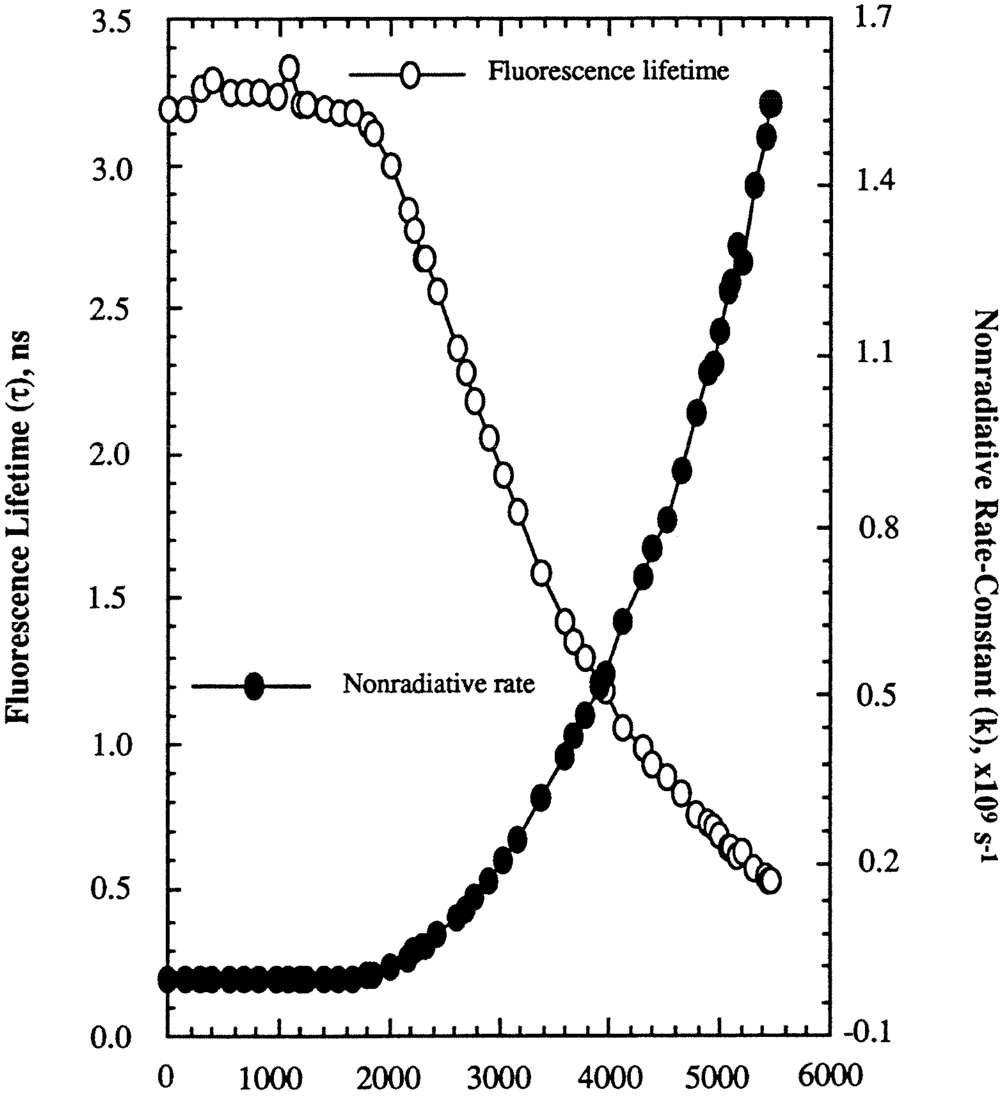
Fluorescence lifetime
Nonradiative rate
Fluorescence Lifetime (τ), ns
Nonradiative Rate-Constant (k), x10⁹ s⁻¹
Excess-Vibrational Energy (Eₓ), cm⁻¹)
3.5
3.0
2.5
2.0
1.5
1.0
0.5
0.0
1.7
1.4
1.1
0.8
0.5
0.2
-0.1
0
1000
2000
3000
4000
5000
6000

Fig. 8.11

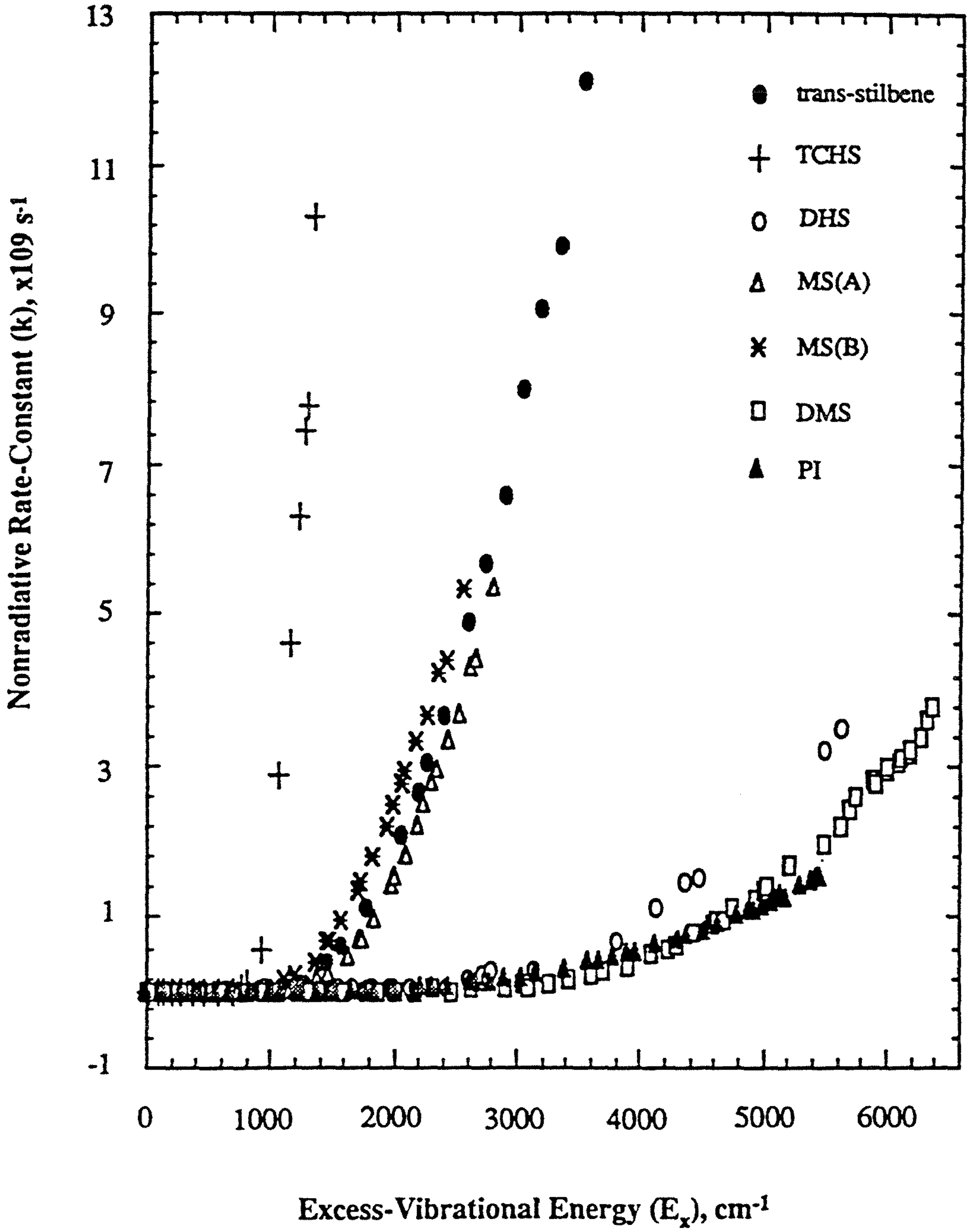
13
11
9
7
5
3
1
-1
0
1000
2000
3000
4000
5000
6000
Nonradiative Rate-Constant (k), x109 s-1
Excess-Vibrational Energy (Ex), cm-1
● trans-stilbene
+ TCHS
○ DHS
△ MS(A)
✱ MS(B)
□ DMS
▲ PI

Fig. 8.12